



Experimental and modeling study of a thermocline latent/sensible heat storage system integrated with a cylindrical-parabolic concentrated solar power plant

Muhammad Asaad Keilany

► To cite this version:

Muhammad Asaad Keilany. Experimental and modeling study of a thermocline latent/sensible heat storage system integrated with a cylindrical-parabolic concentrated solar power plant. Chemical and Process Engineering. Ecole des Mines d'Albi-Carmaux, 2020. English. NNT : 2020EMAC0019 . tel-03793328

HAL Id: tel-03793328

<https://theses.hal.science/tel-03793328>

Submitted on 1 Oct 2022

HAL is a multi-disciplinary open access archive for the deposit and dissemination of scientific research documents, whether they are published or not. The documents may come from teaching and research institutions in France or abroad, or from public or private research centers.

L'archive ouverte pluridisciplinaire **HAL**, est destinée au dépôt et à la diffusion de documents scientifiques de niveau recherche, publiés ou non, émanant des établissements d'enseignement et de recherche français ou étrangers, des laboratoires publics ou privés.



THÈSE

En vue de l'obtention du

DOCTORAT DE L'UNIVERSITÉ DE TOULOUSE

délivré par

IMT – École Nationale Supérieure des Mines d'Albi-Carmaux

présentée et soutenue par

Muhammad Asaad KEILANY

le 18 décembre 2020

Titre :

Experimental and modeling study of a thermocline latent/sensible heat storage system integrated with a cylindrical-parabolic concentrated solar power plant

École doctorale et discipline ou spécialité :

MEGEP : Energétique et transferts

Unités de recherche :

Centre RAPSODEE, UMR CNRS 5302, IMT Mines Albi
Centre PROMES, UPR CNRS 8521, Odeillo-Font Romeu

Directeurs de thèse :

Jean-Jacques BEZIAN , Professeur, IMT Mines Albi
Quentin FALCOZ, Maître-assistant, UPVD, CNRS-PROMES Odeillo

Autres membres du jury :

Benoît STUTZ, Professeur, Université de Savoie Le Bourget du Lac (Rapporteur)
Jean-Pierre BEDECARRATS, Professeur, UPPA Pau (Rapporteur)
Elena PALOMO DEL BARRIO, Professeur, CIC EnergiGUNE Vitoria-Gasteiz Espagne (Présidente)
Sandrine PINCEMIN, Ingénieure de Recherche, EPF Montpellier (Examinatrice)
Mathieu MILHE, Maître-assistant, IMT Mines Albi (Examinateur)
Gilles FLAMANT, Directeur de Recherche Emérite, CNRS-PROMES Odeillo (Examinateur)

**EXPERIMENTAL AND MODELING
STUDY OF A THERMOCLINE
LATENT/SENSIBLE HEAT
STORAGE SYSTEM INTEGRATED
WITH A CYLINDRICAL-
PARABOLIC CONCENTRATED
SOLAR POWER PLANT**

This work is a collaborative research activity between two leading laboratories of renewable energy systems in France. RAPSODEE-CNRS (UMR 5302) Ecole de mines-Albi (Recherche d'Albi en génie des Procédés des Solides Divisés, de l'Énergie et de l'Environnement), and PROMES-CNRS (UPR 8521) (Procédés, Matériaux, Énergie Solaire) Odeillo, in France.

The French “Investments for the Future” program managed by the National Agency for Research funded this work under contract ANR-10-LABX-22-01 (LABEX SOLSTICE) and ANR-10-EQPX-49-(Equipex SOCRATE).

Table of Contents

INTRODUCTION	5
1. LITERATURE REVIEW	11
1.1. SENSIBLE HEAT TES	13
1.2. LATENT HEAT FOR TES	19
1.2.1. PCM applications	19
1.2.2. PCM classifications	19
1.2.3. Prescribed PCM features for TES	21
1.2.4. PCM envelop and encapsulations	24
1.2.5. PCM disadvantages.....	25
1.2.6. PCM thermal performance enhancement methods	28
1.3. NUMERICAL MODELING FOR THERMOCLINE TES	30
1.3.1. Model for sensible heat TES.....	33
1.3.2. Models for melting and solidification of PCM.....	46
1.3.3. Models for latent heat TES.....	51
1.3.4. Models for combined latent and sensible heat TES.....	60
1.4. HEAT TRANSFER CORRELATIONS FOR THERMOCLINE MODELS	64
1.4.1. Convection heat transfer HTF-Filler.....	64
1.4.2. Convection heat transfer HTF-wall.	67
1.4.3. Thermal losses at the outside thermocline wall.	67
1.4.4. Effective thermal conductivity of the HTF and the soild filler	68
1.4.5. Natural convection inside PCM	69
1.5. RESEARCH PROBLEMS AND DISSERTATION OBJECTIVES	71
2. MATERIALS AND METHODS	73
2.1. EXPERIMENTAL SETUP	75
2.1.1. The MICROSOL-R.....	75
2.1.2. Differential Scanning calometry (DSC)	78
2.1.3. Electrical furnace.....	78
2.2. TES MATERIALS	78
2.2.1. Sensible heat storage materials	78

2.2.2. Latent heat storage material	80
2.3. THERMOCLINE PERFORMANCE INDICATORS.....	81
2.3.1. Process duration	84
2.3.2. Thermocline thickness	84
2.3.3. Process efficiency	84
2.4. NUMERICAL MODELING	86
2.4.1. One-dimensional Continuous Solid model.....	87
2.4.2. One-dimensional Dispersion Concentric model.....	93
2.4.3. Heat transfer correlations	98
3. EXPERIMENTAL COMPARISON BETWEEN TWO SENSIBLE HEAT STORAGE MEDIUMS, WITH PARAMETRIC STUDY AND COMBINING APPROACH	101
3.1. EXPERIMENTAL COMPARISON	103
3.1.1. Process Duration	104
3.1.2. Thermocline thickness	105
3.1.3. Charge and discharge efficiencies	107
3.2. C-S MODEL VALIDATION	109
3.2.1. Charge process.....	109
3.2.2. Discharge process.....	111
3.3. PARAMETRIC ANALYSIS	113
3.3.1. Process duration	114
3.3.2. Thermocline thickness	114
3.3.3. Process Efficiency	117
3.4. COMBINING TWO SHSMs IN THE SAME THERMOCLINE TES	119
3.5. CONCLUSIONS.....	122
4. COMBINING LAYER OF PCM TO SENSIBLE HEAT THERMOCLINE, MODELING AND SIZING APPROACH	123
4.1. D-C MODEL VALIDATION.....	125
4.1.1. D-C validation for a sensible heat thermocline TES filled with alumina spheres as SHSM	125
4.1.2. Comparison between C-S and D-C for latent heat thermocline TES of NaNO ₃ PCM spheres	127
4.1.3. Validation from literature experiment	132

4.2. COMBINING A LAYER OF PCM TO SENSIBLE HEAT THERMOCLINE TES	135
4.2.1. Charge process	136
4.2.2. Discharge process	137
4.2.3. Performance comparaisn	138
4.3. PCM LAYER SIZING APPROACH IN COMBINED LATENT TO SENSIBLE HEAT THERMOCLINE TES	139
4.3.1. Analytical method	140
4.3.2. Results and comparison to literature.....	144
4.3.3. Case study thermocline TES of MICROSOL-R	145
4.3.4. Numerical evaluation of the case study	146
4.4. CONCLUSIONS	151
5. EXPERIMENTAL AND NUMERICAL EVALUATION OF COMBINING LATENT HEAT LAYER TO SENSIBLE HEAT THERMOCLINE TES	153
5.1. PCM LAYER DESIGN	155
5.1.1. Material selection	155
5.1.2. Encapsulation design	157
5.1.3. Tube dimensions	158
5.1.4. Safety Analysis	164
5.1.5. Detailed design	167
5.1.6. Layer Assembly and testing	169
5.1.7. The final PCM layer package	170
5.2. MODEL VALIDATION OF THE THERMOCLINE WITH COMBINED TUBES-CONTAINED PCM TO SENSIBLE HEAT FILLER (TPCM-S)	172
5.2.1. Model adjustment	172
5.2.2. Operating conditions of the experiments and simulation.	172
5.2.3. Charge process	173
5.2.4. Discharge process	175
5.3. EXPERIMENTAL EVALUATIONS	178
5.3.1. Charge process	178
5.3.2. Discharge process	186
5.3.3. Stand-by mode	194
5.4. PERFORMANCE EVALUATION OF TPCM-S. AGAINST SINGLE MEDIUM THERMOCLINE	195
5.4.1. Numerical charge tests	195

5.4.2. Numerical discharge tests	199
5.4.3. Discussion	203
5.5. CONCLUSIONS	205
6. CONCLUSIONS SUMMARY AND PERSPECTIVES	207
6.1. PERSPECTIVES	210
7. BIBLIOGRAPHY	213
8. NOMENCLATURE	231
9. LIST OF FIGURES	237
10. LIST OF TABLES	243
11. APPENDIX.....	245
11.1. UNCERTAINTY OF MEASUREMENTS	247
11.2. TEMPERATURE-DEPENDENT THERMOPHYSICAL PROPERTIES OF MATERIALS.....	248
11.3. COMPUTER SPECIFICATIONS.....	249
11.4. CASE STUDY: ODEILLO THERMOCLINE ADDITIONAL POTENTIAL PCMs	250
11.5. COMMERCIAL TUBE DATA	251
12. RESUME LONG DE THESE EN FRANÇAIS	253
12.1. INTRODUCTION	255
12.2. LA CONFIGURATION DE L'EXPERIENCE	257
12.3. PARAMETRES DE PERFORMANCE	260
12.4. RESULTATS EXPERIMENTAUX	261
12.5. LES SIMULATIONS NUMERIQUES.....	265
12.6. RESUME DES CONCLUSIONS	276
12.7. LES PERSPECTIVES	278

INTRODUCTION

In 2015 at the COP21 Paris conference, governments have pledged to reduce greenhouse gas emissions, in order to try to keep the global rise of temperature near the targeted 2°C, while respecting the increasing need of energy to boost their economies. Currently, about two third of greenhouse gas (GHG) emissions in the world are produced by energy-related means [1], while the energy demand is rising quickly, the countries are fulfilling their energy demand by using mainly fossil fuel, 78% as of 2013 [2]. Therefore, advancing renewable energy resources and developing efficient energy storage systems will be the key to achieve Paris COP21 goals of protecting the environment and, at the same time, meet the energy demand of the growing economy.

Concentrated solar power (CSP) is one of the promising renewable energies that could help many countries achieving their pledges to COP21. Indeed, according to IEA [3], CSP could supply about 10% of the global electricity demand in 2050 (about 620 GWhe).

Even though CSP has great potential and many environmental benefits, it has a high capital cost, which needs to be reduced by 30% in order to compete against current commercial power plants, considering only the energy value [4]. However, adding a TES to a CSP plant installed in a high solar irradiance area such as Texas is commercially competitive even to common non-renewable energy resources [4].

One of the main advantages of CSP plants is the ability to store energy on a big scale using thermal energy storage (TES) to provide 24 hours a day operation[5]. Since the TES allows the CSP plants to cope with the intermittent nature of solar radiation by providing energy buffer during transient weather conditions, time-shifting, increasing capacity factor, and having an even distribution of electricity production [6]. Additionally, integrated TES to CSP pictures a stabilization solution to a renewable energy powered grid, such as wind and photovoltaic (PV)[7].

Furthermore, TES has a vital contribution to the development of efficient thermal applications similar to air conditioning heat sinks, space, water heating, and cooling [8].

I. Dincer and A. Rossen [8] summarized the main areas to research in TES development as follows:

- Numerical models that confirm the impact, storage –capacity advantages, performance, reliabilities, optimization, and economic margins.
- Analyze the benefits of localized TES as the function of geographic locations, energy supply, and energy demand.
- Evaluate the potential integration between TES and load control for zones of varying load nature.

- Research the localized TES concept to localized energy generation in the context of total integrated energy systems.
- Investigate advanced TES technologies for their time availability and broader working temperature.

There are three forms to store thermal energy: sensible heat (liquid and solid media, or underground TES), latent heat (solid-liquid, liquid-gas or solid-solid), and thermo-chemical (heat reaction, heat pump, and thermal chemical pipeline)[9]. CSP plants are generally using only three types of TES: sensible heat, latent heat, and thermo-chemical heat storage [10].

Kuravi et al.[11] demonstrated that the most commercially developed storage technology to CSP plants is the two-tank solution Table 1.

Table 1 commercial CSP plants with the integrated TES

Project	CSP technology	TES	TES capacity
SSPS-DCS test facility Almeria, Spain	Parabolic trough	One tank	5 MWh _{th}
Nevada, Solar one USA	Parabolic trough	Oversized filed piping	0.5 h
Holaniku, Hawaii USA	Parabolic trough	Indirect 2 tank	2 h
Planta solar 10 Sevilla, Spain	Central receiver	Steam accumulator	50 min
Planta solar 20 Sevilla, Spain	Central receiver	Steam accumulator	50 min
La florida Badajoz	Parabolic trough	Indirect - Two tanks	7.5 h
Andasol -1 Granada, Spain	Parabolic trough	Indirect - Two tanks	7.5 h (1010 MWh _{th})
Andasol -2 Granada, Spain	Parabolic trough	Indirect - Two tanks	7.5 h (1010 MWh _{th})
Extresol -1 Badajoz, Spain	Parabolic trough	Indirect - Two tanks	7.5 h
Manchasol -1 Ciudad Real, Spain	Parabolic trough	Indirect - Two tanks	7.5 h
Manchasol -2 Ciudad Real, Spain	Parabolic trough	Indirect - Two tanks	7.5 h
La Dehesa, Ciudad Real, Spain	Parabolic trough	Indirect - Two tanks	7.5 h
Puerto Errado 1	Linear Fresnel	Steam accumulator	(No Info.)
Archimede Sicily, Italy	Parabolic trough	Direct - Two tanks	8 h (100 MWh _{th})
Terresol, Gemasolar Seville, Spain	Central receiver	Direct - Two tanks	15 h

Py et al. [5] concluded that about 49% of the two-tank TES cost is attributed to the HTF (molten salts). This percentage is subjected to increase affected by material availability at a higher demand of the projected 10% CSP share of global energy demand by 2050.

On the other hand, thermocline TES could be an economically viable TES solution in CSPs because it replaces a two-tank TES system with a single tank. Moreover, it uses inexpensive filler materials to increase the volumetric heat capacity of the TES and decrease the need for expensive heat transfer fluid (HTF). J.E. Pacheco et al. [12] concluded that a thermocline filled with quartzite rocks and operates with molten salts as HTF costs only 66% of the total investment for two tanks installation, that uses molten salts as a storage medium as well as an HTF.

However, during the TES operation of a charge and discharge process, a thermal gradient layer, typically called the thermocline thickness (or region), develops between the hot and cold regions of the tank. The quality of stored and released energy degrades inside this region, while this layer is expanding during the operation. It could account for up to 33% of total tank height [13], which reduces the efficiency of the system by shortening the useful time of operation and available heat.

Although thermocline TES provides a cost reduction opportunity, it is still not widely used in commercial installations. Companies may be lacking the initiatives to apply the thermocline TES. Where there very few installed projects that led to less or no operational data available for commercial adaptation. Furthermore, some challenges need further research and analysis, such as thermocline thickness, stable output temperature, safety issues, materials issues, and keeping the investment cost competitive to the two tanks system.

In this context, this work aims to

- Compare two sensible heat storage mediums experimentally, and develop proper numerical model to perform a parametric study.
- Develop a numerical model of a thermocline with a layer of phase change material combined to sensible heat storage mediums, and suggest a sizing approach of the PCM layer.
- Provide an experimental and numerical evaluation of combined latent heat layer to sensible heat thermocline.

1. LITERATURE REVIEW

This work covers broad aspects of TES applications such as the sensible heat storage, the latent heat storage, the combined approach between these two, besides the modeling part. Therefore, to facilitate observing recent developments in each of these fields, this section is categorized to the following subsections:

1. Sensible heat TES.
2. Latent heat TES.
3. Numerical modeling of thermocline TES sensible, latent, and combined
4. Heat transfer correlations for thermocline models.
5. Research problem and the dissertation's objectives.

1.1. SENSIBLE HEAT TES

Sensible heat TES systems are essential needs for over 70% of the ongoing CSP plant projects, where they provide reliable, economical, accessible, and widely implemented solutions compared to the other two forms of TES, the latent and thermochemical TES [10].

A proper design of TES for CSP takes into account the following criteria[14]:

- A high energy density of storage material.
- An excellent heat transfer coefficient between HTF and the storage medium.
- Storage material to exhibit good endurance mechanically and chemically at the working temperature.
- Compatible with the HTF and heat exchanger material.
- The charge-discharge operating cycle is entirely reversible.
- Low thermal losses.
- Low cost.
- Low environmental impact.

In CSP plants, there are active and passive TES [10]. In the active TES, the heat storage medium moves through the system, while in the passive one, the storage medium remains inside the storage tank.

The active system can be categorized under two main types, direct and indirect TES. The active-direct system uses the same fluid as HTF as well as in the storage tank, where Figure 1(a) represents an active-direct two-tanks TES. In

contrast, the active-indirect system separates the HTF from the storage tank by a heat exchanger, where Figure 1(b) represents an active-indirect two-tank TES, and Figure 1(c) illustrates an active-indirect thermocline TES.

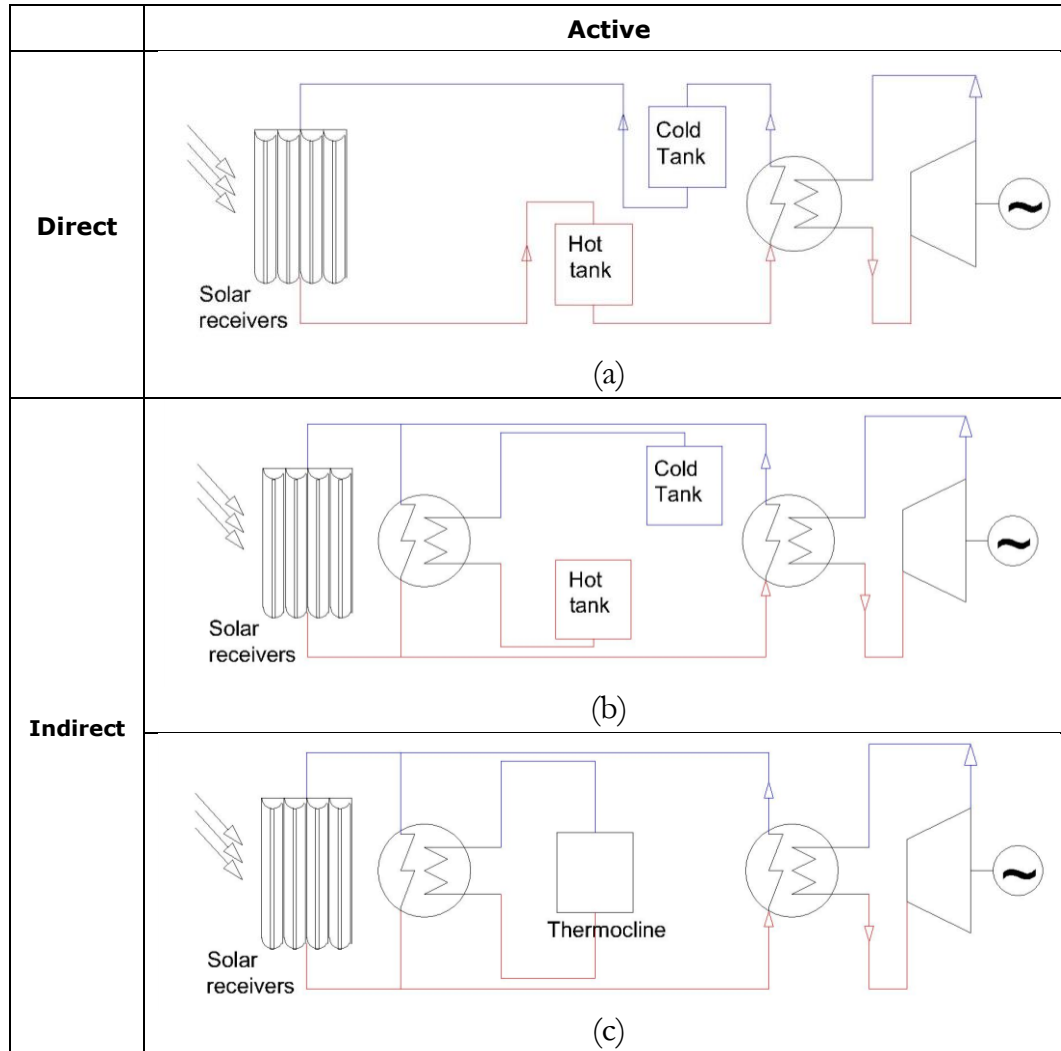


Figure 1 TES for solar power plants (a) direct two-tanks, (b) indirect two-tank, and (c) indirect thermocline.

On the other hand, passive TESs only exist in an indirect configuration, where Figure 2 represents a passive-indirect thermocline that is charged either by the solar field (a) or by a heat exchanger that separates HTF in the solar field from the HTF in the storage system (b).

Generally, the two-tank TES consists of a hot storage tank and a cold storage tank. Where the two-tank system has less thermal stratification potential than the one tank, between hot and cold medium, more importantly, it allows the use of the active-direct TES in the CSP plant[15], which is simple and easy to operate compared to other solutions. The efficiency of such a system over a year of operation was found over 90%[8].

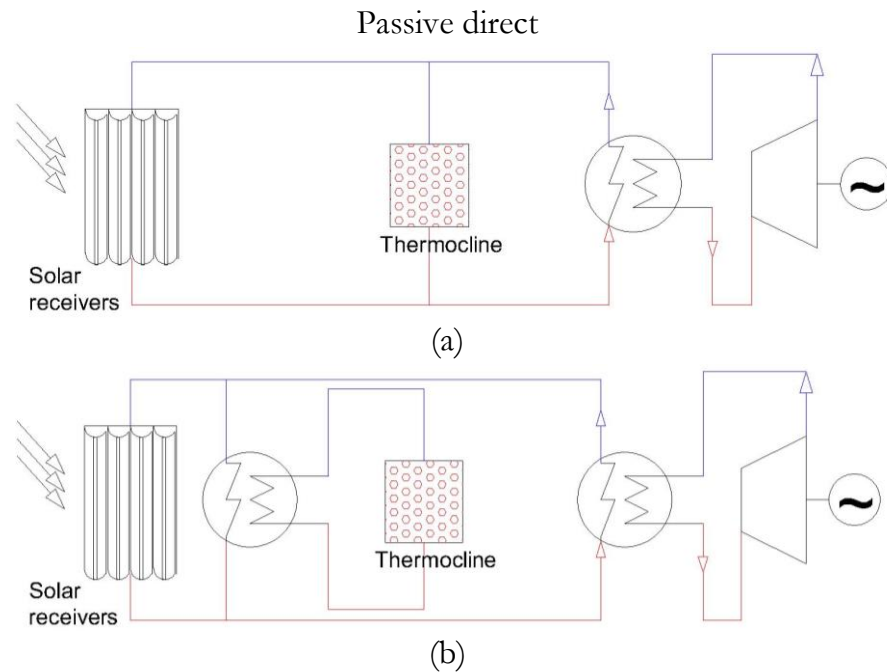


Figure 2 passive TES

The thermocline TES uses only one tank, which reduced the cost of its construction compared to the two-tank system, and reduced the amount of HTF to fill the second tank. However, a high level of thermal stratification during charge and discharge [16] is expected compared to the two-tanks system, which is known as the thermocline thickness.

The thermocline thickness causes a longer charge duration until the outlet temperature reaches the highest temperature. While during discharge, it causes uneven outlet temperature, which is generally required to be stable during the discharge to improve the downstream application performance. Assuming a large heat transfer coefficient between the filler materials and HTF, then the temperature profile should be square, and the thermocline thickness is avoided [16].

Mira-Hernández et al. [17] concluded that using solid filler material in thermocline TES implies a larger thermocline thickness when compared to solely liquid storage. They ascribed that to the higher thermal diffusivity of the solid filler materials compared to the HTF. However, the additional heat exchange limitation between HTF and solid filler when introducing the latter could be the driver for a more significant thermocline thickness, than the thermal diffusion of solid filler.

Bonanos et al.[18] suggested that the most influencing parameters on thermocline thickness are the aspect ratio of tank height over diameter and the thermophysical properties of the solid filler. Furthermore, they indicated that using a smaller tank height and more thermally diffusive solid fillers will cause a larger

thermocline thickness. Other parameters have less impact on thermocline thickness, such as the diameter of the solid filler, porosity, thermo-physical properties of the HTF, and charge time. At the same time, the mass flow rate was not evaluated in this work.

J.F.Hoffmann et al. [19] suggested that there is an optimal mass flow rate at which a maximum discharge efficiency can be harvested from the thermocline TES. The value of this rate depends on the filler particle size. Where applying a low discharge rate at large particle diameter increases thermal losses to the environment as well as the thermal diffusion within the particles. While using a high discharge rate for small particles results in a more significant heat transfer carried by the HTF compared to the heat exchanged between the HTF and the small particle.

Hence, selecting suitable solid filler materials for TES has a significant influence on the properties of the whole TES and its performance. Khare. et al. [20] listed the essential requirements of sensible heat storage medium (SHSM) in Table 2.

Table 2 required characteristics in materials for sensible heat storage

Criteria	description
Thermo-Physical	The higher the thermal conductivity, the better the effective heat transfer.
	Higher energy density decreases the total volume of the required storage and increases thermal capacity.
	Demonstrate thermal stability upon subjecting to thermal cycling.
Chemical	Chemical stability for the projected life cycle of the storage and operating conditions, with minimal material deterioration.
	Satisfies human safety requirements such as non-toxicity, nor explosive potential, even from any decomposed materials may appear during the projected life cycle.
	Compatibility with the HTF as well as tank construction materials, minimal corrosion, and reactivity are required.
Mechanical	Sufficient mechanical stability, with high compressive strength, adequate fracture toughness, and low thermal expansion.
Commercial	Low cost of material, production, and transportation.
	Availability of the materials.
Environmental	Low on no hazardous on the environment.
	Low impeded cost of energy.
	Minimal CO2 footprint.

Furthermore, different liquids were investigated for potential use as SHSM for CSP. Table 3 summarizes the average properties of various liquids used as SHSM [21]–[23].

Besides to liquid SHSM, diverse materials were evaluated for potential use as solid filler SHSM: Table 4 shows data collected from literature [12],[21],[24]–[30].

The liquid SHSM is dominating the commercial installation of TES in the CSP plant [31]. Mainly because it is easier to implement than other media, besides it is widely used in conventional power plants [32]. It also satisfies most of the required criteria for TES illustrated in Table 2, and it avoids using a solid filler that leads to heat exchange limitation between HTF and solid filler.

Table 3 Average properties for liquid storage mediums

Storage materials	$\rho \cdot C_p$ [kWh/m³.K]	ρ [Kg/m³]	k_f [W/m.K]	T range [°C]	cost [€/ton]
HITEC solar salt	n/a	n/a	n/a	133/120	n/a
Mineral oil	0.56	770	0.12	300/200	1,605
Synthetic oil	0.58	900	0.11	350/250	14,198
Silicon Oil	0.53	900	0.1	400/300	21,605
Nitrite salts*	0.76	1825	0.57	450/250	3,086
Nitrate salts**	0.83	1870	0.52	565/265	1,646
Carbonate salts	1.05	2100	2	850/450	8,889
Liquid sodium T_m 98°C	0.38	1042	64.9	530/270	1,481
Sodium(22.2%) potassium(77.8%) eutectic (NaK)	0.19	780	26.3	530/270	1,481
Lead (44.5%) bismuth(55.5%) eutectic (LBE)	0.4	10300	14.9	1200 max	9,630
Therminol	0.49	904	0.11	400 max	18,519
Syltherm XLT	0.34	660	0.06	316 max	21,778
Jarysol ®oil	0.50	836	0.105	350 max	7,177

*48%Ca (NO₃)₂, 7%NaNO₃, 45%KNO₃. **60%NaNO₃, 40%KNO₃

Table 4 Average properties for solid storage mediums

Storage materials	$\rho \cdot C_p$ [kWh/m³.K]	ρ [Kg/m³]	k_f [W/m.K]	T range [°C]	cost [€/ton]
sand-solid-mineral oil	0.61	1700	1.0	300/200	11,200
Reinforced concrete	0.52	2200	1.5	400/200	7,000
NaCl (solid)	0.51	2160	7.0	500/200	23,000
Cast iron	1.12	7200	37.0	400/200	36,500
Cast steel	1.30	7800	40.0	700/200	74,000
Stainless steel	1.12	8030	23	Max 1500	Unknown
Silica fire bricks	0.51	1820	1.5	700/200	14,400
Magnesia fire bricks	1.25	3000	5.0	1200/200	18,500
Granite	0.64	2575	2.8	Max 350	1,400
Quartzite	0.59	2490	2	max 600	30
Marble	0.63	2685	7.7	Max 400	90
Basalt	1.08	2640	3.2	Max 400	30
steel slag	0.83	3000	2.75	Max 1000	Unknown
Cofalit®	0.79	3100	2.05	Max 1000	8
Alumina Ceramics	0.89	3900	18	Max 1200	4500
Industrial ceramics	0.84	3200	1.35	Max 1500	3500~6800
Coal fly ashes	0.73	2600	1.7	Max 1200	Unknown

1.2. LATENT HEAT FOR TES

Phase change material (PCM) has a unique capacity to store and release a large amount of thermal energy at a relatively constant temperature. Most materials experience a phase change at various temperatures with a different rate to absorb/liberate the thermal energy in the form of latent heat of fusion L_{fus} [33].

The interest of this work is the liquid/solid phase change, which is the most commonly used form of PCM.

1.2.1. PCM applications

Phase change material attracted the attention of research and development in different fields because it has a great potential to use as thermal energy storage as well as temperature control applications, Table 5 lists some of its utilizations [34]–[37]:

Table 5 PCM applications

Hot and Cold TES	Temperature control
<ul style="list-style-type: none"> • Full-size PCM storage. • Multilayered PCM storage. • Combine PCM with other types of TES: sensible or thermochemical. • Solar TES with heat pumps: for building applications. 	<ul style="list-style-type: none"> • Space heating and cooling, Integrated into building structure and components. • Provide protection and thermal management to batteries and vehicles. • Protection of delicate electronic components. • Protection of sensitive medical products. • Thermal control of transportation for food and beverages. • Use for personnel human needs, such as vests, clothes, and hot and cold local treatments. • Thermal control of photovoltaic panels (P.V), or Combined P.V thermal applications (PVT).

1.2.2. PCM classifications

The phase change materials for TES are categorized into three main types based on their origin: pure inorganic and organic element, and eutectics, which can be organic or inorganic. Inorganic substances are salt hydrates, metals, and metallic eutectics, while paraffin waxes, esters, acids, and alcohols are organic PCMs [38].

Most organic materials have a relatively low melting temperature, and that limits their applications to room temperature applications, except for sugar alcohol compounds, which have a range of melting points between 93–168 °C [39].

Safari et al. [40] compared organic and inorganic PCM and summarized the advantages and disadvantages of each type of material in Table 6.

Table 6 Advantages and disadvantages of organic and inorganic PCMs

	Organic	Inorganic
Adv.	<ul style="list-style-type: none"> +Average TES density of 150 MJ/m³. +Non-corrosive. +Stable chemically and thermally. +Low subcooling 2-5 K. +Compatible with a wide range of building materials. + Materials have a broad range of melting temperatures. + Small vapor pressure. + Low cost. 	<ul style="list-style-type: none"> +Larger TES density. +Relatively more thermally conductive. +Higher latent heat of fusion. +Lower cost than the organic. +Non-flammable +unchangeable enthalpy of under cycling.
Dis.	<ul style="list-style-type: none"> -Thermal conductivity is very low -Limited surface area. -A significant difference in density between different phases. -Small latent heat of fusion. - Inflammable. 	<ul style="list-style-type: none"> -Harsh materials that corrode most metals. -Chemically and thermally, not stable. It decomposes under high temperatures. -A high potential of subcooling.

In addition to the melting point, the phase change enthalpy, also known as melting enthalpy or latent heat of fusion, is a critical parameter because it controls the amount of stored/released energy for TES. Figure 3 presents PCMs with their various melting enthalpy related to the melting points [34]. It shows that water-salts solutions are suitable for cold storage, paraffins are interesting for heating applications, nitrates work for applications with temperature range 200-300°C, and chloride and carbonates could work when temperature higher than 400°C is required.

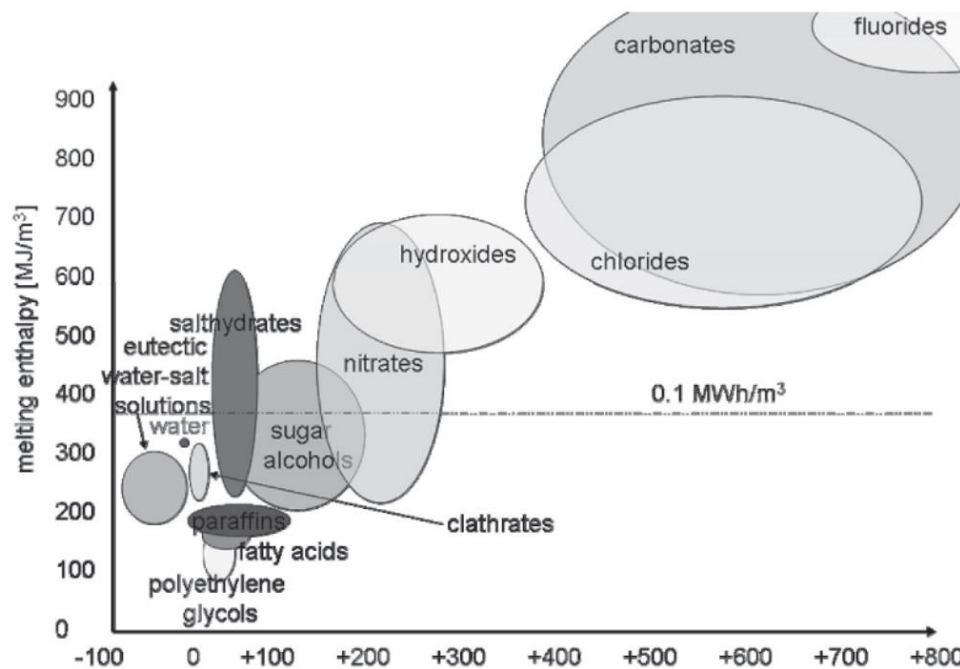


Figure 3 categories of PCMs relating enthalpy of fusions to melting temperatures [34]

1.2.3. Prescribed PCM features for TES

Similar to the materials used in sensible heat TES, PCMs must comply with specific criteria for appropriate utilization in TES. For example, there are some standard requirements between the two sensible and latent heat materials, such as significant thermal heat capacity, conductivity, stability under cycling, and cost-efficient.

Furthermore, PCMs have to satisfy special rules related to their natures, for example, the amount of latent heat of fusion, melting point, the density difference between liquid and solid phases, and compatibility with the encapsulation materials. Various researchers suggested categorizing the mostly required properties for PCM in TES in five aspects: thermal, physical, kinetic, chemical, and economic aspects. Table 7 lists the most commonly prescribed PCM features for the use in TES [41].

Table 7 Prescribed features to use PCM in TES

Criteria	descriptions
Thermal	<ul style="list-style-type: none"> • Phase change temperature within the operating temperature of the application. • High enthalpy of fusion • Significant volumetric heat capacity • Suitable thermal conductivity for both phases
Physical	<ul style="list-style-type: none"> • Significant surface for heat exchange. • Minimum density difference between liquid-solid phases. • Low vapor pressure.
Kinetic	<ul style="list-style-type: none"> • Lowest possible subcooling. • Suitable crystallization rate.
Chemical	<ul style="list-style-type: none"> • Stable with minimal material decomposition and properties deviation during the projected lifetime under thermal cycling. • Nontoxic • Comply with the fire safety rules. • Compatible with its encapsulation material (minimal corrosion) during the project lifetime.
Economical	Sufficient supply is available with economical prices

Table 8 summarizes available data from various literature [38], [42]–[50] for potential PCMs in TES for CSP application at temperature between (168-1083)^oC. The table lists the melting temperature, latent heat of fusion, and other thermo-physical properties for molten salts, eutectics, metals, and metal alloys.

Davignon et al. [51] emphasized the necessity of verifying the provided PCM thermophysical properties from the suppliers before deploying them in TES because they observed a significant variation between the manufacturer data and testing results.

1.2.4. PCM envelop and encapsulations

In most cases, the deployment of PCMs involves using an envelope to contain the PCM from HTF. The encapsulation shape and material are directly affecting the storage performance, due to their influence on the heat transfer coefficient and overall cost. Thus, the design of PCM encapsulations should meet the requirements listed in Table 9, as compiled from [29],[34], [52]–[54].

Table 9 Required specifications for proper PCMs envelop design

Mechanical stability and flexibility	<ul style="list-style-type: none">• Withstand internal pressure resulting from density differences between phases.• Provide the required structural rigidity.• Allow easy PCM filling in, easy to manufacture.
Thermal stability	<ul style="list-style-type: none">• Sustain the maximum working temperature.• Adapt to extension/retraction due to thermal cycling, with a compatible thermal expansion coefficient.
Compatibility	<ul style="list-style-type: none">• Corrosion resistance to PCM as well as HTF at the predetermined temperature.
Integrity	<ul style="list-style-type: none">• Seals the PCM from interacting with the surrounding atmosphere.
Sufficient heat transfer coefficient.	<ul style="list-style-type: none">• It shall provide a significant effective heat transfer coefficient, suitable shape, and thermal conductivity.

Jacob et al. [53] indicated three encapsulation material groups adequate to use with PCM: metallic, inorganic, and organic (plastic). The metallic envelope is convenient for high-temperature applications, but it comes with higher corrosion potential and a higher cost. Inorganic encapsulation material such as silicon dioxide, silica, calcium carbonate, and sodium silicate has a potential of disintegrating from the capsule, and possible mixing between the PCM and the HTF due to their porosity. Finally, some special types of plastics are used for applications in operating temperatures under 300°C with very low thermal conductivity.

Some studies evaluated the compatibility between common PCMs and envelop at the related working temperatures. Stainless steel demonstrated excellent compatibility with various PCMs at their melting temperature [53].

There are three metals to choose from for envelope case: SS 304L, SS 316L, or Carbon steel A36. Kuravi et al. [11] presented the container materials used for high-temperature salts. Further study on metal decay upon subjecting to nitrite salts at relatively high temperatures by Goods et al. [55] showed that the metal decay rate was 6-15 $\mu\text{m}/\text{year}$ at 570°C for SS (304 & 316), and 5 $\mu\text{m}/\text{year}$ at 316°C for A36 Carbon Steel.

Alam et al. [56] reported different shapes of encapsulation, such as cylinder, sphere, and a rectangular box with metals, ceramics, and plastic as encapsulation materials at various working temperatures and PCMs. The authors state that metals proved stability for a considerable number of working hours with harsh PCM materials. For example, chromium-nickel envelope showed stability for 1000 hours at a temperature between 1050°C - 1150°C with copper as PCM. Besides, stainless steel worked for 192 hours at a temperature range 300°C- 450°C with NaNO_3 as PCM.

Muñoz-Sánchez et al. [57] demonstrated that there are two primary processes to manufacture encapsulated PCMs: the standard method, which fills the PCM inside the rigid envelop, and the more innovative approach, which builds the envelope on the PCM substrate.

Peng et al. [58] summarized the new techniques to deposit envelop material on the PCM based on the required size of the final products and the nature of the encapsulation.

For an industrial scale production, there are very few options to select mass-produced PCM-envelop. Salunkhe et al. [54] collected data from manufacturers and points out that most of the PCM-envelops available in the commercial market are for cold storage applications or for low-grade temperature <80°C applications. The lack of commercial encapsulated PCM at relatively high temperatures is probably because of the low demand for this solution; besides, all the criteria listed in Table 9 are more comfortably satisfied for low-temperature utilizations.

1.2.5. PCM disadvantages

PCMs have excellent advantages. However, they come with functional challenges such as low thermal conductivity and subcooling, as well as corrosion, high cost of materials, the extra cost of the envelope, non-isotropic melting,

degradation of thermo-physical properties under long cycling, and volume changing due to density differences between phases [59]. The two mostly addressed disadvantages are low thermal conductivity and subcooling.

1.2.5.1. Low thermal conductivity

The performance of TES using PCM is influenced by the thermal conductivity of the material [60]. The charging process is expected to prolong when low thermal conductivity is presented in the PCM due to the slow movement of the melting front within the PCM. Furthermore, the energy retrieving process during discharge is less efficient due to thermal diffusion losses within the material itself in addition to the slow movement of the melting front in the PCM, which are both caused by the low PCM's thermal conductivity.

The Low thermal conductivity characterizes the most PCMs, except for metallic-based materials. The lowest thermal conductivity is found in organic-based PCMs, followed by inorganic-based PCMs [61].

Figure 4 plots the thermal conductivities of potential PCMs for high-temperature applications as a function of melting temperature for eutectics, hydroxides, nitrates, bromides, carbonates, chlorides, and fluorides. It shows that most of these molten salts have conductivity below 2 W/m.K. Moreover, Na_2CO_3 attracts attention in the multi-tower solar array because it has a high melting temperature [62].

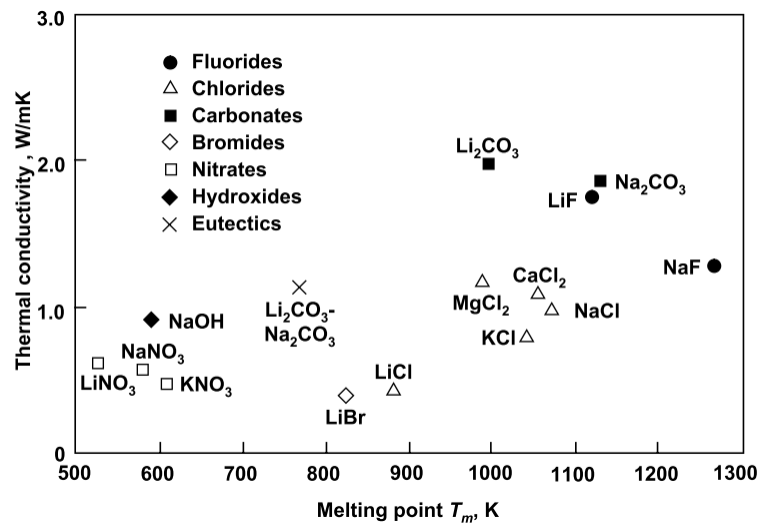


Figure 4 thermal conductivity for high-temperature PCMs [62]

1.2.5.2. Subcooling

Most PCMs demonstrate hysteresis behavior during the phase change process [51]. This phenomenon is often called sub-cooling (or undercooling) in the Liquid-Solid phase change. Subcooling causes the inverse phase change to occur at a different temperature than the original temperature that caused it. The same phenomenon is called superheating in Gas-Liquid phase change [63]. The subcooling in PCM is analyzed by using a Differential-Scanning-Calorimetry (DSC) device [64].

Subcooling is illustrated in Figure 5 in two materials paraffin and hexadecane-water emulsion. The figure plots the heat flow during the heating and the cooling process against measured temperatures for both materials. The paraffin shows a lower degree of subcooling. It starts melting at near 18°C, and it starts its solidification about 15°C. While the water emulsion demonstrates a more significant subcooling, it starts the melting process at 18°C freezes at near zero. The shape of that curve is different for the same material, which reflects a different response to melting compared to solidification.

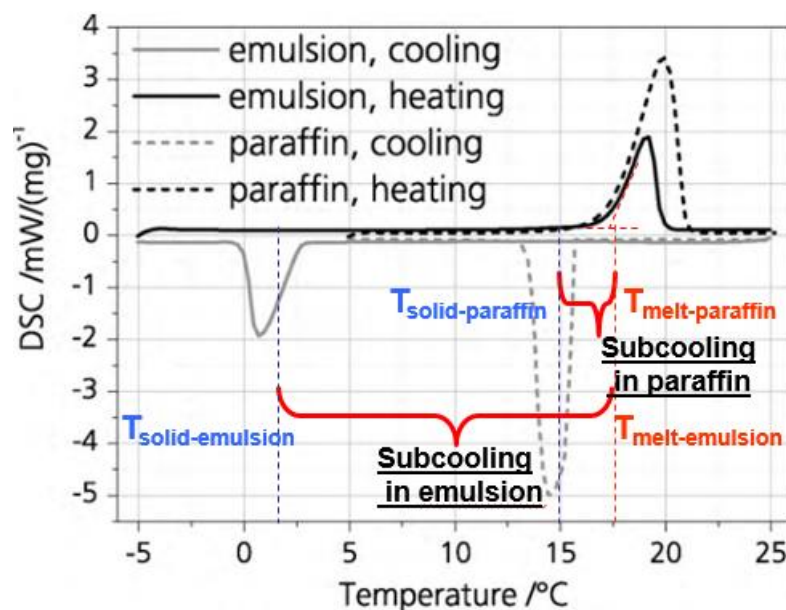


Figure 5 DCS Heat flow for two PCMs paraffin and water emulsion

Even though the temperature ascends to the melting temperature again, this influence is not required in TES because it degrades the quality of stored energy [8]. Water, which is one of the most used PCMs, could solidify at a temperature range between -4~-7°C under atmospheric pressure, but melts at 0°C [40].

The subcooling in PCM is mainly influenced by material properties, amount of material, rate of heating and cooling, and the roughness of the PCM container. Faucheux et al. [65] evaluated the influence of the capsule surface roughness on the water-ethanol PCM solidification process. They found that increasing the roughness of the PCM envelope reduces the subcooling. Furthermore, A. Safari et al. [40] reported that the higher the cooling rate, the higher the subcooling.

1.2.6. PCM thermal performance enhancement methods

Researchers used various methods to improve the thermal behavior of PCMs. These methods can be grouped under two main objectives, improve the heat exchange area between HTF and the PCM, and enhance the thermal behavior of PCM by doping it with nucleating materials. Table 10 summarizes various methods used in enhancing the thermal performance of PCM. Data is compiled from recent references [66]–[70],[71]–[76], and [77]–[82].

Table 10 PCM thermal performance enhancement methods

Improve heat transfer area	Thermal behavior of materials
<u>Miniature capsules:</u> <ul style="list-style-type: none"> Nano and microencapsulation 10nm-1μm. Nano (methyl methacrylate) copolymer shell. 	<u>Porous material to improve thermal conductivity:</u> <ul style="list-style-type: none"> Extended metal mesh Metal foam Copper foam Graphite Expanded graphite Graphite matrices Open-cell metal foam annuli filled Inclined PCM with metal foam
<u>Metallic Fins:</u> <ul style="list-style-type: none"> Aluminum Steel Bronze Copper Graphite foil Pin fin Circular fins Longitudinal fins Internal fins External fins Axial finned tubes 	<u>Conductive nanoparticles:</u> <ul style="list-style-type: none"> graphene nano-platelets Copper nanoparticles CuO nanoparticles Nano magnetite TiO₂ nanoparticles (Titania) SiO₂ nanoparticles (Silica) Al₂O₃ nanoparticles (Alumina) silica-alumina (SiO₂-Al₂O₃) Nanocarbon tubes in carbon foam matrices Multi-wall carbon nanotubes
<u>Improved shape design:</u> <ul style="list-style-type: none"> Shell and tube Multi-tubes and carbon brushes Wavy surface Rectangular, square containers Staggered vertical tubes Staggered horizontal tubes in crossflow. Cascade PCMs 	<u>Improve the enthalpy of fusion</u> <ul style="list-style-type: none"> Graphene Nanoparticles Spongy graphene Silver nanowires
	<u>Improve heat capacity:</u> <ul style="list-style-type: none"> Silica-Nano fluid to improve heat capacity

1.3. NUMERICAL MODELING FOR THERMOCLINE TES

The primary step in providing a reliable numerical simulation to a cylindrical tank thermocline TES is to identify the heat transfer methods. Where there are interactions between three different mediums, HTF, solid filler, and the wall of the thermocline, define the thermal performance of the tank. Balakrishnan et al. [83] suggested that the main challenge in analyzing heat transfer inside thermocline is the overlapping of various means of transfer between the three components, Figure 6 depicts the interactions between different heat transfer methods.

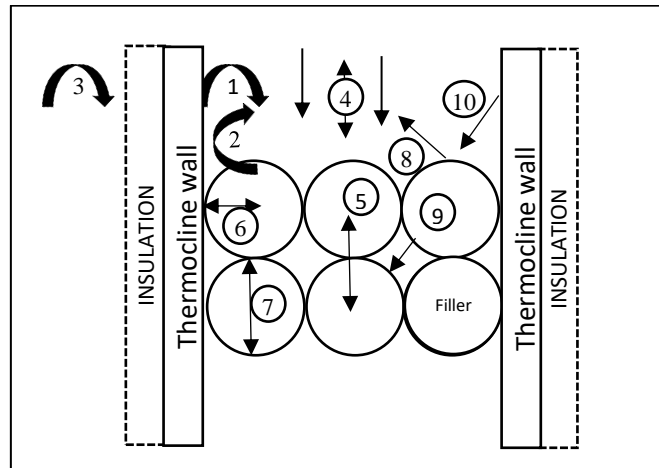


Figure 6 Means of heat transfer in thermocline

Table 11 lists ten heat transfer methods of convection, conduction, radiation, and mixing within the HTF. These interactions are happening during the change of time and at any or all of the three dimensions space. The complexity of the physical model depends on the simplification assumptions, which take into account some heat transfer methods and neglect others.

Table 11 List of heat transfer methods inside thermocline

Heat transfer	The interpretations inside thermocline
Convection	1- HTF to the wall. 2- HTF to solid filler. 3- Wall to the outside environment.
Dispersion	4- Mixing within HTF. (Conduction and convection)
Conduction	5- Particle to particle conduction. 6- Wall to solid filler conduction. 7- The temperature gradient within the solid filler: temperature gradient).
Radiation	8- HTF to solid filler. 9- Particle to particle. 10- Wall to particles.

For example, one of the assumptions is that the radiative heat transfer generally could be neglected, according to Kunii et al. [84], except when using gaseous HTF with large particles at a temperature higher than 625°C. This exception extended to all gaseous systems at a working temperature higher than 300°C [85]. Another assumption is to neglect heat conduction between particles at the contact surface, according to Kunii et al. [84]. Moreover, due to the presence of a uniform radial temperature inside the thermocline, the radial heat conduction can be neglected during developed flow [86],[87].

With these simplifications taken into account, modeling techniques for the dynamic thermal behavior of packed bed TES could be assorted under different categorization methods, single-phase models, and two phases models [15]. The single-phase model assumes that the temperatures of particle and HTF are at local thermal equilibrium at a given position inside the tank. In contrast, two-phase models consider these temperatures different.

Beasley et al. [88] suggested three main groups of models: one-dimensional single-phase, one-dimensional separate-phases, and two-dimensions separate phase. Ismail et al. [89] listed them differently: continuous solid phase models, Schumann's model, single-phase models, models with thermal gradient, one and two-dimensional continuous phase models. The Schumann approach study one spatial dimension, a time-dependent two-phase model.

Garcia et al. [90] classify the models in four sets: Single phase, Schumann, concentric dispersion, and continuous models. Esence et al. [85] considered two main groups based on the thermal gradient inside the solid. The first with negligible thermal gradient: Schumann model, One-dimensional single-phase models, Perturbation model, One-dimensional three-phase models, and Two-dimensional models. The second with a non-negligible thermal gradient inside the solids: One-dimensional intra-particle conduction models and Two-dimensional intra-particle conduction models. Based on fundamental energy equations of HTF and solid particles, Wako et al. [91] proposed three sets of equations: Schumann, Continuous solid phase, and Dispersion concentric model. All studies were built based on Schumann's approach; because it has simplified assumptions along with straightforward initial and boundary conditions [88], then it had been modified according to modified assumptions.









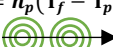


This work adopts and extends Wako et al. [91] approach in classifying physical models based on the energy balance equations of the HTF and the solid filler materials. Thus, Table 12 categorizes the physical models in six main groups as follows:

- 1- Plug flow in HTF, and no heat conduction in filler particles, known as Schumann model.

- 2- Plug flow in HTF considers heat conduction between filler and neglected temperature gradient in filler particles.
- 3- Plug flow in HTF considers heat conduction and assumes concentric symmetrical temperature gradient in filler particles.
- 4- Dispersed flow in HTF does not consider heat conduction nor temperature gradient in filler particles.
- 5- Dispersed flow in HTF considers heat conduction between filler and neglected temperature gradient in filler particles, known as the continuous solid model (C-S).
- 6- Dispersed flow in HTF, and considers heat conduction and assumes concentric symmetrical temperature gradient in filler particles, also called dispersion-concentric model (D-C).

These six groups are used to model sensible heat, latent heat, or combined heat TES. The model can be simplified to one-dimension or extend to 3-dimensions with CFD. Moreover, the model could evaluate thermal losses to the environment by solving an additional energy balance equation at the thermocline's wall or neglect it by assuming an adiabatic tank's wall. However, the model remains under one of these categories

Table 12 Modelling methods of thermocline TES based on energy balance equations of HTF and solid particles

	Fluid	Plug flow	Dispersed flow
			
No heat conduction & No temperature gradient $(1 - \varepsilon)(\rho c)_p \frac{\partial T_p}{\partial t} = h_v(T_f - T_p)$ 	$\frac{\partial T_f}{\partial t} + \vec{v}_f \cdot \nabla T_f = -\frac{h_v}{\varepsilon \cdot (\rho c)_f} (T_f - T_p)$ 	$+ \nabla \left(\frac{k_{eff,f}}{\varepsilon \cdot (\rho c)_f} \nabla T_f \right)$ 	
with heat conduction & No temperature gradient $(1 - \varepsilon)(\rho c)_p \frac{\partial T_p}{\partial t} = h_v(T_f - T_p) + k_{eff} \nabla^2 T_p$ 			
With heat conduction & temperature gradient $\frac{\partial T_p}{\partial t} = \alpha_p \left(\frac{\partial^2 T_p}{\partial r^2} + \frac{2}{r} \frac{\partial T_p}{\partial r} \right)$ $k_p \left(\frac{\partial T_p}{\partial r} \right) = h_p(T_f - T_p) \text{ at } r = R$ 			

The following sections summarize the energy balance equations, main assumptions, validation, and the main finding from the literature for each model.

1.3.1. Model for sensible heat TES

For sensible heat TES, all modeling categories as per Table 12 are used to simulate the sensible heat TES, except for category No.3 as follow:

1.3.1.1. Schumann model: Plug flow in HTF, no heat conduction, nor temperature gradient in filler particles.

Schuman's method [92] is plug flow-no heat conduction, a one-dimensional two-phases model. It allows finding the temperature distribution inside the tank at all axial positions for all the time, at given mass flow.

Assumptions:

- In a porous vertical flow, all mediums are at the same temperature inside the thermocline (HTF, solid filler, and tank's wall).
- Inlet HTF is at a higher temperature than the tank.
- HTF is moving at a constant mass flow rate.
- The thermal gradient inside particles is negligible, $Bi < 0.1$.
- A very well insulated thermocline (adiabatic).
- Disregard conduction between solid filler's particle.
- Disregard conduction inside the fluid, since it is negligible when compared to convection fluid-particle.
- Neglect radiative heat transfer.
- The heat transfer rate from fluid to the filler at any given point is related to the mean difference of fluid and particle temperatures at that point.
- The variation of the volume of HTF due to temperature is negligible.
- Constant heat transfer coefficient, neglecting temperature changes.

Energy balance equations are eq.(1) for the HTF and (2) for the solid filler

$$\varepsilon \cdot (\rho \cdot Cp)_f \cdot \frac{\partial T_f}{\partial t} + \varepsilon \cdot v_f \cdot (\rho \cdot Cp)_f \cdot \frac{\partial T_f}{\partial x} = -h_v \cdot (T_f - T_p) \quad (1)$$

$$(1 - \varepsilon) \cdot (\rho \cdot Cp)_p \cdot \frac{\partial T_p}{\partial t} = h_v \cdot (T_f - T_p) \quad (2)$$

Schumann et al. [92] suggested analytical solutions in which a quick calculation is possible. Although many researchers used this method widely

because it is fast and sufficiently accurate, it neglects some essential aspects such as thermal losses and thermal diffusion in the HTF.

Pacheco et al. [12] used a 2.3 MWh 42.5 m³ thermocline filled with low-cost rocks and molten salt as HTF to validate a Schumann model. The thermocline thickness in the experiment matched the one simulated by the model.

Pacheco et al. [12] studied a scaled-up thermocline using their model to evaluate the performance of industrial-size thermocline TES against two-tank molten salts. They concluded that thermocline could provide similar energy storage capacity and performance of the two tank molten salts with a 33% lower cost.

Lew et al. [93] validated a non-dimensional version of the Schumann model from the experimental literature data. They applied the method of characteristics to reduce the required time for calculation and obtain a grid-independent solution. Finally, they recommended sizing procedures based on dimensionless quantities. Karaki et al. [94] produced linear and exponential analytical solutions to Lew model, and they suggested that a higher heat transfer coefficient leads to better efficiency in the stored energy. Where the charge efficiency is defined as the ratio of charges energy to the maximum energy that could be stored in the thermocline, and the discharge efficiency is defined as the ratio between discharged energy to the maximum energy stored in the thermocline at the beginning of the discharge. Li et al. [95] developed the Lew model by applying a corrected heat transfer coefficient, which takes into account the thermal gradient inside the rocks as per eq.(3).

$$\frac{1}{h_{corrected}} = \frac{1 + \left(\frac{Bi}{5} \right)}{h} \quad (3)$$

Valmiki et al. [96] included the mass of the tank wall in Lew model and compared the numerical results to an experimental thermocline. The tank volume is 45.6 l, which is filled with a pebble as solid filler, and the HTF is synthetic oil. The model showed a good agreement with the experimental results, although the presence of an average error of 5.63% between numerical and experimental non-dimensional temperature readings. Valmiki et al. [96] attributed this error to the two-dimensional attitude of the HTF near the wall and at the inlet, which generally is minimal in a bigger tank than the lab-scale used in the study.

Ben Xu et al. [97] applied the various corrected heat transfer coefficients on different geometries of solid filler such as spheres, plates, solid cylinders, and tubes, then compared the obtained results to analytical solutions. They found a

good agreement between analytical and numerical solutions; however, the higher the filler conductivity, the more discrepancies are observed.

Li et al. [98] compared the 1D Schumann model with a corrected heat transfer coefficient according to eq.(3) of the plate, cylindrical, and tubes filler to an ANSYS® Fluent CFD model results. The comparison indicated a good agreement between the two, which gives an advantage to 1D models against more costly and time-consuming CFD software. However, the study insisted on the necessity of further validation of the 1D Schumann model when using highly conductive HTF as well as solid filler.

Vortmeyer et al. [99] simplified the Schumann model by assuming the solid filler and HTF have the same temperature at each time step (one-phase model). Besides, the second-order derivatives of the temperatures are equal for both media. They validated the model accuracy by comparing its results to experimental results from the literature for a glass sphere bed. Vortmeyer et al. indicated that they neglected the heat capacity of the gaseous HTF, but it should be taken into account if the HTF is liquid.

1.3.1.2. Plug flow in HTF, axial heat conduction between filler, and no temperature gradient in filler particles. (Littman)

While the two energy balance equations of Schumann were found acceptable at a Reynolds number larger than 180, Littman et al. [100] found that the solid filler equation required a new term in order to consider axial heat conduction in the thermocline. They suggested a modified equation of the solid filler as per eq. (5), last term, while for HTF energy balance equation remains the same as per Schumann eq.(4).

$$\varepsilon \cdot (\rho C_p)_f \cdot \frac{\partial T_f}{\partial t} + \varepsilon \cdot v_f \cdot (\rho \cdot C_p)_f \cdot \frac{\partial T_f}{\partial x} = -h_v(T_f - T_p) \quad (4)$$

$$(1 - \varepsilon)(\rho C_p)_p \frac{\partial T_p}{\partial t} = h_v(T_f - T_p) + (1 - \varepsilon)k_p \frac{\partial^2 T_p}{\partial x^2} \quad (5)$$

Hänchen et al. [101] developed a numerical model using this approach and validated the results from the literature of a thermocline filled with rocks and heated with air. Furthermore, the model evaluates the thermal losses through the wall of the tank. They found that small-diameter filler required more pumping work, and the volumetric heat capacity of the filler is the most critical parameter in the TES operation, unlike its thermal conductivity, which did not show any significant influence thanks to simulation. Faster HTF flow and large volumetric

heat capacity of solid filler improve the TES capacity significantly. However, it reduces the storage efficiency

Mertens et al. [102] used Hänchen et al. [101] modeling method to evaluate a case study of 1.5 MW_{elec} thermocline filled with quartzite and air as HTF. They indicated that the turbulence of HTF near the tank wall could be neglected when the ratio between tank diameter to filler diameter is larger than 40.

Mertens et al. [102] evaluated the thermal efficiency and the pressure losses of a thermocline with multiple ratios of thermocline height to tank diameter (H/D), and various filler diameters. They concluded that at the same (H/D) ratio, increasing the filler diameter reduced the efficiency and reduced the pressure drop. At a large H/D ratio, the efficiency reduction due to larger filler diameter is less significant. Moreover, using the solid filler in the thermocline reduced the electrical efficiency of the system by 3.7% because of the extra power required by the pump to overcome the pressure drop resulted from the solid filler.

Zanganeh et al. [103],[104] extended this method. They included the radiative heat transfer inside the thermocline due to the use of gas as HTF at higher temperature than 500°C. The numerical data compared to a 6.5MWh_{th} pilot-scale thermocline filled with pebbles and the HTF is air. The thermal losses in the model remained under 3.5% of the total incoming energy, and the system achieved 89% storage efficiency. Zanganeh et al. [105] deduced that performing an initial charge process increases the thermocline thickness.

Votyakov et al. [106] suggested an additional simplification to this approach and called it the perturbation model. They assumed that both the HTF and the filler are at the same temperature, and deduced a one-dimension, one-phase model (1D-1P) transient model equation. The work validated from the results of a more complex C-S 2D 1P model from the literature. However, they found a small deviation in the thermocline thickness prediction. Bonanos et al. [18] used the perturbation model and performed a sensitivity analysis to identify the main factors affecting the thermocline thickness and charging efficiency. They concluded that tank height, thermal capacity and conductivity of the filler are the most influencing parameters on the thermocline thickness. HTF properties, particle size, void fraction, and charging time have a less significant effect. HTF viscosity had no prominent effect. Mabrouk et al. [107] used a perturbation model and deduced a semi-analytical solution using generalized integral transforms technique (GITT). They verified the model from the literature. The main advantage of this method is the small size of matrices and hence fast computing time.

1.3.1.3. Plug flow in HTF, concentric symmetrical temperature gradient in filler particles.

This modeling approach considers plug flow in the HTF equation while it takes into account the thermal gradient within the solid filler particle. The thermal gradient is assumed radially distributed.

$$\varepsilon \cdot (\rho \cdot Cp)_f \cdot \frac{\partial T_f}{\partial t} + \varepsilon \cdot v_f \cdot (\rho \cdot Cp)_f \cdot \frac{\partial T_f}{\partial x} = -h_v \cdot (T_f - T_p) \quad (6)$$

$$(\rho Cp)_p \frac{\partial T_p}{\partial t} = \frac{k_p}{(\rho c)_p} \frac{1}{r^2} \frac{\partial}{\partial r} \left(r^2 \frac{\partial T_p}{\partial r} \right) \quad (7)$$

Equations (6) & (7) show the energy balance equation of this model approach. To the author's knowledge, no one published a work that uses this method to simulate sensible heat thermal energy storage. This could be attributed to the simplifications it used in the energy balance equation of HTF while using a more sophisticated approach at the solid filler. On the other hand,, this method was used in modeling latent heat TES to keep simple assumptions for the HTF and consider the complex phase-change behavior of the filler, as it appears in the next sections.

1.3.1.4. Dispersed flow in HTF, no heat conduction in filler particles, no temperature gradient (Beasley method).

Similar to the Schumann model, this physical approach depicts no heat conduction with no temperature gradient in the solid filler, but it considers dispersion in HTF. Equations (8) & (9) illustrate the energy balance equation of HTF and solid filler.

$$\varepsilon \cdot (\rho \cdot Cp)_f \cdot \frac{\partial T_f}{\partial t} + \varepsilon \cdot v_f \cdot (\rho \cdot Cp)_f \cdot \frac{\partial T_f}{\partial x} = k_f \frac{\partial^2 T_f}{\partial x^2} - h_v \cdot (T_f - T_p) \quad (8)$$

$$(1 - \varepsilon) \cdot (\rho \cdot Cp)_p \cdot \frac{\partial T_p}{\partial t} = h_v \cdot (T_f - T_p) \quad (9)$$

Riaz et al. [108] suggested an analytical solution to a 1D 1P version of this model and applied it to the Air-Rock thermocline. They simplified this approach by neglecting the axial conduction, considering pure convection for a one-phase model, and neglecting thermal capacity for a gaseous HTF. They compared the analytical solution to the numerical model results with an acceptable error margin.

Beasley et al. [88] worked on a three-phases (3P) model, energy equation of the HTF is two-dimensional (2D) radial and axial orientation, and evaluates axial

and radial effective thermal conductivity. The equation of the filler is 1D and does not consider thermal conductivity nor temperature gradient. The wall equation is 1D, and it involves stored energy in thermocline wall and thermal losses to the outside.

Beasley et al. [88] verified their modeling results from a 0.62 m height and 0.38 diameter thermocline that is filled with soda-lime glass spheres and heated with air.

Cascetta et al. [109] used a 1D 2P approach of this method to evaluate numerically a 5 MWh_{th} thermocline filled with alumina spheres, with three HTF: air, oil, and molten salts. They indicated that the thermal storage performance improved by reducing the particle diameter and increasing the size of the thermocline (height and diameter), furthermore the cycling affected the stored energy negatively, especially for air HTF, while oil and molten salt showed less influence of cycling.

Yang et al. [110] numerically evaluated the discharge process of a quartzite filled thermocline; that is heated with molten salts, using this approach. Furthermore, they assumed compressible HTF flow and solved volume-average mass and momentum transfer with Brinkman-Forchheimer extension to Darcy law to simulate the porous-medium resistance.

Yang et al. [110] observed an increase in the discharge efficiency with larger tank height and smaller particle diameter. For example, the discharge efficiency increased by 12.9% when using a half diameter of the filler. Furthermore, lower discharge efficiency resulted from higher Reynolds numbers.

Angelini et al. [111] solved the continuity equation in addition to the energy balance equations for their modeling approach. They compared the performance of two-tank to a thermocline TES. Angelini et al. found that the thermocline provided only 64% of the stored energy stored in the two-tank. Furthermore, the efficiency in thermocline is 33% lower than the two-tanks. Finally, Angelini et al. [111] concluded that the tank's height should not exceed 14 m to avoid significant thermal losses to the environment.

Mira-Hernández et al. [17] applied the model described in equations (8) & (9) to compare two thermocline setups, molten salts as HTF as well as SHSM, and dual media thermocline with similar HTF and quartzite rocks as SHSM. They solved the momentum, continuity, and energy balance equation using a CFD solver and took the thermal losses to the environment into account. A larger thermocline thickness was observed in the dual media tank setup compared to the single one Figure 7. Mira-Hernández et al. [17] attributed that to the higher thermal diffusivity of the rocks than molten-salts

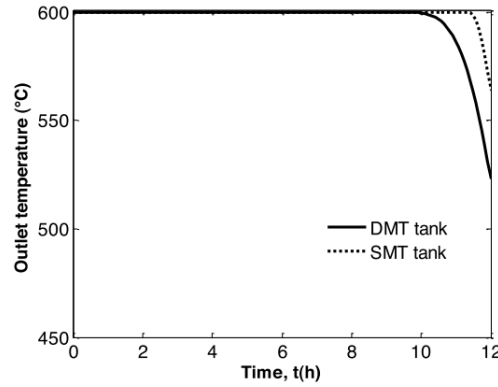


Figure 7 [17] Thermocline outlet temperature evolution in time two thermoclines: SMT at which HTF is the storage medium, DMT dual HTF and solid filler are used as storage mediums

Continuous Solid model (C-S): Dispersed flow in HTF, considers heat conduction and neglects temperature gradient in filler particles.

The main assumptions in C-S models are dispersed HTF flow and continuous, homogenous, and isotropic solid filler (the solid filler is in continuous phase) [91]. There is no temperature gradient inside the filler, and the heat conduction is only in the axial direction of the tank. Eq.(10) & (11) reflect the 1D energy balance equations for HTF and solid filler.

$$\varepsilon \cdot (\rho \cdot Cp)_f \cdot \frac{\partial T_f}{\partial t} + \varepsilon \cdot v_f \cdot (\rho \cdot Cp)_f \cdot \frac{\partial T_f}{\partial x} = k_{eff,f} \frac{\partial^2 T_f}{\partial x^2} - h_v \cdot (T_f - T_p) \quad (10)$$

$$(1 - \varepsilon) \cdot (\rho \cdot Cp)_p \cdot \frac{\partial T_p}{\partial t} = h_v \cdot (T_f - T_p) + k_{eff,p} \frac{\partial^2 T_p}{\partial x^2} \quad (11)$$

Then Mira-Hernández et al. [112] used a one-dimensional (1D), C-S model, on a scaled-up 1010 MWh_{th} thermocline. They optimized the solution and accepted a bigger numerical error, in order to make the model respond very fast to any changes in solar power input in CSP plants.

Anderson et al. [113] developed a 1D two-phases (2P) C-S model and validated their work from an experimental 3m height and 0.05 m ID thermocline filled with 6mm alumina spheres and using air as HTF. The model simulated thermal losses due to natural convection at the outer wall without solving a new equation. Anderson et al. indicated the importance of considering the temperature-dependent thermophysical properties of alumina and air.

Hoffmann et al. [87] provided experimental validation of a 1D three-phases (3P) model. This modeling approach solves an extra energy balance equation to simulate stored energy and thermal losses for the tank wall. The

experimental setup consists of 8.3 kWh_{th} 1.8m height by 0.4 m diameter thermocline filled with 40 mm alumina spheres and heated with thermal oil.

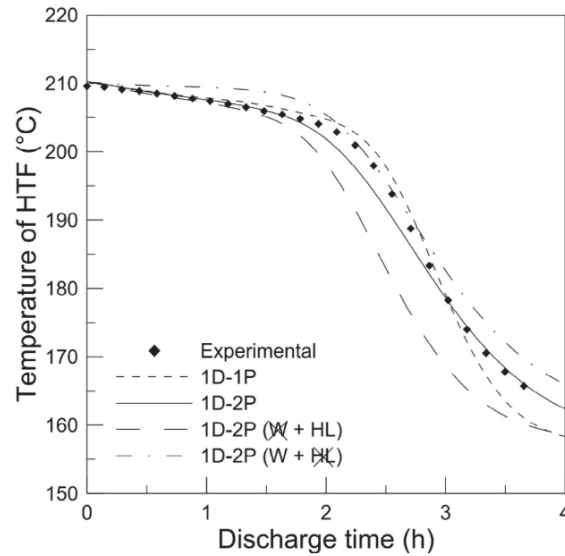


Figure 8 experimental temperature against 1D-1P, 1D-2P, 1D-2P(+wall heat losses), and 1D-2P (+ solving wall energy equation) Hoffmann et al. [87]

Hoffmann et al. [87] concluded that the 1D 3P C-S is more convenient to model the thermocline against 1D-1P, 1D-2P models Figure 8. Furthermore, it provides a fast, reliable, and simple solution compared to complicated 3D models and analytical solutions that required time-consuming procedures for data fitting.

Bruch et al. [114] used a C-S model to simulate multiple charge/discharge cycles for a thermocline. The models are validated with a pilot-scale 3 m height 1 m diameter thermocline that is filled with 20% of 3 mm diameter silica sand, 80% 30 mm diameter silica rock, and the HTF is thermal oil. The pressure drop is calculated from the Ergun equation.

Bruch et al. [114] concluded that the thickness of the thermocline is moving faster numerically than the experiment. However, when considering a correlation to calculate an equivalent density of rock, the model resulted in a better match with the experiment. The correlation takes into account the wall effect, which adds thermal inertia to the numerical model.

Bayón et al. [115] simplified the 1D C-S model to a one-phase (1P) equation, assuming that both HTF and filler have the same temperature all the time. Moreover, they evaluated thermal losses through the tank wall and validated the model from literature experimental results. They suggested an equation for large

TES size to provide minimum thermocline height for given operating conditions, which could result in maximum efficiency, equation (12).

$$H_{min} = \frac{2350 \times 0.25\pi D^2 \times k_{eff}(T_{max} - T_{min})}{P} \quad (12)$$

P: is the thermocline thermal power for charge/discharge operation in Watt.

In further analysis, Bayón et al. [116] used an analytical expression to find an approximated solution of their 1D-1P C-S model. They applied real operating conditions that do not allow fully charging or discharging the thermocline during five consecutive operation cycles. The main finding was a significant increase in the thermocline thickness, which led to lowering the storage efficiency to 50% due to these conditions Figure 9.

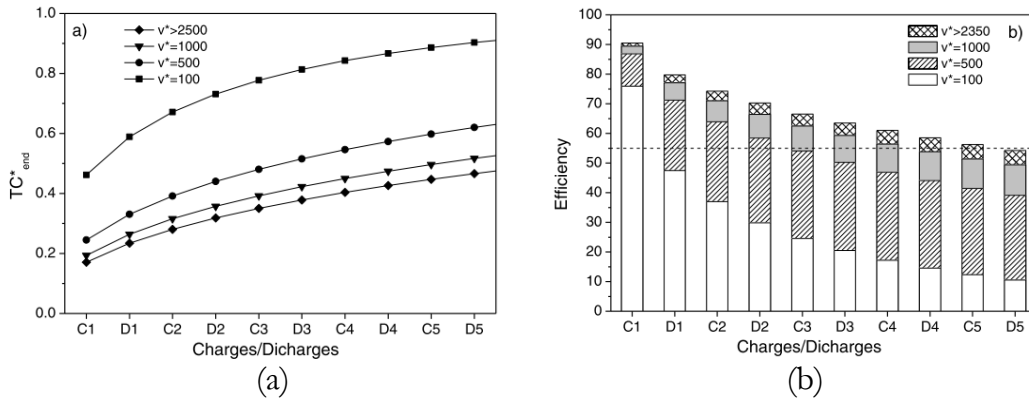


Figure 9 cycling effect on (a) TC thermocline thickness (b) efficiency for multiple non-dimensional velocity $v^* = (\rho C_p) f \cdot H_{tank} \cdot v_f / k_f$ Bayón et al. [116]

Moreover, Bayón et al. [117] used a similar modeling approach to study a thermocline TES that mimics the Andasol power plant. They found that thermocline thickness is lower when using molten salts as HTF and SHSM, compared to HTF and rocks as filler materials. They ascribed this finding to higher diffusivity in the solid filler compared to the molten salts. Furthermore, they recommend the extraction of the thermocline thickness out of the tank before starting the next operation during realistic operation. The process of thickness diminishing could improve the efficiency of the last cycle by about 25%.

Hoffman et al. [87] used a 1D-1P C-S model with effective thermophysical properties that take into account the stored energy in the tank wall, and they also evaluated thermal losses to the surrounding environment. They found that the calculation time is fast, but the results did not match enough the results from a small-scale thermocline experiment. However, the reduced 1D-1P model had an acceptable fit with the collected data Figure 8.

Ehtiawesh et al. [118] simulated the behavior of Solar-one power plant and Sandia Laboratory (SL) prototype thermocline TES using a simple 1P-1D C-S model that neglected thermal losses through the tank wall. The simulated results provided a good accuracy when compared to the data obtained from the two setups. Furthermore, the simulations were done in a sufficiently fast manner.

Anderson et al. [119] solved a 1P energy equation coupled with the Navier-Stokes equations using a CFD solver. They validated the resulted 2D axial and radial temperature distribution against experimental thermocline filled with alumina spheres and hot air at 700°C. They indicated the importance of presenting temperature-dependent thermophysical properties for both HTF and solid filler.

Xu et al. [13] provided a two-dimension (2D) 2P C-S model that considers thermal resistance of the insulation layer and validated their work with an experiment from the literature. The simulated thermocline consisted of molten salt HTF and quartzite rock as a filler. The CFD model solved the continuity and momentum equation in addition to the energy balance equation and considered constant thermophysical properties of the solid filler. Xu et al. tested many correlations for effective thermal conductivity and interstitial heat transfer coefficient and found no substantial variation between the results of the C-S model. This study concluded that: improving the insulation layer improved the uniform cross-sectional temperature distribution, moreover, reducing the interstitial heat transfer coefficient by using more thermally conductive filler, increased the thermocline thickness, and reduced discharge efficiency. Also, the thermocline thickness increased to occupy 33% of the 14m tank height during the discharge process Figure 10.

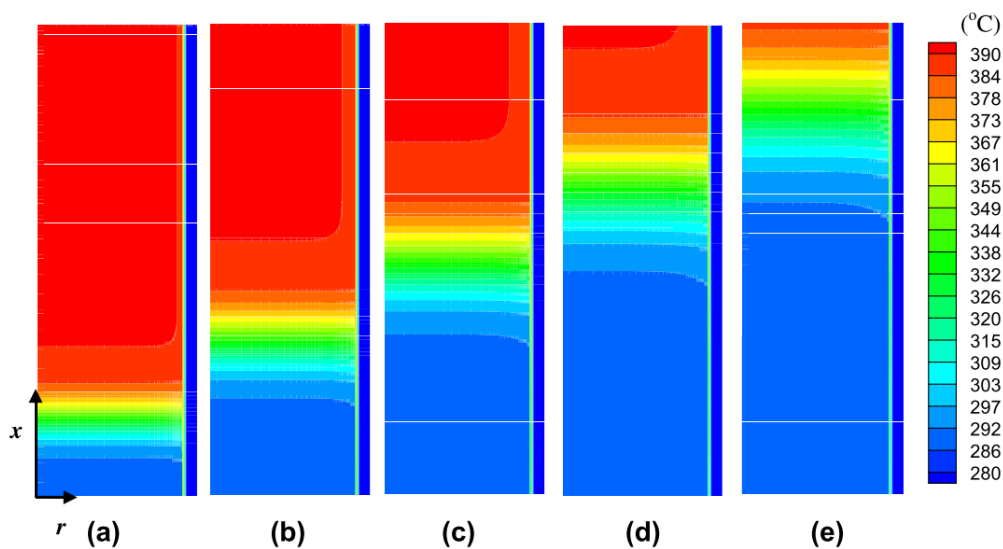


Figure 10 2D temperature distribution of HTF in 14m thermocline (a) 50 min, (b) 100 min, (c) 150 min, (d) 200 min, and (e) 250 min Xu et al. [13]

Applying the same model, Xu et al. [120] analyzed the influence of various parameters on thermocline thickness and discharge efficiency. The study concluded that thermocline thickness is not affected by increasing the HTF flow or increasing the temperature difference of the HTF between inlet and outlet. Moreover, the tank porosity had a minimal influence on the thermocline thickness if it is larger than 0.22. Furthermore, increasing the tank height from 6 m to 14 m reduced the thermocline thickness by nearly 24%, and reduced discharge efficiency by 5%. Moreover, increasing the tank higher improved the radial temperature distribution inside the thermocline with less wall effect. During standby mode, the significant factors affecting the stored energy are the thermal losses, where it was found that increasing thermal losses increased thermocline thickness and vice versa.

1.3.1.5. Dispersion concentric model (D-C): Dispersed flow in HTF, and concentric symmetrical temperature gradient in filler.

Before the advanced computer breakthrough, researchers used to build a D-C model to solve the transient heat transfer problems in thermoclines [91]. However, the main disadvantage for early D-C models is neglecting the thermal conductivity of the solid filler between the particles. Especially when the conduction of the material is significantly changing with the temperature as it is the case when using PCM. To overcome this problem, more recent D-C models add the solid filler conduction to the thermal dispersion in the HTF equation.

Equations (13) and (14) present the general form of energy balance equations for HTF and solid filler, and equation (15) is the boundary conditions for the solid filler.

$$\varepsilon(\rho Cp)_f \frac{\partial T_f}{\partial t} + v_f \cdot \varepsilon(\rho Cp)_f \frac{\partial T_f}{\partial x} = k_x \frac{\partial^2 T_f}{\partial x^2} - h_v(T_f - T_{p(r=R)}) \quad (13)$$

$$(\rho Cp)_p \frac{\partial T_p}{\partial t} = k_p \frac{1}{r^2} \frac{\partial}{\partial r} \left(r^2 \frac{\partial T_p}{\partial r} \right) \quad (14)$$

$$k_p \left(\frac{\partial T_p}{\partial r} \right) = h_v(T_f - T_p) \text{ at } r = R \quad (15)$$

Sagara et al. [121] used a 1D D-C model to evaluate the influence of the specific heats and rate of coefficients on the dispersion in a 25 cm height by 2.5 cm diameter thermocline. The lab-scale setup is used with a 3mm, 0.15mm diameter glass beads filler heated with water. They suggested two correlations to modify the density and heat capacity of solid filler in the energy balance equation of the filler equations (16),(17), respectively.

$$\rho_{p-m} = \rho_p + \varepsilon(\rho_p - \rho_f) \quad (16)$$

$$Cp_{p-m} = \frac{1}{\rho_{p-m}} [(1 - \varepsilon)(\rho Cp)_p + \varepsilon(\rho Cp)_f] \quad (17)$$

Saez et al. [122] worked on a 1D D-C model to optimize thermocline for solar-heated air/rock-bin filler. The model neglected the viscous heating and considered that the particle surface temperature is uniform and the axial thermal conductivity coefficient in the HTF equation calculated as per equation (18).

$$k_{f,x} = 0.7k_f + \varepsilon(\rho Cp)_f v_f R_p \quad (18)$$

Kaguei et al. [123] modified the 1D D-C model with modified axial thermal conductance as per equation (19), to improve the model predictions.

$$k_{f,x} = \begin{cases} 0.7\varepsilon k_f, & Re < 0.8 \\ 0.5.Pr.Re.k_f, & Re \geq 0.8 \end{cases} \quad (19)$$

Chao Xu et al. [124] solved 3 phases (3P) energy equations along with momentum and continuity equations in the radial and axial spaces (2D). They used Equation (19) to evaluate the effective-axial thermal conductivity and verified the results from literature experiments. The numerical study indicated that within the thermocline thickness region, there is a noticeable temperature difference between the surface of the solid particle and its center. This temperature difference diminished at a smaller particle diameter than 19 mm.

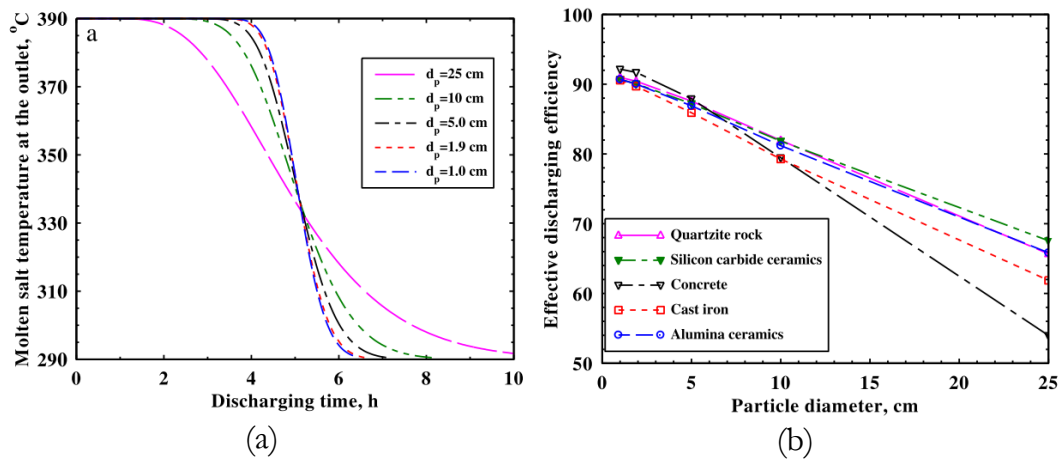


Figure 11 Chao Xu et al. [124] thermocline discharge process

(a) Outlet temperature as a function of time at various solid filler diameter.
(b) efficiency as function to particle diameter for various materials

Moreover, it was found that the larger the filler diameter, the more significant the temperature variation between the filler and HTF, the bigger the

temperature gradient within the particle, the wider the thermocline thickness Figure 11 (a), and the shorter the useful discharge time and the lower the discharge efficiency Figure 11(b). Chao Xu et al. [124] claimed that if the particle diameter is small enough, the discharge efficiency is independent of the filler material properties. Besides, when using a bigger diameter, more thermally conductive materials are preferred to obtain high discharge efficiency.

Ismail et al. [89] evaluated the calculation time for six different modeling approaches 1D 1P, 2D 1P, Schumann model, 1D C-S, 2D C-S, and 1D D-C model. They run all the models for the same thermocline filled with sand on one computer.

Table 13 calculating time for various models Ismail et al.

Model	Computing time [sec]
1D 1P	7.1
Schumann model	29.6
1D C-S	51.6
2D 1P	141.5
1D D-C	574.6
2D C-S	1277.7

Table 13 arranges the calculating time for each model in ascending order. It indicates that a more complex model has a higher computational time cost. Furthermore, 1D approaches reduce computing time by 95% compared to 2D models. Also, the C-S model saved 91% of the calculation time needed in D-C to consider temperature gradient within the solid filler. Ismail et al. concluded that diverse cycling strategies have little impact on thermocline TES general performance, while changes in inlet temperature have a significant effect on the resulted thermal behavior. Moreover, tank porosity affects the thermal storage capacity of the thermocline.

Because of the long computational time for 2D models, they are only recommended to use on specific operating conditions such as a non-uniform incoming flow of HTF, slow mass flow rate, or significant thermal losses at the outside wall of the thermocline [90].

The C-S model approach provides a fast and reasonably accurate simulation method against other approaches for sensible heat TES.

1.3.2. Models for melting and solidification of PCM

When a material undergoes a phase change, it stores/releases thermal energy and develops a boundary layer that separates the two phases. Both phases might have different thermophysical properties. Moreover, the boundary between them moves by the time the material completes its transformation. The problem in simulating this behavior is that it is not possible to describe the position of the moving boundary in advance [125]. This moving boundary problem in numerical simulation is called the Stefan problem [126], where the melting rate is controlled by a non-dimensional quantity recognized as Stefan number (St) represents the ratio of sensible heat to latent heat in a materials equation (20).

$$St = [C_{p_{liq}} \cdot (T_{liq} - T_{phase-change})] / L_{fus} \quad (20)$$

Stefan suggests some simplifications to overcome this obstacle during the simulation as per the following assumptions [34]:

- Neglecting sensible heat storage during the phase change, so latent heat of fusion is the only form of energy storage.
- Neglecting heat convection (natural convection) and the only mechanism of heat transfer is thermal conduction. This assumption produces a linear temperature profile, where the heat flux is relative to the temperature gradient.
- During the phase transition, only the liquid phase is presented at the phase change temperature.

Stefan problem could be expanded to consider both phases of the material liquid and solid during the phase change, which is known as the Neumann problem[126]. However, the solution to this approach can only be applied to rectangular coordinates.

Henry et al. [127] categorized the various methods to simulate the phase change of an encapsulated PCM within an envelope under two main categories analytical and numerical methods. Table 14 summarizes different methodologies used to study the phase change of material.

Table 14 Different methodologies to study the phase change of materials

Analytical methods	Numerical Methods
Neumann methods.	Fixed grid method.
Heat balance integration methods.	Variable grid method.
	Methods of latent heat evolution.
	<ul style="list-style-type: none"> • Apparent heat capacity • Heat source-based • Enthalpy methods

The analytical methods such as Neumann and integration of heat balance are solving Stefan's problem based on the previously mention simplifications. In contrast, numerical methods study additional physical phenomena in the PCM that are neglected by the analytical solution, such as considering the sensible heat storage, natural convection, or variation in temperature during the phase change in the mushy zone in various geometries.

The mostly used numerical methods in simulating the phase change behavior in thermocline TES are heat source, apparent heat capacity, enthalpy, Beasley enthalpy, and enthalpy porosity methods. The following sections introduce these methods.

1.3.2.1. Heat source method

This method was introduced by Bedecarrats et al. [128] and applied to a cold storage system by Kousksou et al. [129]. It depicts that the HTF inside the evaluated control volume has a homogenous temperature. The heat source method modifies the energy balance equation of the HTF by adding a source term (S) to consider heat flux for each capsule in the control volume Equation (21).

$$\varepsilon. (\rho. Cp)_f. \frac{\partial T_f}{\partial t} + \varepsilon. v_f. (\rho. Cp)_f. \frac{\partial T_f}{\partial x} = \frac{\partial}{\partial x_i} \left(\varepsilon. k_f \frac{\partial T_f}{\partial x_i} \right) + S \quad (21)$$

The source term (S) evaluates the heat flux for all involved capsules in the reference control volume equation (22), and it considers the thermal resistance of the envelope materials as well as the thermal resistance of the materials eq.(23), eq.(24), and eq.(25).

$$S = \frac{1}{V_{cr}} \left(N_{sol}(t)\phi_{sol}(t) + N_{liq}(t)\phi_{liq}(t) + \sum \Delta n_{\tau}\phi_{c,\tau}(t) \right) \quad (22)$$

V_{cr} : The volume of HTF in the control volume.

$N_{sol}(t), N_{liq}(t)$ are the number of capsules that are completely at solid or liquid, respectively.

Δn_{τ} is the number of capsules that are undergoing the phase change, this value is determined statistically from experimental data.

The heat flux exchanged with the HTF for each capsule is calculated using a quasi-stationary approximation when the capsule is completely solid, liquid, and undergoing a phase change from eq.(23), eq.(24), and eq.(25), respectively.

$$(\rho \cdot Cp)_{sol} V_{PCM} \frac{dT_{sol}(t)}{dt} = -\phi_{sol}(t) : \phi_{sol}(t) = \frac{T_{sol}(t) - T_f(t)}{TR_f + TR_{env}} \quad (23)$$

$$(\rho \cdot Cp)_{liq} V_{PCM} \frac{dT_{liq}(t)}{dt} = -\phi_{liq}(t) : \phi_{liq}(t) = \frac{T_{liq}(t) - T_f(t)}{TR_f + TR_{env}} \quad (24)$$

$$4\pi r_{c,\tau}^2 \rho_{sol} L_{fus} dr_{c,\tau}(t) = -\phi_{c,\tau}(t) : \phi_{c,\tau}(t) = \frac{T_{melt} - T_f(t)}{TR_f + TR_{env} + TR_{c,\tau}(t)} \quad (25)$$

The use of this method implies knowing the number of capsules at each control volume in addition to performing probability analysis to estimate the number of capsules that are demonstrating phase change.

1.3.2.2. Apparent heat capacity method

Cao et al. [130] suggested this method to simulate the phase change effect at a range of temperatures. In this method, the heat stored/released due to the latent heat of the PCM is calculated in its heat capacity correlation at the given phase change temperature range. Moreover, the sensible heat of the PCM during the phase change process is considered an average between the liquid and solid phases, equation (26).

$$Cp_p = \begin{cases} Cp_p = Cp_{sol}, & k_p = k_{sol} & T_p < T_{sol} \\ \frac{Cp_{sol} + Cp_{liq}}{2} + \frac{L_{fus}}{T_{liq} - T_{sol}}, & k_p = \frac{k_{sol} + k_{liq}}{2} & T_{sol} < T_p < T_{liq} \\ Cp_p = C_{liq}, & k_p = k_{liq} & T_{liq} < T_p \end{cases} \quad (26)$$

The main advantage of this method is to represent PCM behavior over a range of temperatures, which is more realistic compared to other methods. At the same time, it does not provide any prediction to the liquid fraction development.

1.3.2.3. Enthalpy method

The mainframe of this method is to evaluate enthalpy evolution in time instead of temperature explicitly [127]. Equation (27) illustrates the energy balance equation for the PCM.

$$(1 - \varepsilon)\rho_p \frac{\partial h_p}{\partial t} = h_v(T_f - T_p) + (1 - \varepsilon)k_p \frac{\partial^2 T_p}{\partial x^2} \quad (27)$$

Thus, it calculates the enthalpy based on the temperature evaluation at the previous time step (28).

$$h_p = \begin{cases} Cp_{sol} \cdot T_p & : T_p < T_{sol} \\ Cp_{avg} \cdot T_p + L_{fus} \cdot \frac{(T_p - T_{sol})}{(T_{liq} - T_{sol})} & : T_{sol} < T_p < T_{liq} \\ Cp_{liq} \cdot T_p + L_{fus} + Cp_{avg} \cdot (T_{liq} - T_{sol}) & : T_p \geq T_{liq} \end{cases} \quad (28)$$

T_{sol} : is the temperature at which the liquid material starts to solidify.

T_{liq} : is the temperature at which the solid material starts to melt.

Cp_{avg} : is the average heat capacity between the heat capacity at T_{sol} and it is value at T_{liq} .

This method can be applied for both isothermal and non-isothermal melting. However, it is numerically unstable due to its explicit nature

1.3.2.4. Beasley enthalpy method

Beasley et al. [131] suggested modifying the energy equation for the PCM based on the status liquid fraction equation(29).

$$\left\{ \begin{array}{l} \text{if: } T_p < T_m \wedge (\lambda = 0) \rightarrow (1 - \varepsilon)(\rho C p)_{p,sol} \frac{\partial T_p}{\partial t} = h_v(T_f - T_p) \\ \text{if: } T_p = T_m \wedge 0 < \lambda < 1 \rightarrow (1 - \varepsilon)\rho_{p,sol} L_{Fus} \frac{\partial \lambda}{\partial t} = h_v(T_f - T_{melt}) \\ \text{if: } T_p > T_m \wedge \lambda = 1 \rightarrow (1 - \varepsilon)(\rho C p)_{p,liq} \frac{\partial T_p}{\partial t} = h_v(T_f - T_p) \end{array} \right. \quad (29)$$

λ : liquid fraction

Beasley method provided a fast model that predicts the melted fraction inside the capsule. However, it neglects thermal conduction between the capsules.

1.3.2.5. Enthalpy porosity method

Voller [132] suggested the enthalpy porosity technique to provide a rapid and stable alternative solution to the original enthalpy method. The solution adds an enthalpy term to the energy balance equation as per equation (30).

$$H = (1 - \varepsilon) \cdot \rho_p L_{Fus} \frac{\partial \lambda}{\partial t} \quad (30)$$

λ the liquid fraction is evolving according to equation (31) and can be calculated for the new time step from the tridiagonal matrix coefficients.

$$\left\{ \begin{array}{l} \text{if: } T_p < T_m \quad \lambda^{(j,n+1)} < 0 \rightarrow \lambda = 0 \\ \text{if: } T_p = T_m, T_{sol} < T_p < T_{liq} \rightarrow 0 < \lambda < 1 \\ \text{if: } T_p > T_m \quad \lambda^{(j,n+1)} > 1 \rightarrow \lambda = 1 \end{array} \right. \quad (31)$$

This method provides a reliable solution to the phase change and can estimate the liquid fraction for a variety of applications. However, it consumes more time compared to the apparent heat capacity method and not suitable if the PCM melt in a wide range of temperatures.

Apparent heat capacity method provides fast and sufficiently accurate predictions of the PCM behavior. However, it requires accurately defining the thermophysical properties of the PCM, such as the temperature range that phase change is occurring for the required mass of PCM. On the other hand, The most used method in commercial software such as FLUENT® and COMSOL is the enthalpy porosity method because it provides a reliable method to estimate extra parameters such as the liquid fraction that is needed for a wider application.

In order to provide a valid simulation of a latent thermocline TES, one of the latent heat models should be incorporated with a suitable physical model from the listed models in Table 12.

1.3.3. Models for latent heat TES

For TES that is 100% filled with an encapsulated PCM, the literature used all modeling approaches as listed in Table 12 except for model No. 2

1.3.3.1. Schumann model: Plug flow in HTF, no heat conduction, no temperature gradient in PCM capsule.

The assumptions of this modeling method are:

- The encapsulation of PCM is spherical and has an equal size filled with the same amount of PCM for all the encapsulations.
- The specific heat of PCM is changing during the phase change process.
- Constant density for the PCM with constant volume and mass for all the phases.
- Constant average porosity inside the tank (ϵ).

Equations (1) and (2) list the energy balance equations of this model for HTF and PCM, respectively.

Tumilowicz et al. [133] developed a 1D Schumann model with an enthalpy method to demonstrate the phase change in the PCM, with the assumption that the Peclet number of the tank is large enough which allows neglecting heat conduction in the axial direction for both HTF and PCM. They used the method of characterization to solve the numerical scheme and compare the results to an analytical solution, which confirmed the validity of the model.

Xu et al. [134] used a similar modeling approach on a case study of 60MW_{elec.} in a solar power plant with 35% thermal to electricity efficiency. They used the model to optimize the tank height and deduced general instructions to size TES with PCM.

In another study, Xu et al. [135] numerically evaluated three thermoclines using the same HTF (Therminoil VP-1) and three different fillers: granite rocks as SHSM, KOH as PCM, and NaCl-KCl as a second PCM. The comparison indicated that using a PCM offers a 46% smaller thermocline tank size compared to SHSM to deliver the same amount of energy with the same 5 m tank diameter. Elsewhere, Xu et al. [136] used various charge/discharge operations modes to study the effect of cycling on the latent heat TES. Based on the results of this work, they recommended starting the charging process from the low temperature in the

sensible heat TES, while a preheating is required for the latent heat TES, to improve the cyclic performance of PCM storage performance.

Regin et al. [137] provided a mathematical simplification of the Schumann model and applied it to a paraffin PCM in a thermocline with water as HTF. They simulated the phase transition with the enthalpy method while depicting the thermocline as a column of PCM split into several sections, equal to the number of transfer units (NTU). They integrated the energy balance equation at each time step to obtain the outlet temperature for each NTU based on the known inlet temperature. Regin et al. [137] articulated that PCM solidifies in a significantly longer time than it melts, claiming that a lower heat transfer rate causes the delay during solidification. Furthermore, they found that the higher the inlet temperature of HTF (higher Stefan number), the shorter charging time. In addition, the lower the capsule diameter, the faster charge and discharge times are. Finally, assuming isothermal phase change resulted in a 31.6% faster melting time compared to non-isothermal phase change.

Manfrida et al. [138] observed the potential use of PCM TES in CSP plants coupled with an organic Rankin cycle (ORC) turbine. They solved a three-phase equations Schumann approach for HTF, PCM, and wall using commercial software package TRNSYS and simulated the phase change by using the Beasley enthalpy method, the model is validated from literature.

The simulation indicated 83% charge efficiency and 93% discharge efficiency with a 68% average exergy efficiency of the storage.

Plug flow in HTF, Axial heat conduction between filler, and no temperature gradient in the PCM capsule (Littman).

Equations (4) and (5) represent this modeling approach. To the author's knowledge, no one used this method to simulate latent heat TES. At the same time, it was used for the sensible heat TES section (1.3.1.2).

1.3.3.2. Plug flow in HTF, concentric symmetrical temperature gradient PCM capsule.

Equations (6) & (7) present the energy balance equations in this method for HTF and PCM.

Ismail et al. [139] provided a simple 1D 1P model of this approach that calculates PCM behavior with the heat source method. They validated the model from the literature, and then applied it to a horizontal cold storage situation. Ismail et al. advised to use the PVC as encapsulation material instead of copper because

of its cost reduction. Furthermore, its thermal resistance did not affect the system performance significantly. Furthermore, they emphasized on using the mass flow rate as a control parameter of the charge and discharge time.

Nithyanandam et al. [140] evaluated the behavior of an adiabatic thermocline filled with PCM. They neglected the heat conduction in the HTF and between the PCM capsules, because of the ratio of the heat capacity rate of the fluid to axial heat conduction known as Peclet number equation(32) $Pe_{tank} \gg 100$ [141].

$$Pe_{tank} = \frac{v_f}{\alpha} H_{tank} = \frac{(\rho C_p)_f v_f \Delta T}{k_f \Delta T} H_{tank} = Pr \cdot Re_{tank} \quad (32)$$

Nithyanandam et al. [140] studied the PCM behavior applying the enthalpy porosity method, considering thermal resistance of the encapsulation. They demonstrated that a smaller diameter capsule increased the pump work but increased the efficiency of the storage. Furthermore, the higher the mass flow, the bigger the thermocline thickness.

1.3.3.3. Dispersed flow in HTF, and no heat conduction in the PCM capsule nor temperature gradient (Beasley).

This method depends on equation (8) and (9) as energy balance equations for HTF and PCM and Beasley enthalpy method to follow the development of the phase transition of the PCM.

Beasley et al. [131] developed a 1D method that considers a modified axial thermal dispersion of the HTF and corrected the convection heat transfer coefficient with the Biot number of the PCM particle. The model was validated from experimental results.

Wu et al. [142], [143] analyzed a solar-heated PCM thermocline applying this approach. They took into account the thermal losses to the environment through the energy balance of HTF, and they took into account the thermal resistance of the envelope and PCM. The model predicted similar temperatures to the one obtained from the experiment within an acceptable error margin.

Wu et al. [142] observed the influence of HTF inlet temperature and mass flow on the heat release rate during discharge. For example, the efficiency of latent heat utilization increased with the inlet temperature, and increasing mass flow rate increases the heat release rate and reduces the PCM solidification time. Moreover,

the initial temperature has no significant influence on the heat release rate nor the solidification time of the PCM.

Using this 1D model, Li et al. [144] suggested design procedures to optimize the size of thermocline filled with PCM spheres for solar heat applications. With this methodology, Li et al. [144] claimed that PCM TES could provide the required energy to heat a 1964 m³ swimming pool during the winter season, and at the same time, provide an economical solution to TES.

Flueckiger et al. [145] solved a 1D energy balance equation as per this approach in addition to the momentum and continuity equations. The momentum equations simplified using the Darcy-Forchheimer equation. They examined the performance of a conceptual molten-salts/PCM thermocline, and the model accounts for the latent heat in the PCM equation by using the enthalpy method.

Flueckiger et al. found that lowering the melting point of PCM improves the efficiency of PCM utilization. However, it reduces the outlet temperature of the system, which is negatively influencing the downstream process. On the other hand, selecting a PCM with a higher melting temperature results in a higher and more suitable thermocline outlet temperature, while it reduces the efficiency of latent heat utilization. Moreover, using a cascade of three PCM types yielded 9.7% higher annual energy, compared to the quartzite rocks case, and 16% smaller thermocline thickness.

Arkar et al. [146] applied a 2D version of this approach on the HTF equation and used the apparent heat capacity method to simulate the phase change behavior of the PCM.

Arkar et al. validated the model from an air/PCM-paraffin thermocline experiment. They emphasized the importance of the thermophysical properties of the PCM on the management of the thermocline TES.

1.3.3.4. Continuous Solid model (C-S): Dispersed flow in HTF, considers heat conduction and neglects temperature gradient in the PCM capsule.

In this method, equations (10) and (11) are representing the energy balance equation for HTF and PCM.

Izquierdo-Barrientos et al. [147] evaluated the performance of air/PCM. They compared it to a sensible heat model using a 1D 3P approach of this model, and apparent heat capacity method for latent heat effect. They suggested neglecting the stored energy in the tank wall when its diameter is large enough, while for a

small tank's diameter, it cannot be neglected. The model is validated from the experiment.

Izquierdo-Barrientos et al. [147] calculated the energy stored in the tank wall with 16 % and 8% of the total energy stored in their 0.2 m diameter, 0.2 m height cylindrical thermocline for sand and PCM, respectively.

Bellan et al. [148] formulated a 2D 2P numerical model using the C-S approach to evaluate the performance of Therminol 66/PCM-sodium nitrite. Using the enthalpy porosity approach for the phase-change simulation and taking into account natural convection within the PCM capsules, they found that the solidification is longer than melting for all capsule sizes.

Furthermore, natural heat convection inside the capsule increases with the capsule diameter, leading to additional variation in time between the charging and discharging process. Moreover, the bigger the diameter of the sphere, the larger the thermocline thickness. In addition, faster flow rates and higher Stefan number (higher inlet temperature) increased the thermocline thickness during charge.

Using an identical approach, Bellan et al. [149] evaluated the performance of a lab-scale air/encapsulated molten salt PCM, and they concluded that the total stored energy increased by 38% due to the sensible heat of the PCM. Moreover, when increasing the thickness of the polymer encapsulation by 66%, the total charging time increased by 15%, mainly due to the envelope material thermal resistance. Finally, they claimed that melting is faster than solidification due to the prominent influence of natural convection during melting.

Raul et al. [150] compared a 1D C-S model with an enthalpy porosity method to the thermal performance of a lab-scale thermocline filled with PCM encapsulated in stainless steel spheres. During the experiment, they found slight temperature variation at the radial axis of the thermocline, and they confirmed the accuracy of their 1D model.

Raul et al. [150] indicated that increasing the inlet temperature during the melting process increases the efficiency and the stored energy. During discharge, reducing the inlet temperature (the low temperature) increases the efficiency. Moreover, small PCM diameter and high porosity resulted in a thermal efficiency increase, as well as an increase of melting and solidification in the PCM. However, high pumping power is needed to cope with the pressure drop increase inside the thermocline compared to the larger capsule diameter.

Xia et al. [151] used commercial software to solve the continuity, momentum, and energy balance equations for HTF and the PCM spheres, using a 2D -2P approach for encapsulated PCM inside the thermocline, and enthalpy porosity method for the latent heat. They evaluated natural convection during

melting by modifying PCM thermal conductivity. Xia et al. validated their model from the literature and recommended a random packing of the spheres over special packing for the same spheres quantity because it increases the discharge rate. Moreover, they indicated that the encapsulation material and its thickness have a significant effect on the discharge rate. For example, stainless steel encapsulation resulted in a 15% faster discharge rate compared to polyolefin.

1.3.3.5. Dispersion concentric model (D-C): Dispersed flow in HTF, and concentric symmetrical temperature gradient in PCM capsule.

Energy balance equations for this model are similar to the ones used in sensible heat models, Equations (13), (14), and (15). The difference is in modeling the PCM phase transition.

Nithyanandam et al. [86] applied a 1D D-C model and enthalpy porosity method to evaluate a latent heat thermocline TES.

Nithyanandam et al. [86] evaluated natural convection within the PCM capsule by modifying the thermal conductivity of the PCM and emphasized that small PCM diameters increase the efficiency. They suggested that a high Reynold number (high mass flow rate) results in an efficiency reduction and a pressure drop increase. Furthermore, increasing the ratio between latent to sensible heat in the PCM (lower Stefan number), reduces the efficiency of discharge while increases the discharge time. Finally, they found that if the PCM melting temperature is within the TES operating range, changing the PCM (the melting temperature) does not influence the performance of the thermocline.

In another study, Nithyanandam et al. [152] used the same approach to evaluate the Levelized cost of electricity (LCOE) in CSP plants with thermocline filled with encapsulated PCM TES. They claimed that low capsule diameter reduced the capital cost due to efficiency improvements, with a competitive LCOE of about 5.37cent\$/kWh, in addition to a better capacity factor compared to the two tank molten salts. However, they did not include the cost of manufacturing the encapsulated PCM. Elsewhere, with an identical numerical approach, Nithyanandam et al. [153] concluded that using a cascade of PCM in two layers lowered the LCE compared to the one, or the three PCMs case.

Karthikeyan et al. [154] worked on a 1D D-C model with an enthalpy porosity method to evaluate air-PCM thermocline for low-temperature solar air heating application. They found that reducing the size of the capsule, increasing the inlet temperature, and increasing the mass flow rate reduced the charging time.

Karthikeyan et al. argued that increasing PCM thermal conductivity did not yield to better thermocline performance, Figure 12. They indicated that the heat transfer area is the dominant factor in the heat transfer between the HTF and the PCM due to the small sphere's diameter.

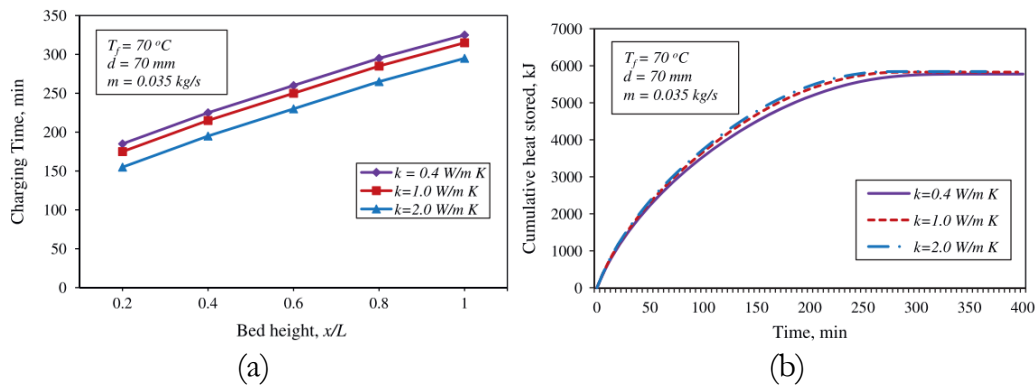


Figure 12 the influence of PCM thermal conductivity on (a) charge time and (b) cumulative stored heat Karthikeyan et al. [154]

Wu et al. [155] applied a 1D D-C model that solves the momentum equation for the HTF, to compare three types of thermocline configurations: one phase change temperature materials (PCT), three cascaded PCTs, and five cascaded PCTs **Erreur ! Source du renvoi introuvable.**

Wu et al. [155] recommended the five PCTs configuration over the other two because it provides more linear HTF temperature distribution in the system, faster charge, a better charge, and discharge efficiencies. On the other hand, this study does not provide an evaluation of the difficulty in finding the multiple PCMs with suitable melting temperatures, as well as the complexity of their envelope design issues such as materials compatibility and mass production limitation.

Elsewhere, Wu et al. [156] used a 2D D-C model to evaluate the transient response of molten-salts HTF filled with PCM spheres. The apparent heat capacity method is used to simulate the phase change phenomena, and the thermal conductivity of the PCM is modified to account for the natural convection inside the capsules. Wu et al. [156] validated their model from the literature. They demonstrated that the bigger the capsule diameter, the larger the thermocline thickness, the lower the discharge efficiency, and the lower the isothermal influence of the PCM on the HTF temperature Figure 13.

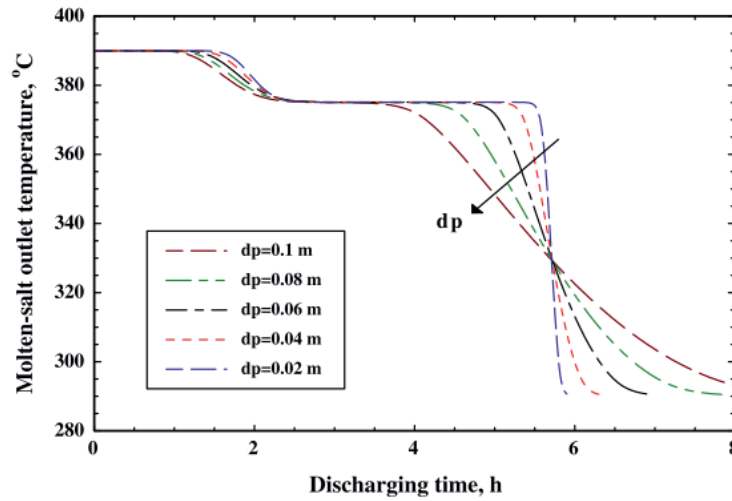


Figure 13 Thermocline outlet temperature during discharge for various capsule diameters Wu et al. [156]

Galione et al. [157] studied natural convection and the phase change inside PCM capsules with a fixed grid enthalpy-porosity CFD code, the code is coupled to a 1D D-C model to evaluate PCM thermocline TES. They compared the resulted thermocline outlet temperature during discharge from three models. The first one is a simple model that neglects natural convection in the capsule and assumes constant phase change PCM properties indicated as (S.C.). The second model is also simple (neglects natural convection within the capsule) but considers variable phase change PCM properties indicated as (S.V.). On the contrary, the last model is a detailed model that accounts for natural convection within the capsule and assume constant phase change PCM properties called (D.C.) Due to similar predictions for all tested models, Galione et al. [157] suggested that natural convection does not have a significant influence on the overall performance of the thermocline.

Oró et al. [158] applied a 1D D-C model in the PCM thermocline for cold storage. They evaluated thermal losses through the tank wall and validated their model against 10L water/organic PCM thermocline.

Oró et al. [158] analyzed three different Nusselt correlations and found similar temperature profiles, suggesting that any of the studied correlations leads to similar accuracy. Furthermore, they indicated that natural convection has no significant influence on the charge and discharge process; however, at a minimal flow rate inside the thermocline, natural convection becomes more influencing.

Peng et al. [159] developed a hybrid 1D model that uses D-C and C-S. The C-S model evaluates the HTF and PCM surface temperature, and then the D-C model estimates the temperature gradient within the PCM based on its HTF and

PCM surface temperature, which are predicted by the C-S model, the iteration continues until the convergence is achieved. The numerical model used apparent heat capacity method and studied a theoretical thermocline filled with encapsulated sodium nitrite (NaNO_2) as PCM and molten salts as HTF.

Peng et al. [159] concluded that reducing the encapsulation diameter leads to faster charge time and higher charging efficiency; on the other hand, a higher mass flow rate reduces the efficiency of charge. Furthermore, increasing the height of the thermocline increases the efficiency of the system significantly.

Elfeky et al. [160] used a 1D D-C model to compare the performance of four types of PCMs at different configurations, using the apparent heat capacity method to simulate phase transition inside the PCM. They evaluated thermal losses through the thermocline wall and validated their model from the literature. Elfeky et al. [160] indicated that the melting time was significantly faster than solidification for all tests due to the thermal resistance of solid PCM. Moreover, three-types PCMs performed better during charge and the discharge with higher efficiency compared to single type PCM, also, for the single type PCM thermocline, the simulation showed that the PCM at the bottom of the tank is not completely melted.

Karthikeyan et al. [161] compared three different models of thermocline filled with encapsulated PCM. The models are Schumann, C-S, and D-C. They tested two setups: air/PCM-(paraffin capsule) and water/PCM-(paraffin capsule). The results of the analysis suggested that the D-C model represented the experimental data more accurately than the other models. However, Karthikeyan et al. recommended using the Schumann model to simulate the gaseous HTF, such as the air, to reduce the computation time since the discrepancies between the model and the experiment are within an acceptable range. The D-C model is more convenient with the liquid HTF such as the water, although it requires considerably more time for calculation.

Although the D-C model is considerably time-consuming compared to the C-S model, it provides more accurate temperature prediction for PCM filler in the thermocline, because it takes into account the thermal gradient within the PCM.

1.3.4. Models for combined latent and sensible heat TES

A reliable numerical model of combining a PCM layer to a sensible heat thermocline TES is important to not only study and evaluate the performance of this solution but to properly design the PCM layer and optimize its size and materials. The main modeling approach is to have separate models for the two layers, the latent heat and the sensible heat, then coupling these two models with correct boundary conditions.

Any of the models presented in Table 12 could be used to simulate the PCM layer as well as the sensible heat layer or a combination of two modeling approaches. However, there are only four approaches used in the literature to simulate a combined thermocline TES so far as per the following:

1.3.4.1. Schumann model: Plug flow in HTF, no heat conduction, no temperature gradient in PCM capsule.

Ahmed et al. [162] used a 1D Schumann model to compare three thermoclines TES. The first is filled only with sensible heat storage and uses solid rod structs SRS as solid filler, the second contains only PCM spheres, and the third thermocline is a combined solution between the two. They used the apparent heat capacity method to simulate the PCM behavior and validated the model from the literature.

Ahmed et al. [162] confirmed that sensible heat only TES is the cheapest solution compared to the latent heat TES and the combined TES. However, the best thermal performance is found in latent heat TES, combined, then the sensible heat TES. Finally, they concluded that the combined solution presented an excellent compromise between the cost and performance compared to the sensible heat and latent heat with the capacity cost of 37\$/kWh_{th} compared to 42\$/kWh_{th} and 35\$/kWh_{th} respectively.

1.3.4.2. Continuous Solid model (C-S)

Hernández et al. [163] conceptualized a thermocline that combines a PCM layer of AlSi positioned at the top of the tank to a sensible heat storage material of steel slag which was placed right below the PCM layer. They applied a 3P 1D C-S model on both thermoclines taking into account thermal losses to the environment. Energy balance equations as presented earlier in equations (10) and

(11), while the phase transition was simulated using the enthalpy porosity method. The study concluded that the optimum design is with a 5% PCM layer of the volume of the tank when comparing 0%, 1%, 2.5%, 5%, 10%, and 20%.

1.3.4.3. Dispersion concentric model (D-C): Dispersed flow in HTF, and concentric symmetrical temperature gradient in filler.

Equations (13) and (14) illustrate the general form of energy balance equations for this type of model.

Galione et al. [164] [165] [166] demonstrated the validity of a 1D D-C model on a three-layer thermocline: PCM at the top, quartz rocks and sand SHSM at the middle, and another PCM at the bottom. They simulated the latent heat effect by using the enthalpy porosity method. The numerical results showed better efficiency in this three-layered thermocline compared to the no-PCM case or more than two layers of PCM.

Using an identical modeling approach Galione et al. [167] evaluated the influence of different inlet temperatures and mass flow rates on the performance of TES. They compared the reference two-tank molten salts to various thermocline options such as solid filler-only, PCM only, and a multilayered PCM. For similar operating conditions, the comparison suggested negligible thermal losses to all cases, less than 1% of stored energy. Multilayer thermocline has a 32% smaller height compared to the solid filler only case for the same thermal storage capacity, which is reducing the required HTF by 32%.

Zhao et al. [168] applied a 1D D-C model to study the effect of some parameters on the thermal performance of multilayer solid PCM thermocline thermal energy storage. In the numerical approach, Zhao et al. [168] used the apparent heat capacity method to simulate the PCM behavior and neglected thermal losses to the environment. Moreover, they considered natural convection inside the capsule by modifying the thermal conductivity of the PCM and evaluated the thermal resistance of the encapsulation. They found that increasing the thermocline's diameter increases the cycle operation, consequently enhancing capacity factor and lowering capital cost per kWh_{th} for given operating parameters. Furthermore, the use of the PCM layers in the thermocline replaced part of the solid filler and increased the operating cycle. However, the higher the amount of PCM, the higher the capital cost.

Zhao et al. [169] used similar modeling approach to simulate a 2000 MWh_{th} TES capacity and compared various thermocline setups to provide the same

capacity: 100% SHSM filler, 100% PCM, 50% low temperature LT-PCM + 50% high temperature HT-PCM, and 10% LT-PCM+ 80% SHSM+10% HT-PCM. Zhao et al. suggested a methodology to size the thermocline. Moreover, the deployment of a multilayered thermocline helps in eliminating the second tank in the two-tank solution, with the same thermal capacity.

Elsewhere, Zhao et al. [170] evaluated the influence of cycling on the TES operation using the same model. They concluded that partial discharge reduced the efficiency due to a broader thermocline thickness, and the latent heat layers acted only as sensible heat storage during the partial charge. In contrast, the efficiency of the TES reduced between 1.1% to 6% only due to real-life operating conditions.

1.3.4.4. Combine C-S to Dispersed flow in HTF and no heat conduction in the PCM capsule nor temperature gradient.

Zanganeh et al. [46] numerically studied combined rocks and encapsulated PCM in thermocline that is charged by 650°C air **Erreur ! Source du renvoi introuvable.** They used a 1D approach of the Littmann method in the sensible part according to equations (4) and (5) for HTF and rocks, respectively; in the latent heat part, the Beasley method presented in section (1.3.3.3) as per equations (8) & (9) for HTF and PCM particle accordingly was used. The model considered the stored energy in the capsule material and neglected its thermal resistance.

Zanganeh et al. [46] evaluated four different sets of combinations of 0% PCM, 0.67% PCM, 1.33% PCM, and 2.67% PCM of the total volume of the thermocline for three PCM types. They concluded that 1.33% stabilized the outlet temperature of the thermocline and provided the best discharge efficiencies between the evaluated cases. The PCM layer, in this case, stored about 4.4% of the total stored energy in the thermocline.

In another study, Zanganeh et al. [171] extended the model to account for the thermal losses to the environment and the radiative heat transfer in the bed. Moreover, they validated the models against a 42 kWh_{th} lab-scale 1.68 m high and 0.2 m diameter cylindrical thermocline, the sensible heat part being filled with rocks, and the latent heat part with AlSi₁₂. The PCM is contained inside a bundle of stainless steel tubes placed in staggered positions. The experimental results demonstrated the ability of the PCM layer to stabilize the outlet temperature of the thermocline at a temperature around the melting point of the PCM.

Geissbühler et al. [172] scaled up this modeling approach to simulate the behavior of two commercial thermoclines with a capacity of 23 MWh_{th} and 1000

MWh_{th}. The results of the model demonstrated a stable outlet temperature with improved discharge efficiency. It also indicated that the exergy efficiency of the storage system is greater than 95%, while the cost of the materials is below 15 \$/kWh_{th}.

Becattini et al. [72] used a similar modeling approach to simulate the performance of a pilot-scale TES. Thermocline consists of two parts connected in serial, an 11.6 MWh_{th} sensible part and a 171.5 kWh_{th} PCM part.

Becattini et al. [72] found that the PCM layer stabilized the outlet temperature of the air. However, the performance of the latent heat storage degraded with each applied cycle, they attributed this degradation to a small leakage of the PCM from the tested tubes and degraded quality of PCM due to phase separation. Moreover, they ascribed that phase separation to the material impurities.

1.4. HEAT TRANSFER CORRELATIONS FOR THERMOCLINE MODELS

Heat transfer correlations are essential in numerical modeling. Not only they simulate the necessary heat transfer phenomena, but also they can be modified to account for complex heat transfer without deploying more complicated and time-consuming model approaches. The correlations account for convective heat transfer between HTF and filler, HTF, and wall, between the external tank's wall and the surrounding air, effective thermal conductivity, and natural convection inside the PCM capsule.

1.4.1. Convection heat transfer HTF-Filler.

Nusselt number (Nu) is a non-dimensional quantity that represents the ratio between convection to pure conduction heat transfer[173] equation(33).

$$Nu_L = \frac{h \cdot L}{k_f} \quad (33)$$

Nu can be estimated from empirical correlations based on specific experimental conditions and two non-dimensional quantities, Reynold number (Re) and Prandtl number (Pr).

Re is the ratio of inertia to viscous forces, equation (34), that determines flow regime (laminar, turbulence, or transitional).

$$Re_L = \frac{\rho \cdot v_f L}{\mu_f} \quad (34)$$

Pr is the ratio of momentum to thermal diffusivities represents the thermal properties of the HTF, equation (35).

$$Pr = \frac{\mu_f / \rho_f}{k_f / \rho_f C_p} = \frac{C_p \cdot \mu_f}{k_f} \quad (35)$$

The convective heat transfer coefficient can be calculated from equation (33), after calculating Nu from the right correlation. Table 15 summarizes mostly used Nusselt correlation in the reference literature with their application.

Table 15 Nu correlations for heat exchange between HTF and particle as they used in the literature

Correlation	App.	ref
$0.6 < Re < 13 \quad Nu = 0.89Re^{0.41}$	Spheres	[99]
$13 < Re < 180 \quad Nu = 1.75Re^{0.49}Pr^{1/3}$		
$180 < Re \quad Nu = 1.03Re^{0.59}Pr^{1/3}$		
$Nu = 2 + 1.1Re^{0.6}Pr^{1/3} \quad Re < 10000$	Spheres	[87][106][109] [122][149][157] [164][165] [166] [167] [168]
$Nu = 2 + 1.354 \cdot Re^{0.5}Pr^{1/3} + 0.0326 \cdot Re^{0.5}Pr^{1/3}$ $Re < 5000$	Spheres	[88]
$Nu = 2 + 2.031Re^{1/2}Pr^{1/3} + 0.049RePr^{1/2}$ $Re < 5000$	Spheres	[131][172]
$Nu = 3.22Re^{0.33}Pr^{0.33} + 0.117Re^{0.8}Pr^{0.4}$	Spheres	[142][143]
$Nu_{rocks} = \frac{2.06}{(1 - \varepsilon_p)} Re_{0,p}^{0.425} Pr_f^{\frac{1}{3}}$ $90 \lesssim Re_{0,p} \lesssim 4000, Pr_f = 0.7$	Rocks	[172]
$Nu_{PCM} = 0.51 C_{row} Re_{max}^{0.5} \cdot Pr^{0.37} \left(\frac{Pr_f@T_f}{Pr_f@T_s} \right)^{0.25}$ $100 < Re < 1000$ C_{row} is a correction factor for less than 20 tubes	Tubes	[171] [172][174]

Xu et al. [13] and Oró et al. [158] evaluated different correlations for spherical solid filler and found that there is no significant influence of the used correlation on the results.

The volumetric overall heat transfer coefficient is calculated from equation (36), knowing the shape factor (α_s) and the heat transfer coefficient (h) related to sphere.

$$\frac{h_v}{h} = \alpha_s \quad (36)$$

The shape factor α_s (m^2/m^3) is the ratio between the total surface area of filler material to the total volume of the tank containing this material [175]. Based on this definition, the shape factor of spheres in a thermocline TES that has tank porosity ε is calculated from equation (37).

$$\alpha_{s-sphere} = \frac{6(1 - \varepsilon)}{d_p} \quad (37)$$

d_s is the sphere diameter

Similarly, the shape factor for horizontal tube filler in a thermocline TES that has tank porosity ε can be calculated from equation (38) [171].

$$a_{s-tube} = \frac{4(1 - \varepsilon)}{d_{tube}} \quad (38)$$

d_{tube} is the tube diameter

Some researchers used a modified convective heat transfer coefficient to account for an essential simplification to their models, such as the thermal gradient inside the filler materials, by considering the Biot number (Bi) of the solid filler. Bi is defined as the ratio of internal thermal resistance of a solid to the boundary layer thermal resistance calculated from equation (39). Bi represents uniformity of temperature in the solid.

$$Bi = \frac{h \cdot L_{ch}}{k_s} \quad (39)$$

* L_{ch} is the characterized length, for a sphere is $\frac{d_s}{6}$, and for a tube $\frac{d_4}{4}$

Table 16 illustrates the correlations used for various applications to modify the convective heat transfer coefficient based on the Bi number.

Table 16 modified heat convection coefficient as they appeared in the literature

Correlation	App.	ref
$\frac{1}{h_{eff}} = \frac{1 + (Bi_s/5)}{h}$ $Bi_s = \frac{hr_s}{3k_s}$	spheres	[95][98][136]
$h_{eff} = \frac{h}{1 + 0.25Bi_{PCM}} : Bi_{PCM} = \frac{hd_{PCM}}{2k_{PCM}}$	spheres	[131][146][171]
$\frac{1}{h_{eff}} = \frac{1 + (Bi_{tube}/5)}{h}$ $Bi_{tube} = \frac{hr_{tube}}{2k_{tube}}$	tubes	[97][98]

1.4.2. Convection heat transfer HTF-wall.

Table 17 lists the correlations used to evaluate the heat transfer coefficients between HTF and the thermocline wall.

Table 17 convection heat transfer between HTF and thermocline wall as appeared in the literature

Correlation	ref
$h_w = \frac{k_f}{d_p} (2.576 Re^{1/3} Pr^{1/3} + 0.0936 Re^{0.8} Pr^{0.4})$	[87][89] [101][160][159][176]
$h_w = \frac{k_f}{d_p} \left(1 - 1.5 \left(\frac{D}{d_p} \right)^{-1.5} \right) Re^{0.59} Pr^{1/3}$	[102]

1.4.3. Thermal losses at the outside thermocline wall.

There are three main approaches to model convection heat transfer at the outer thermocline wall. The first assumes the thermocline as a free-standing wall, vertical plate, or subjected to forced convection. Natural convection is often evaluated using the Rayleigh number (Ra) with an empirical Nusselt correlation. Ra is the non-dimensional product of the Prandtl (Pr) and Grashof number (Gr) that represent natural convection in a fluid equation(40).

$$Ra = Gr.Pr \quad (40)$$

Where Pr represents the thermophysical properties of the fluid, Ra evaluates the ratio of buoyancy forces to viscous forces, equation (41). It defines the ratio of length scale to thickness of the natural convection boundary layer.

$$Gr = \frac{g\beta(T_w - T_\infty)L^3}{\nu^2} \quad (41)$$

g: is the gravitational acceleration constant.

β is the coefficient of thermal expansion for the fluid. (1/T for an ideal gas).

Table 18 summarizes the correlations that are used by the literature with related applications.

Table 18 convection thermal losses at the outer thermocline wall

Correlation	Application	ref
$Nu_{ext} = \left[0.825 + \frac{0.387Ra^{1/6}}{\left(1 + \left\{ \frac{0.492}{Pr} \right\}^{9/16} \right)^{8/27}} \right]^2$	Natural convection	[101][159]
$Nu_{ext} = \frac{4}{3} \left[\frac{7Gr \cdot Pr^2}{5(20 + 21Pr)} \right]^{\frac{1}{4}} + \frac{4(272 + 315Pr)H}{35(64 + 63Pr)D_{tank}}$ $\frac{D_{tank}}{H} \geq \frac{35}{Gr^{1/4}}$ <p>Condition to let vertical cylinder similar to a vertical plate</p>	Natural convection	[113][177]
$Nu_{ext} = 0.664Re_{air}^{0.5} \cdot Pr_{air}^{0.5}$ <p>5 m/sec average wind speed at the outer thermocline wall</p>	Forced convection	[87]

1.4.4. Effective thermal conductivity of the HTF and the solid filler

The effective thermal conductivity of the HTF, as well as the solid filler, are required in the related energy balance equation. Table 19 demonstrates the mostly used correlations to evaluate these quantities as per the application and appearance in the literature.

On the other hand, Xu et al. [13] concluded that for a C-S model using any correlation is acceptable.

Table 19 effective axial thermal conductivity for the various modeling approach

Correlation	Application	ref
$k_{eff} = k_{eff}^0 + k_{eff}^{disp}$		[99]
$k_{eff}^0 = \left(\frac{k_p}{k_f}\right)^{0.280-0.757 \log_{10}\left(\frac{k_p}{k_f}\right)}$	Schumann	[157][164]
$k_{eff}^{disp} = \frac{\dot{m}_f^2 C p_f^2}{h_v} = 0.00232 \cdot k_f Pe^2 : Pe = Re \cdot Pr$	D-C	[165] [166][167]
$\frac{k_{flow}}{k_f} = \frac{Pe_0}{K}$	Littman	[102]
$k_{eff,f} = \varepsilon k_f, k_{eff,p} = (1 - \varepsilon) k_p$	C-S	[87][91] [106] [115][119]
$Pe_f^i = \frac{(\rho C p)_f v_0 l_{ch}}{k_{eff-f}^i} = \frac{Pe_0}{C_0 Pe_0 + k_e^0 / k_f}$		
$C_0 = 0.01$ near the wall		
$C_0 = \frac{1}{11}$ in the central region of the tank	Schumann	[88]
While in the axial direction C_0 varies between 0.2 to 1.0 and Beasley used a middle value of 0.5	D-C	[131][172]
k_e^0 is the stagnant bed effective thermal conductivity		
$k_{f-axial} = 0.7k + \varepsilon \rho C p v r_p$	D-C	[122]
$k_{f-axial} = 0.7 \varepsilon k_f$ at $Re < 0.8$	D-C	[123][124]
$k_{eff-axial} = 0.5 Pr \cdot Re \cdot k_f$ at $Re > 0.8$ or $Pe = 2$	D-C	[147]
$k_{p,eff} = \frac{k_{eff,p}^0 + 0.5 Pr Re_p k_p - k_{f,eff} \varepsilon}{1 - \varepsilon}$		
$\frac{k_{eff}^0}{k_f} = \left(\frac{k_p}{k_f}\right)^{0.280-0.757 \log_{10} \varepsilon - 0.057 \log_{10}\left(\frac{k_p}{k_f}\right)}$	C-S	[147]
Bed stagnation effective thermal conductivity k_{eff}^0		

1.4.5. Natural convection inside PCM

The correlation of natural convection inside the PCM encapsulation varies according to the shape of the envelope. Regin et al. [178] indicated that for natural convection is important when simulating PCM melting inside a horizontal envelope. The natural convection phenomenon is mostly modeled by using empirical correlation to modify the thermal conductivity of the PCM, as listed in Table 20.

Table 20 correlation from the literature to consider natural convection within the PCM envelope

Correlation	Application	ref
$Nu_{conv} = 1.16f(Pr) \left(\frac{D_o - D_i}{2D_i} \right)^{1/4} \frac{Ra^{1/4}}{\left\{ \left(\frac{D_i}{D_o} \right)^{3/5} + \left(\frac{D_o}{D_i} \right)^{4/5} \right\}}$ $f(Pr) = \frac{2.012}{3 \left[1 + \left(\frac{0.492}{Pr_{PCM}} \right)^{9/16} \right]^{4/9}}$ $k_{PCM,eff} = k_{PCM} Nu_{conv}$ $\frac{k_{PCM-eff}}{k_{PCM}} = c Ra^m$	Spheres	[140]
<p>c and m are experimental values 0.18 and 0.25</p> $Ra = \frac{g\beta(T_p - T_{melt}) \left(\frac{d_p}{2} \right)^3}{\nu\alpha}$ $Nu_{conv} \begin{cases} f(Pr_p) \cdot F_{Sph} \cdot Ra^{0.25} & \text{melting} \\ 0.18 Ra^{0.25} & \text{Freezing} \end{cases}$ $f(Pr_p) = 0.778 \left(1 + \left(\frac{0.492}{Pr_{PCM}} \right)^{9/16} \right)^{-4/9}$ $Ra = \frac{\rho_{liq} g \beta C p_{liq} \delta_l^3 (T_f - T_l)}{k_{liq} \mu_{PCM}}$	Spheres	[151][156]
$k_{PCM-eff} = 0.228 Ra_{L-cyl}^{1/4} \left(1 - \frac{d}{D} \right)$ $k_{PCM-eff} = k_{eq} k_{liq}$	Horizontal cylinder	[179]
$k_{eq} = \frac{\overline{Nu}}{Nu_{cond}} : \overline{Nu} = [Nu_{cond}^{15} + Nu_{conv}^{15}]^{1/15}$ $Nu_{cond} = \frac{2}{\ln \left(\frac{d_{in}}{d_{PCM}} \right)} ; Nu_{conv} = \left[\frac{1}{Nu_{d_{PCM}}} + \frac{1}{Nu_{d_{in}}} \right]^{-1}$	Horizontal cylinder	[178]
$Nu_{PCM} = 0.24 Ra_{L-cyl}^{01/4}$	Horizontal cylinder	[180]

1.5. RESEARCH PROBLEMS AND DISSERTATION OBJECTIVES

This work approached the research problem by considering four main areas:

- Evaluate the actual thermal performance of thermocline TES filled with recycled asbestos-containing waste (ACW); as a potential sensible TES medium, compares it to a reference material; alumina spheres, and define the main performance indicators.
- Select an appropriate PCM material to stabilize the outlet temperature of the thermocline at the design temperature range for this installation 300 - 310°C.
- Design the PCM layer shape to avoid direct contact between PCM and HTF, and the PCM material should be compatible with the envelop materials from one side and the HTF inside the thermocline from the other side. Furthermore, optimize the size of the layer to provide an acceptable cost and to increase discharge efficiency compared to sensible heat medium storage. Finally, carry out experiments to evaluate the performance of a two-layer thermocline storage.
- Provide a suitable numerical model for the sensible heat experiments as well as the combined sensible-latent heat TES, validate the model from related experiments, research influence for filler properties on the thermal behavior of the tank, and evaluate the concept of combining a layer of PCM to a sensible heat medium.

2. MATERIALS AND METHODS

2.1. EXPERIMENTAL SETUP

2.1.1. The MICROSOL-R

The MICROSOL-R installation, which is located in France, Font-Romeu-Odeillo-Via is used to perform the main experimental work of this study. Figure 14 illustrates the schematic diagram of the main parts of the MICROSOL-R facility that are used during the experiments.

MicroSol-R is a pilot-scale CSP plant consisting of three parabolic trough collectors C1: North-South axis parabolic trough, C2, and C3 East-West axis parabolic troughs. Each of these solar collectors is 12 m long, 5.76 m aperture, and focal length 1.7m, equipped with 7cm in diameter receiver that gives 50 kW_{th} each, nominal.

TC is the TES, it is a 4 m³ thermocline tank 3.24 m height and 1.276 m internal diameter. The tank contains four vertically-positioned baskets to allow easy access to the solid storage material while filling and emptying. Furthermore, these baskets reduce the possibility of thermal ratcheting.

During the charging process, the valve V1 is opened while the charge pump P1 is activated to allow the synthetic oil HTF to be heated by a 70 kW electrical heater EH. If additional heating power is required, the three-way valve V2 is opened to deploy the solar collectors.

The three-way valve V3 is set to send all the HTF to the thermocline (closed) while the valve V4 is closed. The hot HTF is injected from the topmost tank point, extracting the cold HTF out of from the bottom. This process design limits the thermal stratification due to the density difference between hot and cold HTF during both charge and discharge.

For the discharge, the valve V1 is closed, and the discharge pump P2 starts injecting cold HTF in the thermocline from the bottom. The hot HTF exits the tank from its top, V4 is opened, and the valve V3 is closed.

The HTF is cooled down using three water-cooled heat exchangers HEX1, HEX2, and HEX3. The outlet temperature of HEX3, which represents the inlet temperature of the thermocline, can be controlled using four parameters: the water pump's power P3, and the opening percentage of the valves V6, V7, and V8.

The water is cooled down using a water-glycol-cooled heat exchanger HEX4 operated by the pump P4, where the heat is rejected to the surrounding atmosphere using three electrically operated air fans.

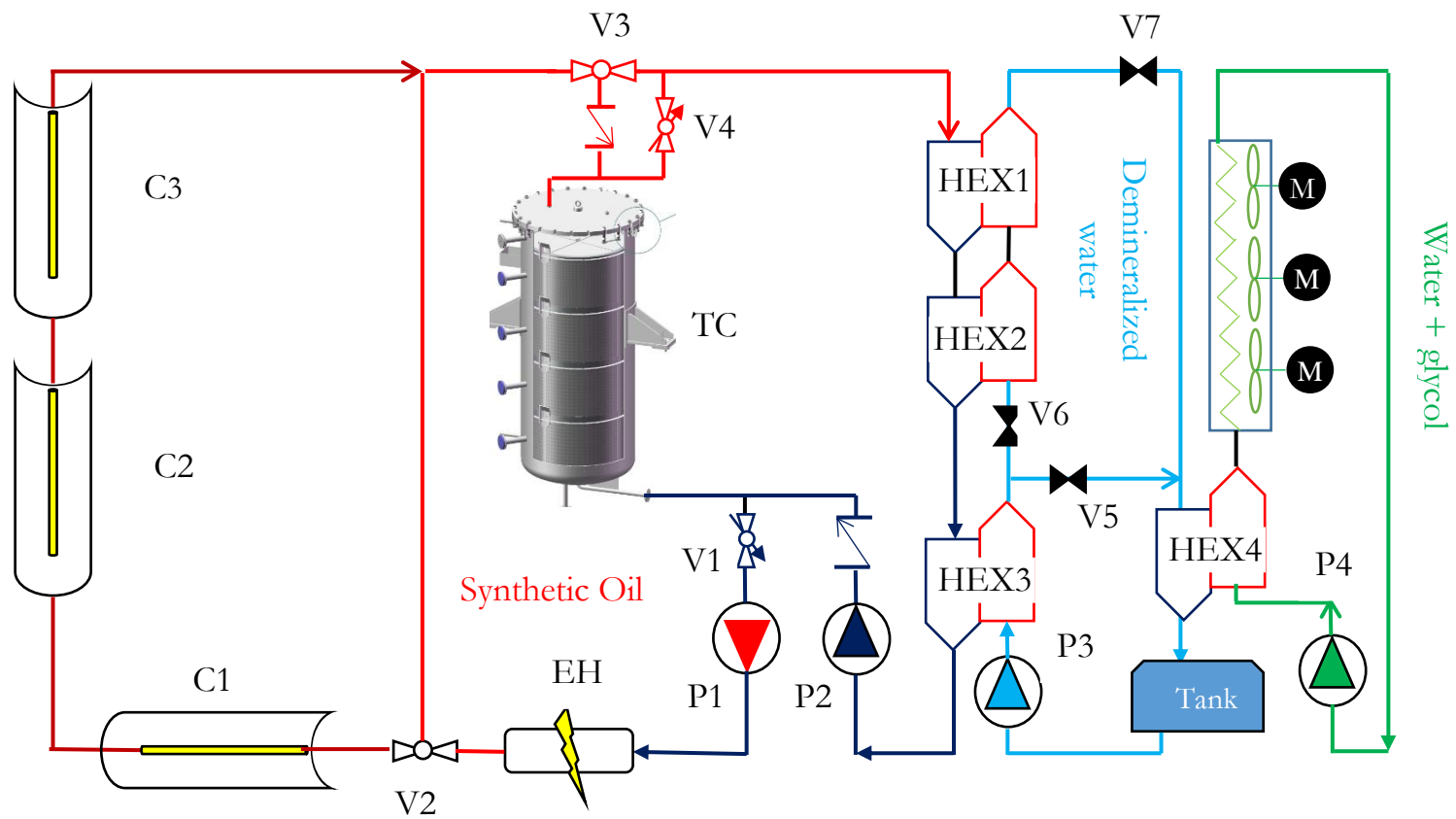


Figure 14. Schematic of MicroSol-R pilot plant

The thermocline contains two buffer zones that include tubular HTF distributors that enable a homogeneous HTF distribution Figure 15.



Figure 15. HTF distributor at the top of the thermocline

The solid bed height is 2.64 m, and thermocouples are used to record HTF temperature every 2 seconds with a precision of $\pm 0.6^{\circ}\text{C}$. They are distributed in the axial and radial positions, as illustrated in Figure 16.

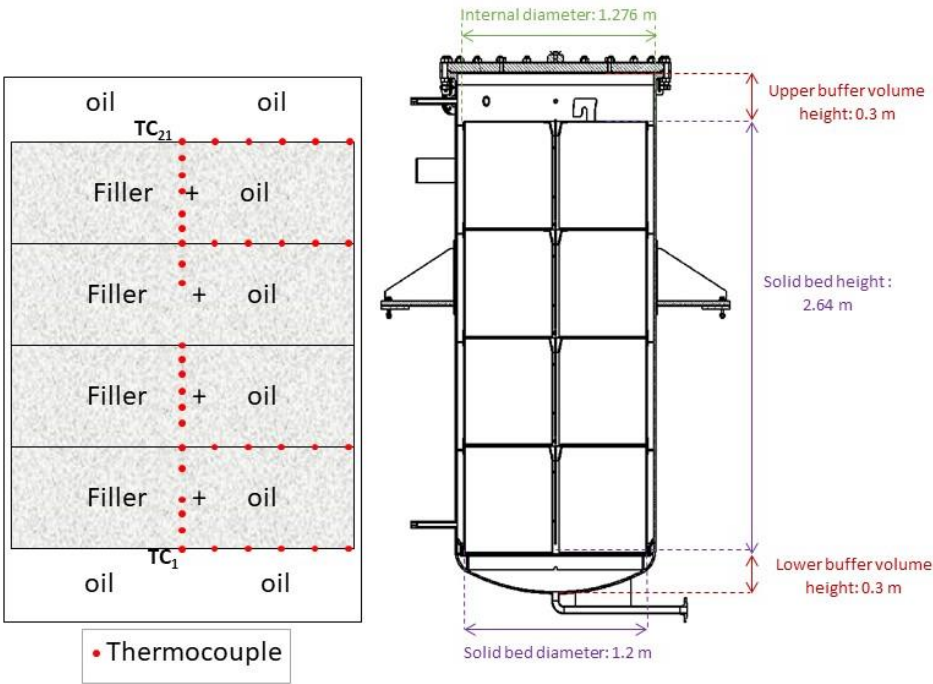


Figure 16. Thermocline tank size and thermocouple positions

The positions of the thermocouples are reflected in Table 21

Table 21 Thermocouples axial positions inside the thermocline

Thermocouple	TC1	TC2	TC3	TC4	TC5	TC6	TC7	TC8	TC9	TC10
Axial position (m)	0.05	0.13	0.23	0.36	0.57	0.61	0.78	0.85	0.96	1.09

Thermocouple	TC11	TC12	TC13	TC14	TC15	TC16	TC17	TC18
Axial position (m)	1.19	1.3	1.76	1.83	1.92	2	2.12	2.32

Thermocouple	TC19	TC20	TC21
Axial position (m)	2.45	2.55	2.64

The uncertainty of measurement is calculated as per Appendix (11.1).

2.1.2. Differential Scanning calometry (DSC)

The TG-DSC 111 de Setaram device is used to characterize the PCM properties and investigate the compatibility between the PCM (NaNO₃) and the HTF (Jarytherm® oil).

2.1.3. Electrical furnace

Nabertherm 30°C - 1600°C electrical furnace is used to melt the PCM inside the tubes on stages and to leak test the filled tubes after sealing. The furnace has 1 m width, 2 m length, and 2m height.

2.2. TES MATERIALS

2.2.1. Sensible heat storage materials

Two ceramics are used as sensible heat storage materials in the thermocline, Alumina spheres, and Cofalit®.

This study selects alumina spheres as reference material with controlled geometry and well-known thermo-physical properties. Alumina was studied as solid filler materials in thermocline TES in various previous studies [113], [119], [181], [182].

Cofalit® is an inert and low-cost post-industrial process rock (recycled material from asbestos wastes), supplied by the French company Inertam [26]. The company produces around 3000 tons yearly by subjecting ACW to plasma torch furnace at 1400°C, then leaving the molten resultant to cool down to ambient temperature without specific operation to control the process [183]. The liquid nature of the primary products allows forming molten Cofalit® in the required shape as molded.

Although the Cofalit® rocks in this work have irregular shapes, the final cooling process of ACW treatment could control the size and shape of the resultant material. Hence, it can easily produce the final product with any required size and shape to fit into the intended application.

Cofalit® was identified as a chemically inactive material [184] and is thermally stable up to 1200 °C [26]. It was found compatible with two common HTF: the binary salt composed of 60% wt. Sodium 40% wt. Potassium nitrates, and the ternary salt composed of 42% wt. Calcium, 15% wt. Sodium, 40% wt. Potassium nitrates [185]. Furthermore, its stability was confirmed when evaluated with synthetic oil used in an experimental setup at 300 °C [30].

Various studies reported a low environmental impact of Cofalit®, as it has no toxicity on the environment and is not subject to lixiviation [26], [27], [186]. Although Jeanjean et al. [187] estimated a carbon footprint of 27.48 gCO₂/kg for Cofalit® production, the environmental impact is due to asbestos thermal treatment (melting) and not to its re-use in a TES tank [183].

In addition to safety consideration, the re-use of Cofalit® provides an economic advantage when compared to an organic HTF, because it costs about 12 \$/ton for the raw material [26], in comparison, the latter costs about 1962 \$/ton [23].

Based on these properties, Cofalit® is an interesting solid filler for sensible heat TES, with significant advantages, such as low cost, relatively high volumetric heat capacity, and revalorization of waste materials.

Total masses accepted by the same thermocline volume were 4000 kg of Cofalit® rocks and 6380 kg of Alumina spheres, resulting in tank porosities difference (void fraction) of 0.614 and 0.485, respectively.

The solid fillers available for this experiment are a rock with an average diameter of 2 cm and 2 cm alumina spheres (as reference material) Figure 17.

Moreover, the HTF fluid is a synthetic oil Jarytherm® DBT that has a working temperature range of 0-350°C.



Alumina spheres



Cofalit ® rocks

Figure 17 . Filler materials shape

Table 22 summarizes the most cited values of temperature-dependent thermo-physical properties for synthetic oil, alumina spheres, and Cofalit® valid in a temperature range of 200 – 300 °C.

Table 22 Thermo-physical properties from literature at temperature range 200 – 300 °C

Type	Jarytherm® DBT oil	Alumina Spheres	Cofalit ®rocks
Tank porosity ε [-]	N/A	0.485	0.614
Particle diameter d [m]	N/A	0.02	0.02 average
Density ρ [kg/m ³]	910 – 836 [25]	3670 [30][181]	3120 [26][188][189]
Heat Capacity C_p [J/kg.K]	2158 – 2476 [25]	1038 – 996 [30]	900 – 964 [176]
Thermal conductivity k [W/m.K]	0.113 - 0.105 [25]	20 – 16 [190]	1.55 – 1.49 [176]
Volumetric Capacity $\rho.C_p$ [MJ/m ³ .K]	1.96-2.07	3.8 - 3.66	2.8-3.0
Thermal diffusivity α [m ² /sec].10 ⁶	0.06-0.05	5.26 – 4.37	0.55–0.5

2.2.2. Latent heat storage material

Sodium nitrate (NaNO₃) is selected as PCM because it has a melting temperature of 308°C [191][45] that fits in the working temperature. Moreover, it has proven compatibility with excellent candidate materials for the envelope.

Stainless steel 304L is selected as encapsulation material because it was tested with NaNO₃ and showed suitable stability for high-temperature salts [11]. Furthermore, it has an acceptable corrosion rate of 6-15 µm/ year at 570°C when

experimented with NaNO_3 [55], which is higher than our planned experiment at 315°C .

Appendix (11.2) lists the temperature-dependent thermophysical properties of all used materials.

2.3. THERMOCLINE PERFORMANCE INDICATORS

The highest temperature during a charge/discharge is T_{high} , and T_{low} is the lowest temperature during the same process. T_{outlet} is the HTF temperature at the tank's outlet. Eq. (42) and Eq. (43) define the non-dimensional HTF temperature and non-dimensional axial coordinate, respectively.

$$\theta = \frac{T_{z,t} - T_{\text{low}}}{T_{\text{high}} - T_{\text{low}}} \quad (42)$$

$$z^* = \frac{z}{H_{\text{tank}}} \quad (43)$$

At the beginning of charge operation, both HTF and the filler are at T_{low} while HTF at T_{high} flows from the top of the tank downwards, then the temperature inside the tank starts to increase from top to bottom Figure 18(a).

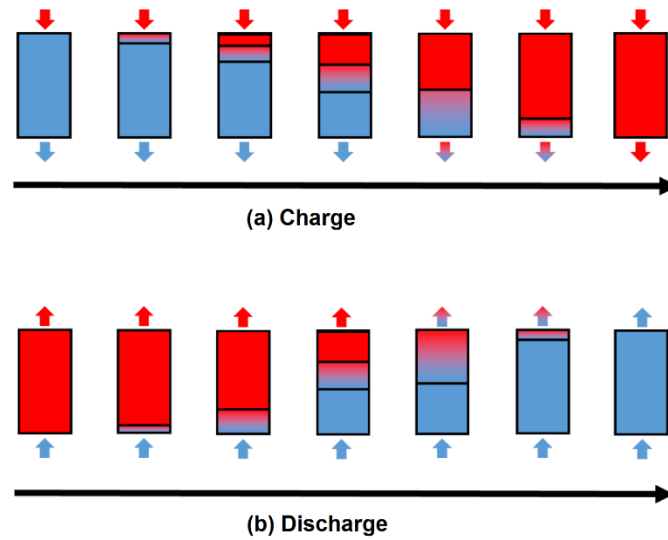


Figure 18 Typical operation in the thermocline TES (a) charge (b) discharge[23]

Reversely during discharge, the HTF and the filler material start at T_{high} , while a cold HTF at T_{low} is pumped-in at the tank's bottom, and the temperature decreases inside the tank from top to bottom Figure 18(b).

During the experiment, there is no limitation on the HTF temperature flowing out of the tank. However, in a real case scenario, a threshold temperature should be taken into account for charge and discharge processes.

For example, increasing the outlet temperature of the thermocline increases the inlet temperature of the solar field during charge, which consequently increases the HTF temperature gain in the solar field to a level that exceeds the maximum allowed temperature of the solar receiver. Hence, the highest temperature at the thermocline outlet during charge that can be sent back to the solar field is defined as the charge threshold temperature T_{thr,c,k_c} Eq.(44) [182]. This threshold temperature limits the charge state of the TES in real operation.

$$T_{thr,c,k_c} = T_{low} + k_c(T_{high} - T_{low}) \quad (44)$$

k_c is an arbitrary charge factor related to operational aspects of the solar field, previous studies considered 20% [182].

The influence of the various charge factors on the thermocline outlet temperature is illustrated in Figure 19(a) [182], which plots the thermocline outlet temperature evolution in time at various at change factors 10%, 20%,30%, 40%,and 50%

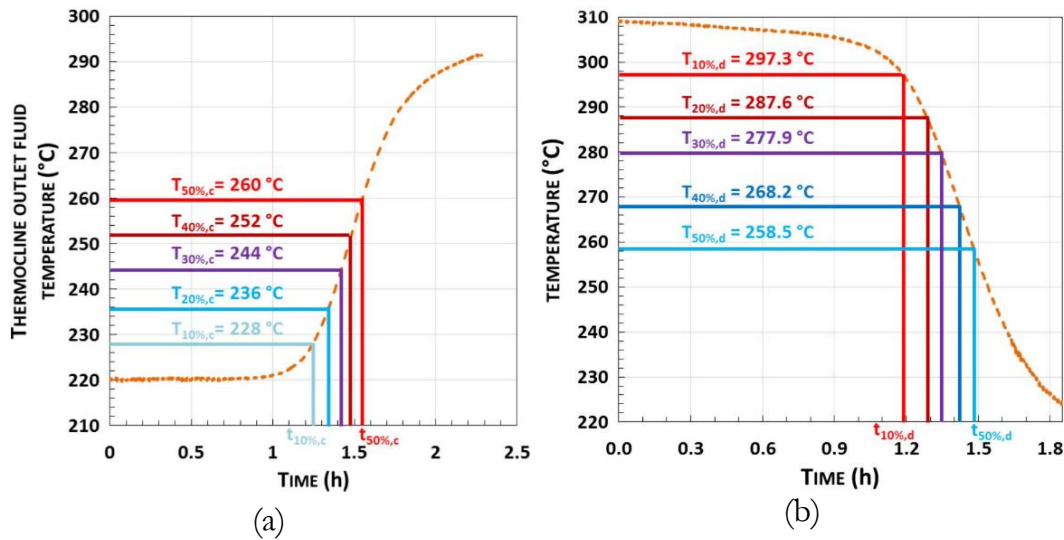


Figure 19 The influence of threshold temperature on the outlet temperature evolution in time during (a) charge (b) discharge of a thermocline[182]

The non-dimensional charge threshold temperature is selected for this work $\theta_{thr,c,20\%} = 0.2$. The process of charging the tank should end when the outlet temperature reaches the charge threshold value $T_{outlet} = T_{thr,c,k_c}$ ($\theta_{outlet} = \theta_{thr,c,20\%} = 0.2$).

In contrast to a charge during discharge, there is a minimum temperature of the fluid that can be sent from the thermocline to the downstream thermal process. Below this temperature, the process cannot run, or its efficiency will be very low. Hence, the threshold temperature of the discharge process is the lowest temperature that the downstream thermal process can utilize T_{thr,d,k_d} eq.(45).

$$T_{thr,d,k_d} = T_{high} - k_d(T_{high} - T_{low}) \quad (45)$$

k_d is an arbitrary discharge factor related to the operation of the downstream process, generally a steam generator. As in previous studies[182]. The influence of multiple discharge factors is investigated on the thermocline outlet temperature during discharge Figure 19(b) [182].

The non-dimensional discharge threshold temperature is at $\theta_{thr,d,20\%} = 0.8$. The discharge operation ends once the HTF temperature at the outlet of the TES reaches the discharge threshold value.

There are six main properties to describe the performance of a TES according to [192][9]:

- 1- **Energy density** is the amount of energy stored per unit volume, kJ/m^3 or kWh/m^3 , also referred to as **specific energy** is the amount of energy stored per unit mass, kJ/kg , or kWh/kg .
- 2- **Capacity**: defines the energy stored in the system and depends on the storage process, the medium, and the size of the system kWh .
- 3- **Power**: defines how fast the energy stored in the system can be charged and discharged kW .
- 4- **Efficiency**: is the ratio of the energy delivered during discharge to the energy needed to charge completely the storage system. It accounts for the energy loss during the storage period and the charging/discharging cycle.
- 5- Charge and discharge **time**: defines how much time is needed to charge/discharge the system.
- 6- **Cost**: refers to either capacity ($\$/\text{kWh}$) or power ($\$/\text{kW}$) of the storage system, and depends on the capital and operation costs of the storage equipment and its lifetime.

This work selects three performance parameters to evaluate the operational behavior of the thermocline TES: process duration, thermocline thickness, and process efficiency, which are defined in the next subsections. For the experimental

evaluation, the thermal capacity is calculated in addition to the performance parameters.

2.3.1. Process duration

The charge or discharge duration is the time required for the tank outlet temperature to reach its charge or discharge threshold temperature, $\theta_{thr,c,20\%}$ resp. $\theta_{thr,d,20\%}$, respectively. Process duration is not only essential to extend the time of useful utilization of stored energy, but it also helps to increase the discharge efficiency.

2.3.2. Thermocline thickness

The thermocline thickness size is the height of the zone inside the tank that is bounded by the two threshold temperatures during charge and discharge eq.(46).

$$H_{Thick} = H(T_{thr,d,20\%}) - H(T_{thr,c,20\%}) \quad (46)$$

The thermocline thickness ratio (named as “thermocline thickness” in the text) is the ratio between the thermocline thickness size to the total tank height, as per (47).

$$\delta = \frac{H_{Thick}}{H_{Tank}} \quad (47)$$

The thermocline thickness is required to be as small as possible because large thermocline thicknesses characterize low TES efficiency [18].

2.3.3. Process efficiency

2.3.3.1. Sensible heat TES

The efficiency of the charging process is the ratio between the accumulated energy and the potential stored energy in the tank Eq. (48) [23]. Due to the significant contribution of the steel in the stored energy in this pilot-scale thermocline TES, all calculations take into account the volumetric heat capacity of the wall and the baskets. Furthermore, efficiency calculations assume that all internal components of the tank (HTF, solid filler, and wall) are at the same temperature at a given height position. Eq. (49), (50), and (51) represent the

accumulated energy in HTF, solid filler, and tank wall accordingly, while Eq.(52), (53), and (54) calculates the potential stored energy for them, respectively.

$$\eta_{charge}(t) = \frac{E_{acc}(t)}{E_{max}} = \frac{E_{acc}(t)_f + E_{acc}(t)_p + E_{acc}(t)_w}{E_{max_f} + E_{max_p} + E_{max_w}} \quad (48)$$

$$E_{acc}(t)_f = \int_0^H (A_{int} \varepsilon(\rho \cdot Cp)_f) \cdot (T_{(z,t)} - T_{low}) \cdot dz \quad (49)$$

A_{int} m²: is the internal surface area of the cylindrical tank

$$E_{acc}(t)_p = \int_0^H (A_{int} (1 - \varepsilon)(\rho \cdot Cp)_p) \cdot (T_{(z,t)} - T_{low}) \cdot dz \quad (50)$$

$$E_{acc}(t)_w = \int_0^H (A_{w,cross} \cdot (\rho \cdot Cp)_w) \cdot (T_{(z,t)} - T_{low}) \cdot dz \quad (51)$$

$A_{w,cross}$ m²: is the cross-sectional surface area of the tank's wall

$$E_{max_f} = V_{tank} \varepsilon(\rho \cdot Cp)_f (T_{high} - T_{low}) \quad (52)$$

$$E_{max_p} = V_{tank} (1 - \varepsilon)(\rho \cdot Cp)_p (T_{high} - T_{low}) \quad (53)$$

$$E_{max_w} = V_w (\rho \cdot Cp)_w (T_{high} - T_{low}) \quad (54)$$

During the discharge process, eq.(55) calculates the discharge efficiency as the ratio of discharged energy to the maximum energy stored in the system at the initial stage.

$$\eta_{discharge}(t) = \frac{E_{discharge}(t)}{E_{max}} \quad (55)$$

Eq.(56) evaluates the discharge energy until the system reaches the cut-off temperature.

$$E_{discharge}(t) = \int_0^t m_f \cdot Cp_f \cdot (T_{outlet} - T_{low}) \cdot dt \quad (56)$$

2.3.3.2. Latent heat TES

In order to accommodate the latent heat of fusion in the efficiency calculation, during the charge phase when $T_{(z,t)} > T_{melt}$, equations (50) and (53) need to be modified according to eq.(57) and eq.(58), respectively.

$$E_{acc}(t)_p = \int_0^H A_{int}(1 - \varepsilon)\rho_p \cdot L_{fus} dz + \int_0^H (A_{int}(1 - \varepsilon)(\rho \cdot Cp)_p)(T_{(z,t)} - T_{low}) dz \quad (57)$$

$$E_{max_p} = V_{tank}(1 - \varepsilon)\rho_p L_{fus} + V_{tank}(1 - \varepsilon)(\rho \cdot Cp)_p(T_{high} - T_{low}) \quad (58)$$

While for the efficiency of the discharge process, eq.(58) should be used instead of eq.(53).

2.4. NUMERICAL MODELING

The various approaches are detailed in (chapter 1). For thermocline TES, various researchers validated the 1D modeling approach to provide reliable temperature prediction of thermocline TES [113][87][150]. Since, the results from 2D and 3D models did not exhibit any significant temperature variation on the radial axis [13], [17], [193]. Moreover, the result of a 1D model has a similar accuracy of a 3D CFD model upon comparison for the same TES [98].

For this work, we choose a one-dimensional Continuous-Solid 1D C-S model for the SHSM filler and one-dimensional Dispersion-Concentric 1D D-C model for the PCM filler Figure 20, as explained in the following sections.

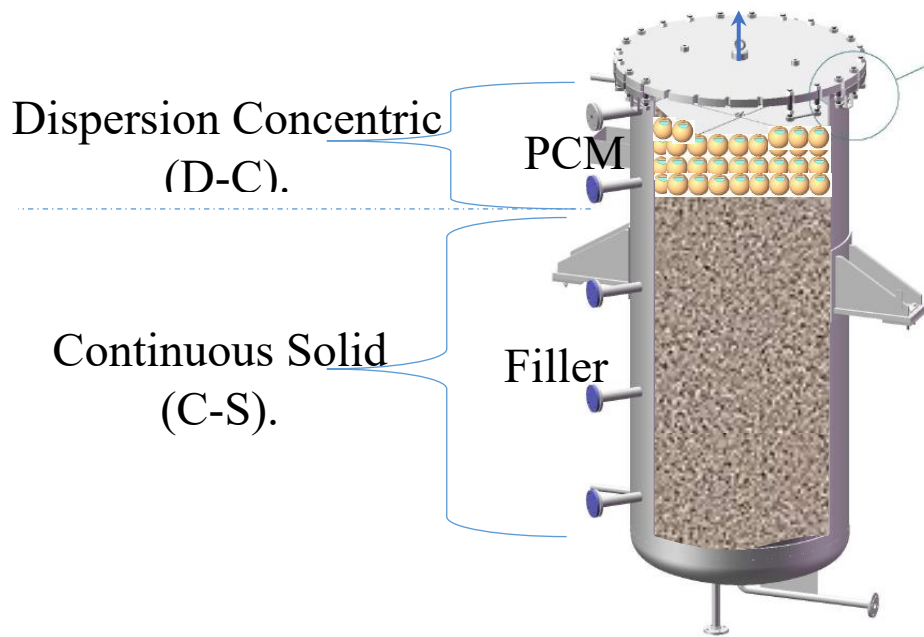


Figure 20 tow-sections PCM and sensible heat thermocline depicted for this work

2.4.1. One-dimensional Continuous Solid model

The main objective of using the 1D C-S model is to have a quick simulation within the largest part of the thermocline (the solid filler) with a good accuracy.

2.4.1.1. Assumptions

- 1D incompressible HTF flow in the axial direction of the tank.
- Heat transfer by radiation is neglected.
- The solid is a continuous, isotropic porous medium.
- The temperature gradient within the solid filler is negligible because $Bi < 0.1$.
- The tank is not adiabatic. Thermal losses to the environment are taken into account by solving the energy balance equation at the thermocline's wall.
- The model neglects the conduction between the tank's wall and solid filler.
- The thermal diffusion of the HTF in the axial direction is taken into account.
- The model uses temperature-dependent thermophysical properties.

Based on these assumptions, a Matlab® program is developed to find approximate solutions for the three separate energy equations for HTF, solid filler, and tank wall eq. (59), eq.(60), and eq. (61), respectively.

$$\begin{aligned} & \varepsilon(\rho C p)_f \frac{\partial T_f}{\partial t} + \varepsilon(\rho C p)_f v_f \frac{\partial T_f}{\partial z} \\ &= k_{f-ax} \frac{\partial^2 T_f}{\partial z^2} + h_v (T_p - T_f) + h_w \frac{A_{f \leftrightarrow w}}{V_{tank}} (T_w - T_f) \end{aligned} \quad (59)$$

$$(1 - \varepsilon).(\rho C p)_p \frac{\partial T_p}{\partial t} = k_{p-ax} \frac{\partial^2 T_p}{\partial z^2} + h_v (T_f - T_p) \quad (60)$$

$$\begin{aligned} (\rho C p)_w \frac{\partial T_w}{\partial t} &= k_w \frac{\partial^2 T_w}{\partial z^2} + h_w \left(\frac{A_{f \leftrightarrow w}}{V_w} (T_f - T_w) \right) \\ &+ \frac{h_{ext} \cdot A_{w \leftrightarrow ext}}{V_w} (T_{ext} - T_w) \end{aligned} \quad (61)$$

2.4.1.2. Reducing the energy balance equations

For HTF eq.(62) shows a reduced form of eq.(59)

$$\begin{aligned} \frac{\partial T_f}{\partial t} &= \hat{a} \frac{\partial^2 T_f}{\partial z^2} + \hat{b} (T_p - T_f) + \hat{c} (T_w - T_f) - v_f \frac{\partial T_f}{\partial z} \\ \hat{a} &= \frac{k_{f-ax}}{\varepsilon(\rho C p)_f} = \frac{k_f}{(\rho C p)_f}; \hat{b} = \frac{h_v}{\varepsilon(\rho C p)_f} \\ \hat{c} &= \frac{h_w}{\varepsilon(\rho C p)_f} \frac{\varepsilon \cdot \pi \cdot D \cdot H_{tot}}{\frac{\pi D^2}{4} H_{tot}} = \frac{h_w}{(\rho C p)_f} \frac{2}{R} \end{aligned} \quad (62)$$

For solid filler, eq.(63) reflects the reduced form of eq.(60).

$$\begin{aligned} \frac{\partial T_p}{\partial t} &= \hat{f} \frac{\partial^2 T_p}{\partial z^2} + \hat{g} (T_f - T_p) \\ \hat{f} &= \frac{k_{p-ax}}{(1 - \varepsilon)(\rho C p)_p} = \frac{k_p}{(\rho C p)_p}; \hat{g} = \frac{h_v}{(1 - \varepsilon)(\rho C p)_p} \end{aligned} \quad (63)$$

And eq. (64) resembles the reduced form of eq. (61).

$$\frac{\partial T_w}{\partial t} = \hat{l} \frac{\partial^2 T_w}{\partial z^2} + \hat{m} (T_f - T_w) + \hat{n} (T_{ext} - T_w) \quad (64)$$

$$\hat{l} = \frac{k_w}{(\rho C_p)_w}; \quad \hat{m} = \frac{h_w}{(\rho C_p)_w} \frac{\varepsilon \cdot 2 \cdot R}{((R + e_{wall})^2 - R^2)}$$

$$\hat{n} = \frac{1}{R_{th}} \cdot \frac{1}{(\rho C_p)_w} \frac{1}{\pi \cdot ((R + e_{wall})^2 - R^2) \cdot H_{tot}}$$

2.4.1.3. Discretization

The model uses the finite difference method for the HTF, solid filler, and tank wall accordingly. The j notation is the axial-position reference, and the n notation is the progress in time.

- Upwind (implicit) time discretization:

$$\frac{\partial T_f}{\partial t} = \frac{T_f^{(j,n+1)} - T_f^{(j,n)}}{\Delta t} \quad (65)$$

$$\frac{\partial T_p}{\partial t} = \frac{T_p^{(j,n+1)} - T_p^{(j,n)}}{\Delta t} \quad (66)$$

$$\frac{\partial T_w}{\partial t} = \frac{T_w^{(j,n+1)} - T_w^{(j,n)}}{\Delta t} \quad (67)$$

- An implicit-time second-order central differencing scheme for diffusion terms:

$$\frac{\partial^2 T_f}{\partial z^2} = \frac{T_f^{(j+1,n+1)} - 2T_f^{(j,n+1)} + T_f^{(j-1,n+1)}}{\Delta z^2} \quad (68)$$

$$\frac{\partial^2 T_p}{\partial z^2} = \frac{T_p^{(j+1,n+1)} - 2T_p^{(j,n+1)} + T_p^{(j-1,n+1)}}{\Delta z^2} \quad (69)$$

$$\frac{\partial^2 T_w}{\partial z^2} = \frac{T_w^{(j+1,n+1)} - 2T_w^{(j,n+1)} + T_w^{(j-1,n+1)}}{\Delta z^2} \quad (70)$$

- An Implicit-time backward difference scheme for the convection terms

$$\frac{\partial T_f}{\partial z} = \frac{T_f^{(j,n+1)} - T_f^{(j-1,n+1)}}{\Delta z} \quad (71)$$

2.4.1.4. Initial conditions

During charge at time $t=0$:

$$T_f^{(t=0)} = T_p^{(t=0)} = T_w^{(t=0)} = T_{initial}^{(t=0)} = T_{Low}$$

For discharge at $t=0$

$$T_f^{(t=0)} = T_p^{(t=0)} = T_w^{(t=0)} = T_{initial}^{(t=0)} = T_{High}$$

2.4.1.5. Boundary conditions

At the thermocline inlet $j=1$, for the HTF:

$$T_f^{(1,n+1)} = T_f^{(0,n+1)} = T_{input}$$

During the charge $T_{input} = T_{High}$, while for the discharge $T_{input} = T_{Low}$. For solid filler and the wall equation, the simulation presumes adiabatic conditions as follow:

$$\begin{aligned} \frac{\partial T_p^{(j=1)}}{\partial z} &= \frac{\partial T_w^{(j=1)}}{\partial z} = 0 \\ T_p^{(1,n+1)} &= T_p^{(0,n+1)} \\ T_w^{(1,n+1)} &= T_w^{(0,n+1)} \end{aligned}$$

At the other side of the thermocline, the model depicts adiabatic conditions at the outlet $j=H$:

$$\frac{\partial T_f^{(j=H)}}{\partial z} = \frac{\partial T_p^{(j=H)}}{\partial z} = \frac{\partial T_w^{(j=H)}}{\partial z} = 0$$

$$\frac{\partial T_f}{\partial z} = \frac{T_f^{(H+1,n+1)} - T_f^{(H,n+1)}}{\Delta z} = 0 \rightarrow T_f^{(H+1,n+1)} = T_f^{(H,n+1)}$$

$$T_p^{(H+1,n+1)} = T_p^{(H,n+1)}$$

$$T_w^{(H+1,n+1)} = T_w^{(H,n+1)}$$

2.4.1.6. System of algebraic equations

Equations (72), (73), and (74) illustrates the non-dimensional form of HTF, solid filler, and tank wall, respectively.

$$\begin{aligned} \hat{A} \cdot T_f^{(j-1,n+1)} + \hat{B} \cdot T_f^{(j,n+1)} + \hat{C} \cdot T_f^{(j+1,n+1)} \\ = T_f^{(j,n)} - \hat{D} \cdot T_p^{(j,n+1)} - \hat{E} \cdot T_w^{(j,n+1)} \end{aligned} \quad (72)$$

$$\hat{A} = \left(-\frac{\Delta t. \hat{a}}{\Delta z^2} - \frac{\Delta t. v_f}{\Delta z} \right); \hat{B} = \left(2\frac{\Delta t. \hat{a}}{\Delta z^2} + \Delta t. \hat{b} + \Delta t. \hat{c} + 1 + \frac{\Delta t. v_f}{\Delta z} \right)$$

$$\hat{C} = \left(-\frac{\Delta t. \hat{a}}{\Delta z^2} \right); \hat{D} = -\Delta t. \hat{b}; \quad \hat{E} = -\Delta t. \hat{c}$$

$$\hat{F}.T_p^{(j-1,n+1)} + \hat{G}.T_p^{(j,n+1)} + \hat{H}.T_p^{(j+1,n+1)} = T_p^{(j,n)} - \hat{I}.T_f^{(j,n+1)} \quad (73)$$

$$\hat{F} = -\frac{\Delta t. \hat{f}}{\Delta z^2}; \quad \hat{G} = 1 + \Delta t. \hat{g} + \frac{\Delta t. \hat{f}. 2}{\Delta z^2}$$

$$\hat{H} = -\frac{\Delta t. \hat{f}}{\Delta z^2}; \quad \hat{I} = -\Delta t. \hat{g}$$

$$\hat{L}.T_w^{(j-1,n+1)} + \hat{M}.T_w^{(j,n+1)} + \hat{N}.T_w^{(j+1,n+1)} = T_w^{(j,n)} - \hat{O}.T_f^{(j,n+1)} - \hat{P}.T_{ext} \quad (74)$$

$$\hat{L} = -\frac{\Delta t. \hat{l}}{\Delta z^2}; \quad \hat{M} = 1 + \frac{\Delta t. \hat{l}. 2}{\Delta z^2} + \Delta t. \hat{m} + \Delta t. \hat{n}$$

$$\hat{N} = -\frac{\Delta t. \hat{l}}{\Delta z^2}; \quad \hat{O} = -\Delta t. \hat{m}; \quad \hat{P} = -\Delta t. \hat{n}$$

Equations (75), (76), and (77) illustrate the resulting system of algebraic equations at each time step with tridiagonal matrices. The tridiagonal matrices of HTF, solid filler, and the wall are Mat_f, Mat_p, and Mat_w, respectively.

Mat_f					$T_f^{(n+1)}$	$T_f^{(n)}$		$T_p^{(n+1)}$	$T_w^{(n+1)}$
\hat{B}	\hat{C}	Inlet B.C			1	1	$-\hat{A}.T_{input}$	1	1
\hat{A}	\hat{B}	\hat{C}			2	2	0	2	2
	\hat{A}	\hat{B}	\hat{C}		.	.	0		.
	
			\hat{A}	\hat{B}			.		
				\hat{A}	\hat{B}		0		
					\hat{C}		0		
Outlet B.C					\hat{A}	$\hat{B} + \hat{C}$	0	j_tot	j_tot

(75)

Mat_p					$T_p^{(n+1)}$	$T_p^{(n)}$		$T_f^{(n+1)}$	B.C
\hat{G}	\hat{H}				1	1		1	$\hat{F}T_p^{(0,n+1)}$
\hat{F}	\hat{G}	\hat{H}			2	2		2	0
	\hat{F}	\hat{G}	\hat{H}		.	.		.	0
		$-\hat{I}.*$.	0
			\hat{F}	\hat{G}				.	0
				\hat{F}	\hat{G}			0	0
					\hat{F}	\hat{G}		j_tot	$\hat{H}T_p^{(+1,n+1)}$

(76)

Mat_w	T _w ⁽ⁿ⁺¹⁾	=	T _w ⁽ⁿ⁾	- $\hat{\theta}.*$	+	T _f ⁽ⁿ⁺¹⁾	+ $\hat{P}.T_{ext}$	-	B.C
$\hat{M} \quad \hat{N}$	1		1			1	$\hat{P}.T_{ext}$		$\hat{L}T_w^{(0,n+1)}$
$\hat{L} \quad \hat{M} \quad \hat{N}$	2		2			2	0		0
$\quad \hat{L} \quad \hat{M} \quad \hat{N}$.		.			.	0		0
$\quad \quad \hat{L} \quad \hat{M} \quad \hat{N}$.		.			.	0		0
$\quad \quad \quad \hat{L} \quad \hat{M} \quad \hat{N}$.		.			.	0		0
$\quad \quad \quad \quad \hat{L} \quad \hat{M} \quad \hat{N}$.		.			.	0		0
$\quad \quad \quad \quad \quad \hat{L} \quad \hat{M}$	j_tot		j_tot			j_tot	0		$\hat{N}T_w^{(+1,n+1)}$

(77)

2.4.1.7. Algorithm of the solution

The Matlab® program is using the following discretization scheme: implicit in time, second-order central difference diffusion term, and first-order central difference convection term [194]. The specifications of the computer used to run the program are listed in the appendix (11.3).

The program solves the three coupled partial non-linear differential equations and uses the Newton-Raphson iteration method with convergence criteria of 10^{-4} . The time step is $\Delta t = 2$ sec, and the size of the control volume is $\Delta z = 0.02$ m [87] for all C-S solid simulation. The simulation updates the thermophysical properties of the materials at each iteration. Figure 21 details the used algorithm in the program.

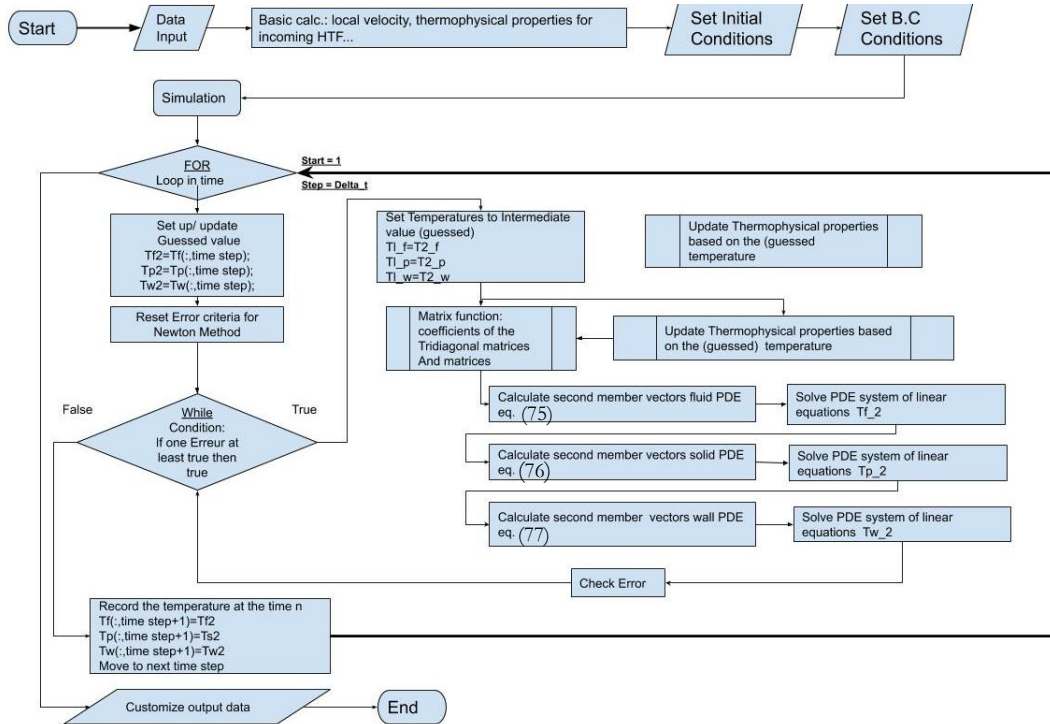


Figure 21. Algorithm of numerical solution for the C-S model

2.4.2. One-dimensional Dispersion Concentric model

For the latent heat part of Figure 20, the 1D D-C model consumes more time in the simulation than the C-S model because it calculates the thermal gradient within the PCM. Furthermore, it provides good accuracy for this kind of application. Therefore, it is used only in the PCM section of the thermocline.

2.4.2.1. Assumptions

- 1D incompressible HTF flow in the axial direction of the tank.
- Heat transfer by radiation is neglected.
- The PCM is encapsulated in a uniform spherical shape container. All PCM capsules are filled with the same PCM mass.
- The temperature gradient within the PCM is assumed to be symmetric-concentric distributed.
- The thermal resistance of the envelope material is neglected.
- The thermal capacity of the envelop materials is embedded in the thermal capacity of the PCM.
- Natural convection of the PCM is taken into account by modifying the thermal conductivity of the PCM.
- The tank is not adiabatic. Thermal losses to the environment are taken into account by solving the energy balance equation at the thermocline's wall.
- The model neglects the conduction between the tank's wall and the PCM capsule.
- The thermal diffusion of the HTF in the axial direction is taken into account.
- The model uses temperature-dependent thermophysical properties for the HTF and PCM.
- Melting and solidification of PCM are modeled using the enthalpy porosity method, which assumes a constant melting temperature during the phase change.
- λ is the liquid fraction of the PCM, its value varies [0-1] and can be calculated as per the enthalpy-porosity method (1.3.2.5)

Based on these assumptions, another Matlab® program is developed to find approximate solutions for the three coupled equations for HTF, solid filler (PCM in this section), and thermocline tank's wall equations (78), (79), and (80), respectively.

$$\begin{aligned} & \varepsilon(\rho C p)_f \frac{\partial T_f}{\partial t} + \varepsilon(\rho C p)_f v_f \frac{\partial T_f}{\partial z} \\ &= k_{f-ax} \frac{\partial^2 T_f}{\partial z^2} + h_v(T_p - T_f) + h_w \frac{A_{f \leftrightarrow w}}{V_{tank}} (T_w - T_f) \end{aligned} \quad (78)$$

The solid filler temperature T_p in the HTF energy balance equation (78) is the surface temperature at the outer surface of the PCM capsule.

$$(\rho C p)_p \cdot \frac{\partial T_p}{\partial t} + \rho_p L_{fus} \frac{\partial \lambda}{\partial t} = \frac{1}{r^2} \frac{\partial}{\partial r} \left(k_p r^2 \frac{\partial T_p}{\partial r} \right) \quad (79)$$

For the solid filler, eq.(79) (131) represents the energy balance equation of the PCM where λ is the liquid fraction (1.3.2.5).

$$\begin{aligned} (\rho C p)_w \cdot \frac{\partial T_w}{\partial t} &= k_w \cdot \frac{\partial^2 T_w}{\partial z^2} + h_w \cdot \left(\frac{A_{f \leftrightarrow w}}{V_w} \cdot (T_f - T_w) \right) \\ &+ \frac{h_{ext} \cdot A_{w \leftrightarrow ext}}{V_w} \cdot (T_{ext} - T_w) \end{aligned} \quad (80)$$

2.4.2.2. Reducing the energy balance equations

The energy balance equations (78) and (80) of the HTF and the tank's wall respectively are reduced in a seminar manner to the C-S model reductions.

Equation (81) represents a reduced version of the energy balance equation for the PCM.

$$\begin{aligned} \frac{\partial T_p}{\partial t} &= \hat{f}_{r_i} \frac{\partial T_p}{\partial r} + \hat{g} \frac{\partial^2 T_p}{\partial r^2} - \frac{L_{fus}}{C_p} \frac{\partial \lambda}{\partial t} \\ \hat{f}_{r_i} &= \frac{2}{r_i} \frac{k_p}{(\rho C p)_p}; \quad \hat{g} = \frac{k_p}{(\rho C p)_p}; \quad r_j = j \cdot \Delta r : j = 0, 1, 2 \dots M \end{aligned} \quad (81)$$

2.4.2.3. Discretization

The discretization method is similar to the C-S and applied to the radial coordinates as follow :

- Upwind (implicit) time discretization:

$$\frac{\partial T_p}{\partial t} = \frac{T_p^{(r_i, n+1)} - T_p^{(r_i, n)}}{\Delta t} \quad (82)$$

- An implicit-time second-order central differencing scheme for diffusion terms:

$$\frac{\partial^2 T_p}{\partial r^2} = \frac{T_p^{(r_{i+1},n+1)} - 2T_p^{(r_i,n+1)} + T_p^{(r_{i-1},n+1)}}{\Delta r^2} \quad (83)$$

- An Implicit-time backward difference scheme for the first-order derivative term

$$\frac{\partial T_p}{\partial r} = \frac{T_p^{(r_{i+1},n+1)} - T_p^{(r_i,n+1)}}{\Delta r} \quad (84)$$

2.4.2.4. Initial conditions

During charge at time $t=0$:

$$T_f^{(t=0)} = T_p^{(r_i,0)} = T_w^{(t=0)} = T_{initial}^{(t=0)} = T_{Low}$$

$$\lambda^{(j,n)} = 0$$

For discharge at $t=0$

$$T_f^{(t=0)} = T_p^{(r_i,0)} = T_w^{(t=0)} = T_{initial}^{(t=0)} = T_{High}$$

$$\lambda^{(j,n)} = 1$$

If the system starts from partially charged/discharged status the liquid fraction at the initial condition evaluated from the below eq.(85)

$$\lambda^{(j,initial)} = \frac{T_p^{(r_i,initial)} - T_{sol}}{T_{Liq} - T_{sol}} \begin{cases} \lambda^{(j,initial)} < 0 \rightarrow : \lambda = 0 \\ \lambda^{(j,initial)} > 1 \rightarrow : \lambda = 1 \end{cases} \quad (85)$$

T_{sol} : is the temperature at which the liquid material starts to solidify.

T_{liq} : is the temperature at which the solid material starts to melt.

2.4.2.5. Boundary conditions

During the charge $T_{input} = T_{High}$, while for the discharge $T_{input} = T_{Low}$.

The boundary conditions for the solid filler with this model are:

$$\frac{\partial T_p}{\partial r} = 0 \text{ at } r_i = 0 \text{ at the center of the capsule}$$

$i = r_{tot} \rightarrow r_i = R_p$ at the inside surface for the sphere

$$k_p \frac{\partial T_p}{\partial r} = h(T_f^{(N_x,n+1)} - T_p^{(R_p,n+1)}) \quad (86)$$

2.4.2.6. System of algebraic equations

Eq. (87) is the non-dimensional form of eq.(81)

$$\begin{aligned} \hat{F} \cdot T_{PCM}^{(r_{i-1},n+1)} + \hat{G} \cdot T_{PCM}^{(r_i,n+1)^k} + \hat{H} T_{PCM}^{(r_{i+1},n+1)} \\ = T_{PCM}^{(r_i,n)} - \lambda^{(r_j,n+1)^k} \cdot \frac{L_{fus}}{Cp_{avg.}^{(r_j,n)}} + \lambda^{(r_j,n)} \cdot \frac{L_{fus}}{Cp_{avg.}^{(r_j,n)}} \end{aligned} \quad (87)$$

$$\hat{F} = -\frac{\Delta t \hat{g}}{\Delta r^2}, \quad \hat{G} = 1 + \frac{\Delta t \hat{f}_{r_i}}{\Delta r} + 2 \frac{\Delta t \hat{g}}{\Delta r^2}, \quad \hat{H} = -\frac{\Delta t \hat{f}_{r_i}}{\Delta r} - \frac{\Delta t \hat{g}}{\Delta r^2}$$

$Cp_{avg.}$: is the average heat capacity between the heat capacity at T_{sol} and it is value at T_{liq} .

For the boundary condition at the center of the solid filler $i=0$ $r_i=1$, the matrix coefficients need modification as per eq.(88) and eq.(89) [195][196].

$$\hat{G}(1) = \left(1 + \frac{\Delta t}{\Delta r^2} 6 \cdot \hat{g} \right) \quad (88)$$

$$\hat{H}(1) = \left(-\frac{\Delta t}{\Delta r^2} 6 \cdot \hat{g} \right) \quad (89)$$

At the solid filler surface, the boundary non-dimensional form of the equation appears in eq.(90)

$$\begin{aligned} \hat{F}_R \cdot T_p^{(R_p-1,n+1)} + \left(\hat{G}_{R_p} - \hat{H}_{R_p} \cdot \hat{I} + \hat{H}_{R_p} \right) \cdot T_p^{(R_p,n+1)} \\ = T_p^{(R_p,n)} - \hat{H}_{R_p} \cdot \hat{I} \cdot T_f^{(Nx,n+1)} \\ \hat{I} = h \frac{\Delta r}{k_{PCM}} \end{aligned} \quad (90)$$

The updated liquid fraction is evaluated from eq.(91)

$$\begin{aligned} \lambda^{(r_j,n+1)^{k+1}} = \lambda^{(r_j,n+1)^k} - \frac{Cp_{avg.}^{(r_j,n)} \cdot \hat{G} \cdot \left(T_{melt} - T_p^{(r_j,n+1)^k} \right)}{L_{fus}} \end{aligned} \quad (91)$$

$$\begin{cases} \lambda^{(r_j,n+1)^{k+1}} < 0 \rightarrow : \lambda = 0 \\ \lambda^{(r_j,n+1)^{k+1}} > 1 \rightarrow : \lambda = 1 \end{cases}$$

Eq. (92) reflects the system of the algebraic equations for the solid filler.

$$\begin{vmatrix} \hat{G}(1) & \hat{H}(1) & & & \\ \hat{F} & \hat{G} & \hat{H} & & \\ & \hat{F} & \hat{G} & \hat{H} & \\ & & \ddots & \ddots & \ddots \\ & & & \hat{F} & \hat{G}_{R_p} - \hat{H}_{R_p} \cdot \hat{I} + \hat{H}_{R_p} \end{vmatrix} \begin{vmatrix} T_p^{(1,n+1)} \\ T_p^{(2,n+1)} \\ T_p^{(r_i,n+1)} \\ \vdots \\ T_p^{(R_p,n+1)} \end{vmatrix} = \begin{vmatrix} T_p^{(1,n)} \\ T_p^{(2,n)} \\ T_p^{(r_i,n)} \\ \vdots \\ T_p^{(R_p,n)} \end{vmatrix} + \begin{vmatrix} 0 \\ 0 \\ 0 \\ 0 \\ \hat{H}_{R_p} \cdot \hat{I} \end{vmatrix} T_f^{(Nx,n+1)} \quad (92)$$

2.4.2.7. Algorithm of the solution

The Matlab® program for the D-C model uses a similar discretization scheme to the C-S model for this work. The criterion of convergence is 10^{-4} , the time step is $\Delta t = 0.5$ sec, the size of the control volume Δz is equal to the capsule diameter, and the number of radial components is 10. The model depicts the thermocline as per Figure 22, where at each control volume, it calculates the temperature of the HTF and tank wall. Then it evaluates the temperature gradient for the spheres. The simulation updates the thermophysical properties of the materials at each iteration.

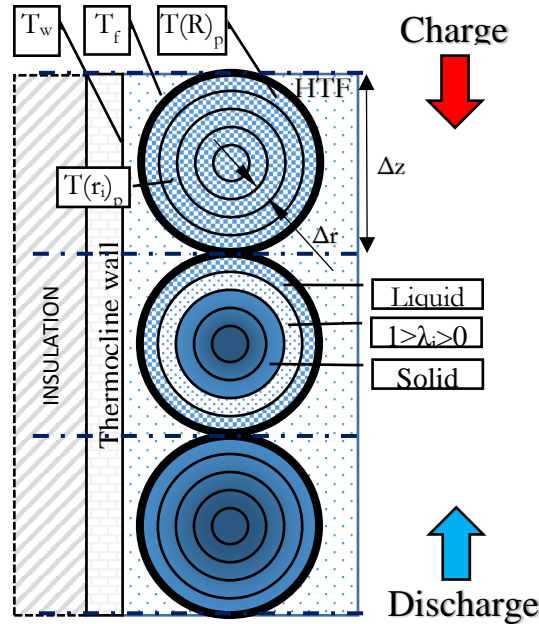


Figure 22 D-C model control volume

Figure 23 explains the algorithm of the MatLab program.

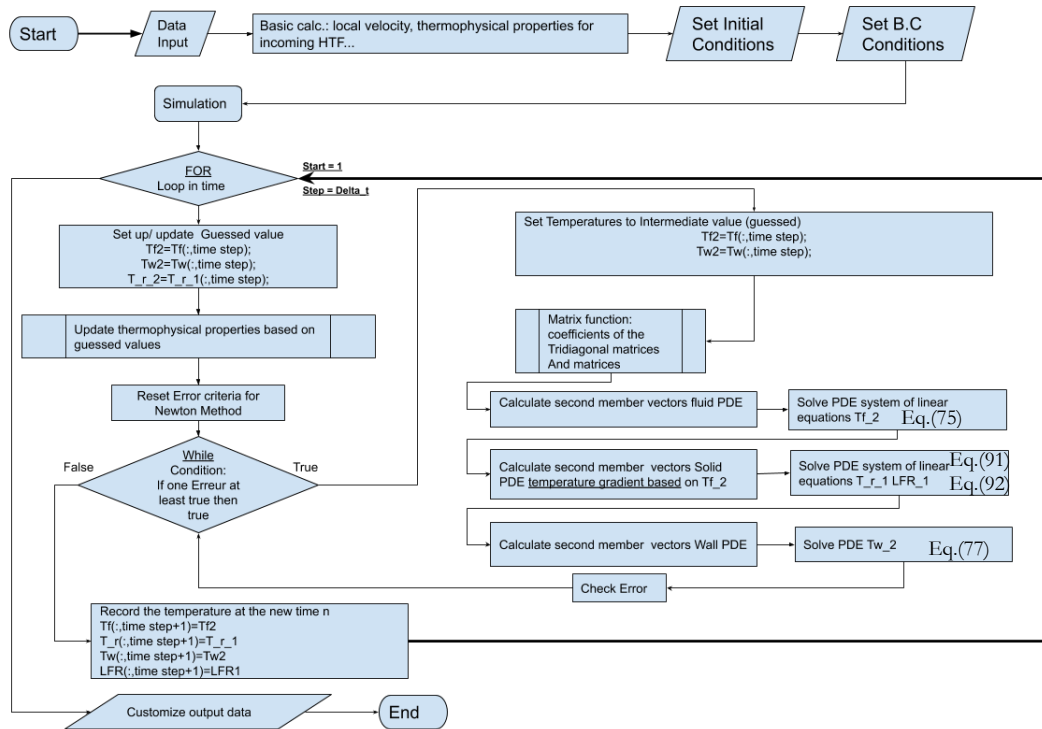


Figure 23 Solution algorithm for the D-C model

2.4.3. Heat transfer correlations

The numerical models in this work applied the following correlations in order to simulate the various heat transfer methods in the thermocline Table 23:

Table 23. List of correlations used in the modeling part of this work

Correlation	C-S	D-C
Volumetric heat convection f-p	$h_v = \frac{6(1 - \varepsilon)k_{f,eff}[2 + 1.1Re_p^{0.6}Pr^{1/3}]}{d_p^2} \quad (93)$	
Convection heat transfer f-w	$h_w = \frac{k_f}{d_p}(2.576Re_p^{1/3}Pr^{1/3} + 0.0936Re_p^{0.8}Pr^{0.4}) \quad (94)$	
Thermal losses to the environment	$Nu_{ext} = \left[0.825 + \frac{0.387Ra^{1/6}}{\left(1 + \left\{ \frac{0.492}{Pr} \right\}^{9/16} \right)^{8/27}} \right]^2 \quad (95)$ $Ra = Gr \cdot Pr, \quad Gr = \frac{g\beta\Delta TH^3}{\nu^2}$	
Effective thermal conductivity C-S model	$k_{f-ax} = \varepsilon k_f \quad (96)$ $k_{p-ax} = (1 - \varepsilon)k_p \quad (97)$	$k_{f-ax} = k_e^0 + k_e^{dyn} \quad (98)$
Spheres D-C model	$k_e^0 = \left(\frac{k_p}{k_f} \right)^{0.280 - 0.757 \log_{10} \left(\frac{k_p}{k_f} \right)} \quad (99)$	
	$k_e^{dyn} = 0.5k_f\varepsilon Re \cdot Pe_f \quad (100)$	
Natural convection inside PCM capsules	$\frac{k_{p-eff}}{k_{PCM}} = 0.18Ra^{0.25} \quad (101)$ $Ra = \frac{g\beta(T_p - T_{melt})\left(\frac{d_p}{2}\right)^3}{\nu\alpha}$	
The thermal capacity of envelope material in spheres [46]	$(\rho C_p)_{eff-PCM} = \frac{(\rho C_p V)_{Solid,PCM} + (\rho C_p V)_{Envelop}}{V_{tot}} \quad (102)$	
The thermal capacity of envelope material in tubes[171]	$(\rho C_p)_{eff-PCM} = \frac{m_{PCM}C_{PH-PCM} + m_{env}C_{env.}}{V_{Tubes}} \quad (103)$	

For the Cofalit® simulation, the rocks depicted as regular spheres with a diameter equal to the hydraulic diameter, as it is defined by Li et al. [95] in Eq.(104)

$$d_{ch} = \frac{\varepsilon \cdot d_r}{4 \cdot (1 - \varepsilon)} \quad (104)$$

d_r is the average diameter of the rocks

3. EXPERIMENTAL COMPARISON BETWEEN TWO SENSIBLE HEAT STORAGE MEDIUMS, WITH PARAMETRIC STUDY AND COMBINING APPROACH

In this work, the thermocline is filled with sensible heat storage medium (SHSM) before adding the PCM layer at its top. Furthermore, it is important to study the actual performance of environmentally friendly filler material such as the Cofalit® and compares it to reference material. Therefore, the main objectives of this chapter are:

- Compare the actual thermal performance of the same thermocline filled with two different SHSMs, Cofalit®, and alumina spheres.
- Validate the 1D C-S model from the experiments.
- Numerically investigate the influence of the particle diameter, porosity, thermal conductivity, and volumetric heat capacity on the thermal behavior of TES.
- Observe the potential use of two SHSM in one thermocline TES.

This chapter is based on the article published in J. Energy storage “Experimental evaluation of vitrified waste as solid fillers used in thermocline thermal energy storage with parametric analysis,” M. A. Keilany, M. Milhé, J. Bézian, Q. Falcoz, and G. Flamant, 2020, vol. 29, no. June, p. 101285, DOI (10.1016/j.est.2020.101285) [197].

3.1. EXPERIMENTAL COMPARISON

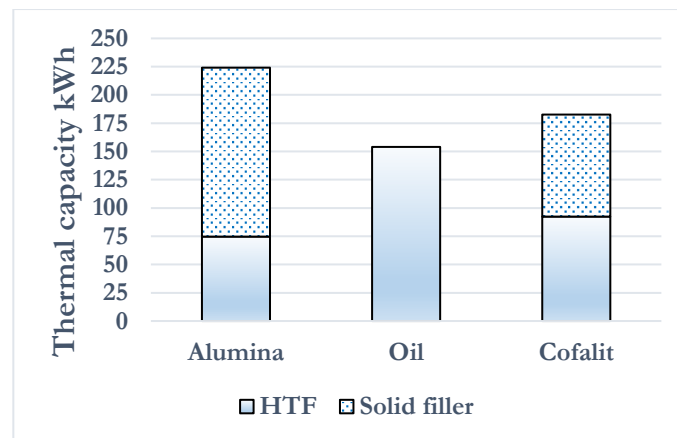


Figure 24 Comparison between thermal storages for the same 4 m³ thermocline filled with three SHSMs synthetic oil, alumina, and Cofalit at temperature 290-220°C

Figure 24 compares the thermal storage of the same thermocline with three SHSMs Jarysol® oil, alumina spheres, and Cofalit® rocks. The thermophysical properties are evaluated as an average value according to (Table 22), and the

thermal storage is calculated with 70°C temperature difference for the tank volume with the measured bed porosity for each case.

Figure 24 confirms that using alumina increases the thermal storage of the thermocline that is only filled with HTF by 46%, and reduced the need for HTF by 50%. Cofalit® increased the thermocline thermal storage by 17% and reduced the need for HTF by 41.5% compared to the only oil case.

The discharge tests apply constant operating conditions, with similar HTF mass flow rate as well as temperature difference for both solid fillers. During the charge tests, the same approach was chosen but with a lower mass flow rate and smaller temperature difference compared to the discharge one to achieve constant inlet temperature using the electrical heater. Table 24 illustrates the experimental operating conditions.

Table 24 Experimental conditions for the experiments

Process	Charge	Discharge
Mass flow rate [kg/h]	2600	2950
Temperature range [°C]	248 – 280	290 – 220

3.1.1. Process Duration

Figure 25 plots the evolution of the non-dimensional outlet temperature of the thermocline during the charge time for both materials. It indicates that Cofalit® reached threshold temperature ($\theta_{outlet} = 0.2$) at 82 min, 20 min faster than alumina spheres, which takes about 102 min. Additionally, the Cofalit® takes about 144 min to reach full-charged status compared to 180 min for the alumina, which represents a 20% faster charge.

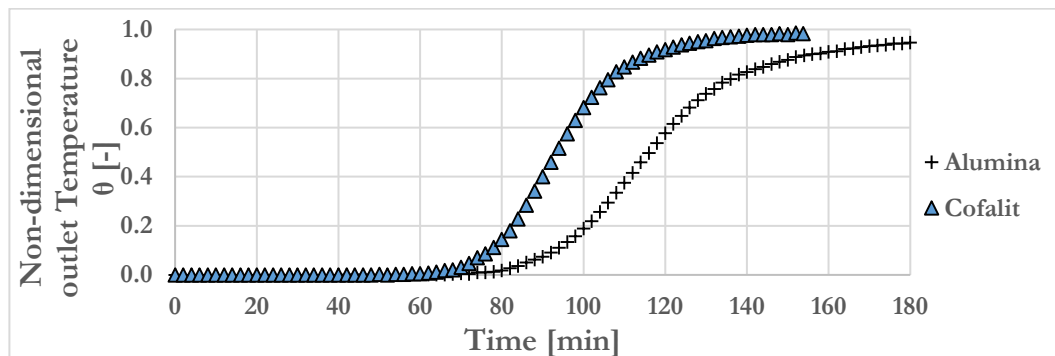


Figure 25 non-dimensional outlet temperature evolution in time during charge (alumina and Cofalit®)

For discharge, Figure 26 reflects that Cofalit® reached the threshold temperature of the discharge ($\theta_{outlet} = 0.8$) at 67 min compared to 80 min in alumina, which is 15% shorter.

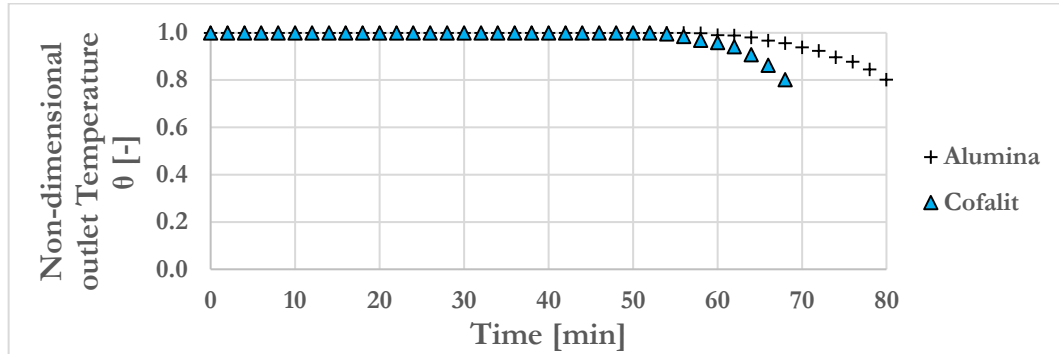


Figure 26 non-dimensional outlet temperature evolution in time during discharge (alumina and Cofalit®)

Shorter charge and discharge time in Cofalit® compared to alumina can be attributed to smaller density and larger tank's porosity with Cofalit® compared to alumina, which led to a lower filler mass inside the thermocline, 4 and 6.4 tons respectively. Furthermore, the heat capacity of Cofalit® is lower than alumina with 0.93 and 1.01 kJ/kg.K, respectively.

Consequently, alumina spheres need more time to charge and can provide useful energy longer than Cofalit®. However, the ratio of discharge time to the charge time in Cofalit® is 89% compared to 82% for alumina, which indicates a better total cycle performance (charge/discharge) with Cofalit®.

3.1.2. Thermocline thickness

Figure 27 plots the estimated thermocline thickness δ for both materials against charge time. The figure shows that the thickness increased sharply at the beginning of the process until it reached a maximum value before it started to be extracted influenced by the increase of the thermocline outlet temperature[198]. The thermocline thickness at the time that the thermocline outlet temperatures reached its threshold value ($\theta_{outlet} = 0.2$) is 26% with Cofalit® compared to 31% with alumina.

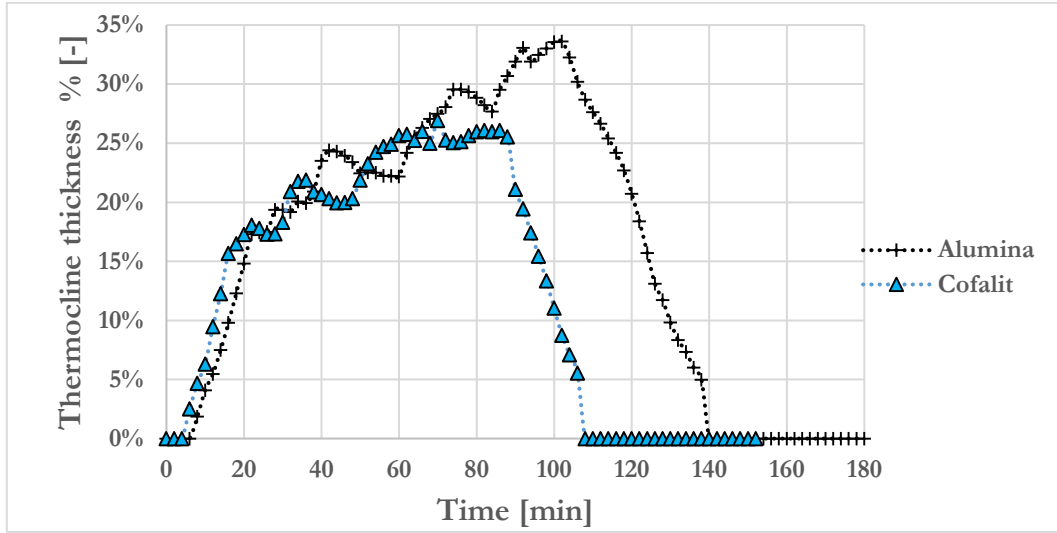


Figure 27 Thermocline thickness against the charge time (alumina and Cofalit®)

Figure 28 illustrates the measured thermocline thickness with Cofalit® and alumina spheres against discharge time. It reflects that the thermocline thickness at the time the thermocline outlet temperature reached ($\theta_{outlet} = 0.8$) are 20% and 26% for Cofalit® and alumina respectively.

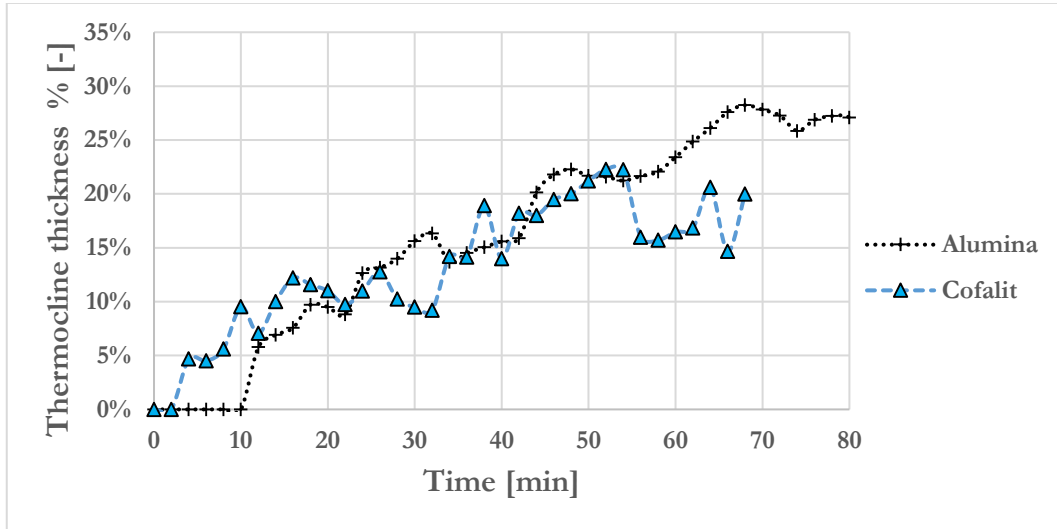


Figure 28 Thermocline thickness against the discharge time (alumina and Cofalit®)

Smaller thermocline thickness in Cofalit® compared to alumina can be explained by a smaller thermal diffusivity, as the same tank size is used with similar charge rate and temperature difference. (Table 22). Mira-Hernández et al. [17] observed a similar trend previously. Moreover, a higher convection coefficient is

expected in the Cofalit® case compared to alumina due to non-homogeneities in the particle shapes, which would result in a larger heat exchange surface.

Cofalit® has a significantly lower thermal conductivity than alumina (1.52 and 18 w/m.K), respectively) and lower volumetric heat capacity at average temperature (2.9 and 3.73 MJ/(m³.K), respectively), consequently lower thermal diffusivity. Furthermore, thermocline thickness was found smaller in Cofalit® during charge and discharge in respect of alumina, which suggests that the lower thermal diffusion, the better energy utilization during both operations.

However, the thermal storage in Cofalit® is lower than alumina Figure 24, with about 20% for the same tank size.

3.1.3. Charge and discharge efficiencies

The definition of charge and discharge efficiencies for this work was illustrated in (2.3.3).

Figure 29 plots the charge efficiency against the charge time for both materials. It shows that both materials have similar charge efficiency trends. Although, in theory, 100% efficiency is possible by definition in eq.(48), in real operation, the charge should stop at the time when the thermocline outlet temperature reaches its threshold temperature ($\theta_{outlet} = 0.2$) at 82 min for Cofalit® and 102 min, for alumina. The charge efficiency is about 82% and 80%, respectively.

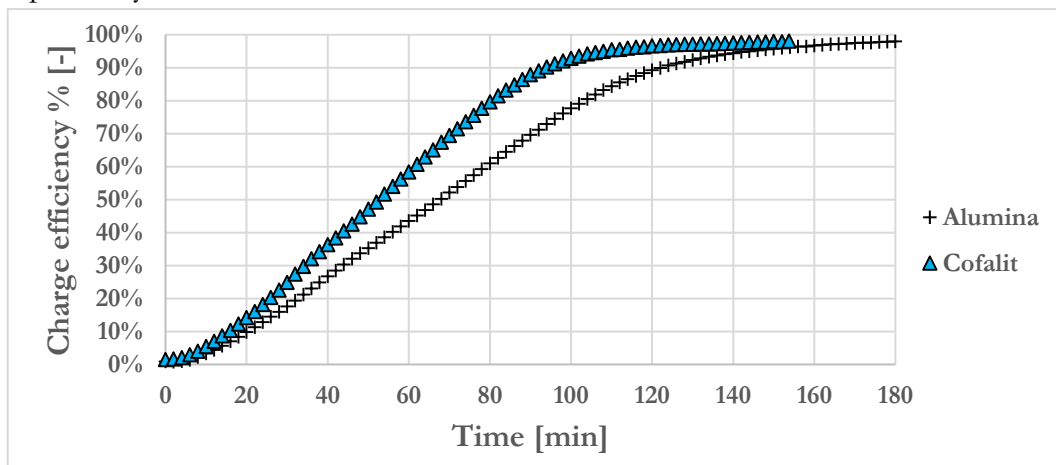


Figure 29 Charge efficiency evolution in time (alumina and Cofalit®)

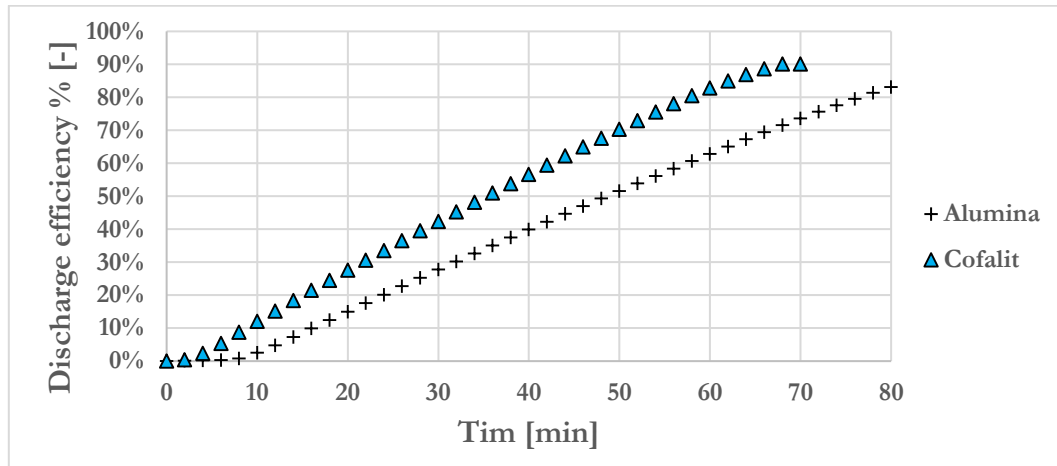


Figure 30 Discharge efficiency versus non-dimensional outlet temperature (alumina and Cofalit®)

Figure 30 illustrates the discharge efficiency evolution as a function of time for the Cofalit®, as well as the alumina. The thermocline reached ($\theta_{outlet} = 0.8$) at 67 min, and 80 min, respectively, resulting in a better discharge efficiency with Cofalit® than alumina, with 90% and 83%. Better efficiency with Cofalit® can be attributed to the lower thermocline thickness, which leads to higher efficiency, as it was previously observed [18].

Furthermore, smaller particle diameter results in better efficiency because it increases the heat exchange surface between the solid filler and the HTF [52]. Cofalit® has a lower average diameter than alumina, due to the mechanical sieving that was used to segregate the pile of Cofalit®. Which leads to a wider particle size distribution with a significant amount of particles with diameter less than 2 cm.

3.2. C-S MODEL VALIDATION

The C-S model used for this work (2.4.1) assumes that there is no temperature gradient within the solid filler. To validate this approach, Table 25 plots the estimated Biot number for alumina and Cofalit® at 290°C. It evaluates the local Bi number at the local velocity of the HTF from eq. (39). It illustrates that the Bi for both materials is less than 0.1, which validates the assumption to neglect the thermal gradient within the solid filler.

Table 25 Biot number of Cofalit® and alumina for this experimental setup

Material	Tank's Porosity	Temp K	Diameter [m]	Bi
Cofalit®	0.61	563.15	0.02	0.084
Alumina	0.485	563.15	0.02	0.015

The validation of the model's results is checked by comparing the non-dimensional temperatures profile as predicted by the C-S model to the one obtained from the experimental measurements. Both temperatures, the one predicted by the model and the one measured from the thermocouples are non-dimensionalized as per eq.(42).

The non-dimensional temperature profile is plotted against non-dimensional axial coordinates at 15 min intervals. The model applies the same initial conditions of the experimental one, as listed in Table 24.

3.2.1. Charge process

For the charging process, the model assumes that the HTF, solid filler, and the tank's wall are at 248°C (T_{low}), while the HTF is injected into the thermocline at a constant mass flow rate of 2600 kg/h. The model uses the experimental inlet temperatures of the HTF as the inlet temperature for the model for each time step. The HTF inlet temperature increased gradually at the beginning of the charge process from 248°C (T_{low}) until it stabilized at 280°C (T_{high}) for the rest of the process.

Figure 31 and Figure 32 compare the simulated temperature profile of the model to the experimental one for alumina and Cofalit®, respectively. A good agreement is demonstrated between simulated results and experimental data in both materials during the charging process. The Cofalit® case Figure 32 showed a small deviation between simulation and the experiments at some time intervals, which can be attributed to the non-homogenous shape of the Cofalit®

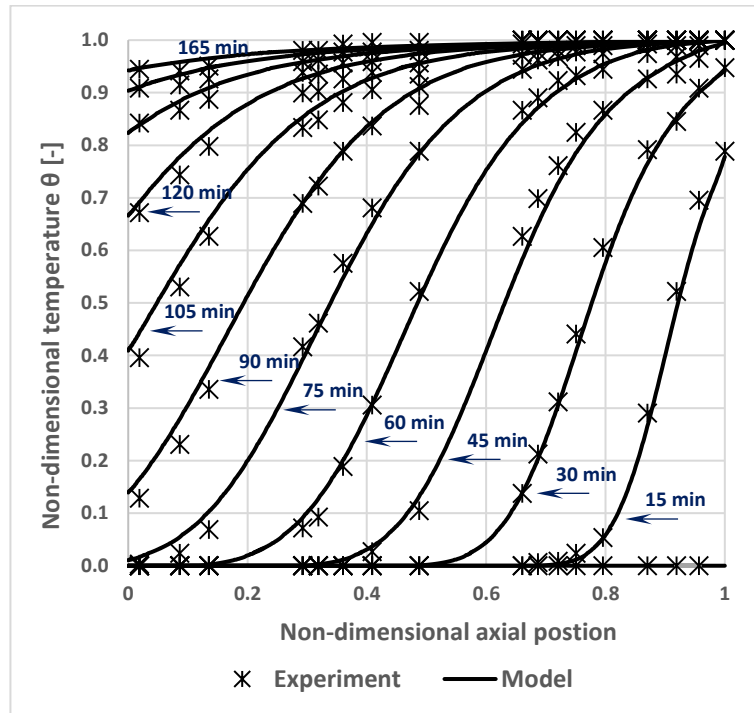


Figure 31 Temperature profile for alumina, model against experiment during charge

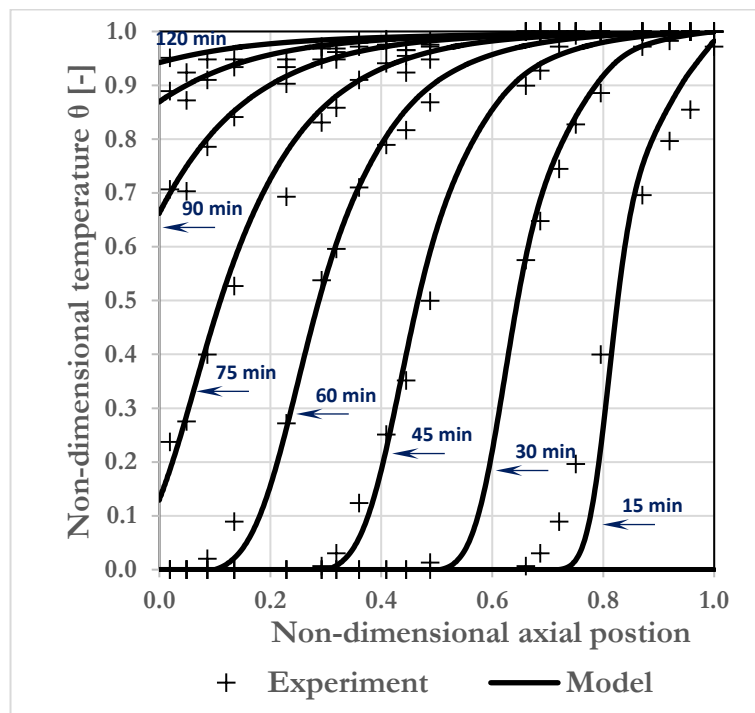


Figure 32 Temperature profiles for Cofalit®, model against experiment during charge

3.2.2. Discharge process

For the discharge process, the model assumes that the HTF, solid filler, and the tank's wall are at 290°C (T_{high}), while the HTF is injected into the thermocline at a constant mass flow rate of 2900 kg/h and constant temperature 220°C (T_{low}).

The model temperatures slightly deviated from the experimental ones in both cases, at temperatures lower than 20% of the maximum temperature near the inlet of the thermocline (at the bottom), Figure 33, and Figure 34, respectively. This deviation can be ascribed to the discrepancies between the constant inlet temperature of the thermocline assumed by the model, and the actual unstable inlet temperature.

Therefore, the model provided a suitable accuracy of the predicted temperature profile compared to the experiments during the discharge process for alumina as well as Cofalit®.

Hence, the model is validated for both processes, charge, and discharge as well as for two materials that have different thermophysical properties and different shapes, where alumina has a homogenous spherical shape, and Cofalit® has a non-homogeneous pattern with various size and shape.

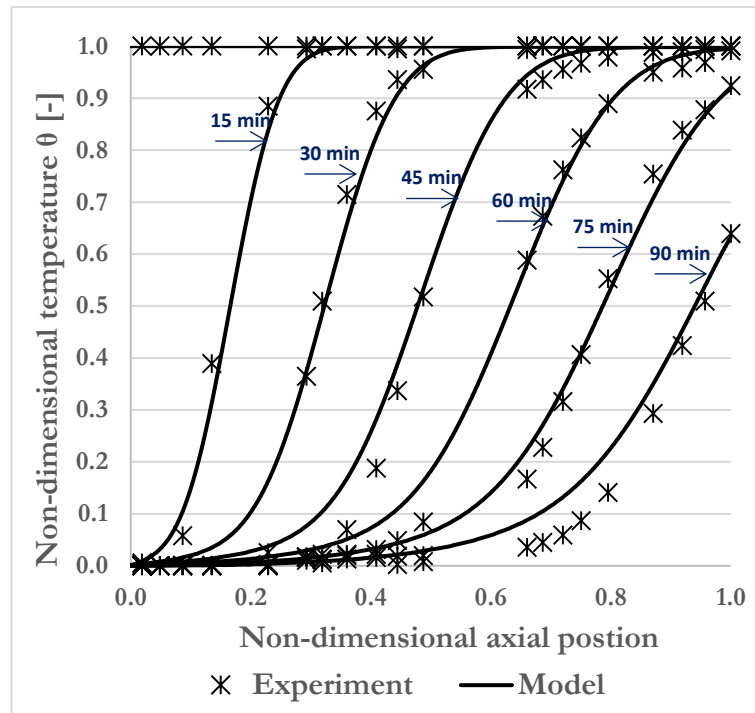


Figure 33 Temperature of alumina during discharge model Vs. experiment

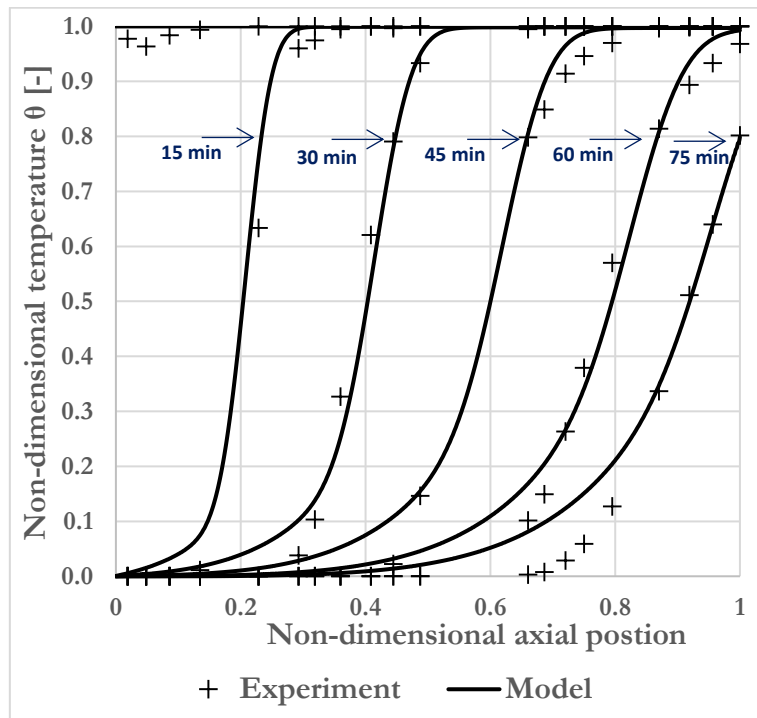


Figure 34 non-dimensional temperature of Cofalit® during discharge model Vs. experiment

3.3. PARAMETRIC ANALYSIS

The validated C-S model is used to perform a parametric analysis to study the influence of particle diameter, porosity, thermal conductivity, and volumetric heat capacity on the thermal behavior of the TES tank.

The heat capacity of the reference material (alumina spheres) is varied in the simulation by a factor between 0.25 to 2.5 inclusive. For example, factor one corresponds to alumina and factor 2 corresponds to cast iron $6.6 \text{ MJ/m}^3\text{K}$ [25], the thermal conductivity of the filler materials is increased from 0.25 to 30 W/m.K , the particle diameter is varied between $(0.005 - 0.05 \text{ m})$, and the porosity is changed from 0.3 to 0.7. Moreover, the value of each parameter is assumed independent from all other evaluated parameters, and the thermocline volume remains constant for all simulations. Furthermore, to facilitate the analysis, the normalization of parameters varies according to eq.(105).

$$X = \frac{x - x_{min}}{x_{max} - x_{min}} \quad (105)$$

Table 26 illustrates the operating conditions that are used in the simulations.

At the beginning of the charge process, HTF, solid filler, and the tank's wall are assumed at $T_{low} = 220 \text{ }^\circ\text{C}$. The HTF is injected at the top of the thermocline at a constant rate and constant temperature; $T_{high} = 290 \text{ }^\circ\text{C}$. The performance parameters of the charge are evaluated when the outlet temperature of the thermocline reached its threshold value of $234 \text{ }^\circ\text{C}$ ($\theta_{outlet} = 0.2$).

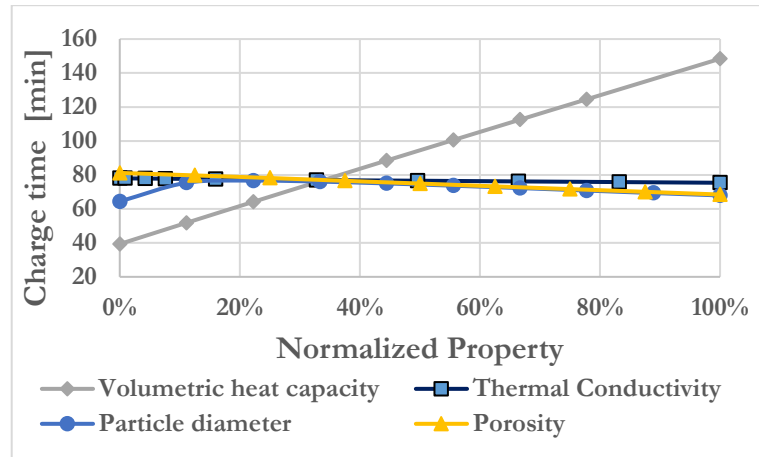
During the discharge, all mediums in the thermocline are considered at $T_{high} = 290 \text{ }^\circ\text{C}$, and the HTF is entering the thermocline at a constant rate at $T_{low} = 220 \text{ }^\circ\text{C}$. And the discharge performance parameters are evaluated at the end of the process when the thermocline outlet temperature reaches its threshold value $276 \text{ }^\circ\text{C}$ ($\theta_{outlet} = 0.8$).

Table 26 Numerical conditions for the parametric analysis

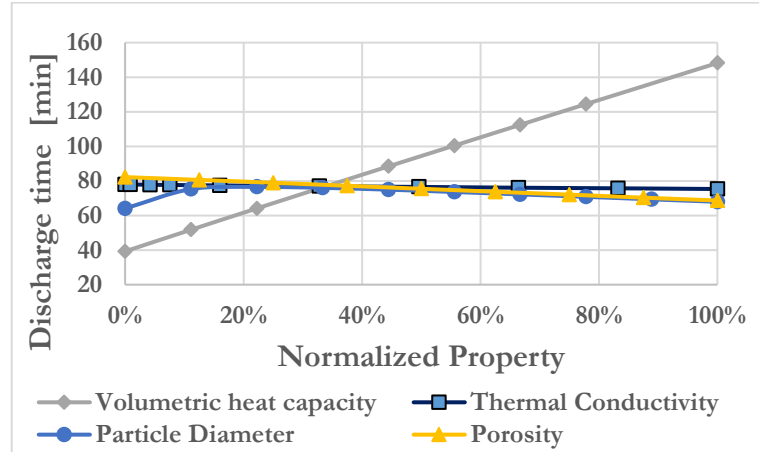
Process	Charge	Discharge
Mass flow rate [kg/h]	2950	2950
Temperature range [°C]	290 – 220	290 – 220
Threshold temperature [°C]	234	276

3.3.1. Process duration

Figure 35 plots process duration against the normalized parameter (a) for charge and (b) for discharge. It shows that the significant factor in controlling process duration is the volumetric heat capacity. A 10% increase in volumetric heat capacity generates a 10.9% longer charge as well as discharge duration.



(a)

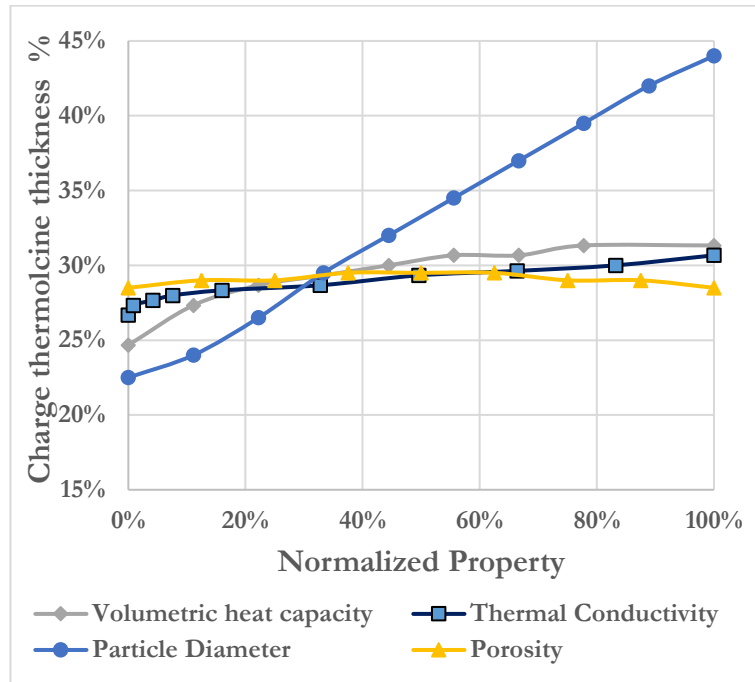


(b)

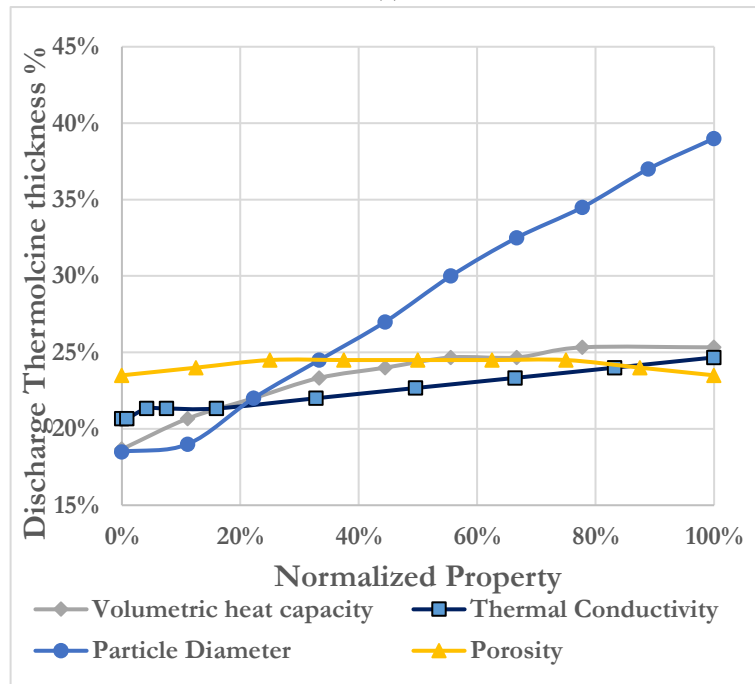
Figure 35 Process duration against system parameters (a) charge (b) discharge

3.3.2. Thermocline thickness

Figure 36 illustrates the development of thermocline thickness as a function of studied parameters for (a) charge (b) discharge. It demonstrates that the significant parameter is the particle diameter.



(a)



(b)

Figure 36 Thermocline thickness against system parameters (a) charge (b) discharge

The volumetric heat capacity and thermal conductivity have a small influence while the packed-bed porosity has no significant influence. This behavior can be explained by looking at the energy balance equation eq.(60) and spread it with the basic terms as per the following equation (106):

$$\frac{\partial T_p}{\partial t} = \underbrace{\frac{k_p}{(\rho C p)_p}}_{\text{diffusion term}} \cdot \frac{\partial^2 T_p}{\partial z^2} - \underbrace{\frac{h}{(\rho C p)_p} \frac{6}{d_p^2}}_{\text{Volumetric convection term}} \cdot (T_p - T_f) \quad (106)$$

- Increasing the particle diameter reduces the area of heat exchange between the solid filler and the HTF, reduces the volumetric convection term eq. (106), and increases thermocline thickness.
- Although increasing the heat capacity of the filler reduces the diffusion term in the eq.(106), it reduces the volumetric convection term, which is the dominant heat transfer mechanism during the process, consequently increases the thermocline thickness.
- Increasing the thermal conductivity increases the diffusion term in the equation; therefore, the thermocline thickness increases. However, its influence is small compared to the first two factors
- The porosity appears in the energy balance equation only in calculating the local Re number of the particle eq.(34). Hence it has no significant influence on the thermocline thickness.

Moreover, thermocline thickness during charge is about 6% wider compared to discharge for the evaluated parameters, similar to the experimental finding; this could be explained by the higher velocity of the cold front compared to the hot front for the same material equation (107) [199].

$$v_{\text{thermal front}} = \frac{\dot{m}_f C p_f}{A_{\text{int}} \cdot (1 - \varepsilon) (\rho C p)_p} \quad (107)$$

Where the speed of the thermal front depends mainly on the volumetric heat capacity of the solid filler. For example, at the cold thermal front, the low temperature will result in a low thermal capacity of the solid temperature, which will decrease the denominator of the eq.(107) and increase the speed of the cold thermal front. In contrast, at the hot thermal front, the high temperature of the solid filler will increase the denominator of eq.(107) which will result in a slower movement of the hot thermal front compared to the cold thermal front [110].

Therefore, during the charge, the thermocline thickness will expand more than the discharge Figure 37.

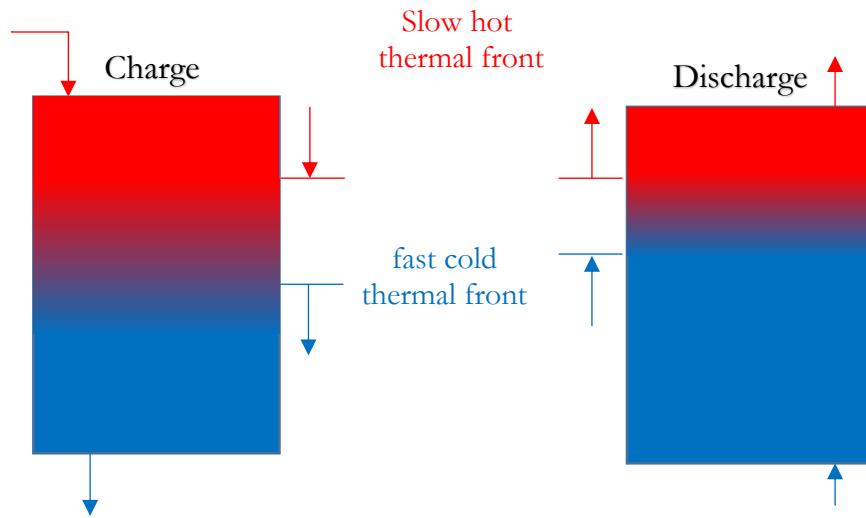


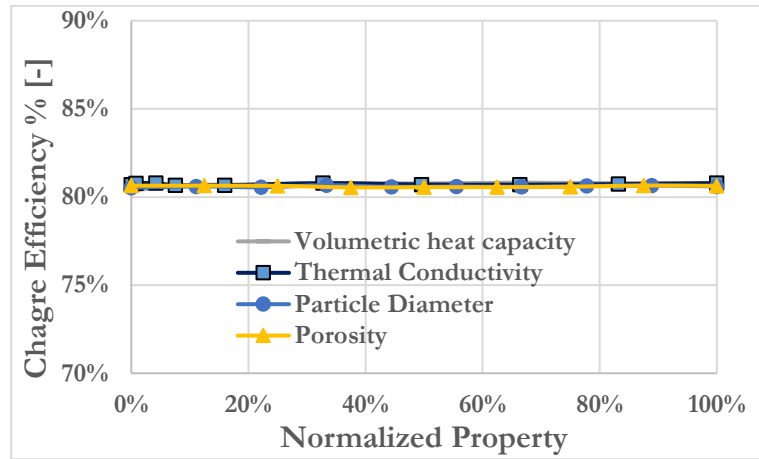
Figure 37 faster thermal front in the cold region of the thermocline compared to the slower thermal front in the hot region

3.3.3. Process Efficiency

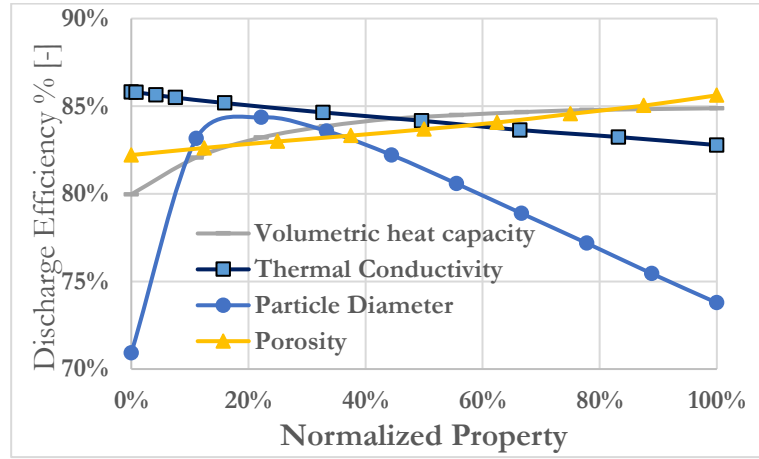
Figure 38 (a) shows that the efficiency of charge as defined in eq.(48) is independent of evaluated parameters.

On the other hand, Figure 38 (b) suggests that particle diameter has a prominent influence on the discharge efficiency as it is defined in eq(55). Moreover, an increase of the volumetric heat capacity increases the discharge efficiency before it reaches a plateau. While using more conductive material reduces discharge efficiency. Contrarily, high values of porosity increase it.

The discharge efficiency versus particle diameter exhibits a maximum at about 20% normalized property after a rapid increase, and then it starts to reduce by 1.4% each 10% diameter increase rate. After reaching the optimum particle diameter, increasing the diameter reduces the heat exchange area, hence reducing the discharge efficiency. Similar behavior of discharge efficiency was found by Hoffmann et al. [19]. It was indicated that a high ratio of heat flux (carried out) by the HTF to heat flux (exchanged) between HTF and solid fillers, could explain the lower efficiency at a very small particle diameter. Thus, the mass flow rates needed to be optimized to minimize this ratio and improve the efficiency. Their experimental work indicated two optimum mass flows 0.02 kg/sec, and 0.03 for two diameters 0.012 m and 0.04 m, respectively, and the same solid filler, quartzite.



(a)



(b)

Figure 38 Process Efficiency against system parameters (a) charge (b) discharge

This finding suggests that it is possible to find an optimum particle diameter for a given solid filler at a specific operating condition mass flow rate and temperature difference. This optimum value allows for a longer discharge time as well as high discharge efficiency and a low thermocline thickness. Moreover, it is recommended to avoid very small filler materials that may lead to three main problems. First, the degradation of HTF thermo-physical properties due to contamination with the fine particles. second, small particles could precipitate at thermocline's bottom during charge, preventing the tank's wall to go back to its original shape when cooled down at discharge, and this results in a severe strain on the tank wall [27]. Finally, it may fall below the optimum value which can reduce the discharge efficiency.

3.4. COMBINING TWO SHSMS IN THE SAME THERMOCLINE TES

One of the main objectives of this work is to increase the useful discharge time of the thermocline by combining two materials, the primary solid filler and a layer of a higher thermal capacity material like the PCM. Therefore it is interesting to evaluate the concept of combining two sensible heat storage materials numerically. The main solid filler is assumed Cofalit® because it has a low price and excellent thermal performance. Moreover, the added layer is SHSM with high thermal capacity Figure 39.

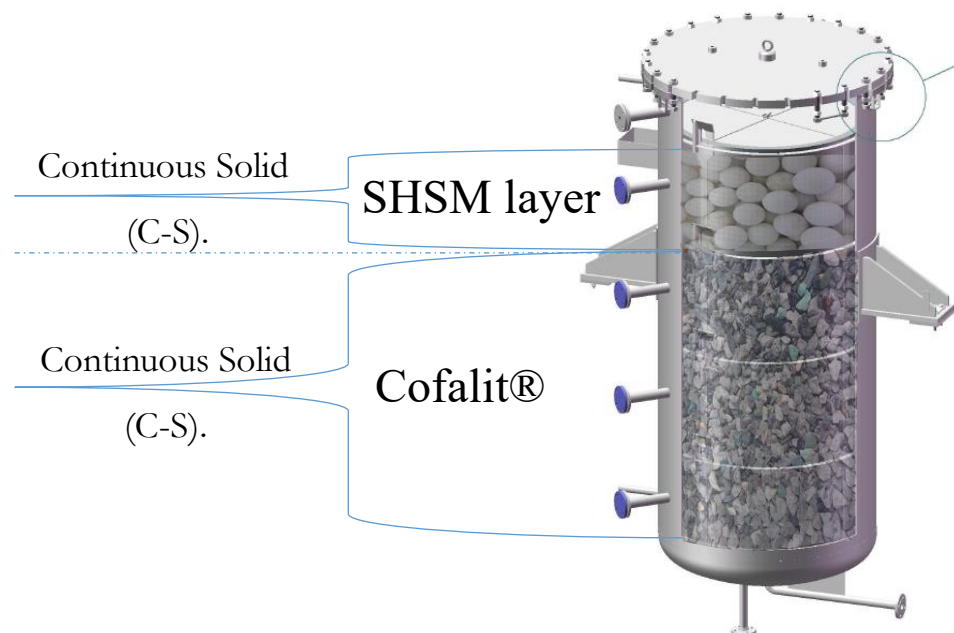


Figure 39 combining high thermal capacity SHSM to Cofalit ® in one thermocline Cofalit®

The numerical analysis is using the following assumptions:

- The main solid filler and the added layer are modelled with the C-S approach in the simulation.
- The added layers are filling 25% of the thermocline height; this percentage is selected because it corresponds to one basket filling in the thermocline.
- Cofalit® is filling 75% of the thermocline height.
- The SHSM in the top layer of the thermocline has the same diameter, porosity, and thermal conductivity than alumina.
- The heat capacity of the added layer increases by a factor from 1 to represent alumina spheres, up to 2.5, which represents a SHSM with

the equivalent heat capacity of the PCM latent heat of fusion, at designated operating conditions. For example ($C_{p_{\text{alumina}}} = 1017 \text{ J/kgK}$ $\times 70 \text{ }^\circ\text{C} \times 2.5 \approx 178 \text{ kJ/kg}$).

- The discharge conditions remain as per Table 26.

Figure 40 plots the simulated temperature of the HTF exiting the thermocline TES during the discharge. It compares the outlet temperature of a thermocline filled from the reference case of 100% Cofalit® to the combined cases [75% Cofalit® +25% Alumina], [75% Cofalit® +25%(1.5Cp)Alumina], [75% Cofalit® +25%(2Cp)Alumina], and [75% Cofalit® +25%(2.5Cp)Alumina]. It illustrates that the discharge time extended following to the addition of the layer of higher thermal capacity materials.

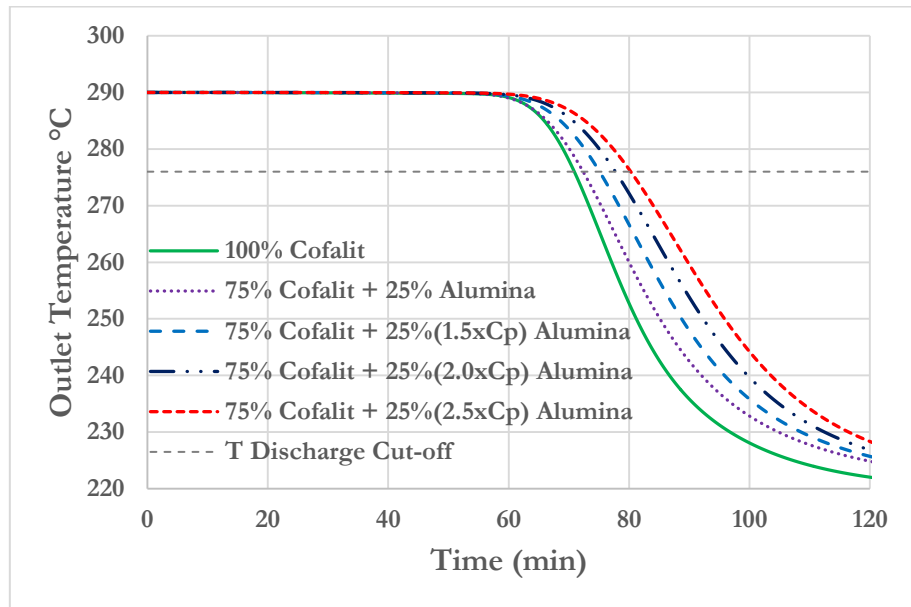


Figure 40 Thermocline outlet temperature during the discharge time for two SHSMs

Table 27 shows the resulted performance parameters for the various solutions evaluated. The discharge efficiency drops from 87% in Cofalit to about 81% in all combined solutions.

The thermocline thickness remains the same when a layer of alumina is added compared to the 100% Cofalit®, then is reduced by increasing the thermal capacity of the added layer.

The duration rises nearly by 2% by adding a layer of 25% alumina, and then it increases by about 3.5% for each 50% increases of the thermal capacity compared to the 100% Cofalit® case.

Table 27 Discharge performance parameters of Cofalit and alumina thermoclines against the combined two SHSMs solution

Solid filler setup	Efficiency [%]	Thickness [%]	Duration [min]
100% Cofalit	87.23%	23.22%	70.9
75% Cofalit 25% Alumina	81.14%	23.28%	72.4
75% Cofalit 25%(1.5xCp) Alumina	81.15%	21.29%	75.1
75% Cofalit 25%(2.0xCp) Alumina	81.08%	19.94%	77.7
75% Cofalit 25%(2.5xCp) Alumina	80.95%	18.96%	80.3

These results suggest that combining two SHSMs could be an interesting solution when there is a need to extend the duration of the discharge for a given tank size. However, the disadvantage of this solution is the cost of the added materials, especially if it exceeds the value of a bigger size tank. Moreover, the size of the added layer has to be optimized with different available solid fillers in order to find the best combination that satisfies the technical constraints of operation at a suitable cost.

3.5. CONCLUSIONS

Cofalit® has the potential to increase the thermal capacity of thermocline by 18% and reduces its solid filler material cost by 40% when compared to oil SHSM.

The performance of asbestos-based waste material known as Cofalit® was compared experimentally against alumina spheres as reference ceramic material, using the MICROSOL-R CSP. The main results are as follows,

Cofalit® has a 22% lower volumetric heat capacity than alumina, which results in a 20% faster charge time and a 15% shorter discharge time.

The thermocline thickness is found lower in Cofalit® than alumina, 26% against 31% for the charge, and 20% against 26% for the discharge processes, respectively.

The process efficiencies for Cofalit® are better than for alumina with 82% against 80% for the charge and 90% against 83% for the discharge, respectively.

Cofalit® outperforms alumina ceramic at the temperature level of this work, 300 °C, due to its smaller average diameter as well as lower volumetric heat capacity and inhomogeneous shape.

A parametric analysis applying a 1D C-S model evaluated the influence of particle diameter, porosity, thermal conductivity, and volumetric heat capacity of a solid filler on the thermal behavior of a thermocline TES. It indicated that there could be an optimum particle diameter for a given material at specified operating conditions, which provides a high discharge efficiency and small thermocline thickness.

Volumetric heat capacity has an essential influence on the thermal behavior of the thermocline. An increase of volumetric heat capacity increases the process duration, while it decreases the discharge efficiency and increases the thermocline thickness. Thermal conductivity and porosity (assumed independent from particle diameter) have less influence on the thermal behavior.

Combining two different storage media in the same thermocline could be a plausible solution to extend the useful discharge time at a given thermocline size, particularly when the added layer material has significant thermal capacity.

4. COMBINING LAYER OF PCM TO SENSIBLE HEAT THERMOCLINE, MODELING AND SIZING APPROACH

In order to develop the solution of thermocline TES with added PCM layer to SHSM, a suitable modeling approach should be selected. Hence the main objectives of this chapter are:

- Validate the use of a 1D D-C model (2.4.2) with a thermocline filled with PCM spheres.
- Combine D-C to C-S model to simulate the thermal performance of a thermocline filled with alumina spheres and a layer of PCM spheres.
- Suggest a sizing approach of the PCM layer, and use the model to evaluate the performance of the thermocline with various PCM layer sizes.

4.1. D-C MODEL VALIDATION

4.1.1. D-C validation for a sensible heat thermocline TES filled with alumina spheres as SHSM

As the first step of model validation, the C-S model (which was validated in 3.2) is used to validate the accuracy of the D-C model for the use with a thermocline filled with alumina spheres as SHSM. The main difference between the two modeling approaches is that the C-S model neglects the thermal gradient inside the solid's sphere, and the D-C takes it into account.

In this section, both models are using the thermocline filled with alumina spheres with the operating conditions listed in Table 28

Table 28 numerical operating condition for the thermocline filled with alumina spheres (D-C vs. C-S)

Process	Charge	Discharge
Mass flow rate [kg/h]	2950	2950
Temperature range [°C]	315 – 220	315 – 220
Threshold temperature [°C]	239	296

For the charge process, HTF, solid filler, and the tank's wall are assumed at T_{low} 220 °C at the beginning of the process. The HTF is injected at the top of the thermocline at a constant rate and constant temperature, T_{high} =315 °C. The performance parameters of the charge are evaluated when the outlet temperature of the thermocline reached its threshold value of 239 °C ($\theta_{outlet} = 0.2$).

At the beginning of the discharge, all mediums in the thermocline are considered at T_{high} 315 °C, and the HTF is entering the thermocline at a constant

rate at T_{low} 220 °C. And the discharge performance parameters are evaluated at the end of the process when the thermocline outlet temperature reaches its threshold value 296 °C ($\theta_{outlet} = 0.8$).

Figure 41 plots the outlet temperatures of the thermocline against time for charge and discharge of both models. It confirms the validity of the D-C model with very similar results during the charge and discharge.

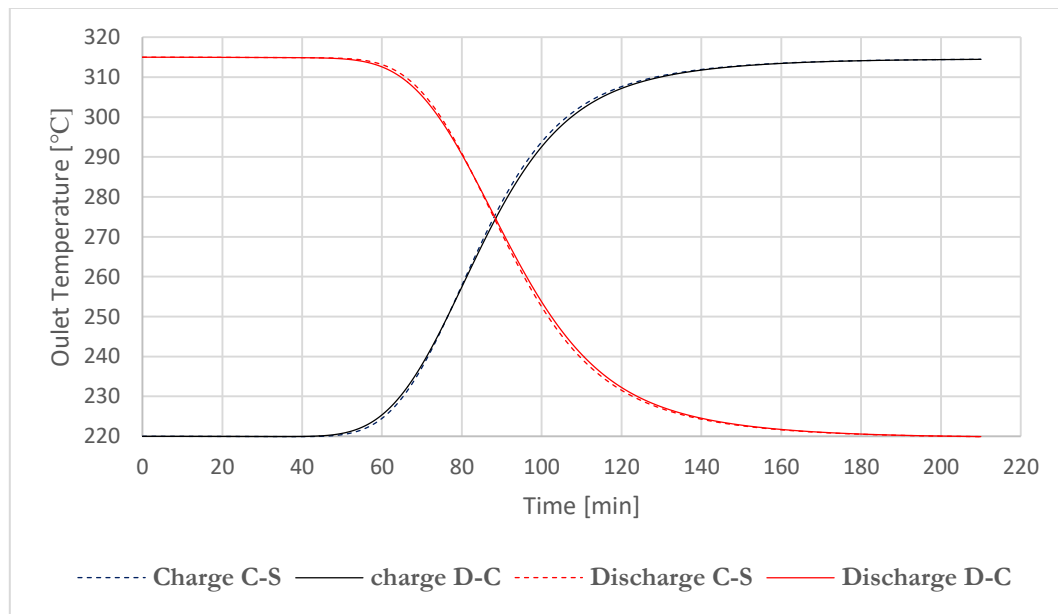


Figure 41 C-S and D-C model's comparison of the HTF temperature at the thermocline outlet against time for charge and discharge

Table 29 Performance indicators Comparison C-S to D-C for thermocline filled with 2 cm alumina spheres

Parameter	Charge		Discharge	
	C-S	D-C	C-S	D-C
Process efficiency	81.24 %	80.55 %	78.90 %	78.01 %
Thermocline Thickness	32.58 %	34.09 %	25.76 %	26.52 %
Process duration min	71.33	70.63	77.20	76.87
calculation time sec	7.5	207	8	208

Furthermore, Table 29 summarizes the obtained performance indicators from both models. It shows a very close prediction between the two models for charge and discharge operation.

These results validate the use of the D-C model with a thermocline filler with SHSM. However, the C-S is 96 % faster than the D-C with similar accuracy for the alumina spheres case. The D-C model solves the temperature gradient on the particle level, which required more calculation time. Hence, the use of the C-S model is still favorable over the D-C when the $Bi < 0.1$.

4.1.2. Comparison between C-S and D-C for latent heat thermocline TES of NaNO_3 PCM spheres

Before applying a C-S model to solid filler materials in the thermocline TES, the Biot number must be verified. Bi can be calculated as per eq.(39), based on the assumptions that the PCM spheres has the same packed-bed porosity, and natural convection is neglected inside the PCM spheres, where Nu is evaluated from eq.(108).

$$Nu = 2 + 1.1Re^{0.6}Pr^{1/3} \quad (108)$$

Table 30 illustrates that the Bi of the NaNO_3 PCM capsules for the 4 diameters is larger than 0.1, which implies the necessity to address the temperature gradient within this PCM.

Table 30 Biot for NaNO_3 PCM at various spheres diameters

Material	Porosity	Temp K	Diameter [m]	Bi
NaNO3	0.485	588.15	0.02	0.52
			0.04	0.75
			0.06	0.94
			0.08	1.10

Plenty of methods are available to model the melting solidification of the PCM (1.3.2). In this work, we chose the Enthalpy Porosity Method (EPM) (2.4.2). Additionally, the apparent heat capacity method ($C_p\text{-eff}$) (1.3.2.2) is easy to deploy to compare the numerical results and performance of the codes. Both enthalpy porosity and apparent heat capacity methods can be applied to the D-C model and the C-S model. Beasley et al. [88] suggest a correlation that simplifies the temperature gradient in the solid filler into an effective heat transfer coefficient correlation eq.(109) in the C-S model.

$$h_{eff} = \frac{h}{1 + 0.25Bi_{PCM}} : Bi_{PCM} = \frac{hd_{PCM}}{2k_{PCM}} \quad (109)$$

4.1.2.1. Modeling assumptions

The numerical model in this section use the following assumptions:

- 2 cm diameter spheres of NaNO_3 are filling the entire thermocline.
- The time step Δt is 0.5, and the size of the control volume Δz is 0.02m (the sphere diameter).
- The control volume size on the axial direction of the
- The container material is stainless steel with a 1 mm thickness.
- The packed-bed of PCM spheres has the same porosity of alumina spheres one.
- Neglect the envelop thermal resistance because of its high conductivity and small thickness [46][139].
- Neglect the natural convection inside the spheres due to their small diameter [157].
- The models consider the thermal capacity of the envelope using eq. (110).

$$(\rho C_p)_{eff PCM} = \frac{(\rho C_p V)_{PCM} + (\rho C_p V)_{Envelop}}{V_{tot}} \quad (110)$$

4.1.2.2. Numerical comparisons between four models

Figure 42 plots the HTF temperature at the thermocline TES outlet against the discharge time of the C-S model with Cp-eff, C-S model with EPM, D-C model with Cp-eff, and D-C model with EPM.

It illustrates that, for the same physical model C-S or D-C, the Cp-eff is underestimating significantly the phase change process compared to the EPM, which results in a shorter phase change, consequently, a shorter discharge process. This could be attributed to the way Cp-eff is considering the phase change process eq.(111). Where the heat capacity of the PCM during a phase change is inversely proportional to the temperature difference at which the melting/solidification is happening, hence the phase change process in this method is mainly influenced by this temperature range without taking into account the amount of melted material, which limits the phase change [200].

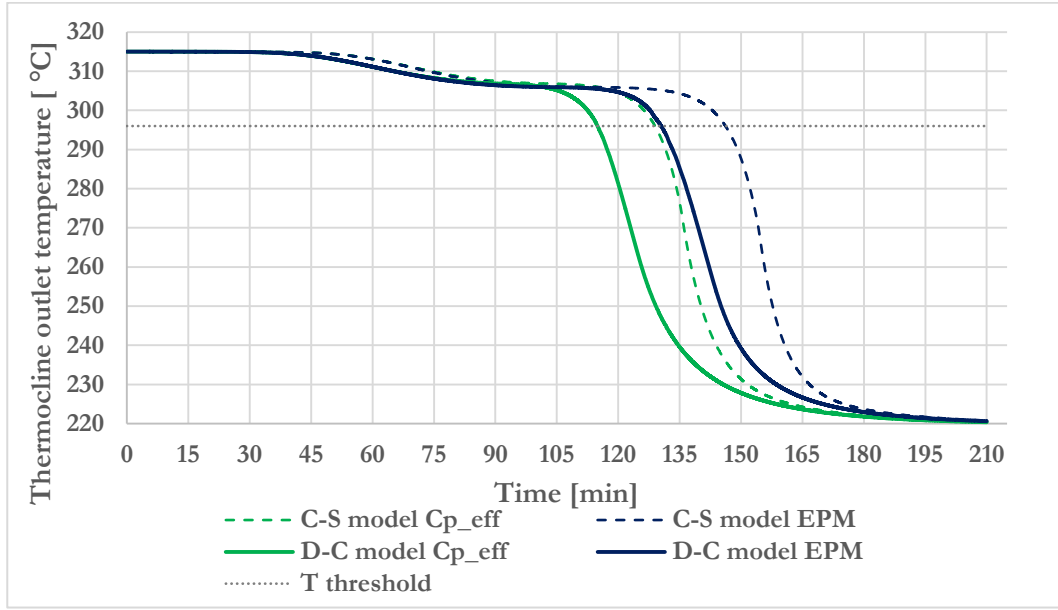


Figure 42 the outlet temperature during discharge of the thermocline filled with 2cm PCM spheres as per the four models

$$Cp_p = \begin{cases} Cp_p = Cp_{sol.}, & T_p < T_{sol} \\ \frac{Cp_{sol.} + Cp_{liq}}{2} + \frac{L_{Fus}}{T_{liq} - T_{sol}}, & T_{sol} < T_p < T_{liq} \\ Cp_p = Cp_{liq} & T_{liq} < T_p \end{cases} \quad (111)$$

Furthermore, Figure 42 indicates that the predicted discharge process is longer (more optimistic) in the two C-S models than the D-C ones at the threshold values, with respect to the latent heat modeling method. This could be explained by the additional thermal losses that the D-C model considers compared to the C-S model, which are represented as a symmetric thermal gradient within the PCM sphere.

For example, when evaluating the PCM sphere located in the last control volume of the thermocline during discharge as depicted in Figure 43.

Figure 44 shows the temperature gradient within the reference sphere as approximated by the D-C EPM, and compares it to the uniform sphere temperature as depicted by the C-S EPM. It reflects how underestimating the thermal gradient in the PCM sphere leads to a longer isothermal process and overestimating the overall discharge time.

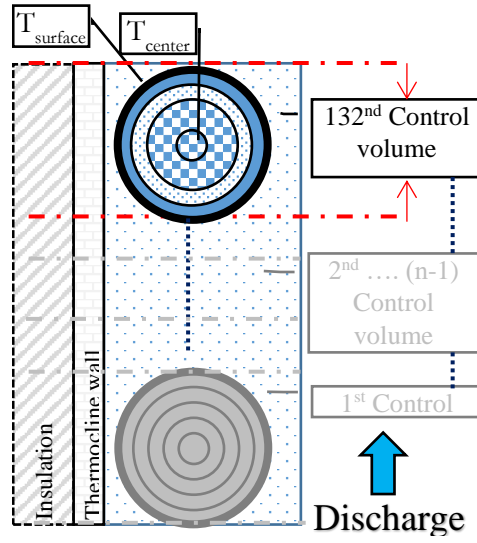


Figure 43 D-C model discretization during discharge

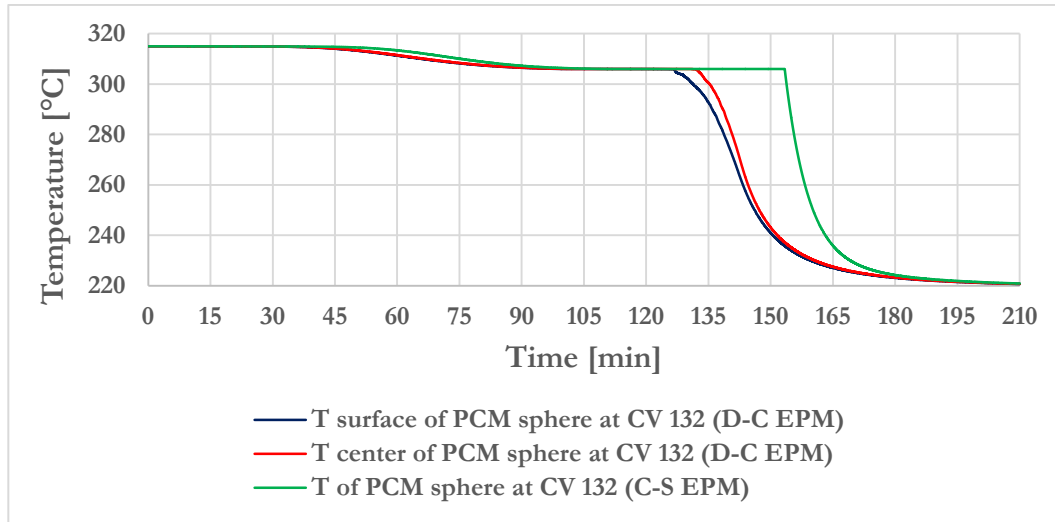


Figure 44 surface and center temperatures of the PCM sphere located at last control volume during discharge of D-C EPM model compared to the sphere temperature of a C-S EPM

Moreover, the EPM approach can approximate the liquid fraction distribution within the PCM sphere in both C-S and D-C model. Figure 45 illustrates the liquid fraction in the same reference sphere when the thermocline outlet temperature reached its threshold value for the D-C and C-S models. The C-S model estimate a constant value of the liquid fraction at about 57%, while the D-C model approximates a distribution of liquid fraction due to the thermal gradient with about 70% of the PCM unsolidified yet.

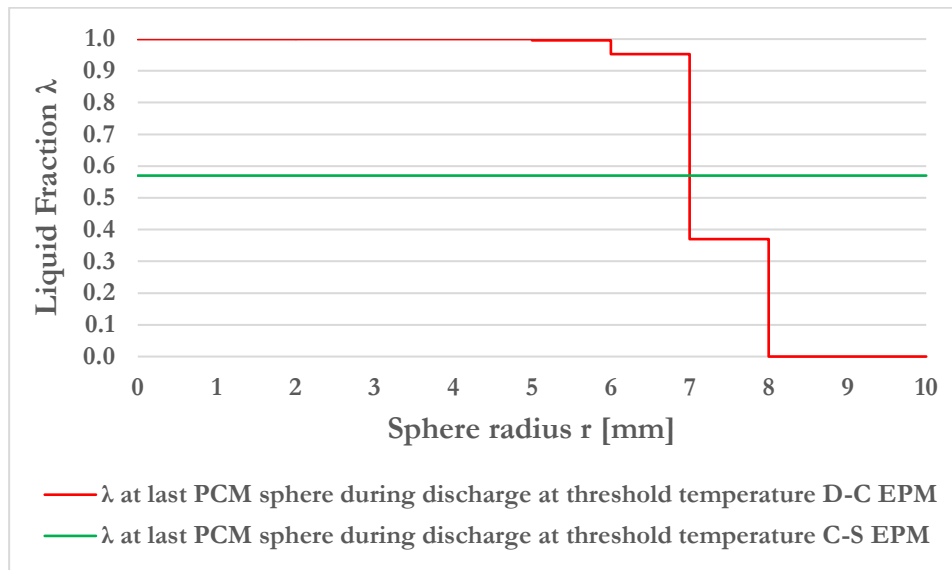


Figure 45 estimated Liquid fraction of the PCM as per D-C EPM and C-S EPM at the sphere 132 during discharge when the threshold temperature is reached

Figure 46 compares the temperature gradient within the reference sphere (indicated in Figure 43), as estimated by the D-C model Cp-eff to the temperature of the same sphere as approximated by the C-S Cp-eff.

Figure 46 indicates that the isothermal process lasts longer in the C-S than the D-C, influenced by the underestimating of the thermal gradient within the PCM sphere.

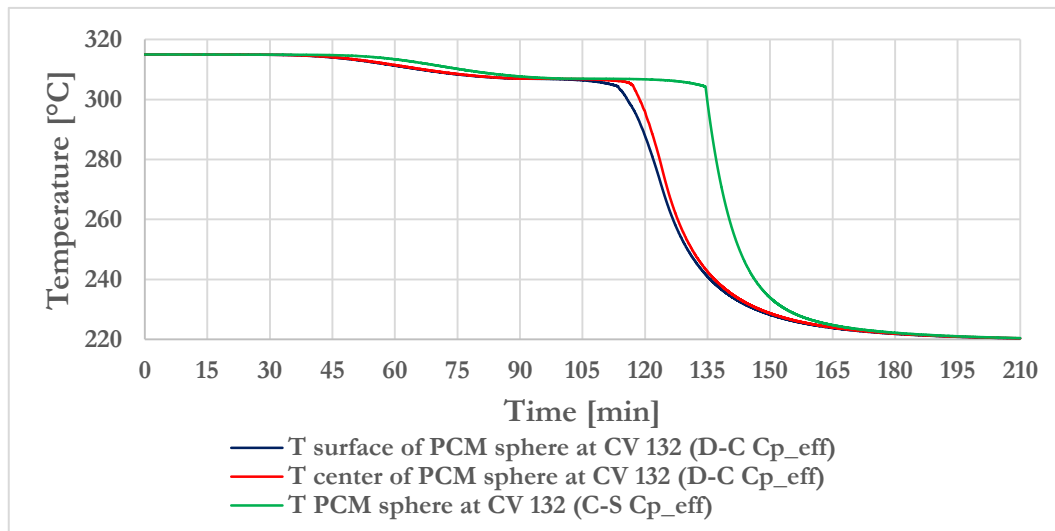


Figure 46 surface and center temperatures of the PCM sphere located at last control volume during discharge of D-C Cp-eff model compared to the sphere temperature of a C-S Cp-eff

Table 31 summarizes the performance indicators for the various models as resulted from the models. The C-S overestimates the discharge efficiency by about 1.5 % with respect to 91 % that is the result of the D-C models. The thermocline thickness is underestimated in the C-S models compared to the D-C models. For example, using the EPM the resulted in thickness is 10% and 16%, respectively. And using the Cp-eff it is 12% and 18%, respectively.

The discharge process is overestimated in the C-S models by 11 % with respect to the D-C model. C-S and DC models predict 145 min and 130 min applying EPM, and 128 min and 115 min applying Cp-eff respectively.

Table 31 Performance indicators Comparison C-S to D-C of thermocline filler with 2cm PCM spheres during the discharge process

Parameter	EPM		Cp-eff	
	C-S	D-C	C-S	D-C
Process efficiency	92.5 %	90.9 %	92.3 %	90.7 %
Process Thickness	9.8 %	15.9 %	11.4 %	18.0 %
Process duration min	145.0	130	128	115
calculation time sec	35	285	36	258

In this work, we choose the D-C model to simulate the thermal behavior of thermocline filled with PCM because it accounts for the thermal gradient within the PCM sphere where the Bi of the PCM sphere is higher than 0.1 Table 30. Furthermore, the EPM is chosen to approximate the influence of the latent heat of fusion because it provides reasonable accuracy. It also overcomes the major shortage of the Cp-eff method (not accounting for the amount of melted material in the calculation [200][127]).

4.1.3. Validation from literature experiment

The previous section developed the reasoning of selecting the D-C model with EPM for this work, to simulate the thermal behavior of the encapsulated PCM section in the thermocline TES. This section validates the D-C EPM model from the experimental results provided by Raul et al. [150].

Raul et al.[150] used A164 as PCM, which is commercial grade organic material with a melting temperature of 168.7 °C and encapsulated in stainless steel 316 spheres with 1mm thickness and 29 mm diameter, the spheres being 95% filled

with the PCM. They used a Hytherm 600 oil as HTF. Table 32 summarizes the thermophysical properties of the used materials in Raul et al.[150] work.

Table 32 Thermophysical properties of HTF, PCM, and Stainless steel used in Raul experiment

Material	ρ [kg/m³]	C_p [J/kgK]	k [W/mK]	L_{fus} [J/kg]	T_m [°C]	μ [kg/ms]
Hytherm 600	720.9	3097.4	0.116	-	-	0.0195
A164	1500	2013.3	0.45	249700	168.7	0.0063
SS316	8030	502.48	16	-	-	-

The thermocline TES is surrounded by 0.2 m of insulation material. The HTF is injected at the thermocline topmost point, with its temperature raised from ambient temperature up to 184°C gradually. Table 33 summarizes the experimental details of Raul et al.[150].

Table 33 Experimental conditions of Raul et al. [150] setup

HTF Maximum inlet Temperature	184 °C
volumetric flow rate	8.05 lpm
porosity	0.6
Storage wall thickness	3.4 mm
Ambient Temperature	32 °C
Tank inner height	0.36 m
Tank inner diameter	0.17 m
PCM sphere inner diameter	29 mm
PCM sphere outer diameter	31 mm
The thickness of the insulation layer	0.2 m

Figure 47 plots the experimental inlet and outlet temperatures evolution in time, as provided by Raul et al. [150]. It compares it to outlet temperature as simulated by the D-C-EPM explained in this work (2.4.2). The model used the variable inlet temperature of the experiment as an input temperature.

Figure 47 shows that the model reasonably predicted the outlet temperature of the thermocline, while the fluctuation in the experimental data could be attributed to unstable flow and error of measurement. Moreover, the tank-to-particle diameter ratio of 5.5 is smaller than 30, which causes the HTF velocity near the tank wall to be significantly larger than in the tank's center, causing unbalance heat transfer and uneven temperature distribution[171], that the model is not considering.

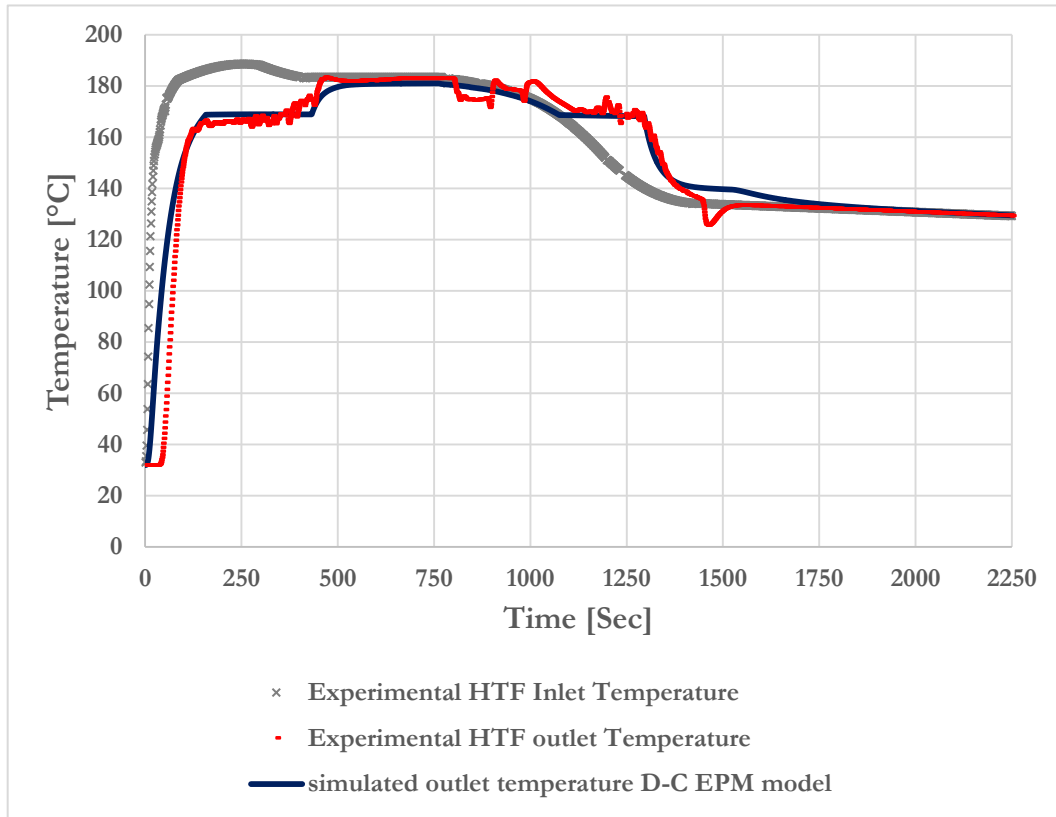


Figure 47 Inlet/outlet HTF temperature against time for Raul and outlet temperature as predicted by the D-C-EPM model

Since the C-S model is validated for the sensible heat storage part of the thermocline, and the D-C EPM model is validated for the latent heat storage part, the two models can be coupled to simulate the behavior of a thermocline filled with a sensible heat solid filler and a PCM layer Figure 48.

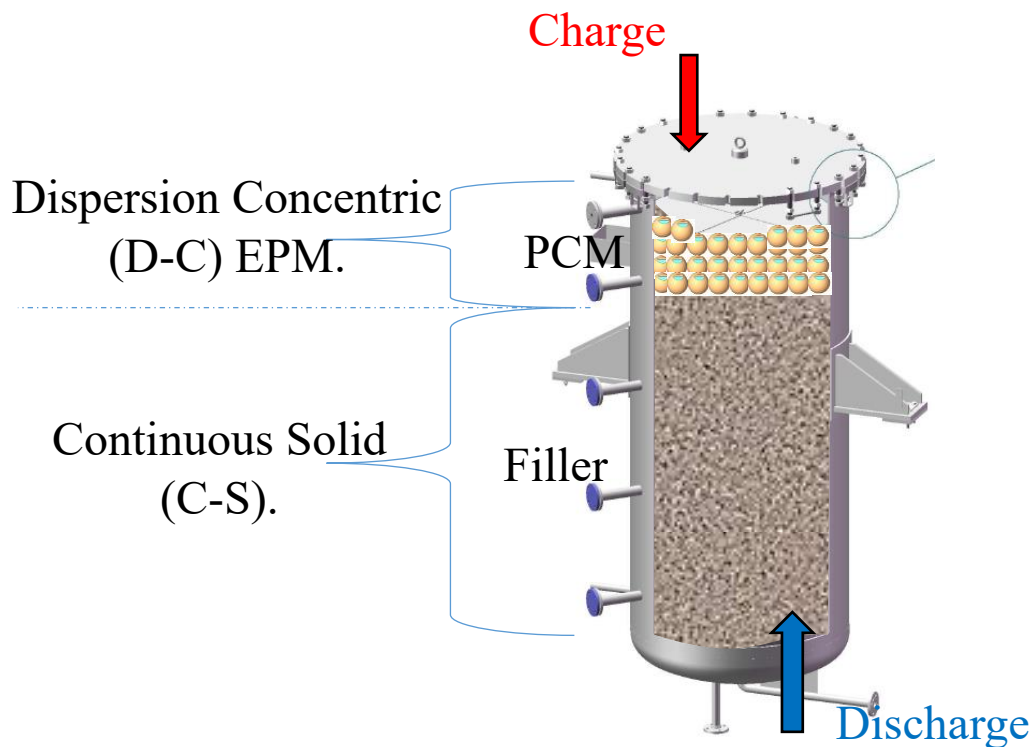


Figure 48 combining a layer of PCM to sensible heat thermocline TES

4.2. COMBINING A LAYER OF PCM TO SENSIBLE HEAT THERMOCLINE TES

One of the main objectives of this study is to provide a numerical evaluation of combining a PCM layer to a sensible heat filled thermocline.

The C-S model provided a fast and accurate numerical solution for the sensible heat TES because the Bi number of solid filler is below 0.1. However, the C-S model cannot be used in the PCM layer because the Bi corresponding to PCM sphere is larger than 0.1. Hence the D-C EPM is chosen to simulate the PCM layer thermal behavior because it considers the thermal gradient within the spheres and predicts the isothermal behavior of the PCM during the phase change process at reasonably accepted accuracy.

Hence in this section, we simulate the thermal performance of a thermocline that is filled with 75 % sensible heat storage medium (alumina spheres) and 25 % latent heat storage medium (NaNO_3 encapsulated in a stainless steel envelope). The PCM volumetric ratio [% vol.], which is the ratio between the

volume of the PCM layer to the total internal volume of the thermocline, is arbitrary chosen for this preliminary evaluation at 25 % vol. The internal sectional area of the thermocline is equal to the internal sectional area of the PCM layer. Hence, the PCM volumetric ratio represents the ratio of the height of the PCM layer to the total height of the thermocline.

The simulation applies the previously validated C-S model (3.2) in the sensible heat storage part of the thermocline, and the D-C EPM model (validated in 4.1.3) in the PCM part. The two models are coupled to represent two regions of the tank Figure 48. The PCM spheres are located at the top and the alumina spheres at the bottom.

4.2.1. Charge process

During charge, the HTF enters the PCM section at $T_{\text{high}}=315^{\circ}\text{C}$ and constant mass flow, then it exits from the bottom-most of the thermocline, while at the beginning of the process, all mediums inside the tank are at $T_{\text{low}} 220^{\circ}\text{C}$.

The simulation uses the same assumptions of the previous section (4.1.2.1) and identical testing conditions to Table 28. Coupling the two models is performed by considering the outlet of the PCM region model as the inlet of the alumina spheres bed model at each time step.

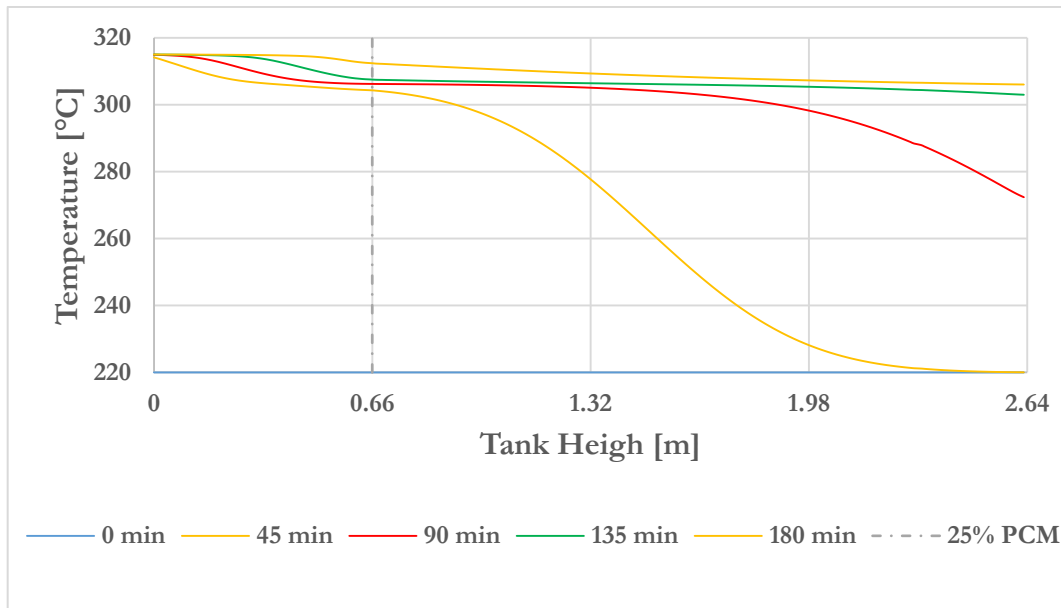


Figure 49 HTF temperature profile during the charging process of a thermocline containing 25% PCM and 75% alumina

Figure 49 plots the temperature profile of the HTF for the combined solution during a charge process at 45 min time interval. It shows that for the first 45 min of charge, the isothermal melting of the PCM started to be reflected on the HTF temperature in the PCM layer around the melting point of the PCM of 306°C. Furthermore, the outlet temperature of the PCM layer becomes constant controlled by the PCM melting point and, consequently, the inlet temperature of the alumina sphere part.

When all the PCM is melted (after 135 min of charge), the temperature elevates at the PCM layer outlet, raising the inlet temperature of the alumina part slowly until the end of the simulation.

4.2.2. Discharge process

At the beginning of the discharge, all medium inside the thermocline is assumed to be fully charged at T_{high} 315°C, and the HTF enters the sensible heat storage part of the thermocline at T_{low} 220° with a constant mass flow rate. Then the HTF exits from the PCM layer. During the discharge process, the two models are coupled to make the sensible heat part outlet temperature is the input of the PCM at each time step.

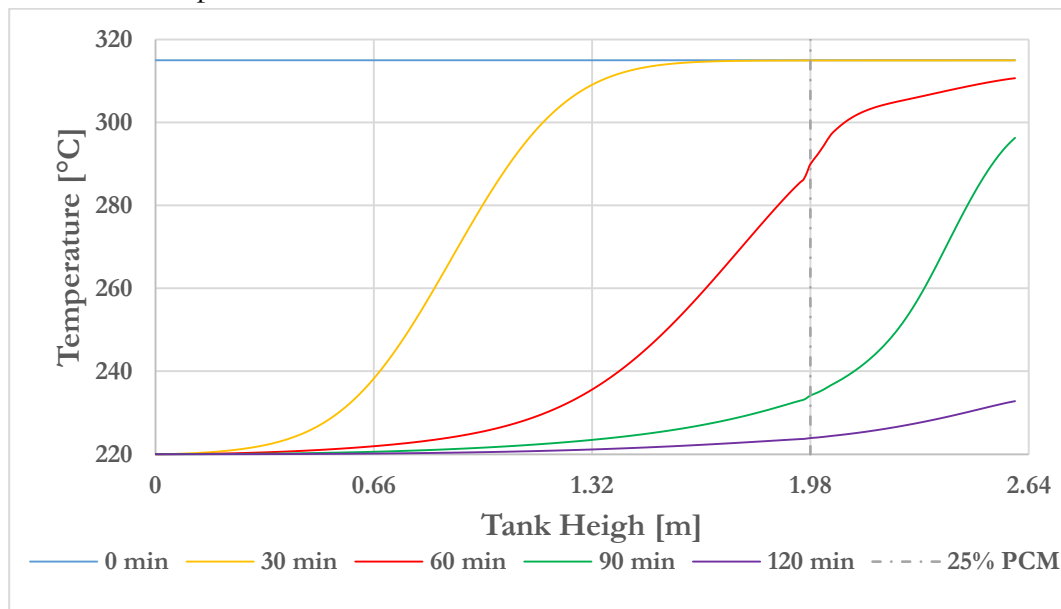


Figure 50 HTF temperature profile during the discharge process of a thermocline contains 25% PCM and 75% alumina

Figure 50 shows the temperature profile during the discharge. In this process, the PCM influence is evidenced in the HTF temperature between 60 min and 90 min of discharge. Moreover, the temperature profile in the PCM layer

illustrated different steepness due to the phase change in the PCM during the solidification process.

4.2.3. Performance comparaison

Table 34 summarizes the resulted performance indicators of the combined case versus the 100% alumina spheres thermocline. The charge efficiency and duration until the threshold value are very near to the charge of 100 % alumina spheres thermocline. However, the thickness increased in the combined solution to 35% compared to 33% in the 100% alumina sphere.

Table 34 Performance indicators during charge/discharge of a thermocline filled 25% PCM 75% alumina spheres compared to 100% alumina spheres

Parameter	Charge		Discharge	
	25%PCM 75% alumina	100% alumina	25%PCM 75% alumina	100% alumina
Process efficiency	81 %	81 %	88 %	78 %
Thermocline Thickness	35 %	33 %	7%	26 %
Process duration [min]	72	71	93	77

The discharge process is significantly improved due to the 25 vol.% PCM layer, as the efficiency increases from 78 % in alumina thermocline to about 88 % in the combined case, the thickness during discharge reduced from 26 % to 7 %, and the useful time increased 20 % from 77 min to 92 min respectively.

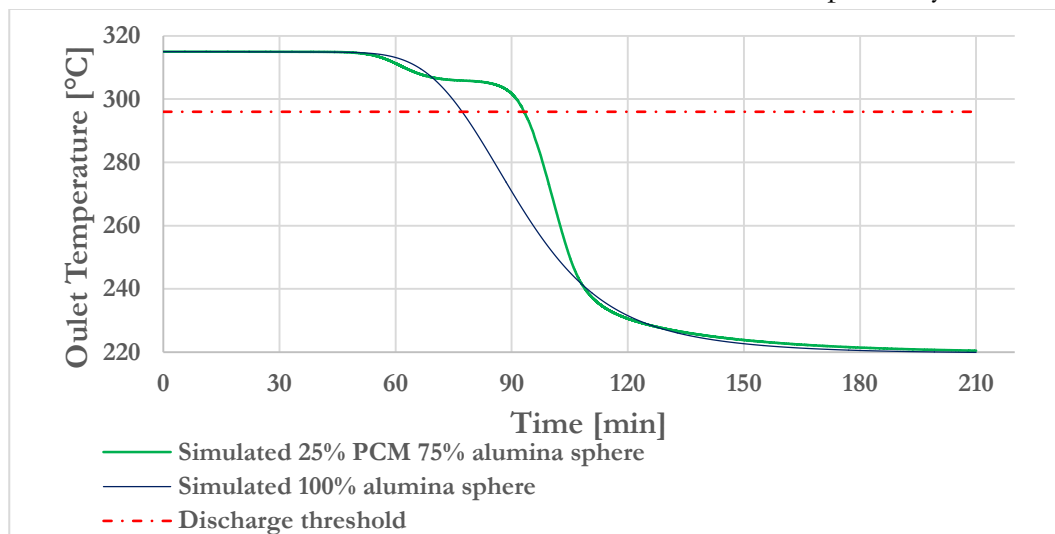


Figure 51 Thermocline outlet temperature evolution in time comparison between 100% alumina sphere and 25% PCM-75% alumina sphere

Figure 51 compares the thermocline outlet temperature evolution in time for both cases, 100% alumina spheres, and the combined case. It illustrates that the discharge time in the combined case is extended due to the PCM influence on the HTF.

Although, the model predicts that adding 25 vol.% PCM layer results in thermocline performance parameter improvements, the amplitude of the effect depends on the state of the PCM. These results are limited to the assumption that the thermocline is fully charged, and all storage mediums inside the thermocline started the discharge process at T_{high} . Therefore, in a real case, the improvements of discharge could be less when the charge has to stop at threshold value, when all the PCM might not be melted yet in the spheres.

Furthermore, the 25 vol.% PCM ratio is arbitrarily chosen for this simulation, where theoretically, this ratio could vary from 1% up to 100% when filling the whole thermocline. Therefore, a practical approach is needed to decide the size of the PCM layer for a given thermocline TES filled with solid filler as SHSM.

4.3. PCM LAYER SIZING APPROACH IN COMBINED LATENT TO SENSIBLE HEAT THERMOCLINE TES

Section 4.2 assumes that the PCM fills 25 vol.% of the tank, which improves the discharge performance by extending the discharge time 21 % and increasing the discharge efficiency by about 13 %. On the other hand, the layer size requires optimization to limit the effect on cost. In other words, what is the recommended layer size needed in a thermocline to have suitable performance improvements during the discharge process? Otherwise, it is theoretically possible to fill the tank with 100 % PCM.

Zanganeh et al. [46] numerically tested three volumetric ratios 0.67 vol.%, 1.33 vol.%, and 2.67 vol.% of PCM to stabilize the thermocline outlet temperature. They concluded that 1.33 % PCM used in their case is sufficient to maintain the air temperature at the outlet with decent discharge efficiency.

Hernández et al. [163] evaluated five ratios 1 vol.%, 2.5 vol.%, 5 vol.%, 10 vol.%, and 20 vol.% of PCM at the top of their thermocline. They indicated that 5 vol.% reflected the best duration gain per layer for the discharge process.

Each of these researches suggested a suitable percentage to their specific case with a given tank size, thermophysical properties of the PCM. The method

used in this literature is to test three or five different ratios numerically, then choose the ratio associated with the longer discharge duration; therefore, the recommended ratios cannot be generalized. Hence, the following section suggests a general method to estimate the size of a PCM layer at the top of a thermocline.

4.3.1. Analytical method

The objective in this work is set to have the best increase in discharge efficiency because the discharge time increased with the size of the PCM layer.

Based on the definition of discharge efficiency in this work presented in (2.3.3.2), we can rearrange the discharge efficiency equation to eq.(112).

$$\eta_{discharge} = \frac{E_{discharge}}{E_{max}} = \frac{E_{max} - E_{remained}}{E_{max}} \quad (112)$$

$$E_{remained} = E_{max}(1 - \eta_{Discharge})$$

Where $E_{remained}$ is the portion of the energy that cannot be discharged due to the limitation of $\theta_{thr,d,20\%}$.

The maximum potential energy in the thermocline eq.(113) can be split into two terms based on temperature differences, high and low-grade energy eq.(114).

$$E_{max} = [V_{tank}\varepsilon(\rho Cp)_f + V_{tank}(1 - \varepsilon)(\rho Cp)_p + V_w(\rho Cp)_w](T_H - T_L) \quad (113)$$

$$E_{max} = E_{L.G} + E_{H.G} \quad (114)$$

The high-grade energy represents the potential energy between the highest temperature in the system until the discharge cut-off temperature eq.(115).

$$E_{H.G} = [V_{tank}\varepsilon(\rho Cp)_f + V_{tank}(1 - \varepsilon)(\rho Cp)_p + V_w(\rho Cp)_w](T_H - T_{thr,d,20\%}) \quad (115)$$

The low-grade potential energy illustrates the remaining potential energy from the discharge cut-off temperature until the lowest temperature in the system eq.(116).

$$E_{L.G} = [V_{tank}\varepsilon(\rho \cdot Cp)_f + V_{tank}(1 - \varepsilon)(\rho \cdot Cp)_p + V_w(\rho \cdot Cp)_w] \cdot (T_{thr,d,20\%} - T_L) \quad (116)$$

By substituting eq.(114) in eq.(112), the remained energy can be expressed by the two terms, eq.(117).

$$E_{remained} = E_{H.G} \cdot (1 - \eta_{Discharge}) + E_{L.G} \cdot (1 - \eta_{Discharge}) \quad (117)$$

The required volume of PCM to provide a specific amount of energy in a thermocline E_{PCM} can be obtained from eq.(118)[144].

$$V_{PCM} = \frac{E_{PCM}}{(1 - \varepsilon_{PCM}) \cdot [(\rho C p)_{Liq}(T_H - T_m) + L_{fus}\rho_m + (\rho C p)_{sol}(T_m - T_L)]} \quad (118)$$

The methodology suggested in this section uses two scenarios to estimate the volume of the PCM based on eq.(118). In the first one, the required energy from the PCM is set to the high-grade remained energy, while in the second one, it is set to the total remained energy (both high-grade and low-grade).

For both scenarios, the PCM layer shall replace a part of the original solid filler with the same size as its volume.

4.3.1.1. Scenario 1 recover high-grade energy

In the first scenario, the objective is to recover the high-grade energy using the latent heat of fusion of the PCM while neglecting the sensible heat stored in the PCM. This ensures extending the discharge time at a relatively constant temperature, which is the phase change isothermal temperature. So we set the required energy by the PCM to equal the remained high-grade energy, according to eq.(119).

$$E_{PCM} = E_{H.G}(1 - \eta_{Discharge}) \quad (119)$$

The volume of PCM to provide this energy can be calculated by eq.(120) calculates for the designated thermocline.

$$V_{PCM} = \frac{E_{PCM}}{(1 - \varepsilon_{PCM})[L_{fus}\rho_m]} \quad (120)$$

Figure 52 explains the steps of the direct calculation of the first scenario to estimate the PCM quantity.

4.3.1.2. Scenario 2 recover all remained energy

The second scenario assumes that the PCM provides the whole remained energy eq.(121) and it includes the sensible heat capacity of the PCM in the calculation according to eq. (118).

$$E_{PCM} = E_{remained} = E_{max}(1 - \eta_{Discharge}) \quad (121)$$

Figure 53 develops the second scenario to estimate a larger size of the PCM layer.

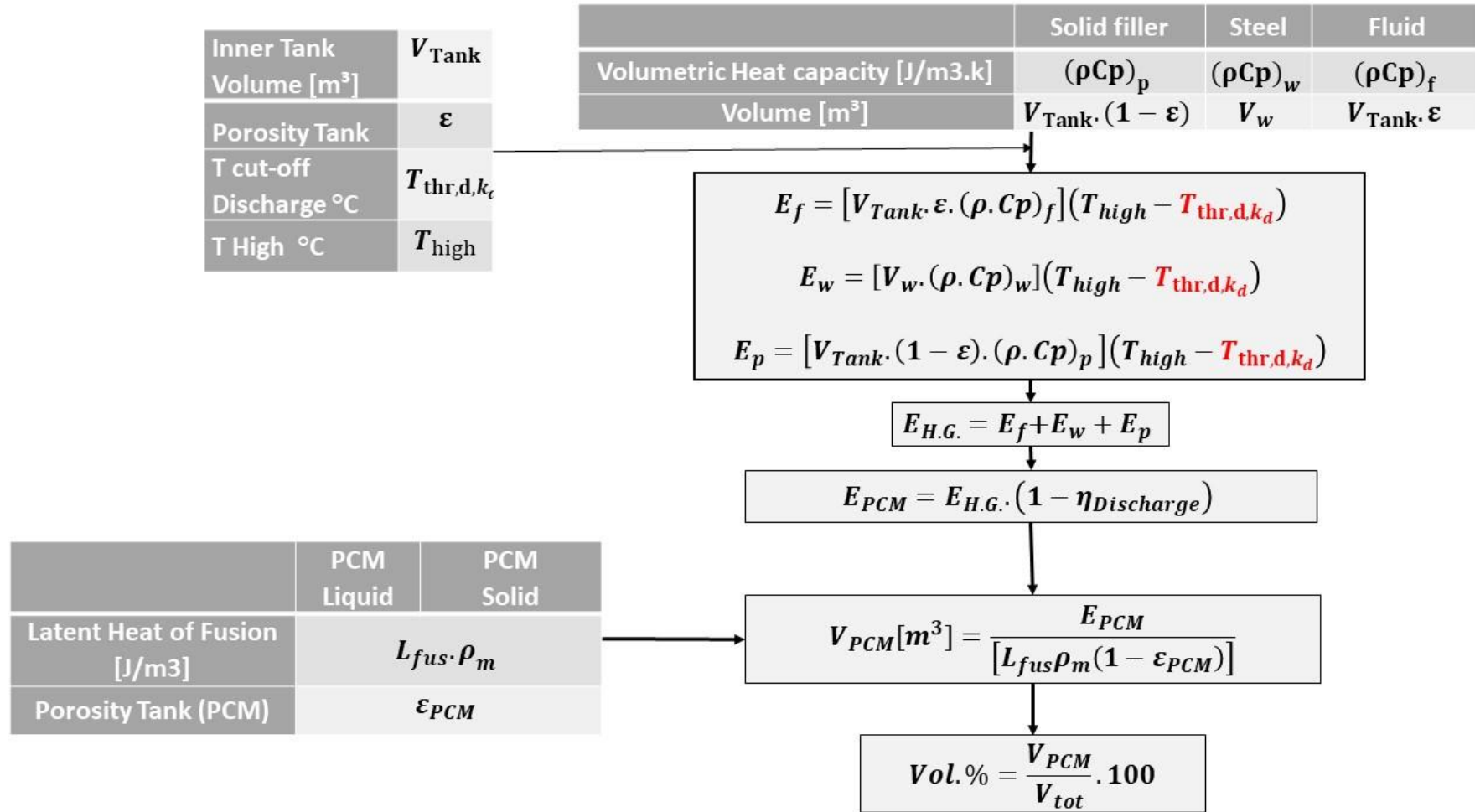


Figure 52 Scenario 1 of PCM quantity estimation based on high-grade energy

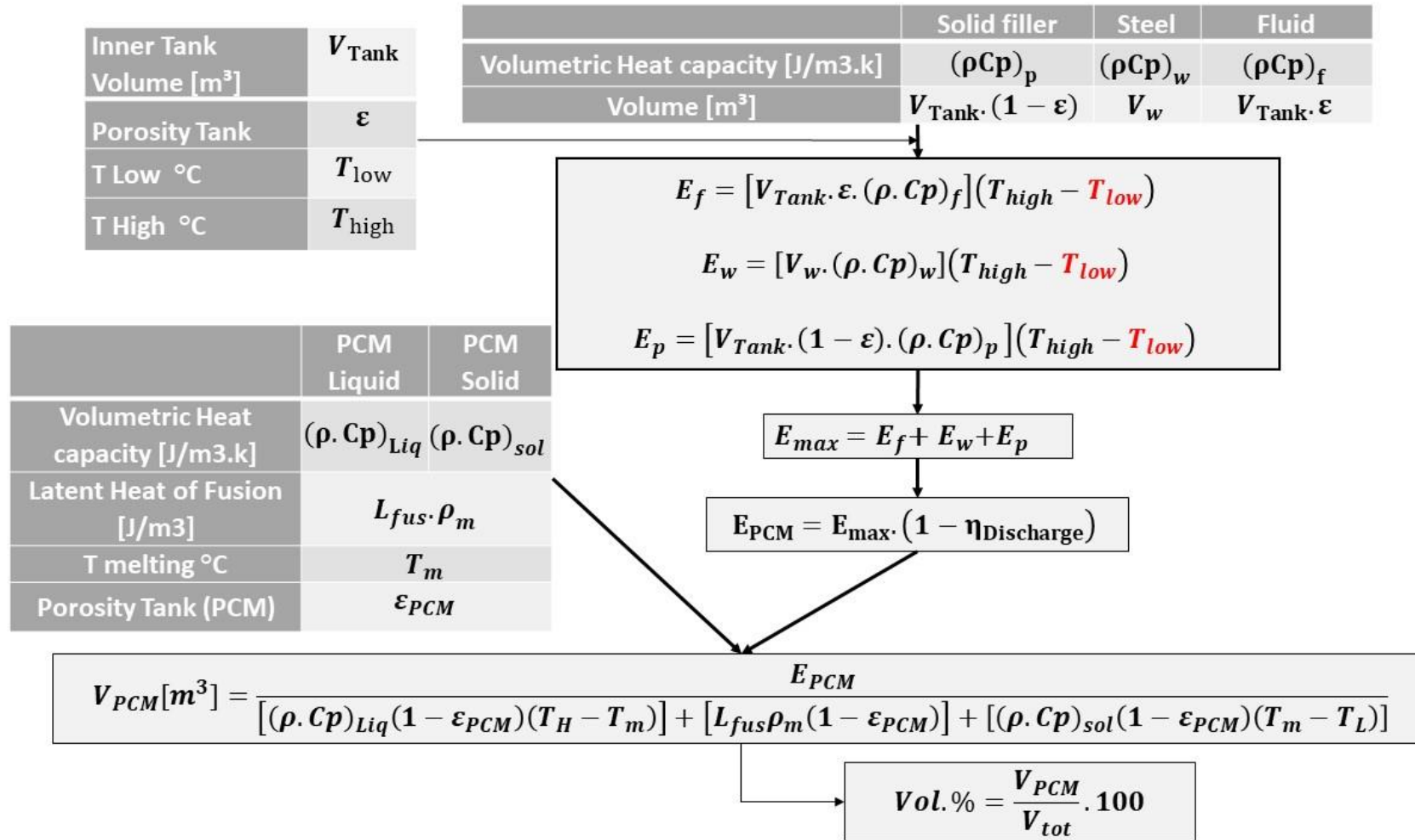


Figure 53 Scenario 2 of PCM quantity estimation based on the whole remain energy

4.3.2. Results and comparison to literature

Zanganeh et al. [46] numerically evaluated 3 PCMs at the top of a thermocline filled with rocks with three volumetric ratios 0.67 vol.%, 1.33 vol.%, and 2.67 vol.% of PCM. The HTF is air working at a temperature range between 150 and 650 °C and a cut-off temperature at 590 °C. The efficiency of discharge of the thermocline without the PCM is indicated as 92 %. Using these input data and the thermophysical properties provided by Zanganeh et al. [46], Table 35 compares the results from the two scenarios to their conclusions. It shows that the required volumetric PCM ratios, as per scenario1, are very close to the authors findings, while scenario2 ratios are higher than the paper's conclusions.

Table 35 Suggested PCM quantities for three PCMs according to Zanganeh [46], scenario1, and scenario2

T Melting [°C]	Latent heat of Fusion [kJ/kg]	Material	Conclusions	Required PCM	
				Scenario1	Scenario2
642	360	PCM1	1.33 %	1.21 %	5.54 %
632	858	PCM2	0.67 %	0.59 %	2.84 %
615	640	PCM3	0.67 %	0.78 %	3.26 %

The thermocline in Hernández et al. [163] case was filled with steel slag with air at 100 / 650 °C, the cut-off temperature is 550 °C, and the discharge efficiency is about 80 %. They simulated the discharge of a thermocline with five different PCM ratios 1, 2.5, 5, 10, and 20 vol.% at its top.

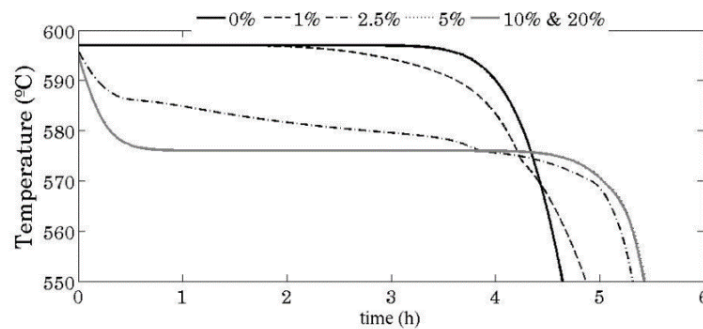


Figure 54 The thermocline outlet temperature for various PCM percentages ratios [163]

Table 36 compares the results according to scenarios 1 and 2 to Hernández et al. [163] conclusions. It indicates that the PCM ratio suggested in the paper comes in between the two scenarios values; it is almost double the scenario1 amount and about half the scenario2 amount.

Table 36 Suggested PCM quantities for the PCM according to Hernández [163], scenario1, and scenario2

T Melting [°C]	Latent heat of Fusion [kJ/kg]	Material	Conclusions	Required PCM	
				Scenario1	Scenario2
576	560	ASi12	5 %	2.33 %	9.90 %

Hernández et al. [163] argued that according to their model, the discharge time reaches its maximum value at 5 % PCM while increasing the PCM ratio to 10 %, and 20 % does not provide any significant discharge time increase, Figure 53. However, from the same figure, it can be inferred that 2.5 % has the best increase in the discharge time to PCM ratio, consequently the best gains in discharge efficiency, because doubling this amount to 5 % leads to little improvement. The 2.5 vol.% ratio is very near to scenario1 estimation.

These two comparisons show that scenario1 is a plausible method to obtain the PCM ratio analytically, with adequate discharge time and discharge efficiency.

4.3.3. Case study thermocline TES of MICROSOL-R

The two scenarios are applied in this section to estimate the required ratio of PCM for the two studied SHSMs in the thermocline TES at the MICROSOL-R, alumina spheres and Cofalit® (Table 22). The main objective is to obtain the highest increase in the discharge efficiency while extending the discharge time of the thermocline by adding a layer PCM, and the size of this layer is estimated using the two scenarios.

According to the numerical results, the discharge efficiencies are 80 % for the alumina spheres case and 86 % for the Cofalit® case (3.1.3). The PCM is NaNO₃, and the discharge cut-off temperature is 296 °C. T_H and T_L are 315 °C and 220 °C, respectively.

Table 37 Estimated ratio of NaNO₃ for alumina and Cofalit® thermoclines both scenarios

Main filler	T Melting [°C]	Latent heat of Fusion [kJ/kg]	Required PCM		T _H /T _L [°C]	T cut- off [°C]
			Scenario1	Scenario2		
Alumina	306.6	162	8.12 %	19.00 %	315/220	296
Cofalit			6.01 %	14.16 %		

Table 37 illustrates the estimated volumetric ratio of NaNO_3 for the two scenarios. It shows that both scenarios calculate higher PCM ratios for the alumina sphere thermocline than for the Cofalit® using the same PCM. Which is related to two main parameters: lower discharge efficiency and higher thermocline thermal capacity for the alumina spheres case compare to Cofalit®.

The first scenario suggests about 8.12% for the alumina spheres case and 6.01% for the Cofalit® case, and the second one indicates 19% and 14.16%, respectively. Additional case study was performed for the MICROSOL-R thermocline with additional PCMs appendix (11.4).

The next section evaluates the thermocline thermal performance at these PCM ratios and other ratios between 1 vol.% to 40 vol.%.

4.3.4. Numerical evaluation of the case study

This section applies the combined model presents in (4.2) with a PCM volumetric ratio that increases from 1 % to 40 % of the thermocline height. The numerical simulation evaluated two cases base on the two SHSMs evaluated in this work previously (3.1) alumina spheres and Cofalit®. The objective is to evaluate the performance indicators during the discharge process due to the increase of the PCM ratio and compares the findings to the ones suggested by the two scenarios discussed in (4.3.1.1) and (4.3.1.2).

The simulation uses the model input listed in Table 28, where all the storage mediums at the beginning of the discharge are at $T_{\text{high}} 315^{\circ}\text{C}$, and the HTF is entering the thermocline from the bottom at a constant mass flow and temperature $T_{\text{low}}=220^{\circ}\text{C}$. The model starts with 1 vol.% PCM ratio and performs the simulation then records the performance parameters when the thermocline outlet temperature reaches the threshold value of 296°C . The model increases the ratio by 1% and repeats the same operation until it evaluates 40 PCM layer sizes.

4.3.4.1. Combined NaNO_3 to alumina sphere-based thermocline

Figure 55 plots the discharge efficiencies against the increase of the PCM ratio. It shows that increasing the ratio of PCM increases the discharge efficiency. However, the rate of increase is not constant and could be divided into three ranges. The first range is between the first ten ratio values (1% - 10%), where the discharge efficiency has the largest increase, about 5% from 81.4% up to 86.2%. The second range is between second 7 ratios (11% - 17%) the discharge efficiency

increased only by 1% from 86.5% to 87.5%, thereafter the increase is about 1.5% in the remaining 28 ratios between (18% - 40%).

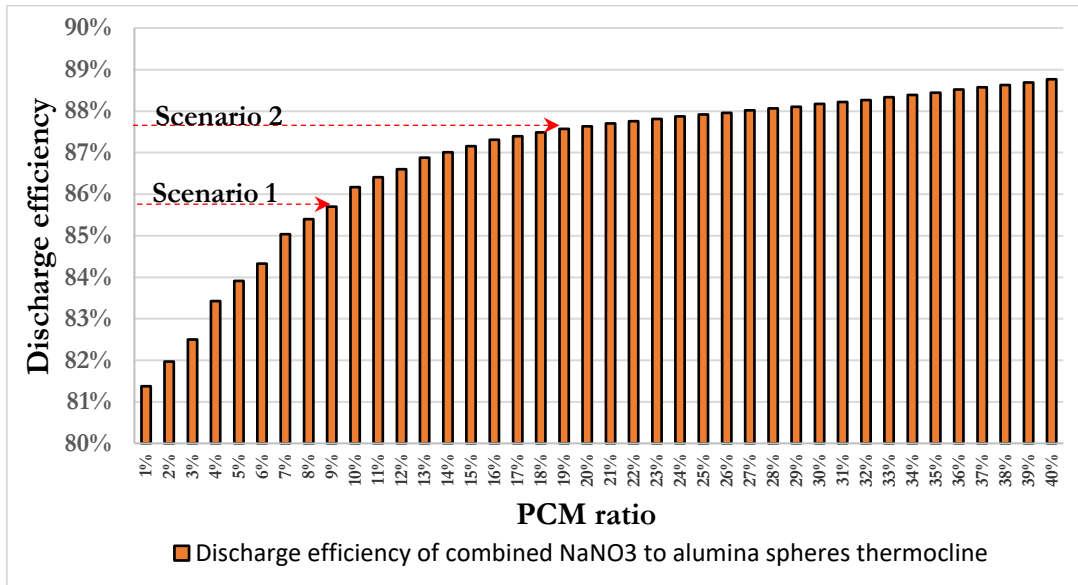


Figure 55 discharge efficiency versus PCM ratios for combined NaNO₃-alumina sphere thermocline

Scenario1 estimated the suitable PCM ratio of 8%, which corresponds to 85.4% discharge efficiency. This ratio is near the maximum limit of the first range (1% - 10%). While the value estimated by scenario2 is 19% resulted in 87.5% discharge efficiency, the latter ratio is located near the lower limit of the third range of (18% - 40%).

Hence, it could be suggested that senario1 and senario2 estimate a range of PCM ratios for a combined PCM to sensible heat storage thermocline. The first one is associated with the best discharge efficiency increase. While exceeding the second one will not have a significant impact on the discharge efficiency.

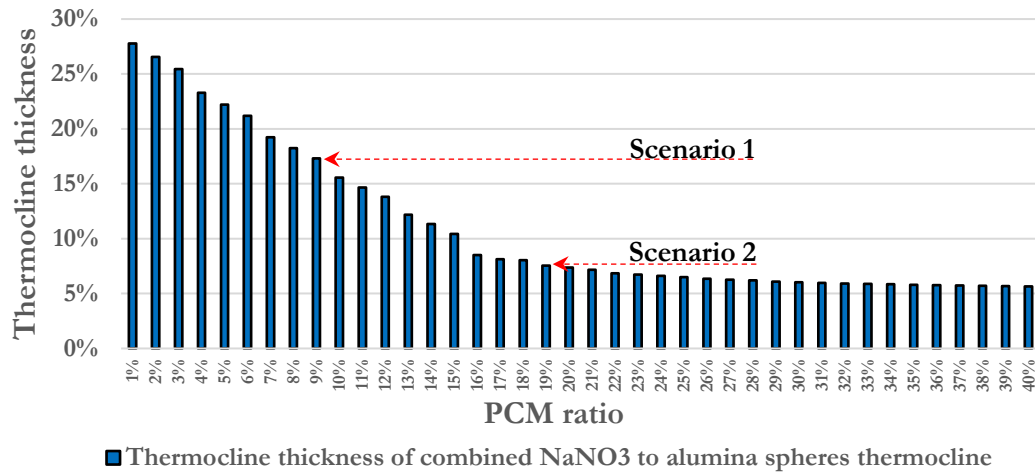


Figure 56 thermocline thickness during discharge versus PCM ratios for combined NaNO₃-alumina sphere thermocline

Figure 56 plot the resulted thermocline thickness during discharge against the PCM ratios. It shows the thickness decreased from 27% to 8.5% when the PCM ratio increase from 1% to 16%, respectively. After that, the thickness remained relatively constant at about 6% for the rest of the tested PCM ratios. The thermocline thicknesses associated with the PCM ratio of scenario1 and scenario2 are 17% and 7.5%, respectively.

The discharge time increases with the PCM ratio as illustrated in Figure 57, which is attributed to the increment of the thermal capacity of the thermocline when increasing the layer size. While other parameters remain unchanged during the simulations, such as the mass flow rate, the sphere diameter, and the TES tank size.

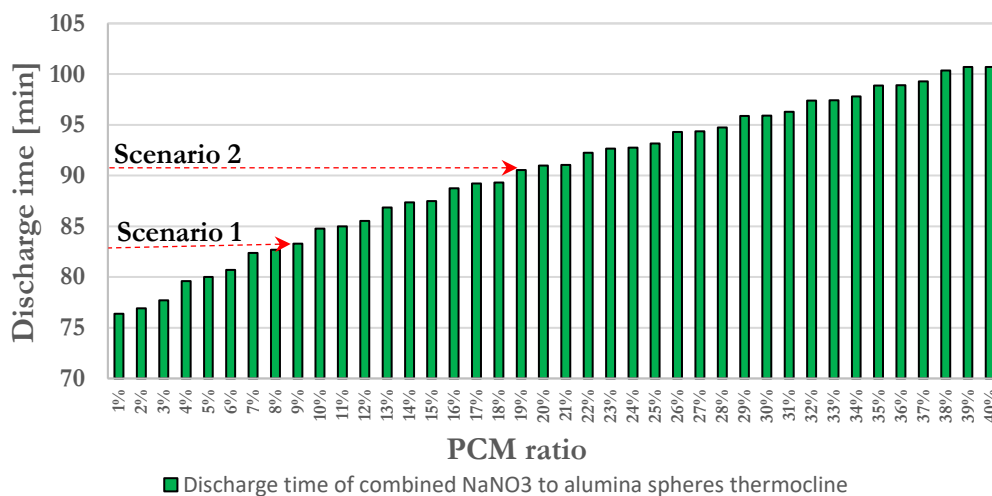


Figure 57 discharge time versus PCM ratios for combined NaNO₃-alumina sphere thermocline

These numerical results indicate that the analytical scenarios can find a range of recommended PCM ratios for the alumina sphere case [8% -19%]. The lower limit corresponds to the best increase of discharge efficiency, and the higher limit is associated with a slightly higher discharge efficiency and significantly better thermocline thickness. The discharge time always increases with the PCM ratio.

4.3.4.2. Combined NaNO₃ to Cofalit®-based thermocline

For a thermocline filled with Cofalit®, Figure 58 reflects the increase in the discharge efficiency in response to the increase in the PCM ratio. It shows that the discharge efficiency increased steadily for a PCM ratio between 1 % and 12 %, and from 86.7% to 89%, respectively. After that, the discharge efficiency is slowly increased from 89% up to 90% between the range of ratios (13% -40%).

The estimated discharge efficiency corresponding to scenario1 and scenario2 for Cofalit® based thermocline are 87.9% and 89%, respectively. Exceeding the estimated ratio of scenario2 does not reflect any significant improvement of the discharge efficiency.

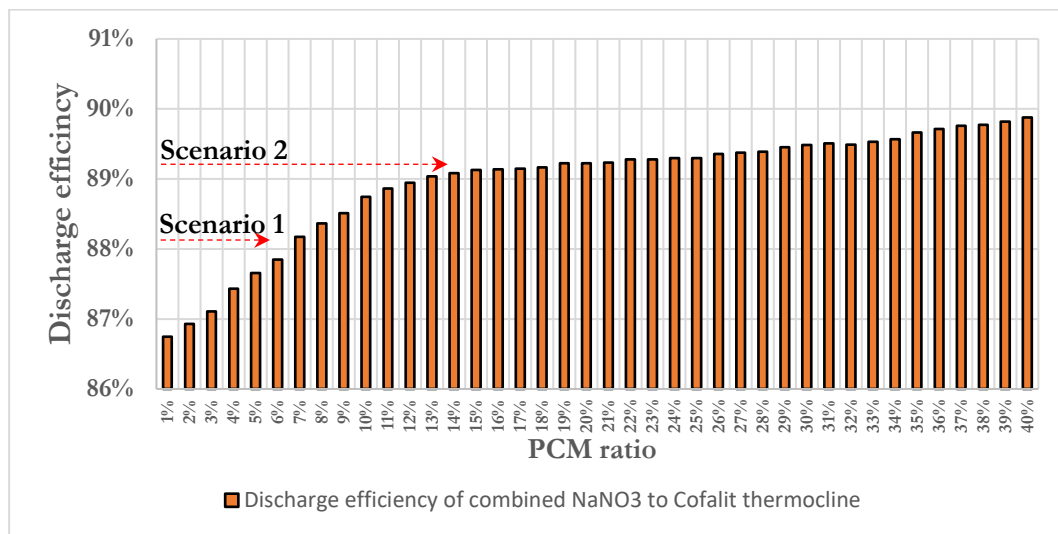


Figure 58 discharge efficiency versus PCM ratios for combined NaNO₃-Cofalit® thermocline

The resulted thermocline thickness from the simulation for each PCM ratio is plotted in Figure 59. It shows that the thermocline thickness reduced with the increase of PCM ratio from 1% to 12%. Furthermore, the thermocline thickness remains relatively constant at about 6% for the rest of the tested ratios.

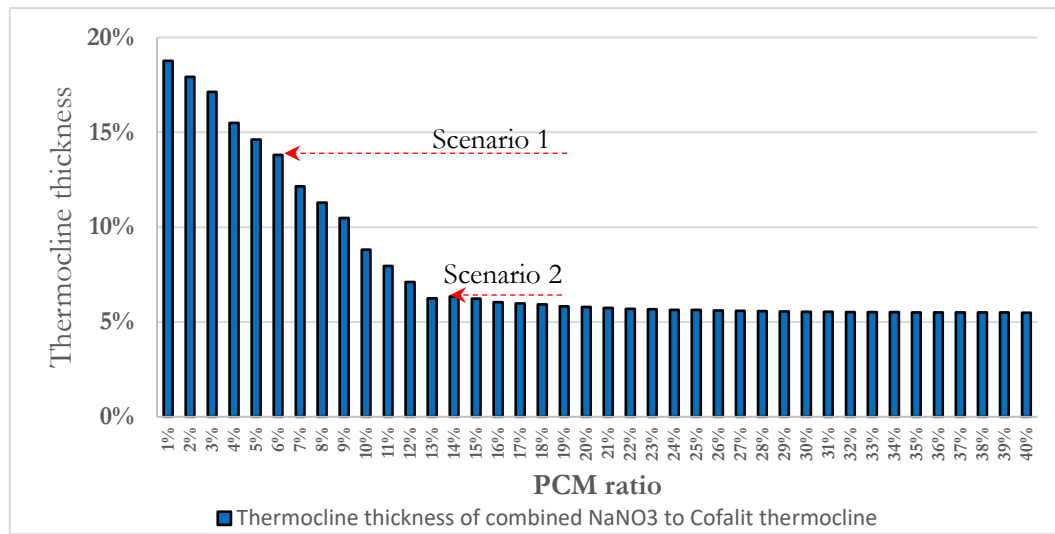


Figure 59 thermocline thickness during discharge versus PCM ratios for combined NaNO₃-Cofalit® thermocline

Similar to the alumina spheres case, the discharge time in the Cofalit® based thermocline increases with the increase of the PCM ratio.

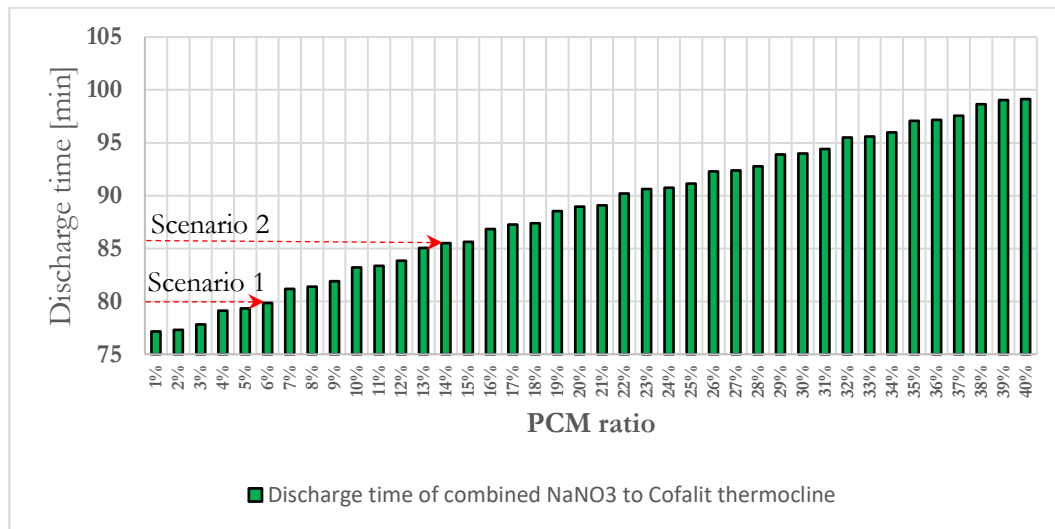


Figure 60 discharge time versus PCM ratios for combined NaNO₃-Cofalit® thermocline

Figure 58 and Figure 59 suggest that a 12 % PCM ratio has the best discharge increase and lower thermocline thickness for the Cofalit® case. This ratio is between the range estimated by scenario 1 and 2 [6 % - 14 %], respectively.

The suggested PCM-layer sizing approach in this work (4.3.1) provides a quick and general method to estimate a range of recommended volumetric PCM ratios to improve the discharge efficiency of a thermocline TES. The method applies the design parameters of any given thermocline to calculate two PCM

ratios. The lowest value is expected to result in the highest increase in discharge efficiency while selecting the highest ratio should ensure having the best increase in discharge efficiency and lower thermocline thickness. The discharge time increases with the increase of the PCM ratio.

However, this method is not an optimization method. For example, it could help estimate the quantity of PCM, while using this amount efficiently in the thermocline is a more complex process. Furthermore, achieving an optimum ratio of PCM is not a clear-cut answer in this work. It depends on additional factors such as the cost of PCM materials, the cost of the envelope, the envelope shape, and the cost of PCM-envelope production compared to the benefits of using this PCM layer (techno-economic feasibility study).

4.4. CONCLUSIONS

The C-S model provides an excellent solution to simulate the thermal behavior of a thermocline filled with solid filler where the $Bi < 0.1$. At the same time, the D-C model is better for the cases where $Bi > 0.1$.

The enthalpy porosity method (EPM) affords a reliable way to model the melting/solidification compared to the effective heat capacity.

The validity of the D-C EPM model is checked with experimental findings from the literature.

A C-S model is coupled to a D-C EPM model to simulate the thermal behavior of a combined 25% NaNO_3 to 75% alumina spheres thermocline.

The performance of the combined thermocline is improved compared to the SHSM only case during the discharge. The (25% NaNO_3 -75% alumina spheres) thermocline exhibits a 13% better discharge efficiency, a 70% lower thermocline thickness, and a 21% a longer discharge duration than the 100% alumina spheres case. The charge performance was very similar between the two evaluated cases.

A general and fast sizing approach is suggested to estimate a range of recommended PCM ratios for a combined thermocline. A good agreement was found between literature conclusions and results from this method.

It was found that a ratio of NaNO_3 between 8.5% and 19% is recommended for the alumina spheres based thermocline, and a range between 6.5% and 14.5% for the Cofalit® case.

5. EXPERIMENTAL AND NUMERICAL EVALUATION OF COMBINING LATENT HEAT LAYER TO SENSIBLE HEAT THERMOCLINE TES

This chapter evaluates experimentally a thermocline TES filled with alumina spheres as SHSM and a PCM layer, where it covers the following aspects:

- The development of the PCM layer design from spheres to tubes, taking into account the compatibility between various materials.
- The model modification to fit the PCM layer design change and the model validated from the experimental results.
- An experimental evaluation of the thermocline with a PCM layer at its top, at various HTF mass flow rates and temperature differences.
- A numerical comparison of the thermal behavior between the combined solution and a 100% alumina spheres-filled thermocline.

5.1. PCM LAYER DESIGN

The PCM layer design process involves a material selection for both the PCM and its envelope, selecting the envelope shape and dimensions, safety analysis for the selected material, tuning of the final design, and the details of the fabricated layer.

5.1.1. Material selection

5.1.1.1. PCM

The most suitable material as PCM for this work is found to be sodium nitrate (NaNO_3), which has a reported melting temperature of about 306°C in the literature [191][45], and available on the local market at a low price and suitable purity $>99\%$ [44].

A sample of 31.61 mg of NaNO_3 (Commercial grade purchased for this work) is analyzed using the differential scanning calorimetry (DSC). The sample was heated at a constant rate of $10^\circ\text{C}/\text{min}$ from 30°C up to 400°C then cooled down at the same rate. The heat flow curve from the DSC (Figure 61) confirms that NaNO_3 has about 169 kJ/kg latent heat of fusion, and the material melted at 307°C and solidified at 304.3°C .

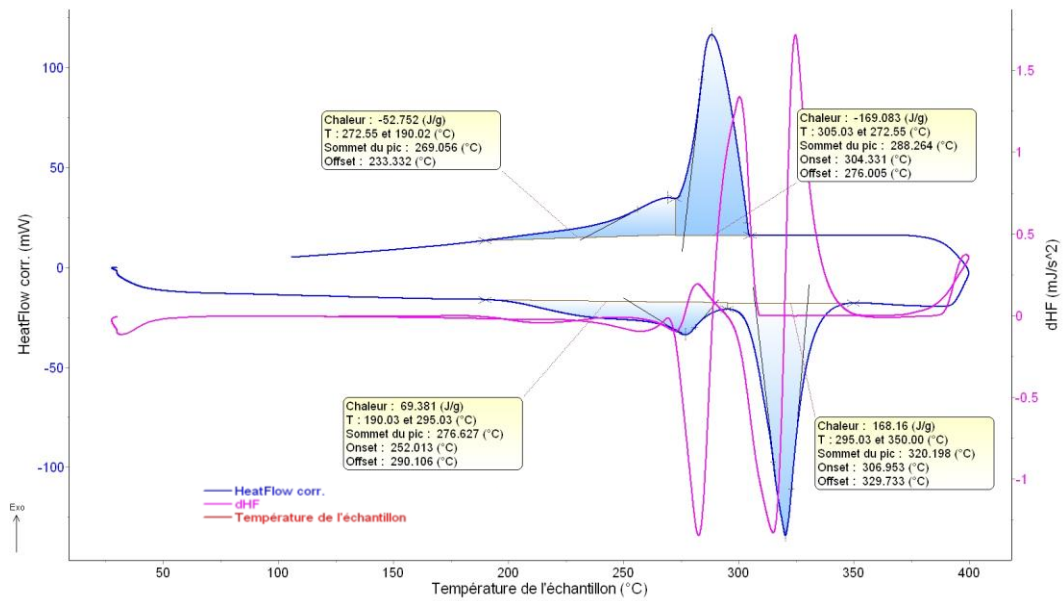


Figure 61. DSC results for the commercial NaNO_3

5.1.1.2. Envelope

Stainless steel SS304 meets the criteria of envelope selection (Table 9). It was used as capsule materials with NaNO_3 at a working temperature of 350°C [11][56]. Furthermore, Goods et al. [55] confirmed that the SS304 metal decay rate is 6-15 $\mu\text{m}/\text{year}$ when using a mixture of NaNO_3 and KNO_3 at 570°C. This low rate of degradation of SS304 with NaNO_3 entitled it to be used for long term service following Table 38 [34]. The table indicates a recommended service life of any material based on its weight loss rate due to corrosion.

Table 38 Guide for corrosion weight loss used in the industry

mg/cm ² year	mm/ year	Recommendation life time
>1000	2	Completely destroyed within days
100 to 999	0.2 - 1.99	Not recommended for service greater than a month
50 to 99	0.1 - 0.19	Not recommended for service greater than one year
10 to 49	0.02 - .09	Caution recommended on the specific applications
0.3 to 9.9	-	Recommended for long term service
<0.2	-	Recommended for long-term service: no corrosion other than because of surface cleaning was evidenced.

Moreover, the stainless steel is currently widely used in heat exchangers with various solar salts as HTF in several operational CSP plants [201][202].

5.1.2. Encapsulation design

In the previous chapter, we suggested that the thermocline filled with alumina spheres needs about 8.5% volumetric ratio of NaNO_3 to obtain the best discharge increases and to extend the discharge time accordingly. Hence, the required number of PCM spherical containers can be calculated considering the following design constraints: the outer diameter of the PCM spheres is 2 cm, the thickness of the envelope is 1mm, the bed porosity is 0.485, and the sphere contains 15 % air to cope with the thermal expansion of the PCM [203].

Table 39 calculates the corresponded number of spheres to the 8.5% ratio PCM for various diameters 2, 4, 6, and 8 cm. It illustrates that this experiment needs about 111000, 12000, 3305, and 1359 spheres, respectively.

We could not find any commercially available stainless steel spheres filled with NaNO_3 (ref: figure 1 Commercial suppliers for encapsulated) for this work.

Table 39 the estimated number of spheres to fulfill the 8.5% PCM volumetric ratio of the thermocline

D_{out} [mm]	D_{in} [mm]	air/ Sphere [%]	ε	PCM Ratio [%]	PCM Volume [m³]	Inner Volume [m³]	Number of spheres
20	18	10%	0.485	8.5%	2.87E-01	2.6E-06	110555
40	38					2.44E-05	11750
60	58					8.68E-05	3305
80	78					2.11E-04	1359

The encapsulation design was revised to a more feasible and attainable solution: using tubes, due to the large sphere numbers and the limited time and budget to fabricate a customized solution.

Wei et al. [174] concluded that spheres have the best thermal performance, followed by horizontal tubes, flat plates, and vertical tubes. Therefore, this work considers a horizontal-tube design because it should provide the second-best thermal performance after the spheres.

Figure 62 illustrates the tubes' preliminary design at the upper thermocline basket, where the containers are placed in a staggered position. The concept is used by Zanganeh et al. [171].

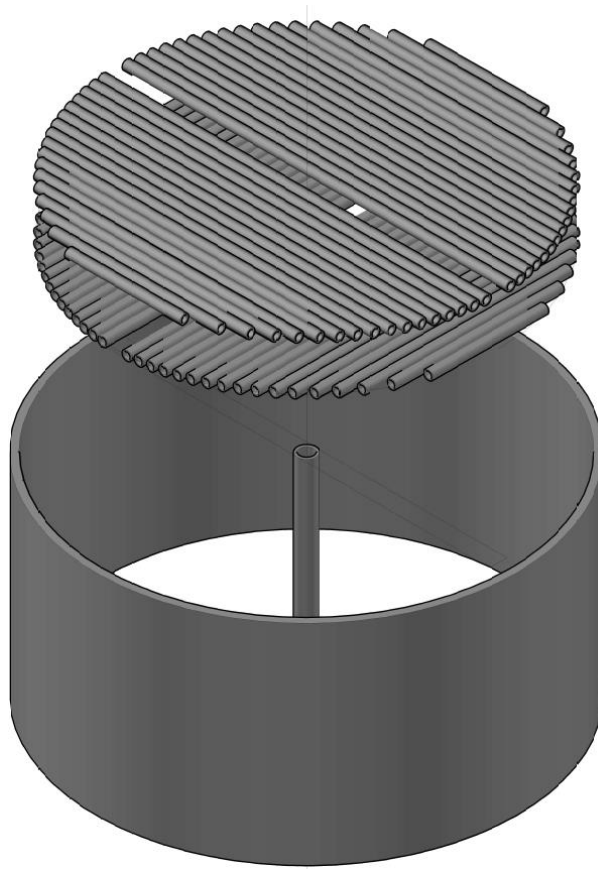


Figure 62. Tubes design of the PCM capsules for the topmost basket inside the thermocline

5.1.3. Tube dimensions

There are many SS304L pipes options in the market with various diameters and thicknesses (Appendix 11.5). For our evaluated case, the tube thickness should be the minimum value that maintains the tube mechanical integrity, which minimizes the envelope thermal resistance and increases the container's internal volume. We selected a 1.6 mm tube thickness and subjected it for further analysis.

To select a suitable tube diameter for this experiment, a model was developed that uses the commercial datasheet of the tubes and the thermocline design data to calculate the following: porosity in the PCM layer, the dimensions of each tube in the row, the ratio of the mass of PCM/envelope material, and the final height of the layer. The model assumes the following to evaluate the thermal resistance of the filled tubes:

- The PCM layer is a heat exchanger consisting of tubes placed in staggered positions in crossflow.
- Operating temperatures are ($T_{\text{high}} = 315^{\circ}\text{C}$), ($T_{\text{thr,d,kd}} = 296^{\circ}\text{C}$), and ($T_{\text{m}} = 306^{\circ}\text{C}$) during discharge process.

- Constant flow rate as well as inlet temperature of HTF.
- Uniform density and thermal conductance for the PCM during the phase change process.
- There is no fouling due to oil contamination.
- The PCM occupies 85% of the tubes' inner cavity in a concentric manner (Figure 63).

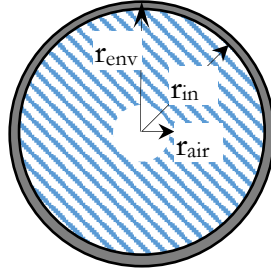


Figure 63. PCM concentric distribution inside the tubes

The global thermal resistance of the tubes is evaluated from Eq.(122).

$$R_{tot} = R_{conv.} + R_{env.} + R_{PCM} \quad (122)$$

Eq.(123), eq.(124), and eq.(125) calculate the three thermal resistances.

$$R_{env.} = \frac{\ln(r_{env}/r_{in})}{2 \cdot \pi \cdot k_{env} \cdot L_{tot, n \text{ rows}}} \quad (123)$$

$$R_{PCM} = \frac{\ln(r_{in}/r_{air})}{2 \cdot \pi \cdot k_{PCM} \cdot L_{tot, n \text{ rows}}} \quad (124)$$

$$R_{conv.} = \frac{1}{h_{env} \cdot A_{env}} \quad (125)$$

Eq.(126) estimates the global heat transfer coefficient of the layer.

$$h_{env} = \frac{Nu \cdot k_f \cdot T_{avg}}{d_{env}} \quad (126)$$

The model uses the Zukauskas correlation to obtain Nu number eq.(127) [173].

$$Nu = C_{row} \cdot C_{Re} \cdot Re_{max}^m \cdot Pr_{f, T_{avg}}^{0.36} \cdot \left(\frac{Pr_{f, T_{avg}}}{Pr_{f, T_m}} \right)^{0.25} \quad (127)$$

$$\left(\begin{matrix} C_{Re}=0.27, m=0.6: Re_{max} \geq 1000 \\ C_{Re}=0.51, m=0.5: Re_{max} < 1000 \end{matrix} \right) v_{f, max} = v_f \frac{S_T}{S_T - d_{env}}$$

S_T is the distance between two consecutive tubes in the same row.

C_{row} is the correction factor for the number of rows below 20, as per (Table 40).

Table 40. Number of rows correction factor [173]

N_L	1	2	3	4	5	7	10	13	16
Aligned	0.7	0.8	0.86	0.9	0.92	0.95	0.97	0.98	0.99
Staggered	0.64	0.76	0.84	0.89	0.92	0.95	0.97	0.98	0.99

N_L is the number of rows.

Furthermore, the model applies eq.(128) to calculate the shape factor [171].

$$a_s = \frac{A(tot)_p}{V_{tot}} = \frac{\frac{V_p}{L_{ch}}}{\frac{V_{tot} - V_f}{L_{ch}}} = \frac{(1 - \varepsilon)}{L_{ch}}$$

$$L_{ch} \stackrel{\text{def}}{=} \frac{\text{Area}}{\text{Volume}} : \text{for tubes } \frac{\pi \cdot d_{env} \cdot L_{tube}}{\frac{\pi \cdot d_{env}^2}{4} \cdot L_{tube}} = \frac{4}{d_{env}}$$

$$a_s = \frac{4(1 - \varepsilon)}{d_{env}} \quad (128)$$

Table 41 illustrates the results according to each tube size. It shows that the porosity reduces with the tube diameter increase, the corresponding total reduction in porosity is 10% of the smallest tube diameter. Moreover, the PCM-to-envelope mass ratio increases steadily from 48% in the smallest tube size to 77.8% in the largest one. Furthermore, the shape factor, which represents the heat exchange area, degrades with increasing the tube diameter. In contrast, the total number of required tubes that represents the cost of production reduces.

Table 41. Calculated PCM parameters based on the commercial data of pipe

d_o [mm]	21.3	26.7	33.4	42.2	48.3	60.3	73	88.9	101.6	114.3
Porosity ε	0.462	0.440	0.426	0.419	0.411	0.409	0.410	0.430	0.416	0.431
No. Rows in the layer	31	23	17	13	11	9	8	6	5	5
Length of tubes [m]	1128	695	421	258	193	127	93	55	41	36
Layer height [mm]	815.3	729.1	652.8	613.6	586.3	587.7	624	563.4	533	596.5
No. of tubes to fabricate	1240	782	476	286	220	144	112	60	50	40
Final PCM/Tank vol. [%]	8.6%	8.9%	8.9%	9.1%	9.1%	8.8%	9.6%	8.8%	8.7%	9.7%
Shape factor [m²/m³]	187.8	149.8	119.8	94.8	82.8	66.3	54.8	45.0	39.4	35.0
Area of heat exchange[m²]	64.2	51.3	39.9	31.6	27.4	21.9	19.6	14.4	12.4	12.2
PCM/envelop mass[%]	48.0%	53.8%	56.5%	60.3%	63.8%	66.8%	70.1%	72.7%	75.0%	77.6%
R_{env.} [m.K/W]	1.44E-06	1.83E-06	2.38E-06	3.04E-06	3.53E-06	7.54E-06	9.33E-06	1.28E-05	1.49E-05	1.52E-05
R_{PCM.} [m.K/W]	2.27E-04	3.69E-04	6.08E-04	9.93E-04	1.33E-03	2.02E-03	2.75E-03	4.62E-03	6.19E-03	7.14E-03
R_{tot.} [m.K/W]	3.71E-04	5.59E-04	8.67E-04	1.32E-03	1.70E-03	2.47E-03	3.25E-03	5.31E-03	6.97E-03	7.93E-03

Figure 64 plots the thermal resistances of the envelope, PCM, and the total thermal resistance, according to eq.(122) for each diameter. It shows that the low conductivity of the PCM governs the overall thermal resistance, while the thermal resistance of the envelope material is negligible compared to the PCM

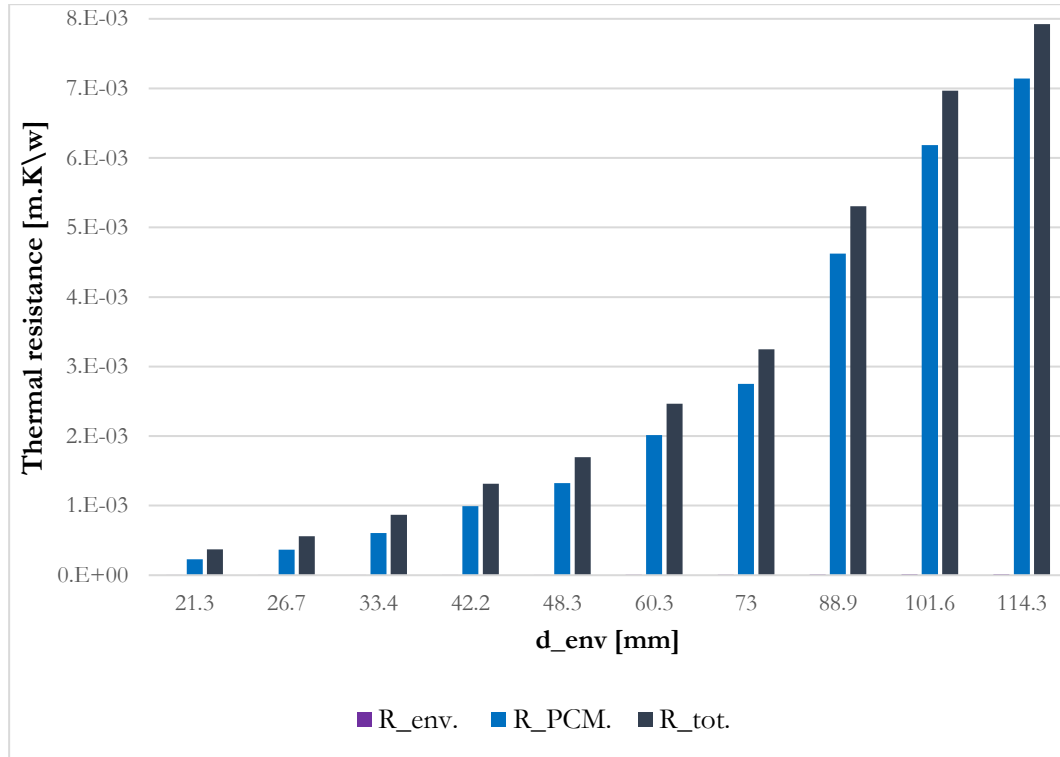


Figure 64. Envelope, PCM, and total thermal resistances for the evaluated tubes

To facilitate the selection, Figure 65 plots the total number of tubes in the layer, the shape factor, and the overall thermal resistance for each diameter normalized by the maximum value to the related parameter.

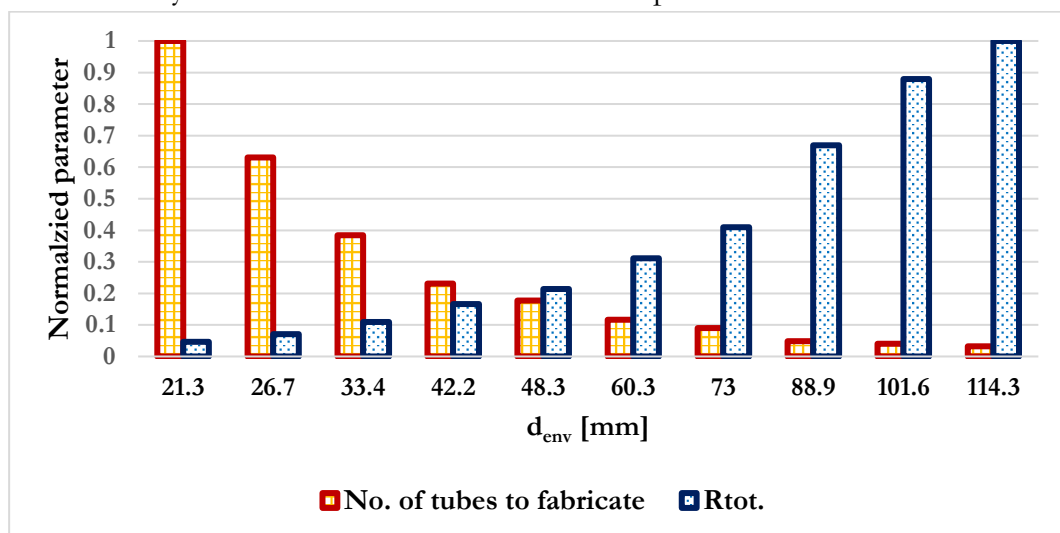


Figure 65. Normalized parameters for each tube diameter

It illustrates that the two sizes, 42.2 mm and 48.3 mm, have a reasonable number of tubes and relatively low thermal resistance. Small diameters of 21.3, 26.7, and 33.4 mm require many fabrications of cells 1128, 695, 421, respectively. Moreover, a big diameter of 88.9, 101.6, and 114.3 mm has significantly higher thermal resistance than the smaller sizes. Hence, the tube diameter of 48.3 mm is selected for this work, which corresponds to PCM layer of 11 rows, each of them has 20 various tubes size, 9.1 vol.% PCM to tank volume and about 64% PCM to envelope material ratio (Table 41).

5.1.4. Safety Analysis

The main concern when using the NaNO₃ with the synthetic oil Jarytherm® DBT is fire because sodium nitrate is considered “class I oxidizers” which is the minimum out of four hazard classes [204], and the oil is fuel. Therefore, two analyses were performed to ensure a low level of risk. The first one is to evaluate the integrity of the tube to withstand the internal pressure from the PCM density change between solid to liquid and minimize potential leakage. The second one is to evaluate the just-in-case scenario of accidentally mixing the two materials.

5.1.4.1. Internal pressure

The maximum allowable internal pressure for a cylindrical container can be calculated from hoop stress eq.(109)[205].

$$P_{max} = 2 \cdot SE \cdot \frac{e_{tube}}{d_o} \quad (129)$$

e_{tube} : the thickness of the tube.

SE: is the maximum allowable stress for the materials

SE = 0.85 TS/4: TS: tensile strength of the material.

From eq. (109), a 48.3 mm diameter, 1.6 mm SS304 tube can tolerate up to 47 bar. The maximum pressure expected inside the container due to the density difference between the solid and the liquid phase is estimated from eq.(130)[33], which neglects the envelope material's thermal expansion.

$$P_{max} = P_{atm} \left(\frac{V_{void} - \frac{m_{PCM}}{\rho_{sol}}}{V_{void} - \frac{m_{PCM}}{\rho_{liq}}} \right) \quad (130)$$

An air volume is suggested to allow the PCM to expand without stressing the tube's wall. The air ratio is defined as the ratio of air volume to the inner volume of the encapsulation expressed in vol.%.

Figure 66 plots the internal pressure within a 48.3 mm outer diameter SS304 tube of 1.6mm thickness against various air ratios. It confirms that NaNO_3 must have a minimum of 10.7 % air ratio to avoid exceeding the maximum allowable pressure for this type of tube [206].

An air ratio of 14% is selected for the current work to allow maximum PCM filling while maintaining a reasonable pressure allowance margin. Moreover, the expected working pressure at this ratio (5 bar) is far below the 16 bar supplier recommended value of working pressure for the threaded end-cap.

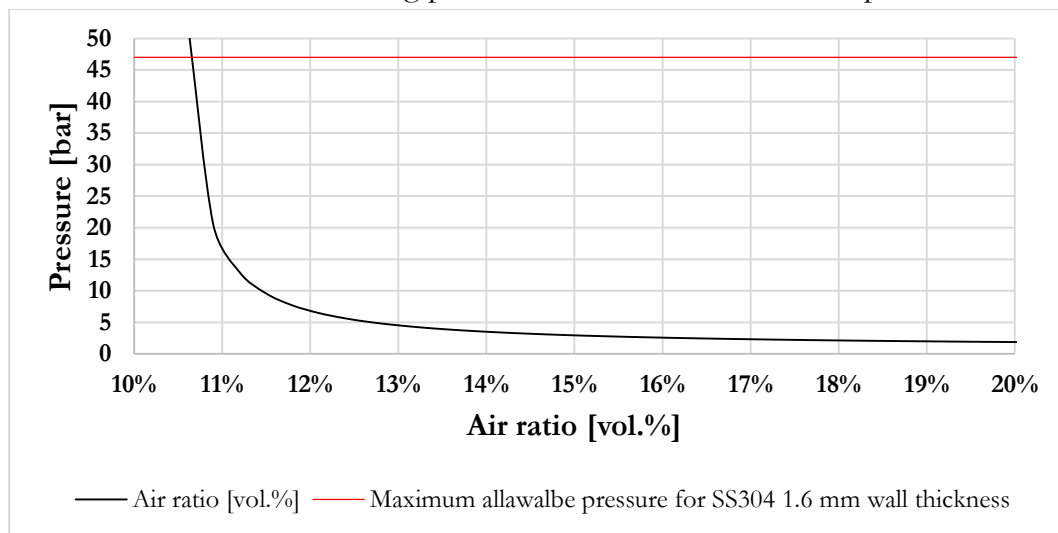


Figure 66. Internal pressure versus air ratios of NaNO_3 fill SS304 48.3/45.1 tube

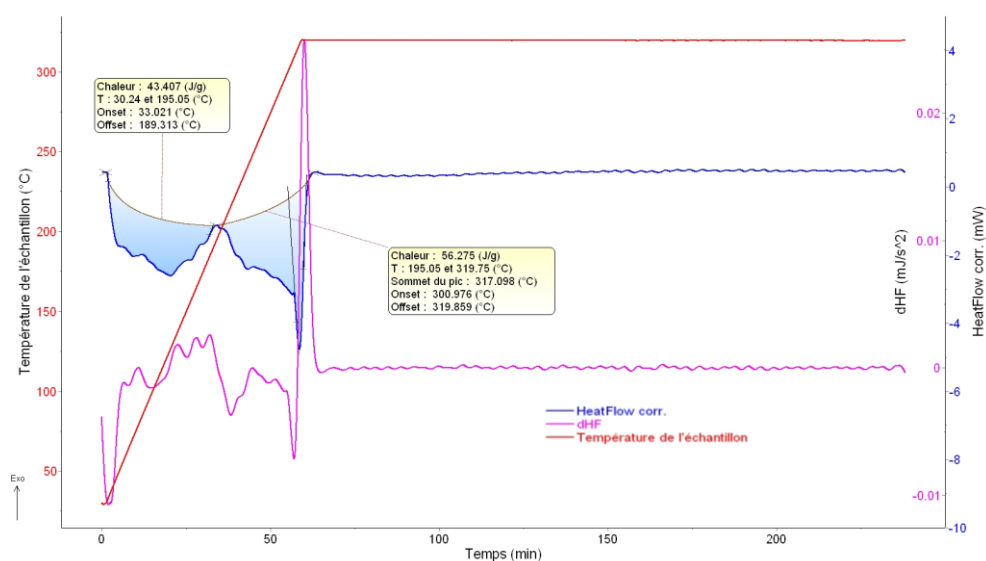
5.1.4.2. NaNO_3 and HTF compatibility

Pacheco et al. [12] evaluated the Therminol® as HTF and NaNO_3 as SHSM. They concluded that any fire incident's primary cause would be mixing the hot oil vapor with Oxygen from the air, while "accidentally mixing the two components should not create combustion". Moreover, NaNO_3 is thermally stable with a harmless formation of nitrite (NaNO_2) and Oxygen (O_2) at 380 °C at atmospheric pressure [206][207]. Furthermore, the leading cause of nitrate salts explosion is ascribed to the ammonia nitrate and not to NaNO_3 or KNO_3 [204].

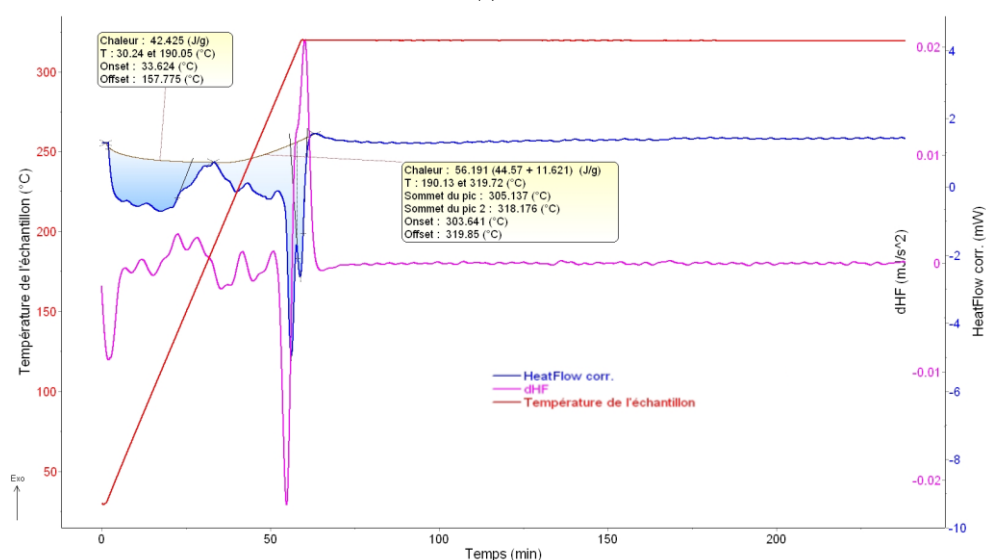
Although no direct contact between the PCM and oil is ensured in this experiment (5.1.1.2)(5.1.2), The reactivity of mixing NaNO_3 with Jarytherm® oil is investigated. Two analyses are performed. The first simulates a PCM leakage into

the HTF with a weight ratio of 9% NaNO₃ to 91% oil. The second one simulates a small oil into the PCM encapsulation with a weight ratio of 84% NaNO₃ to 16% oil.

The first analysis tests (100% oil) and (91 wt.% oil- 9 wt.% NaNO₃) in the DSC. The temperature was increased at a constant rate of 5°C/min up to 320°C and maintained for 180 min. During the test, no exothermic reaction is observed. Furthermore, the DSC measurements showed no abnormalities between the two samples, Figure 67 (a) & (b), respectively. A slight peak appears in heat flow (Figure 67 (b)) in the PCM mixed sample, which is attributed to NaNO₃ melting.



(a) 100% oil

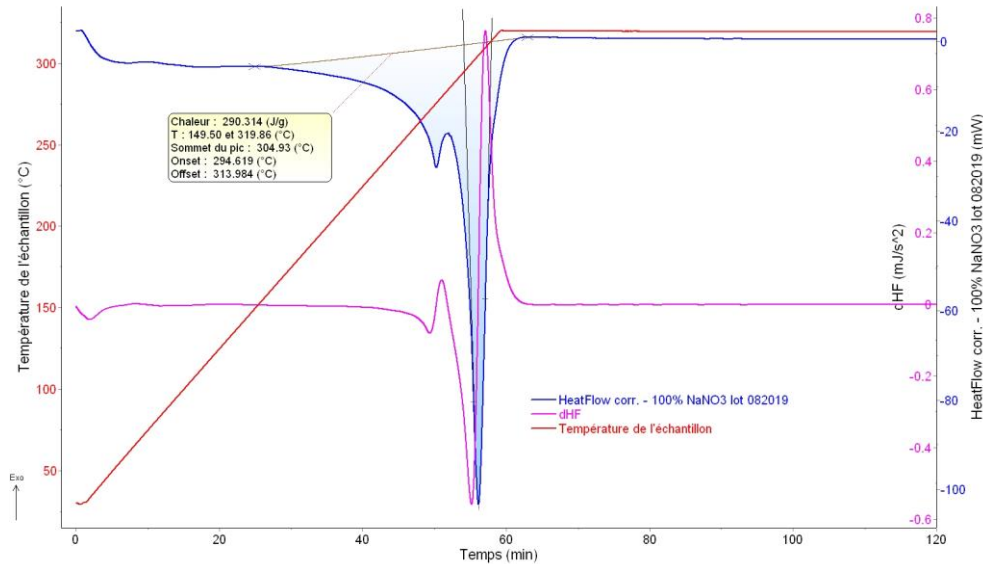


(b) 91% Oil 9%NaNO₃

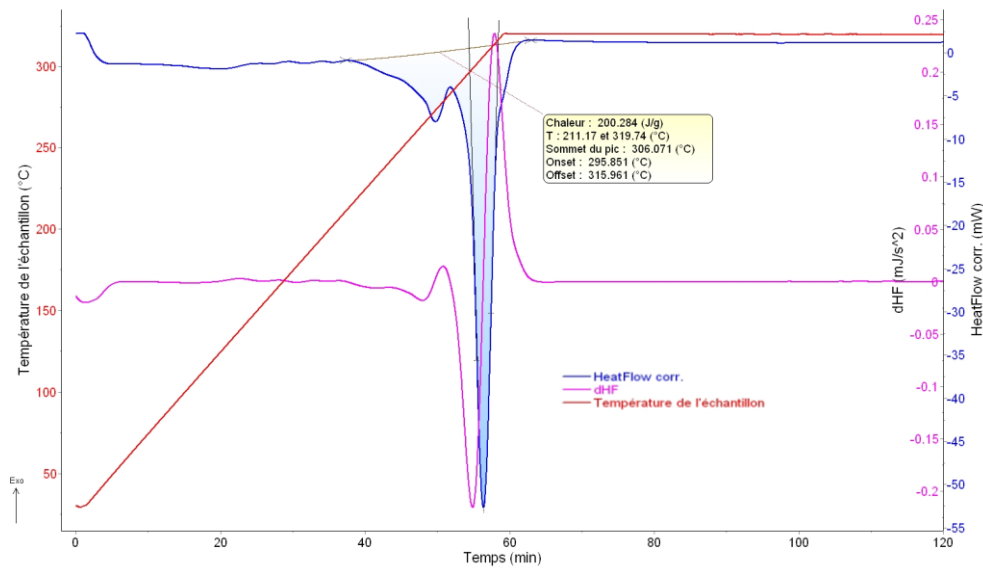
Figure 67. DSC measurements (a) 100% Oil (b) 91%wt.Oil-9%wt.NaNO₃

For the second analysis, the two tested samples are (100% NaNO₃) and (16 wt. % oil 84 wt. % NaNO₃). The DCS parameters are the same applied in the first

analysis. Figure 68 compares the heat flow between the two samples. There is no exothermic reaction, moreover, the 100% PCM sample has a bigger overall heat than the mixed sample due to its bigger thermal capacity.



(a) 100% NaNO₃



(b) 16% Oil 84% NaNO₃

Figure 68. DSC measurements (a) 100% NaNO₃ (b) 86%wt. NaNO₃-16%wt.Oil

5.1.5. Detailed design

The rows number has been revised to 7 instead of 11 for the 48.3 mm diameter tubes for limited budget reasons in the final design. The resulting volumetric ratio of PCM is 5.5% instead of the initial 8.5%. Figure 69 illustrates

the PCM layer's final design with ten different tubes length; each of them must be repeated 14 times, resulting in 140 tubes.

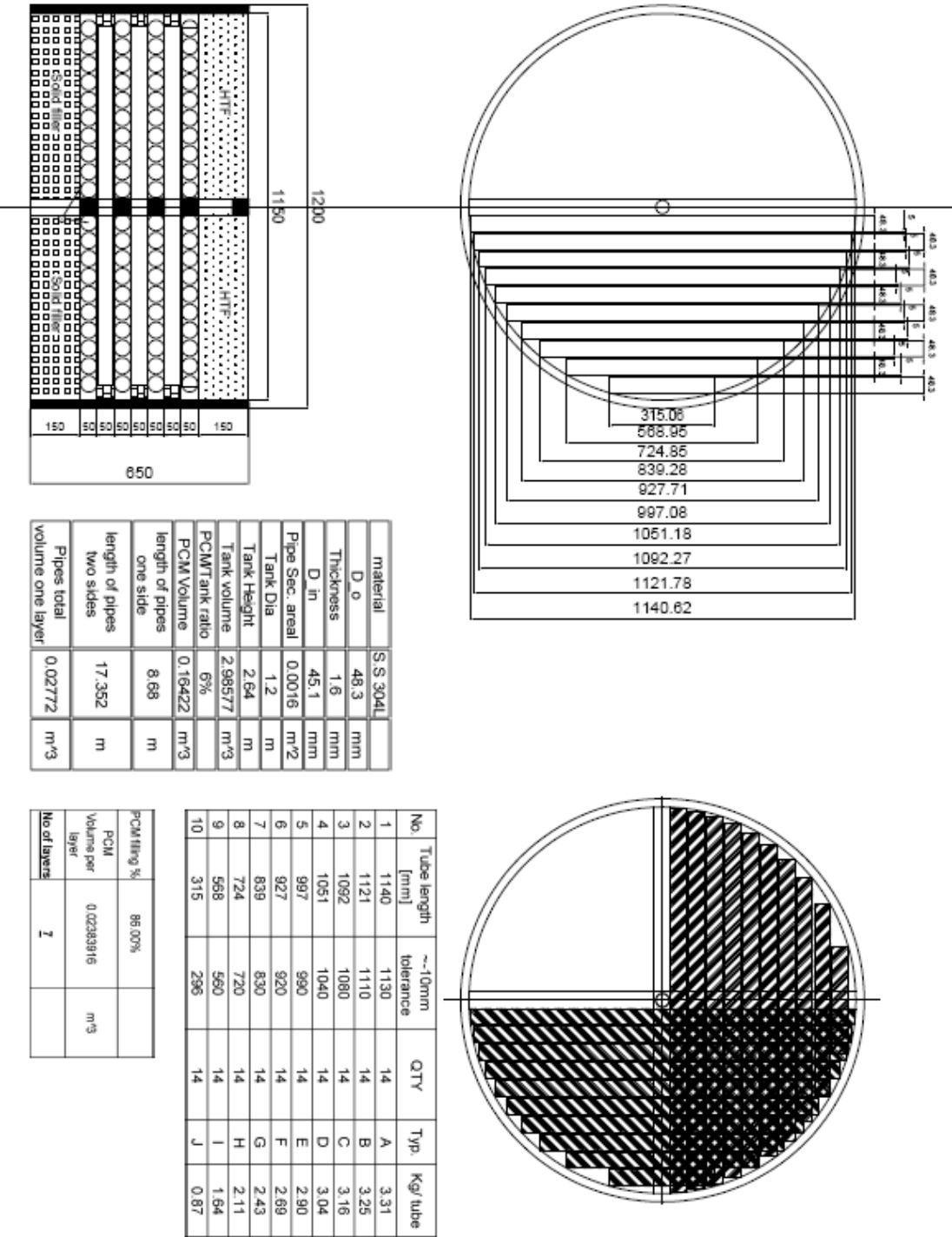


Figure 69. PCM layer design drawings

5.1.6. Layer Assembly and testing

The NaNO_3 is shipped in bulk, and the salt had to be filled inside the tubes on different melting steps, which results in accumulating the required amount of PCM with a filling density of 86%.

The tubes were received from the supplier at the required sizes with one side sealed with a welded end cap, and the other side is closed with a threaded end cap Figure 70.



Figure 70. Stainless steel tubes as received from the supplier

The filling procedures were as follows:

- 1- Measure the tare weight of the empty tubes.
- 2- Vertically fill the solid salt NaNO_3 inside the tubes (Figure 71(a)).
- 3- Placing the vertical tubes in the electric furnace to melt the salts and allow extra space (Figure 71(b)). This step ensures no leakage from the bottom of the tubes.
- 4- Add more PCM in the tubes.
- 5- Repeat steps 3 and 4.
- 6- Add the final mass of PCM to reach the intended weight and record the tubes' gross weight.
- 7- Seal the tubes with Deacon 770-P® (high-temperature tube's sealant) and a copper washer (Figure 71(c)).
- 8- Place the tubes horizontally inside the furnace and subject the containers to 3 cycles of melting/solidification (Figure 71(d)).
- 9- Visually inspect for any possible leakages.
- 10- Check each tube for hidden leakages by comparing its gross weight before and after cycling.



(a)



(b)



(c)



(d)

Figure 71. Main steps of filling the PCM inside the tubes

5.1.7. The final PCM layer package

The final arrangement of tubes in the PCM layer is illustrated in Figure 72. Furthermore, Table 42 reflects for each row: the mass of filled PCM, the mass of stainless steel, the volume of tubes, and the average filling ratio. It shows that PCM mass represents 58% of the total weight of the layer. The final measured porosity of the PCM layer is 0.508.



Figure 72. The final PCM layer package

The final ratio of the PCM layer volume to the thermocline is about 13.25% instead of the opted 5.5% (5.1.5). Although the volumetric ratio of the PCM itself is about 5.5%, the final PCM layer volume is influenced by the following factors:

- The additional air volume relative to PCM, which is added to contain PCM thermal expansion.
- The additional envelope material's volume with respect to the PCM.
- The packing porosity of the PCM layer is different from the porosity of the sphere.

Table 42. PCM mass, envelope mass, envelope volume, and filling ratio for each row

Row	m_{env} [kg]	m_{PCM} [kg]	V_{tube} [m ³]	Filling ratio
1	34.72	48.12	0.031	86.63%
2	34.72	48.25	0.031	86.86%
3	34.71	48.07	0.031	86.51%
4	34.72	48.29	0.031	86.87%
5	34.72	48.21	0.031	86.78%
6	34.70	48.10	0.031	86.59%
7	34.69	48.21	0.031	86.80%
Total	242.98	337.24	0.22	

5.2. MODEL VALIDATION OF THE THERMOCLINE WITH COMBINED TUBES-CONTAINED PCM TO SENSIBLE HEAT FILLER (TPCM-S)

The resulted TES solution of Thermocline that Combines Tubes-contained PCM (SS304-NaNO₃) with Sensible heat filler (alumina spheres) is named TPCM-S.

5.2.1. Model adjustment

- The PCM's energy balance equation in the D-C model has to be modified for tubes instead of spheres eq. (131) and eq.(132).

$$(\rho C p)_p \cdot \frac{\partial T_p}{\partial t} + \rho_p L_{fus} \frac{\partial \lambda}{\partial t} = \frac{1}{r} \frac{\partial}{\partial r} \left(k_p r \frac{\partial T_p}{\partial r} \right) \quad (131)$$

$$\begin{aligned} \frac{\partial T_p}{\partial t} &= \hat{f}_{r_i} \frac{\partial T_p}{\partial r} + \hat{g} \frac{\partial^2 T_p}{\partial r^2} - \frac{L_{fus}}{C p} \frac{\partial \lambda}{\partial t} \\ \hat{f}_{r_i} &= \frac{1}{r_i} \frac{k_p}{(\rho C p)_p}; \hat{g} = \frac{k_p}{(\rho C p)_p}; r_j = j \cdot \Delta r : j = 0, 1, 2 \dots M \end{aligned} \quad (132)$$

- The thermal capacity of the PCM has to be updated with the actual tube sizing Table 42, to account for the thermal capacity of the envelop materials as per eq.(103)(2.4.3)
- The shape factor used for tubes refer to eq.(128)
- The convection heat transfer is updated as per eq.(127) and Table 40.

5.2.2. Operating conditions of the experiments and simulation

The experimental conditions used in the model validation are illustrated in Table 43. The simulation uses the experimental inlet temperature as an inlet temperature of the model.

Table 43. Experimental and numerical conditions for the TPCM-S

Process	Charge	Discharge
Mass flow rate [kg/h]	2700	2000
Temperature range [°C]	286 – 315	312 - 226

5.2.3. Charge process

The charge starts from temperature T_{low} 286°C, while the inlet temperature of the HTF increased gradually from T_{low} to T_{high} 315°C using the electrical heater, then it remains constant until the end of the process.

5.2.3.1. Temperature profiles

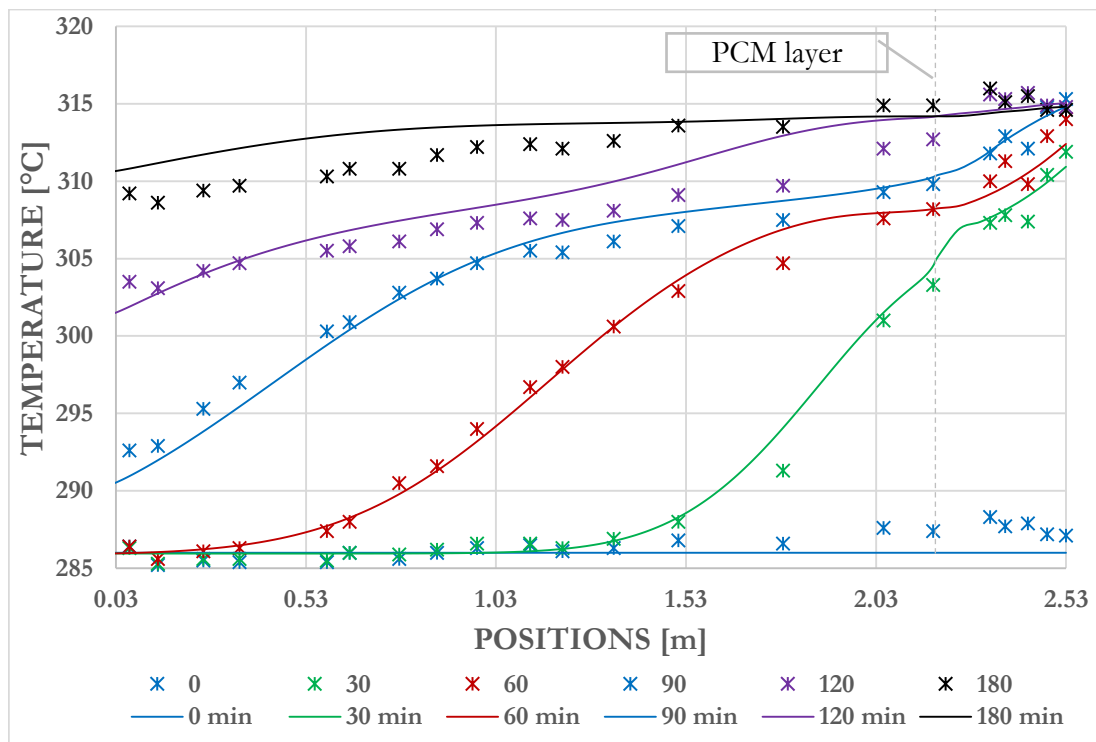


Figure 73. Temperature profile of TPCM-S during the charge process, model against experiment

Figure 73 compares the thermocline's temperature profile resulting from the model and the experimental one during the charge process. It confirms that the model is in good agreement with the measured temperature during the experiment. The PCM's influence is observed in the experiment and the simulation at about 307 °C, which is very near the melting temperature of the NaNO_3 .

5.2.3.2. Radial temperature distribution

The radial temperature evolution within the PCM layer is analyzed by plotting the temperatures obtained from the thermocouples located within the PCM layer. The thermocouples are located at six horizontal levels as illustrated in (Figure 74)

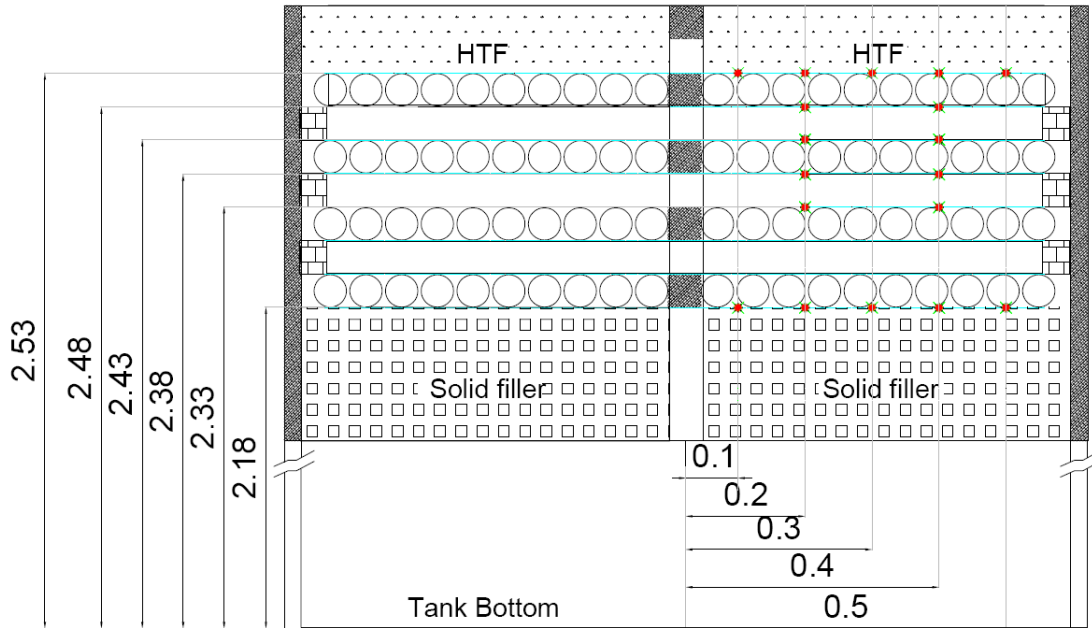


Figure 74 Radial thermocouples positions at the PCM layer in the TPCM-S experiment

Figure 75 plots the radial temperature evolution during the charge process at six different positions.

The thermocouples readings demonstrated a homogeneous HTF temperature distribution at the tank's radial direction, which supports the assumption of one-dimensional behavior for the model. A small fluctuation in the temperature is observed at thermocouples located at 2.18 m, which can be explained by the inconsistency of HTF velocity between two different filler materials, the alumina spheres and NaNO_3 tubes.

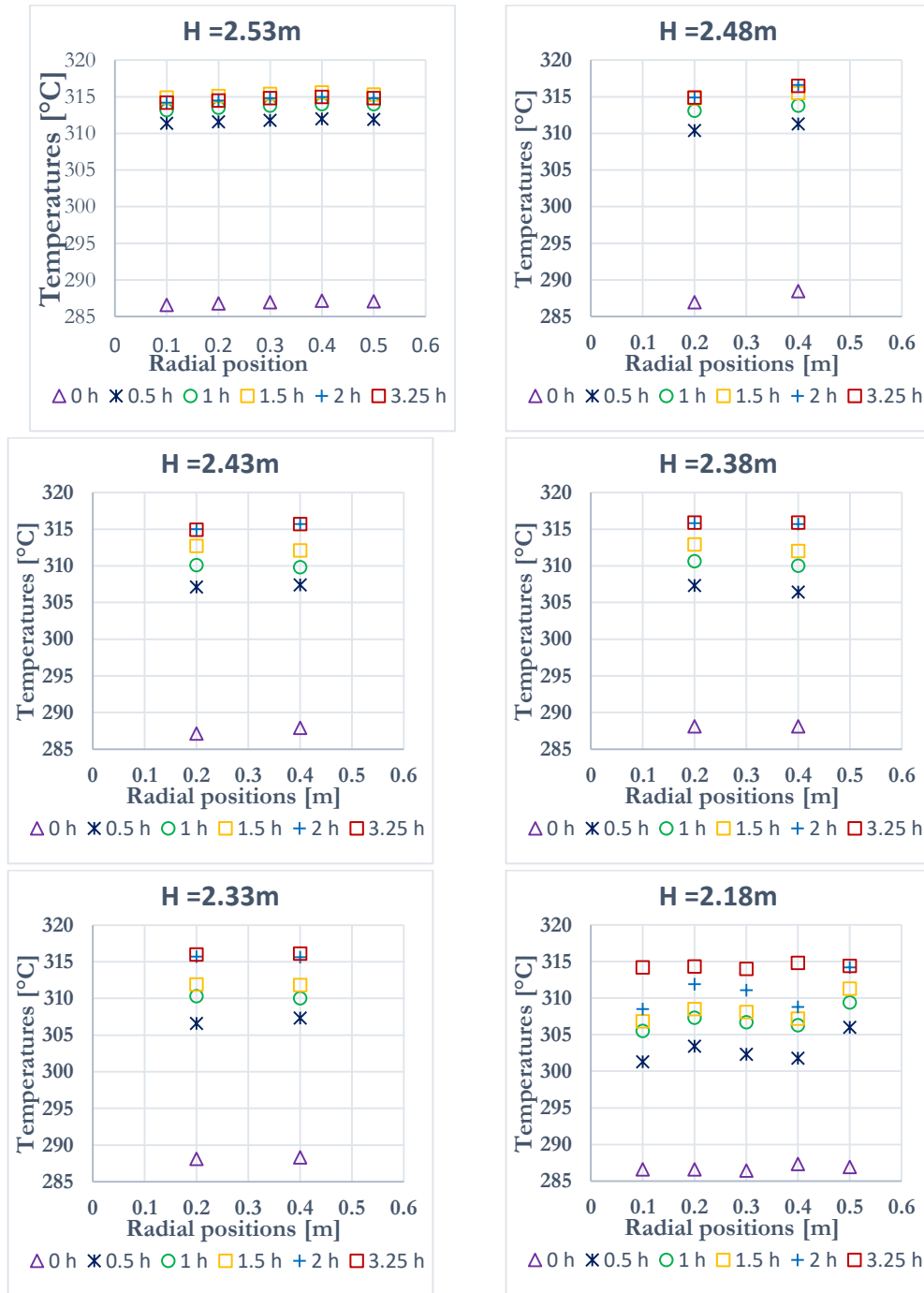


Figure 75. Radial temperature evolution during the charge at six axial reference positions TPCM-S experiment

5.2.4. Discharge process

During the discharge, all the mediums inside the thermocline are at T_{high} 315°C, while the HTF is entering the tank at T_{low} 226°C with a constant mass flow rate.

5.2.4.1. Temperature profile

During the discharge operation, the model predicts a temperature profile similar to the experimental one, Figure 76. The model results deviated from the experimental one at the last 30 min of the process due to the unstable mass flow rate in the experimental setting.

The isothermal behavior of the PCM is reflected in the HTF temperature after 75 min at about 307 °C

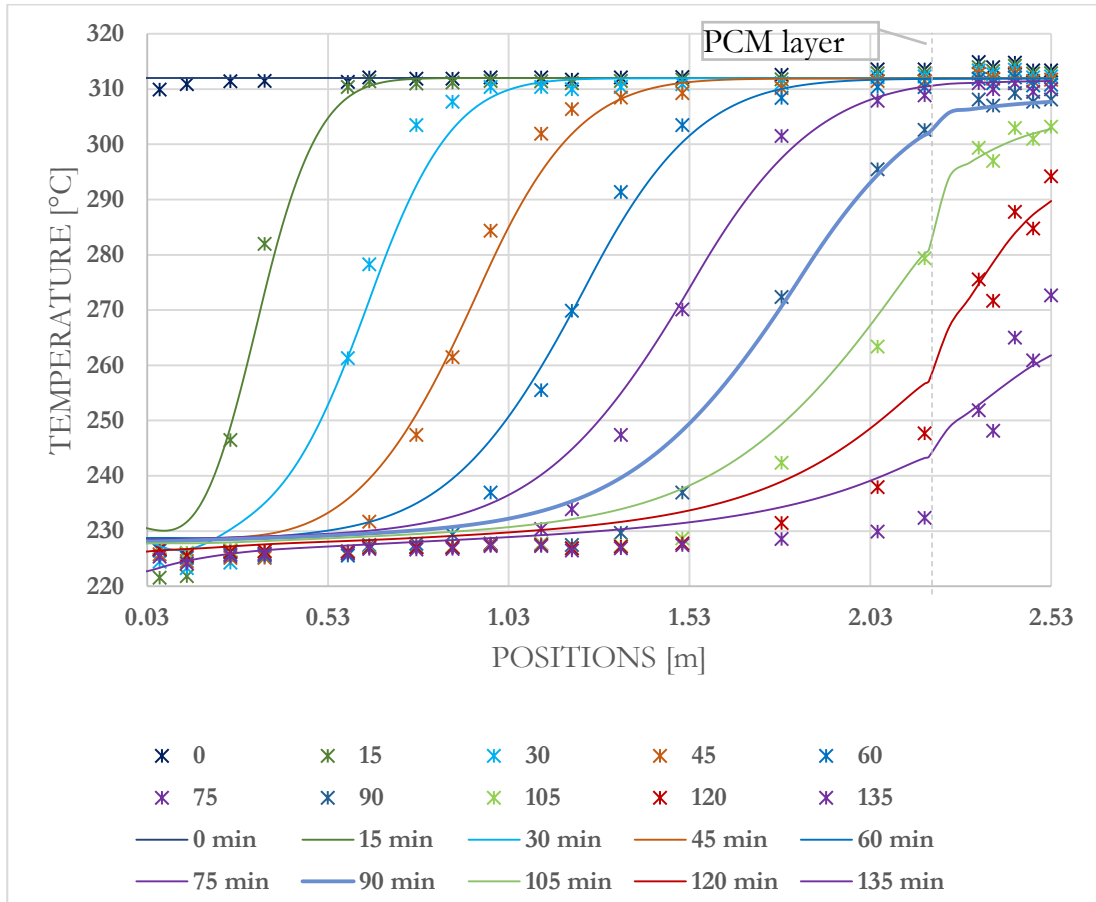


Figure 76. Temperature profile of TPCM-S during the discharge process, model against experiment

5.2.4.2. Radial temperature distribution

Similar to the charge process, the radial temperature evolution maintained a one-dimensional evaluation during the discharge operating (Figure 77). Furthermore, a small deviation in the radial temperature distribution is observed at the interface position between the PCM tubes and alumina spheres. The magnitude of the fluctuation increases with the temperature decrease.

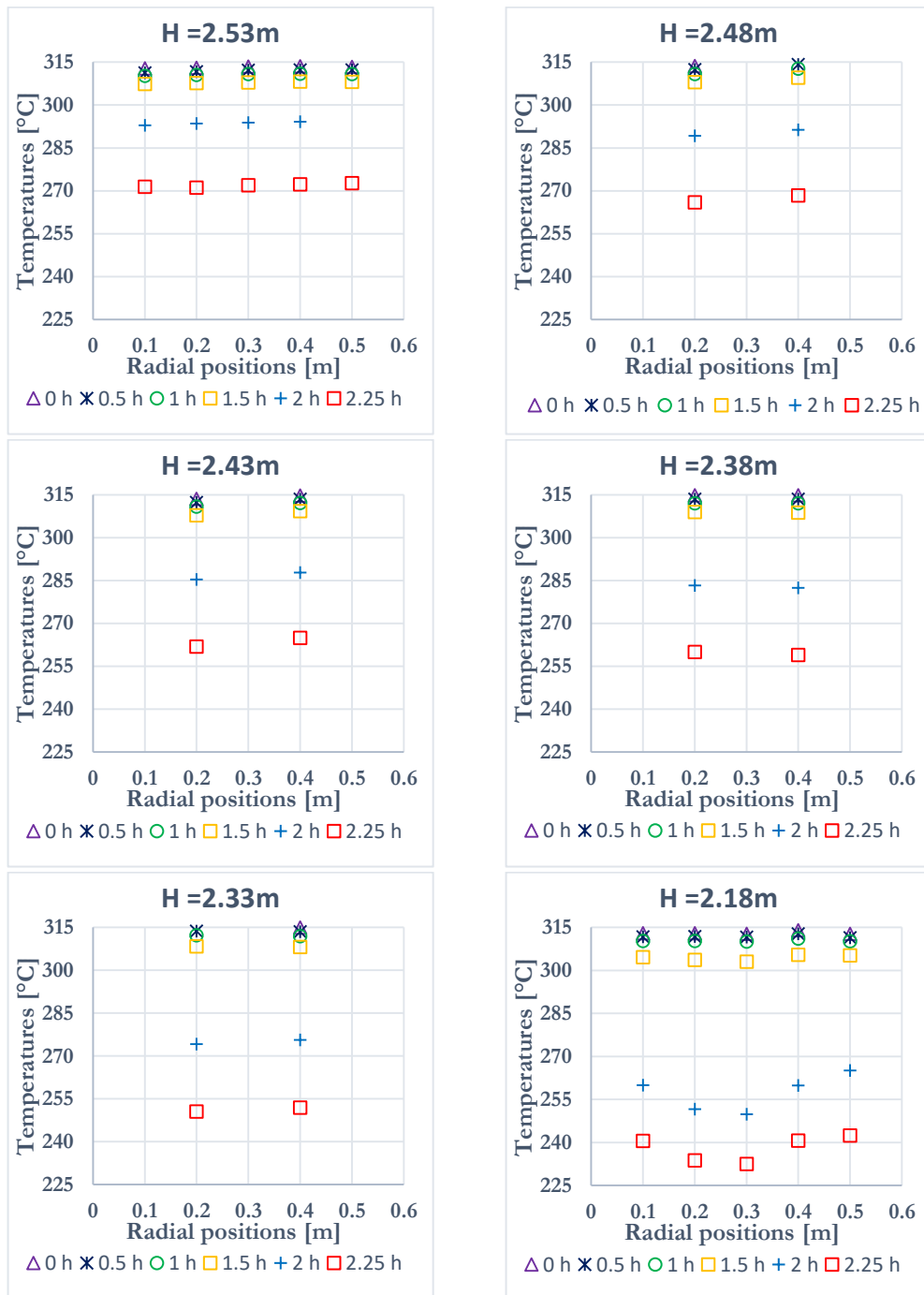


Figure 77. Radial temperature evolution during the discharge at six axial reference positions TPCM-S experiment

The homogenous radial temperature distribution within the PCM layer during charge and discharge attest the one-dimensional behavior of the HTF inside the thermocline.

The experimental results confirm the accuracy of the model during both processes, charge and discharge, affirming the validity of the TPCM-S numerical simulation.

5.3. EXPERIMENTAL EVALUATIONS

This section analyzes the thermocline thermal behavior that combines tubes-contained NaNO_3 with alumina spheres (TPCM-S). The experimental performance indicators are evaluated during charge and discharge at two different temperature differences as well as three mass flow rates. The temperature profile during a short stand-by is also observed.

5.3.1. Charge process

It is not possible to perform a charge process with a large temperature difference between the inlet and the outlet of the thermocline in one-step in this work. Mainly due to the electrical-heater power limitation, for example, we could not inject HTF at 315°C while the HTF within the thermocline is at 225°C . Hence, the charge had to be performed at multiple stages. Figure 78 illustrates the thermocline inlet/outlet temperature and the mass flow rate for a typical charge process. The charge has to be done from 220°C on three successive stages to achieve the targeted 315°C temperature.

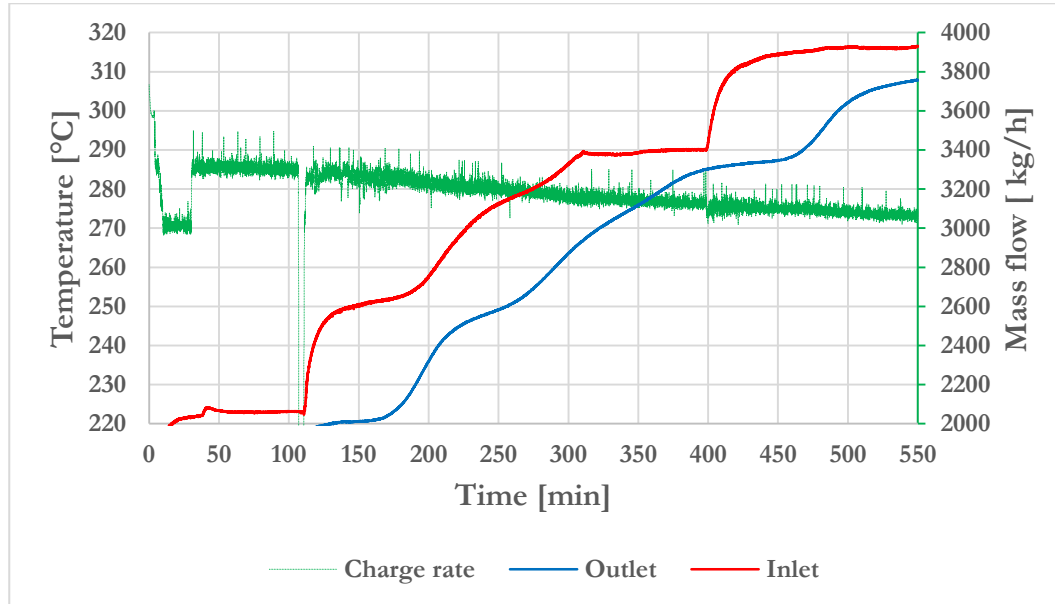
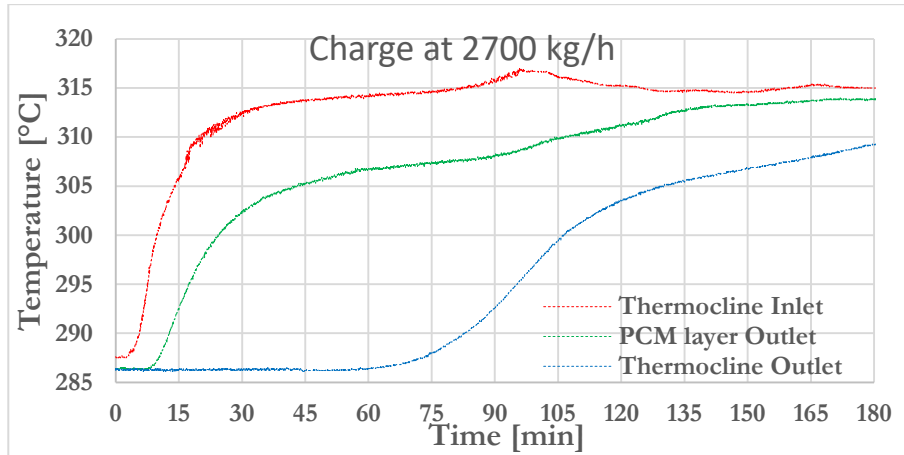


Figure 78. Typical charge of the thermocline in the MICROSOL-R 220°C - 320°C at a constant mass flow rate

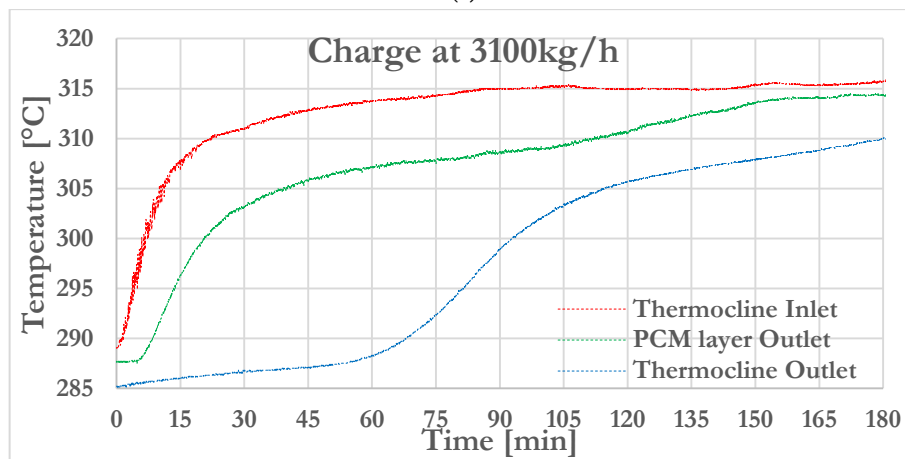
Therefore, this section is focused on the last step of charge because it includes the NaNO_3 phase change at its melting temperature where two temperature differences are evaluated 285°C - 315°C and 295°C - 330°C .

5.3.1.1. Charge from 285°C to 315°C

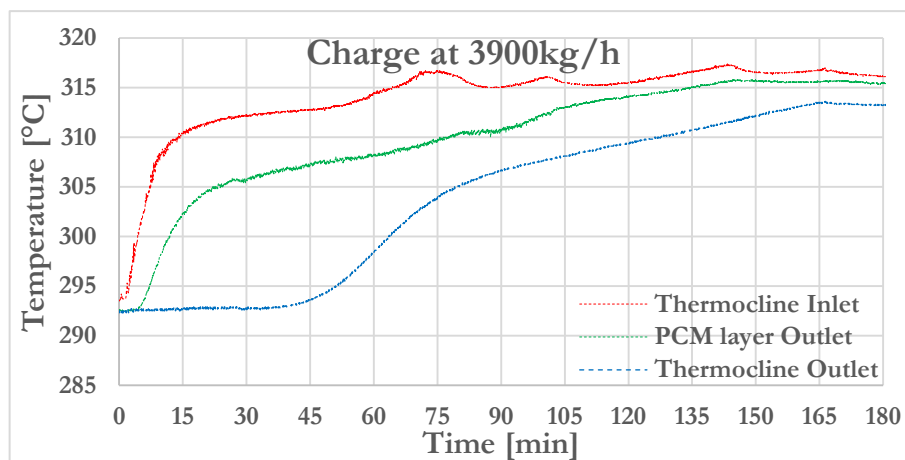
5.3.1.1.1. Inlet/outlet temperatures evolution in time



(a)



(b)



(c)

Figure 79. Experimental results for charge process (285-315) °C at various mass flow rates of TPCM-S

Figure 79 represents the temperature evolution in time during the charging process at three different locations: the inlet of the thermocline, the outlet of the PCM layer, and the outlet of the thermocline. The inlet of the thermocline is the top of the PCM layer during the charge.

The charges are performed from 285°C up to 315°C, with three mass flow rates: Figure 79 (a) 2700 kg/h, (b) 3100 kg/h, and (c) 3900 kg/h. The figure shows that the increase in mass flow rate does not have a significant influence on the HTF temperature at the outlet of the PCM layer, while it charges the system faster, which can be seen by following the evolution of the temperature at the thermocline outlet.

The HTF temperature at the PCM layer outlet demonstrates the phase change effect at 306°C near the melting points of the NaNO₃.

Furthermore, the PCM layer has no influence on the curve at the thermocline outlet temperature for the studied range of mass flow rates, which can be attributed to the fact that the HTF exiting the PCM layer has to charge a large amount of alumina spheres before exiting the thermocline.

5.3.1.1.2. Thermocline thickness

Performing the thermocline thickness evaluation during the charging process for this experiment is not entirely representative, mainly because if we apply the same criteria (2.3) $k_c = k_d = 20\%$ it will result $T_{thr,c,20\%} = 291^\circ\text{C}$ and $T_{thr,d,20\%} = 309^\circ\text{C}$. At such thermocline outlet temperature during charge, the PCM is not melted yet, and that is for all the mass flow rates (Figure 79).

More importantly, at such a high discharge threshold temperature of 309 °C, the PCM's melting point should not be reached yet, and this opposes the purpose of using PCM for TES.

To avoid this problem caused by the charging system limited power (and temperature) in this experiment (Figure 78), the threshold temperatures are assumed to be $T_{thr,c} 298^\circ\text{C}$, and $T_{thr,d} 304^\circ\text{C}$. Thus, the evolution of the thermocline thickness can be analyzed but not its magnitude.

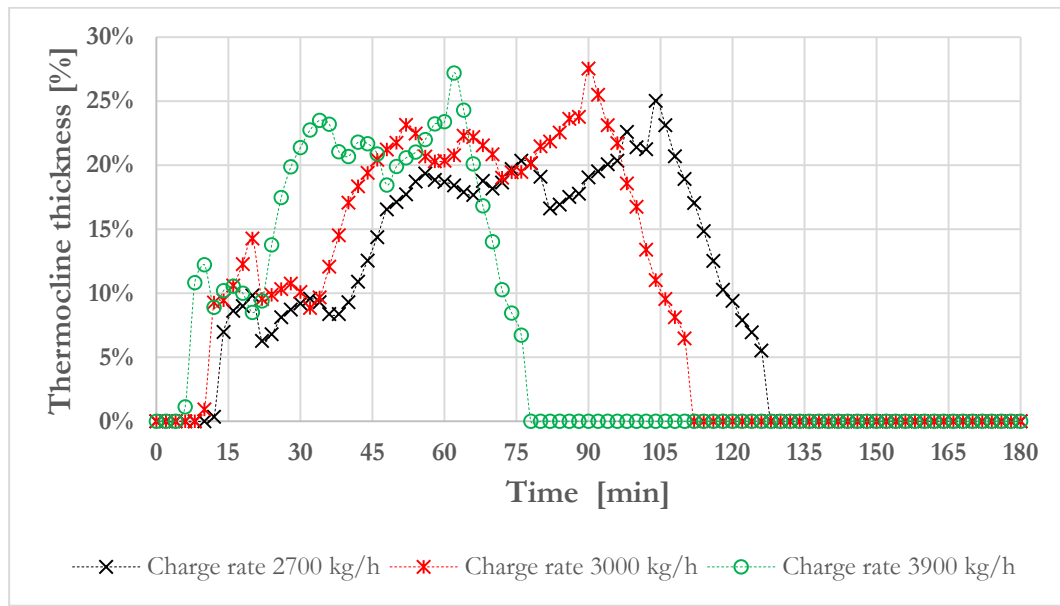


Figure 80. Experimental thermocline thickness during charge (285-315) °C at various mass flow rates of TPCM-S

Figure 80 plots the resulted time evolution of thermocline thickness for the charges between 285-315°C. It indicates that the thermocline thickness raised sharply at the beginning of the charge, then flattened before it continued to increase gradually to reach its maximum, then quickly dropped when the thermocline is fully charged. The observed plateau in the thermocline thickness near 20% could be attributed to the PCM melting, which prevents the HTF temperature from rising; consequently, attenuating the thickness increases.

Moreover, It illustrates that the thickness developed and diminished faster at higher mass flow rates than lower mass flow rates, with similar magnitude. That is because the higher the mass flow rate, the faster the charge is.

5.3.1.1.3. Charge efficiency

The efficiency during the charge time between 285°C up to 315°C is plotted in Figure 81. It shows that higher mass flow rates are associated with a slightly better charge efficiency.

However, taking into account the presumed value to stop the charge at $T_{thr,c} = 298^{\circ}\text{C}$, the charge should be ended at 105 min, 90 min, and 62 min for the three mass flow rates presented in Figure 79 (a), (b), and (c) respectively. Therefore, the resulted efficiencies are 65%, 60%, and 50%, with respect to the three tested mass flow rates 2700 kg/h, 3100 kg/h, and 3900 kg/h.

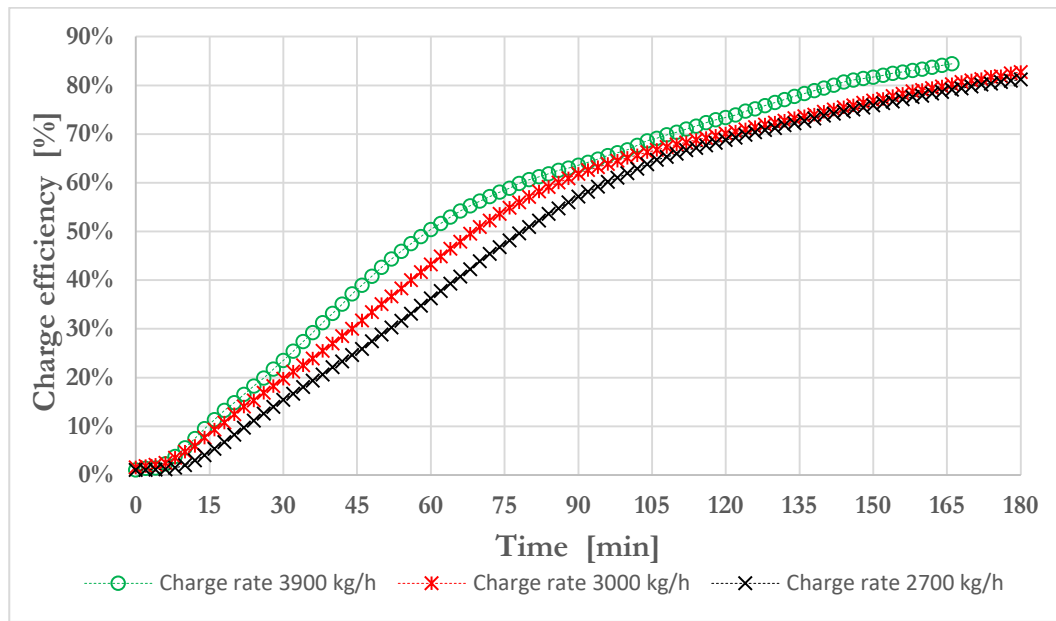


Figure 81. Experimental efficiency during charge (285-315) °C at various mass flow rates of TPCM-S

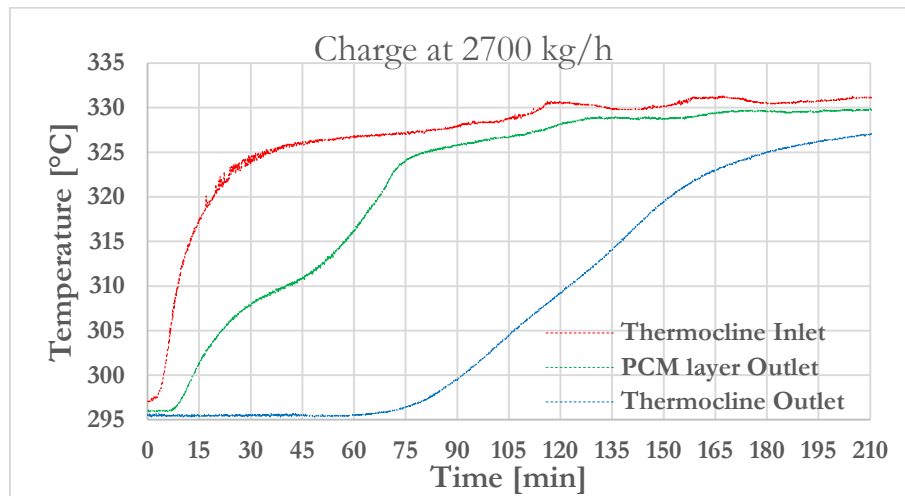
Although the absolute values are not entirely representative of a charge operation at a more significant temperature difference, their magnitudes suggest that a lower mass flow rate is favorable for better charge efficiency. This also agrees with the findings of Bédécarrats et al. [208] to recommend a slow charge rate for a thermocline filled with a PCM unit for cold storage.

5.3.1.2. Charge from 295°C to 330°C

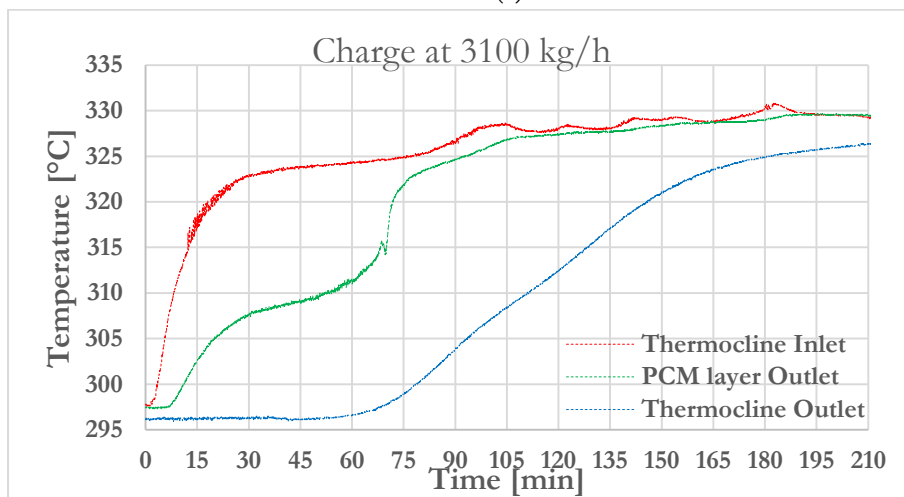
5.3.1.2.1. Inlet/outlet temperature evolutions in time

Figure 82 illustrates a charge experiments with a higher temperature difference (295°C up to 330°C), at the three mass flow rates: Figure 82 (a) 2700 kg/h, (b) 3100 kg/h, and (c) 3900 kg/h.

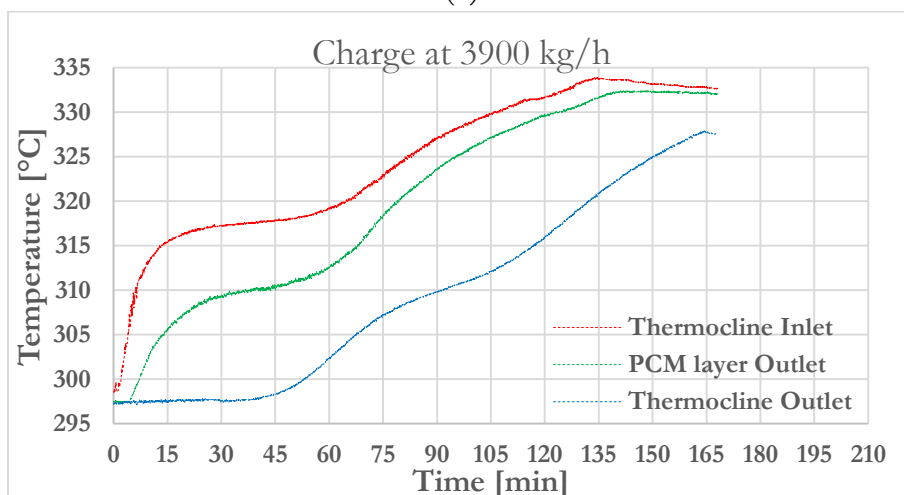
When comparing the PCM layer outlet temperature to the one related to previous tests (Figure 79 at 285°C up to 315°C), the phase change is happening faster, where the curve illustrates a shorter time at a constant temperature.



(a)



(b)



(c)

Figure 82. Experimental results for charge process (295-330) °C at various mass flow rates of TPCM-S

Moreover, the HTF reflected a stable temperature at about 309°C compared to the 307°C in the previous tests, suggesting that NaNO₃ is melting at a relatively higher temperature. This effect could be attributed to emerging the sub-cooling phenomena in the PCM due to higher inlet temperature.

The same behavior was observed by Bédécarrats et al. [208], where higher inlet temperature than the melting points of the PCM and higher mass flowrates led to more prominent subcooling in the cold storage system.

In Figure 82 (c), the thermocline outlet temperature seems to exhibit a wave shape, which is caused by an additional charging step. This could be observed by evaluating the thermocline inlet temperature behavior, which is similar to the behavior shown in Figure 78. In this case, due to the higher mass flow rate, the electrical heater could not provide enough heating power to the HTF to reach the 330°C at one-step, and the thermocline is charged until its outlet temperature reached near 306 °C, then the heater starts increasing the temperature for the required 330°C.

5.3.1.2.2. Thermocline thickness

Figure 83 plots the resulted thermocline thickness in time for a charge with elevated inlet temperature 295-330°C. The thickness for the 3900 kg/h fluctuated significantly due to the two-steps filling enforced by the electrical heater limited power.

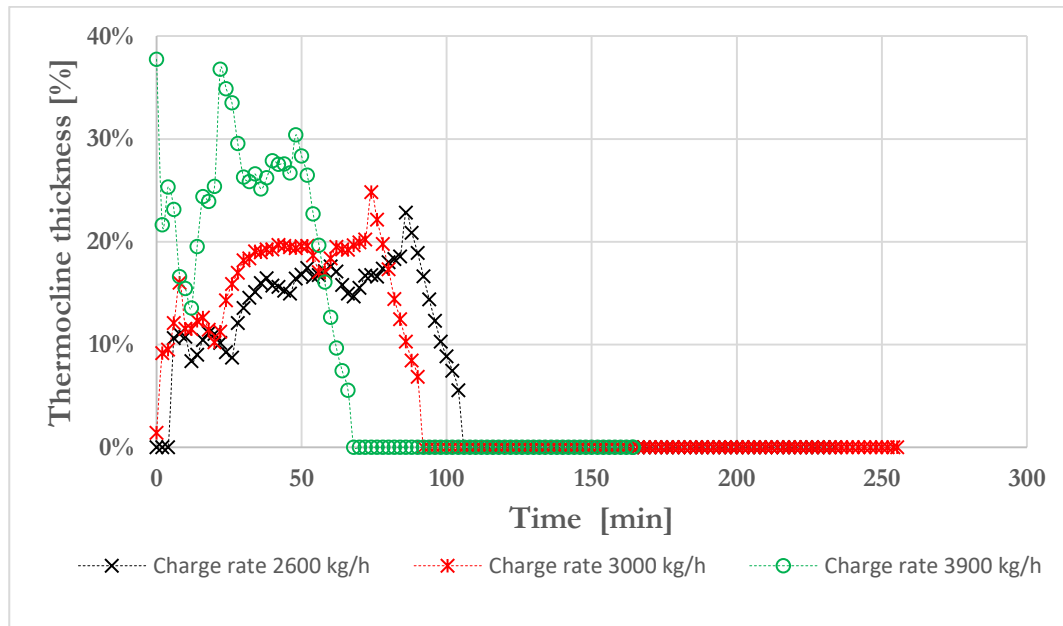


Figure 83. Experimental thermocline thickness during charge (295-330) °C at various mass flow rates of TPCM-S

Contrarily to the other two flows, the thickness raised quickly at the beginning of the process, then flattened for some time before it continues to rise again less sharply then flattened for a longer time near its maximum. The observed plateau in the thermocline thickness could be attributed to the PCM melting, which prevents the HTF temperature from rising; consequently, attenuating the thickness increases.

Moreover, the order of magnitude of the thermocline thickness is smaller at the higher temperature difference than at the lower one, which is mainly attributed to the increase of the charging temperature T_{high} while the threshold values remain the same.

5.3.1.2.3. Charge efficiency

The efficiency of charging the thermocline with a higher HTF temperature 330°C show similar behavior to the one from process 285°C up to 315°C (Figure 84). The charge efficiency at the threshold temperature is 47%, 40%, and 25% for the three tested mass flow rates 2600 kg/h, 3000 kg/h, and 3900 kg/h. These low efficiencies are not representative because of the small temperature difference applied, while their magnitude suggests that lower charge rates are associated with slightly better efficiency.

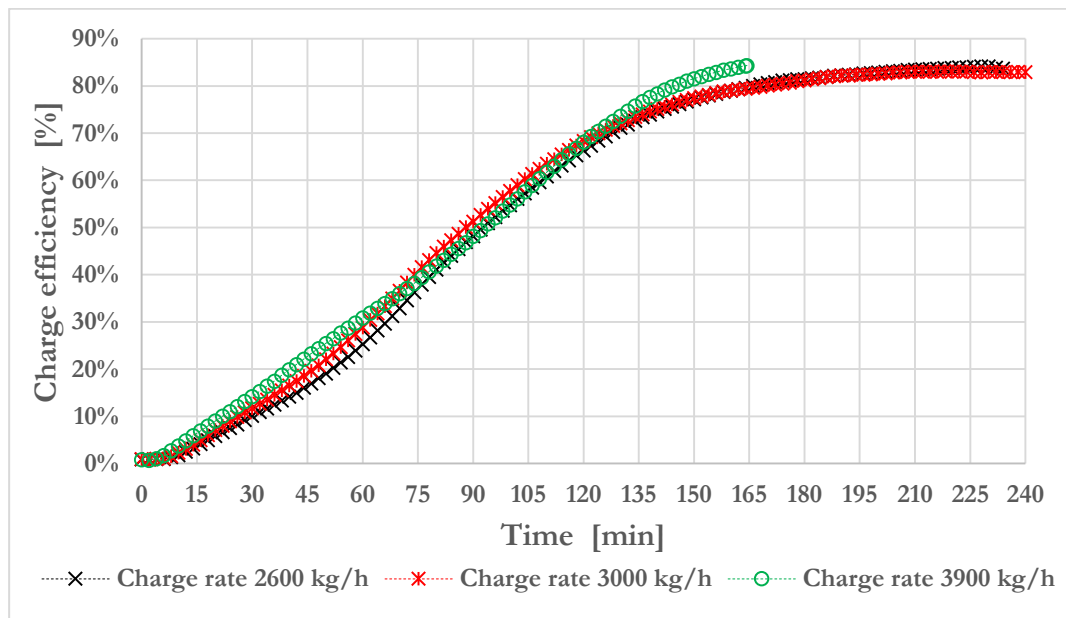


Figure 84. Experimental efficiency during charge (295-330) °C at various mass flow rates of TPCM-S

5.3.2. Discharge process

In contrast to charge, the discharge process is more flexible and allows us to achieve discharge at a greater temperature difference in one-step. Therefore, two ranges were tested 315⁰C-220⁰C and 330⁰C to 225⁰C.

5.3.2.1. Discharge from 315⁰C to 220⁰C

5.3.2.1.1. Inlet/outlet temperatures evolution in time

Figure 85 shows the temperature evolutions with time for a discharge process between 315⁰C -220⁰C, at three different mass flow rates (a)1600 kg/h, (b) 2000 kg/h, and (c) 3000 kg/h. The temperatures are plotted at the PCM layer inlet and the thermocline outlet to illustrate the different slopes that the HTF temperature experiences between the alumina spheres and the PCM layer. The outlet of the thermocline is the PCM layer outlet during the discharge operation.

The PCM influence on the thermocline outlet temperature is highlighted with a dotted circle in Figure 85. The results indicate that the higher the discharge rate, the smaller the influence of the PCM solidification. The influence of phase change is reflected on the HTF temperature at 305⁰C for all three mass flow rates, where the curve changes its slope.

Figure 85 indicates that the higher the discharge rate, the shorter the discharge time, the discharges reach its threshold temperature of 296⁰C ($\theta_{thr,d,20\%} = 0.8$) at near 153 min, 118 min, and 75 min for 1600 kg/h, 2000 kg/h, and 3000 kg/h, respectively.

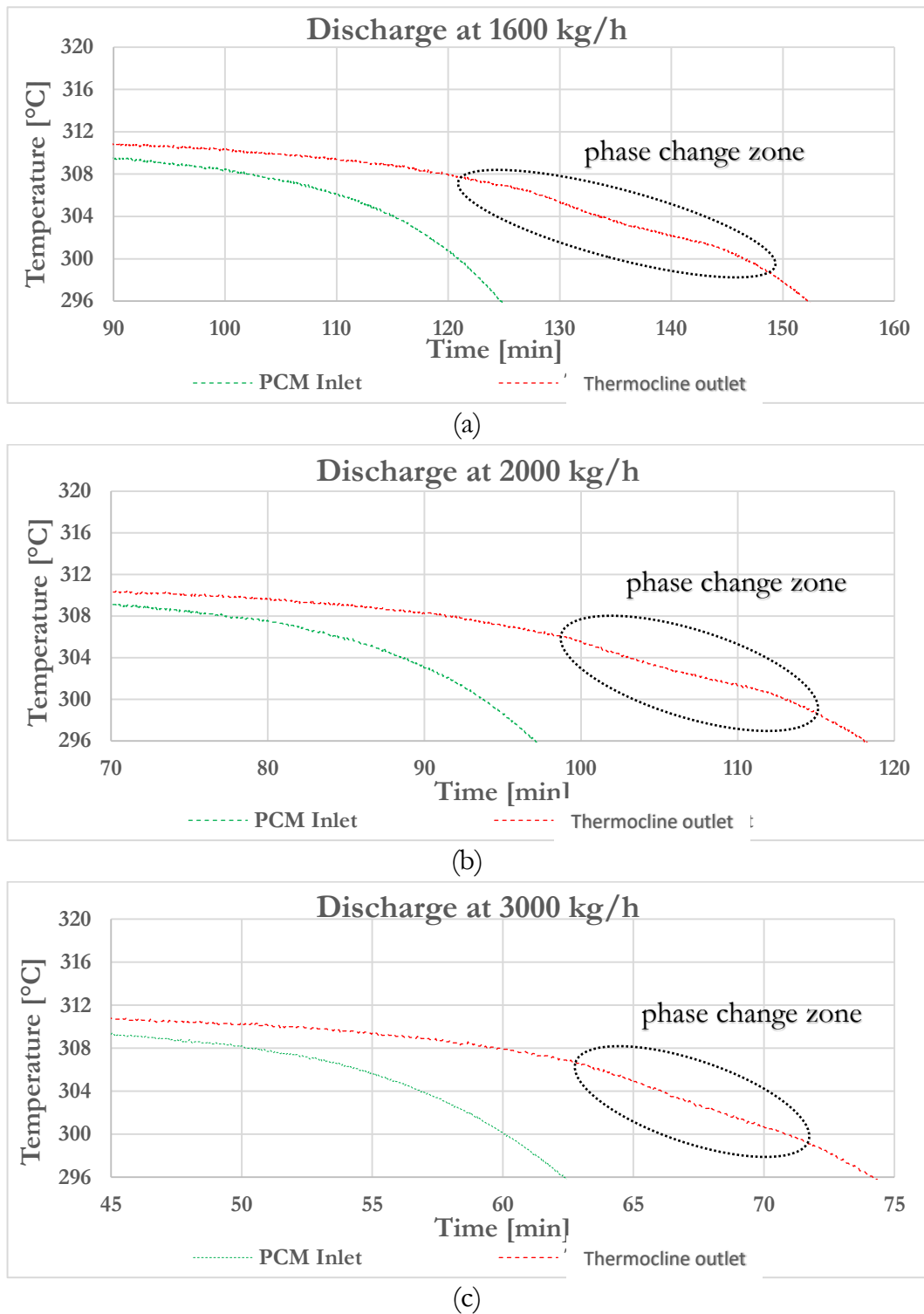


Figure 85. Experimental results for the discharge process (315-220) °C at various mass flow rates of TPCM-S

5.3.2.1.2. Thermocline thickness

The thermocline thickness is evaluated for the discharge process at a charge Threshold temperature of 239 °C ($\theta_{thr,c,20\%} = 0.2$), and a discharge threshold temperature of 296 °C ($\theta_{thr,d,20\%} = 0.8$).

Figure 86 reflects the thermocline thickness obtained during the discharge process between 315°C-220°C for the three mass flow rates. It shows that the thickness developed and diminished faster with higher mass flow rates with about 20% maximum value. Moreover, at the discharge threshold temperature, the thickness is 10%, 13%, and 15% at a mass flow rate of 1600 kg/h, 2000 kg/h, and 3000 kg/h, with respective discharge time of 153 min, 118 min, and 75 min.

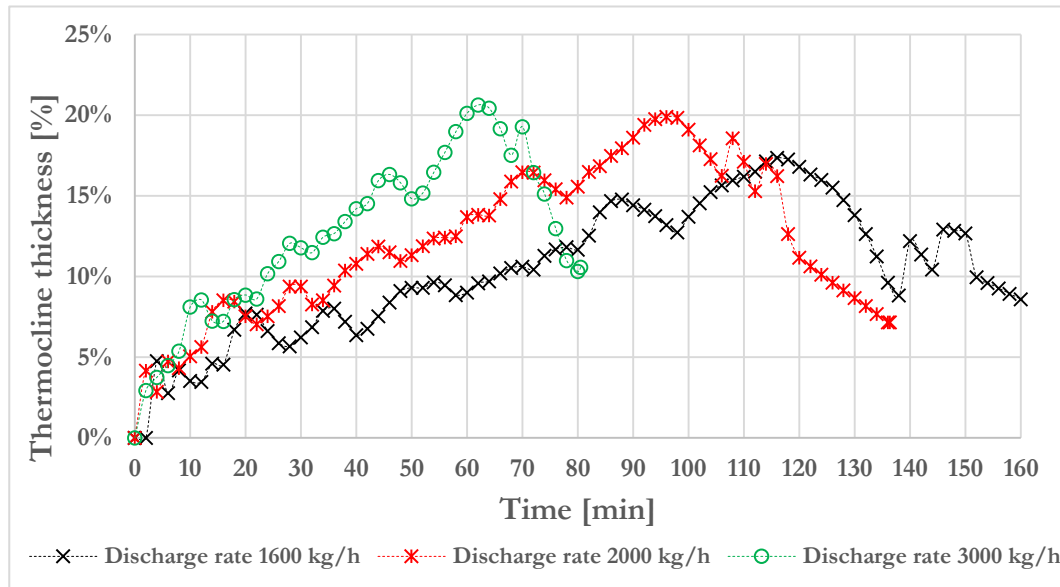


Figure 86. Experimental thermocline thickness during discharge (315-220) °C at various mass flow rates of TPCM-S

5.3.2.1.3. Discharge efficiency

The efficiency of the first three discharge tests at 315°C-220°C is plotted against time in Figure 87. It indicates that discharge efficiency increased with a discharge rate. However, Figure 88 reflects that the associated values of the efficiencies with the referenced threshold temperatures are about 83% for three tested mass flow rates.

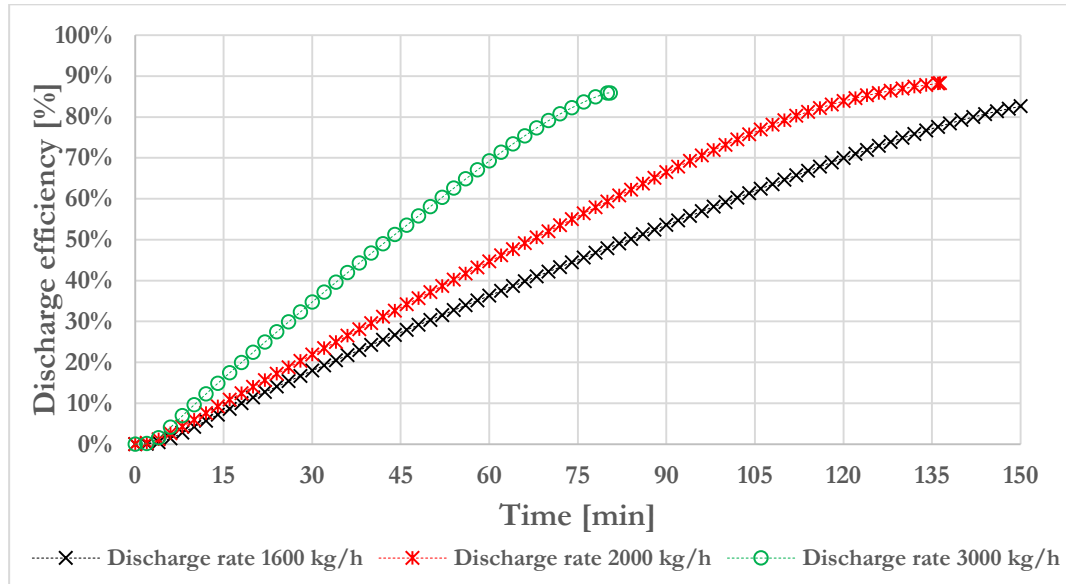


Figure 87. Experimental efficiency during discharge (315-220) °C at various mass flow rates of TPCM-S

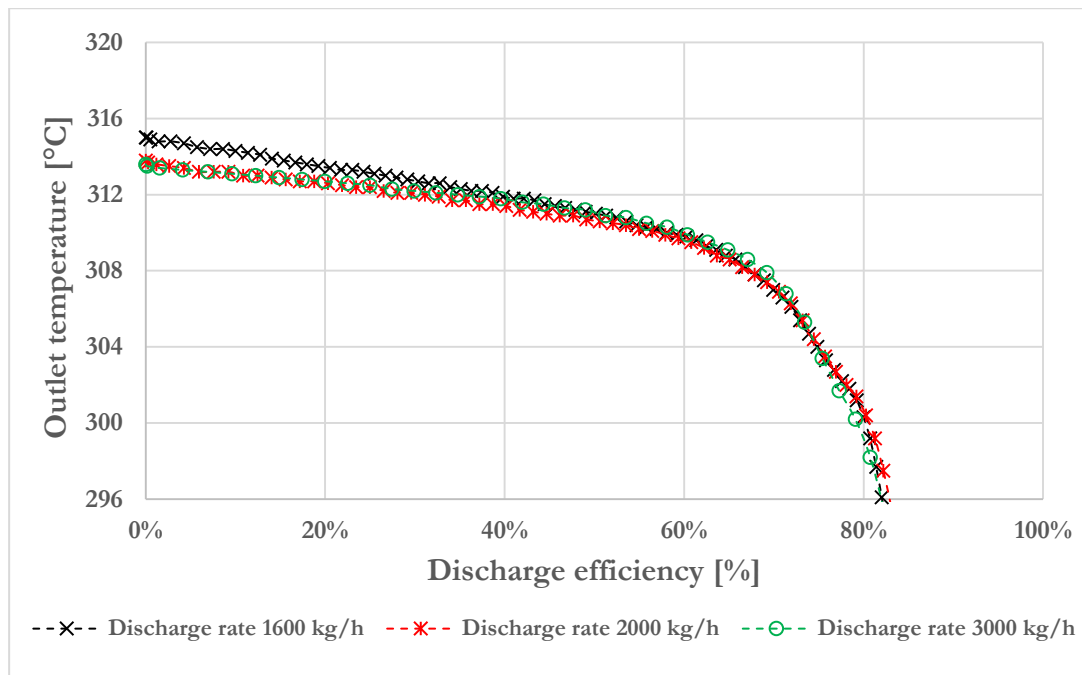


Figure 88. Outlet temperature versus efficiency during discharge (315-220) °C at various mass flow rates of TPCM-S

5.3.2.2. Discharge from 330°C to 225°C

5.3.2.2.1. Inlet/outlet temperatures evolution in time

Figure 89 plots the temperatures at the thermocline inlet, thermocline outlet, and the PCM layer inlet in time for discharge between 330°C and 225°C. The mass flow rates for these tests are (a) 1600 kg/h, (b) 2400 kg/h, and (c) 3000 kg/h. The graph highlights the expected region of the PCM solidification influence on the HTF temperature. Like for the lower temperature difference, the PCM influence is less observed on the HTF temperature by increasing the discharge rate.

Figure 89 indicates that increasing the thermocline initial stored energy by elevating the temperature from 315°C to 330°C increased the discharge time at the same threshold temperature and the same discharge rate. The process lasts about 170 min compared to 150 min at 1600 kg/h and 80 min compared to 75 min at 3000 kg/h. The thermal capacity of the material explains this increase in discharge duration. Furthermore, the HTF temperature indicates the NaNO_3 phase change at about 305°C, similar to the previous tests.

However, increasing the highest temperature in the system will increase the inlet temperature during the charge, consequently increasing the chance to develop the sub-cooling in the PCM (5.3.1.2.1), which affects the charge efficiency and might lead to a drop in the efficiency of the cycle.

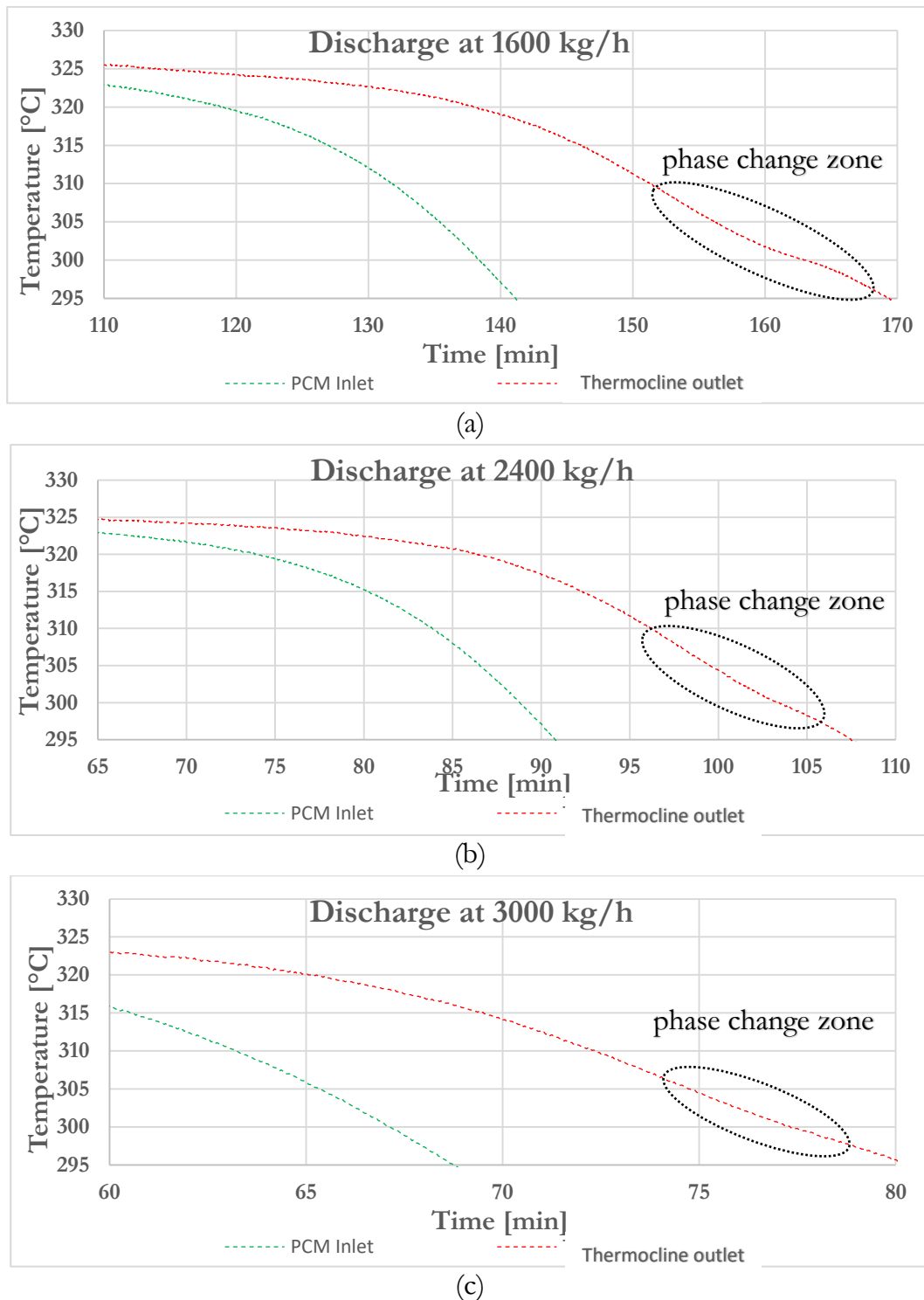


Figure 89. Experimental results for the discharge process (330-225) °C at various mass flow rates of TPCM-S

5.3.2.2.2. Thermocline thickness

Figure 90 plots the thermocline thickness development at a higher temperature difference than the previous tests, while the same threshold temperatures are used.

The thermocline thickness is 10%, 15%, and 14% for the 1600 kg/h, 2400 kg/h, and 3000 kg/h, and the respective discharge times are 170 min, 107 min, and 80 min. Figure 90 indicates that lower mass flow rates are associated with smaller thermocline thickness at the end of the discharge.

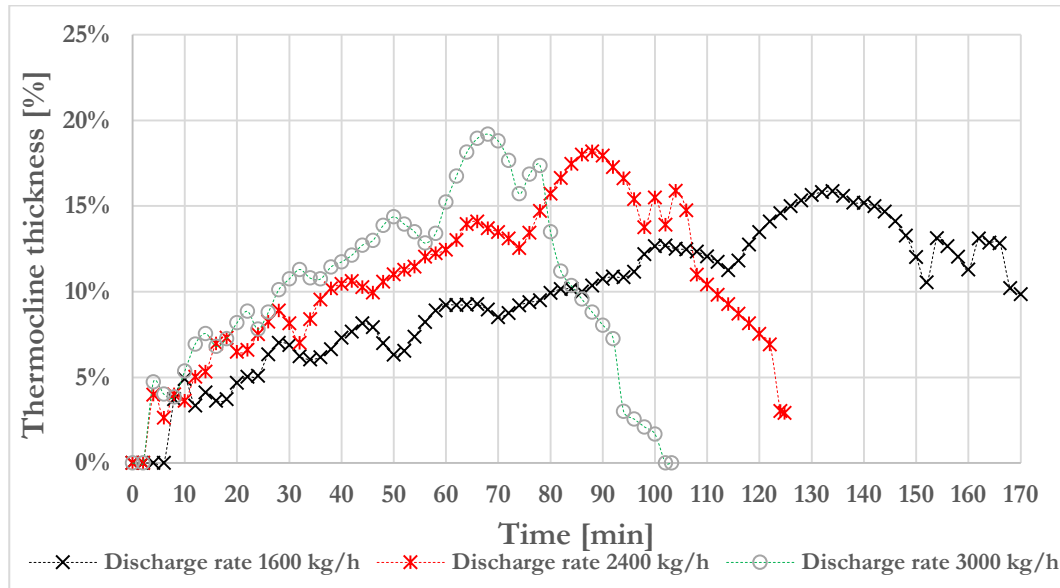


Figure 90. Experimental thermocline thickness during discharge (330-225) °C at various mass flow rates of TPCM-S

5.3.2.2.3. Discharge efficiency

Similarly to the lower temperature difference, the rate of change in discharge efficiency increase with the mass flow rate (Figure 91). While the discharge efficiencies at the threshold temperature are 83%, 83%, and 80% for the three mass flow rates 1600 kg/h, 2400 kg/h, and 3000 kg/h, respectively Figure 92.

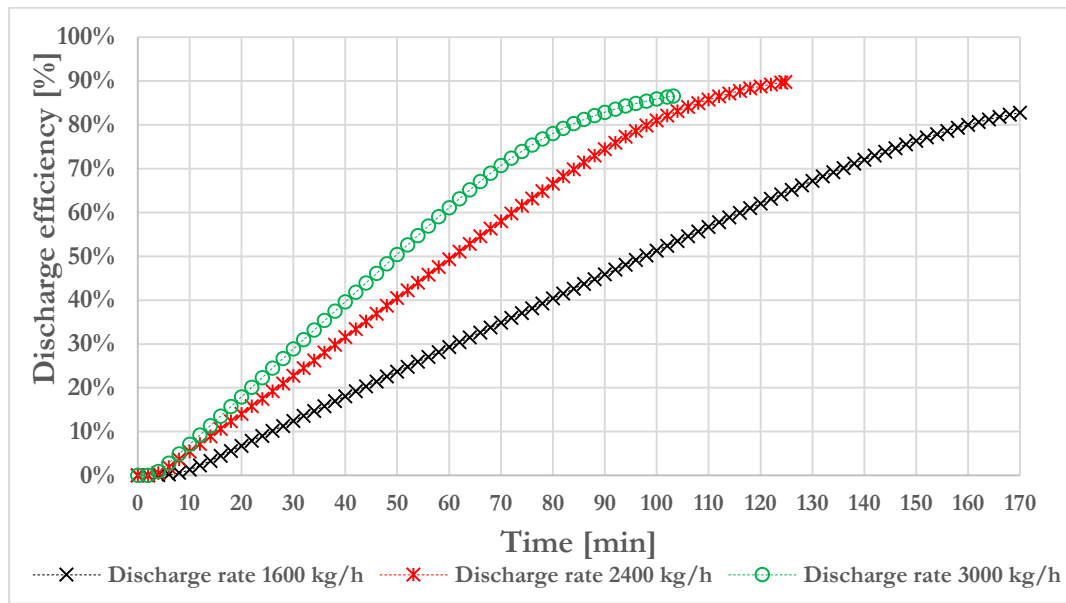


Figure 91. Experimental efficiency during discharge (330-225) °C at various mass flow rates of TPCM-S

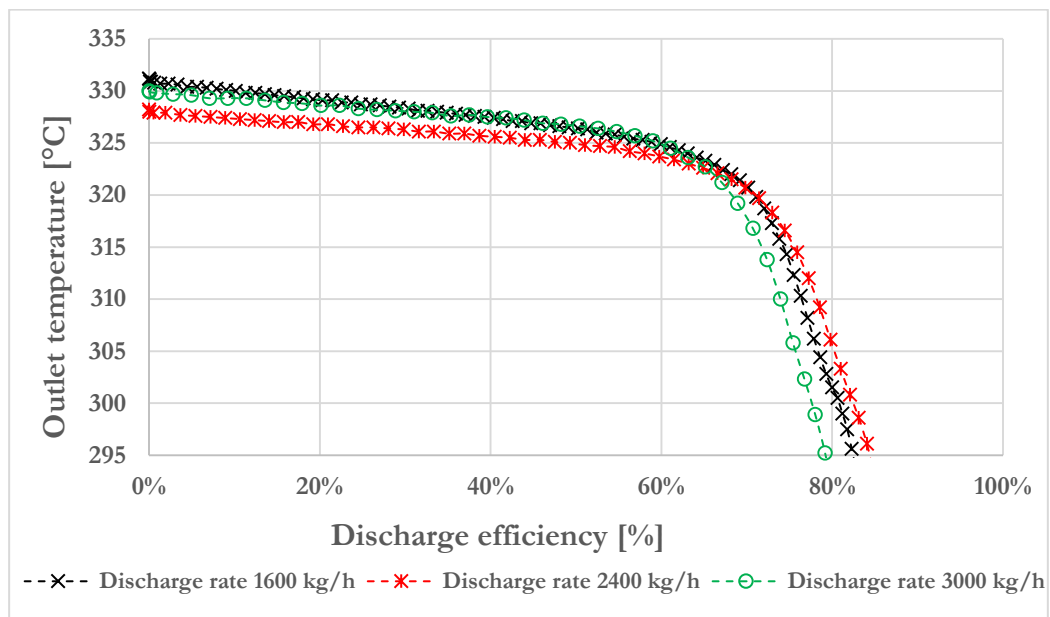


Figure 92. Outlet temperature versus efficiency during discharge (330-225) °C at various mass flow rates of TPCM-S

The results from the thermocline thickness and discharge efficiencies suggest that an optimum mass flow rate can be achieved, which is accompanied by best discharge efficiency and small thermocline thickness. For example, the 1600 kg/h seems to be near the optimum mass flow rate for this experimental setup with an 83% discharge efficiency and 13% thermocline thickness, which remains valid at elevating the temperature difference of 330°C - 225°C. Hoffmann et al.

indicated a similar finding [19] that an optimized mass flow rate for solid filler could improve thermocline performance.

5.3.3. Stand-by mode

To evaluate the thermal behavior of the thermocline during a stand-by, we discharged the system from 310°C to 220°C and stopped the operation when only the PCM layer is at 310°C while most of the remaining thermocline is at a lower temperature. Figure 93 plots the temperature profile inside the thermocline during this stand-by period of about five hours.

During the first hour, the PCM temperature loses about 3°C from its initial value due to natural convection within the thermocline and thermal losses to the environment. Then it remains stable at 304°C for the next 4 hours, the end of the test. This temperature is near to the solidification temperature of the PCM, which suggests that phase-change could happen within the tubes in a stand-by mode affected by the remained thickness inside the thermocline

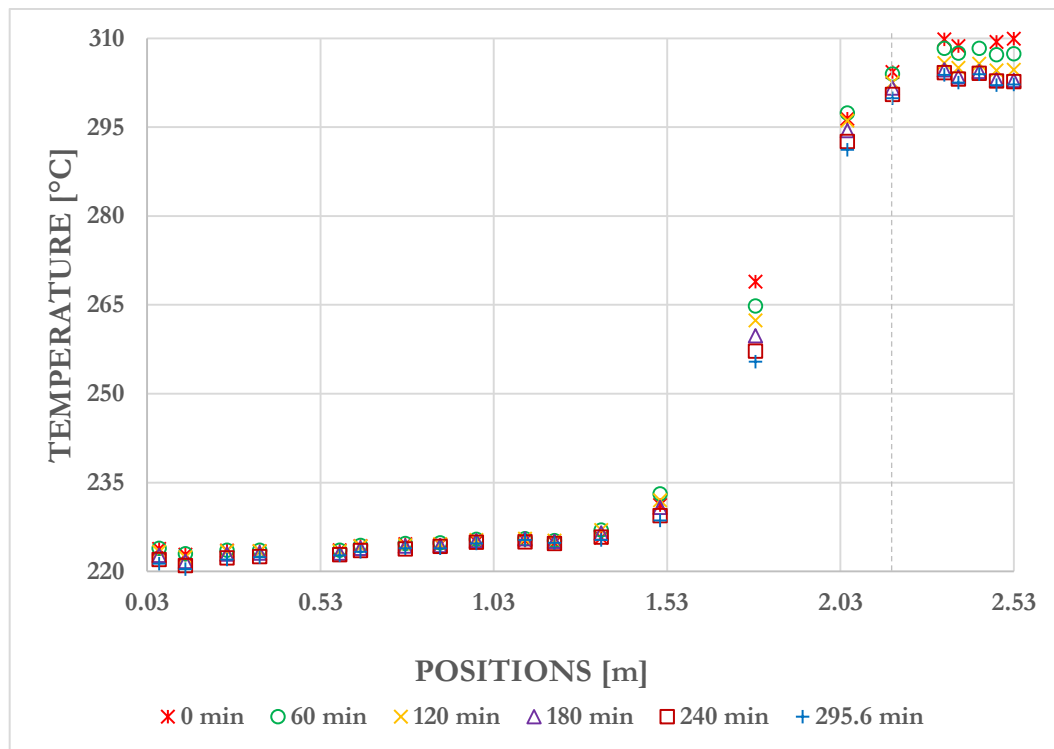


Figure 93. Temperature profile of the of TPCM-S during a stand-by period of 5h

5.4. PERFORMANCE EVALUATION OF TPCM-S. AGAINST SINGLE MEDIUM THERMOCLINE

It is interesting to compare the resulted performance of TPCM-S to the same thermocline filled with alumina spheres as a single medium sensible heat storage material (TSMS) at the same operating conditions.

However, no experiments with the alumina spheres filler were conducted at the same temperatures or the various mass flow rates of the TCTPCM-S tests. Therefore, this section compares the thermal performance between TPCM-S and the TSMS using the two models. The D-C with EPM validated in (5.2) is used to simulate the TPCM-S, and the C-S model validated (3.2) is used to simulate the TSMS. The comparison applies the numerical operating conditions illustrated in Table 44 for both models.

Table 44. Numerical operating conditions for comparing TPCM-S to TSMS thermocline

Process	Charge	Discharge
Mass flow rate [kg/h]	1600	1600
Temperature range [°C]	315 – 220	315 – 220
Threshold temperature [°C]	239	296

5.4.1. Numerical charge tests

For the charging process, the storage mediums are assumed at T_{low} 220°C, while the HTF is injected at a constant mass flow rate of 1600 kg/h and constant temperature T_{high} 315°C.

Figure 94 compares the HTF temperature evolution time at the thermocline outlet, TPCM-S, against TSMS. The Figure shows that the TPCM-S needed about 14% more time than TSMS to reach the charge threshold temperature, 143.3 min and 125.9 min, respectively. Table 45 summarizes the performance parameters resulting from the numerical simulation with better charge efficiency and smaller thermocline thickness in the TPCM-S than the TSMS.

Table 45 performance parameters TPCM-S and TSMS during the charge at 1600 kg/h

Thermocline	TPCM-S	TSMS
Duration [min]	143.3	125.9
Thickness [%]	35.85%	32.58%
Efficiency [%]	84.27%	81.21%

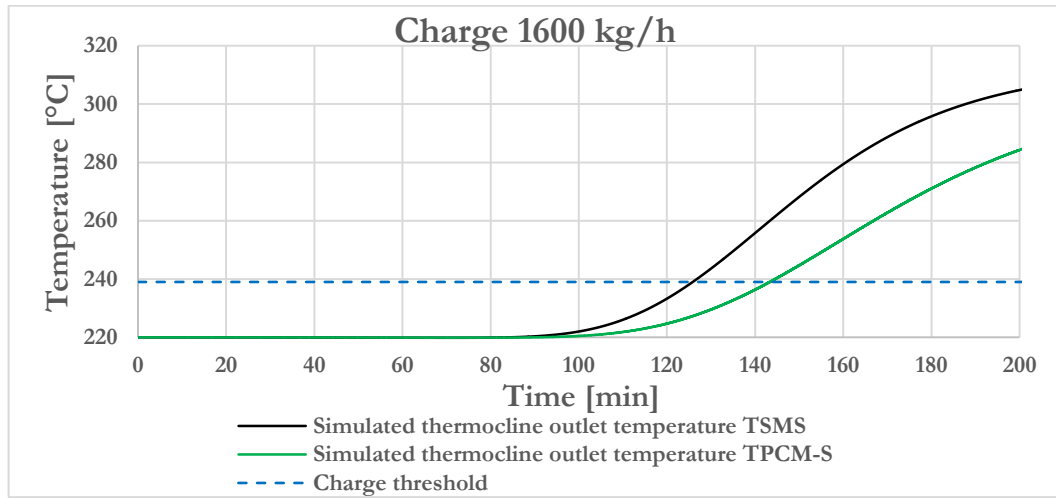


Figure 94. The simulated thermocline outlet temperature evolution with time during charge (220-315) °C, TPCM-S versus TSMS at 1600 kg/h

Figure 95 evaluates the PCM liquid fraction distribution along the last tube radius of the PCM layer during charge (Figure 74 in TPCM-S) at the threshold temperature. It confirms that all the PCM melted with liquid fraction of one at all radial positions.

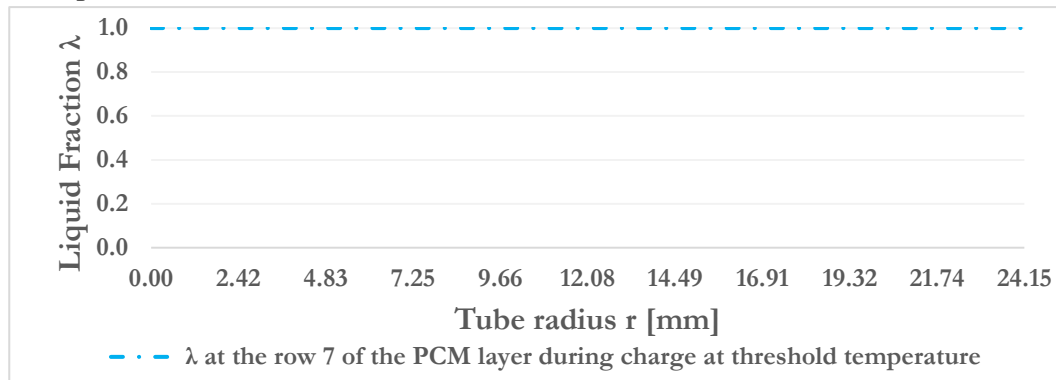


Figure 95. Estimated Liquid fraction at the tube 7 during charge when the threshold temperature is reached at 1600 kg/h

5.4.1.1. The influence of increasing the mass flow rate

Additional two mass flow rates are applied in the simulation with the same previous operating temperatures Table 44, 3000 kg/h, and 3900 kg/h.

Figure 96 illustrates the HTF temperature evolution time at the thermocline outlet, TPCM-S against TSMS at (a) 3000 kg/h, and (b) 3900 kg/h. The Figure illustrates that at 3000 kg/h, the TPCM-S charges in 73 min compared to 66.6 min in the TSMS, which is about 10% longer at 3000 kg/h. And about 9% longer at 3900 kg/h, 55.4 min, 50.9 min, respectively.

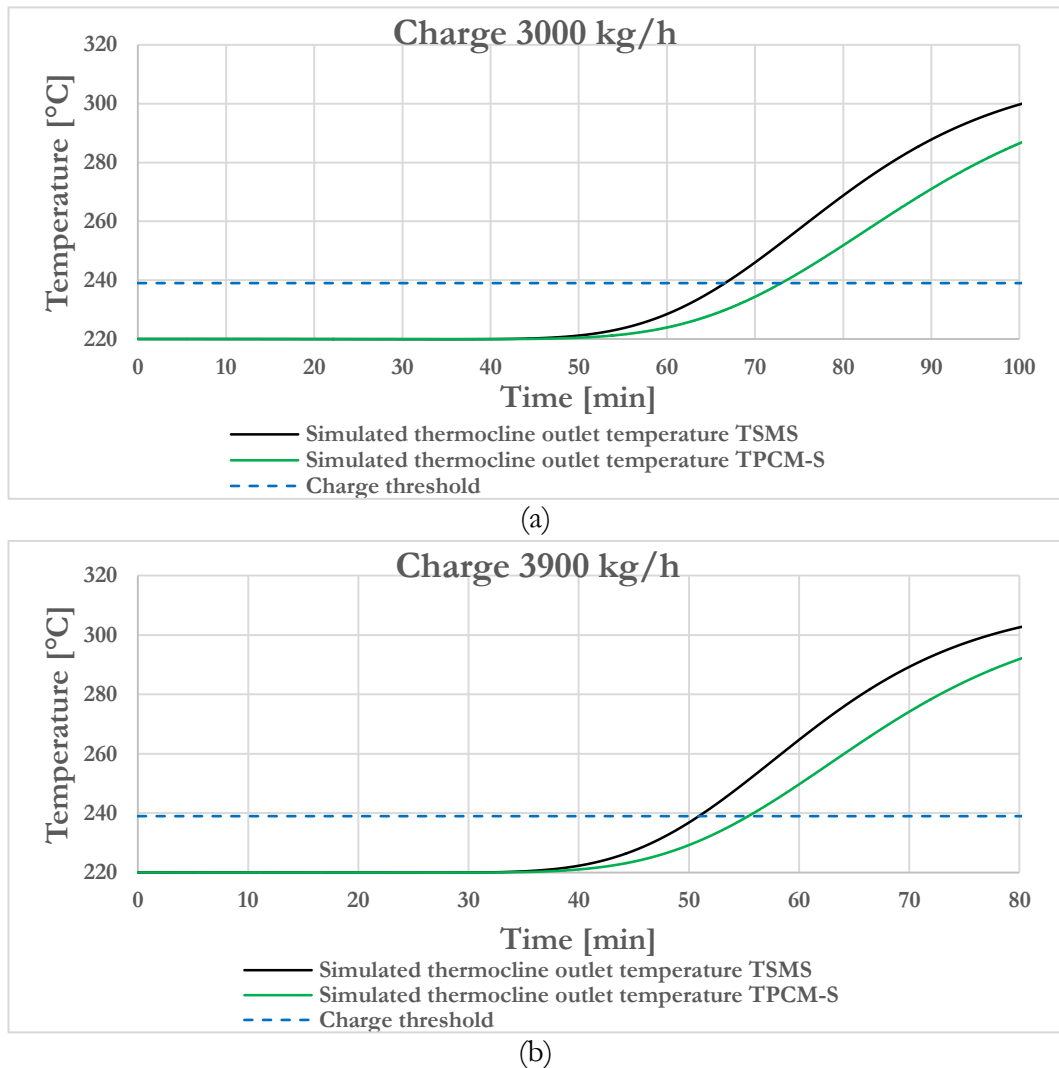


Figure 96. Simulated thermocline outlet temperature evolution in time during charge (220-315) °C, TPCM-S versus TSMS at (a) 3000 kg/h, and (b) 3900 kg/h

Table 46 outlines the performance parameters that are obtained from the charge simulation for TPCM-S and TSMS. It points out that the thermocline thickness has a similar order of magnitude for both cases at various mass flow rates. While the charge efficiencies remain at the same order of magnitude.

Table 46. Performance parameters comparison during the charge at various mass flow rates between TPCM-S and TSMS

Thermocline	TPCM-S	TSMS	TPCM-S	TSMS
mass flow [kg/h]	3000		3900	
Duration [min]	73.0	66.6	55.4	50.9
Thickness [%]	36.63%	33.33%	34.59%	33.33%
Efficiency [%]	80.53%	80.99%	79.39%	80.74%

Figure 97 evaluates the PCM liquid fraction distribution along the last tube radius of the PCM layer during charge (**Erreur ! Source du renvoi introuvable.**)

n TPCM-S at the threshold temperature. It indicates that for 3000 kg/h, the PCM is entirely melted with liquid fraction of one, while for 3900 kg/h, the PCM is still in the solid phase.

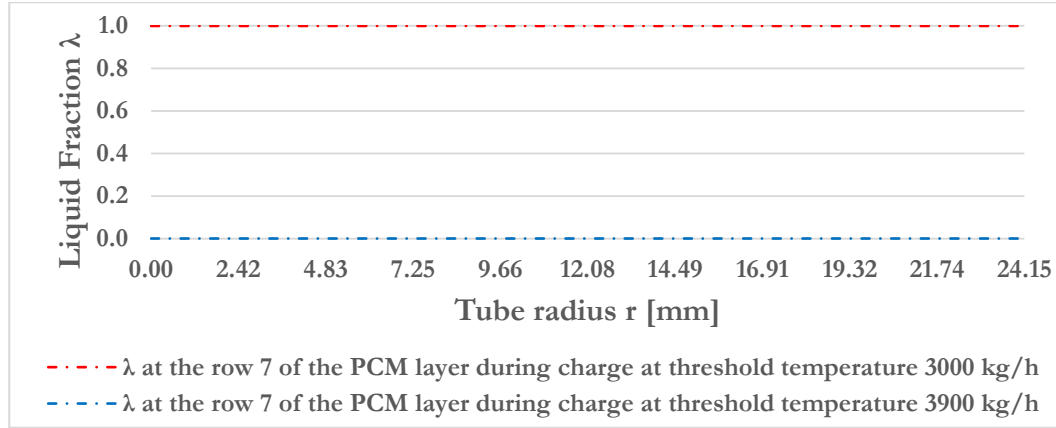


Figure 97. Estimated Liquid fraction at the tube 7 during charge when the threshold temperature is reached at 3000kg/h and 3900kg/h

Figure 98 plots the liquid fraction distribution within the seven tube rows against the radius at the threshold temperature. It indicates that only the first two rows have an entirely melted PCM, and about 40% of the PCM is melted in the third row while the remaining four rows are still in the solid phase, which should significantly affect the performance of the subsequent discharge process in actual operation. This result emphasizes the previously indicated recommendation (5.3.1.1.1) that a high mass flow rate is not favorable during charge, complying with the finding of Bédécarrats et al. [208].

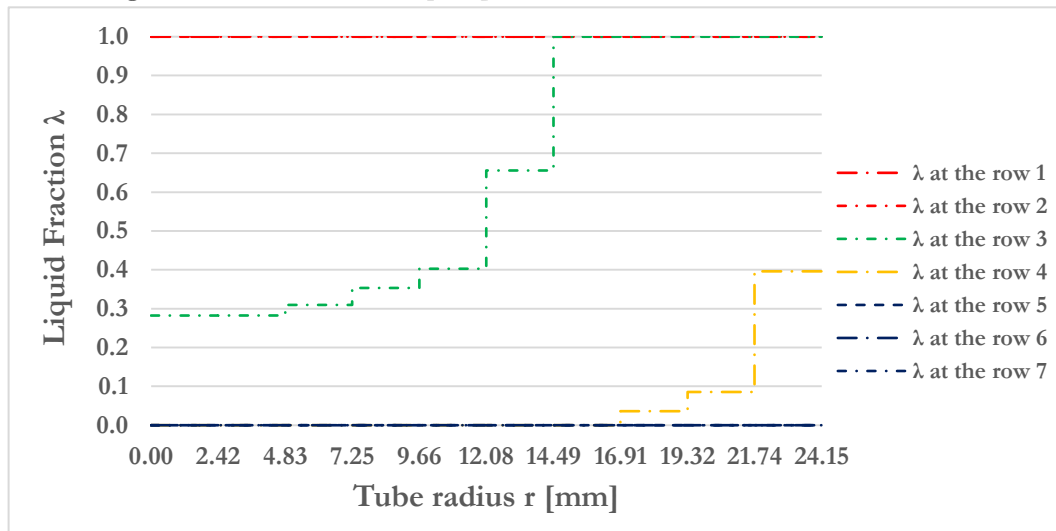


Figure 98. Estimated Liquid fraction at all tubes as depicted by the D-C EPM at the end of the charge at 3900kg/h

5.4.2. Numerical discharge tests

During the discharge tests, all storage mediums are assumed at T_{high} 315°C, while the oil is injected at a constant mass flow rate of 1600 kg/h and constant temperature T_{low} 220°C (Table 44).

Figure 99 compares the simulated outlet temperature of the thermocline during discharge between the TPCM-S and TSMS. The PCM solidification influence appears on the HTF temperature at about 306°C. Hence the TPCM-S discharged duration is about 12% longer than the TSMS, 150 min and 134 min, respectively.

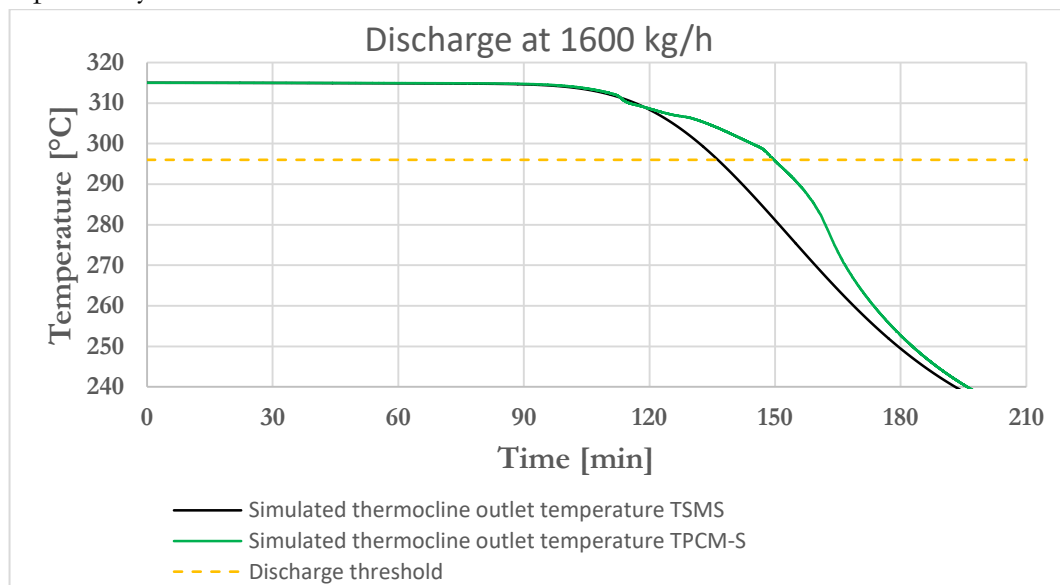


Figure 99. Simulated thermocline outlet temperature evolution in time during discharge (315-220) °C, TPCM-S versus TSMS at 1600 kg/h

Table 47 lists the resulted performance indicators from both simulations at 1600 kg/h. The thermocline thickness was reduced to 16% in the TPCM-S compared to 22% in the TSMS, and the discharge efficiency increased to 86% by comparison to 79%, respectively. The results confirmed that using the PCM layer reduced the thickness and increased the efficiency.

Table 47. Performance parameters TPCM-S and TSMS during discharge at 1600 kg/h

Thermocline	TPCM-S	TSMS
Duration [min]	149.37	134
Thickness [%]	16.04%	22.2%
Efficiency [%]	86.25%	79.12%

The thermocline thickness reduction could be attributed to the PCM phase-change influence, as depicted in Figure 100. Which suggests that the thermocline thickness in the TPCM-S is developed as follow:

- (1) The thickness starts to form and moves up with the HTF direction.
- (2) The thickness expands, and the hot thermal front moves faster than the cold thermal front (Figure 37).
- (3) The hot thermal front reaches the PCM layer at the tank top, where the PCM stops it from moving up due to the phase-change.
- (4) The hot thermal front continues to be fixed by the phase-change, while the cold thermal front moves up quickly, and the thickness is reduced.
- (5) The phase change is finished, so both the hot and cold thermal front could move up further until the end of the process.

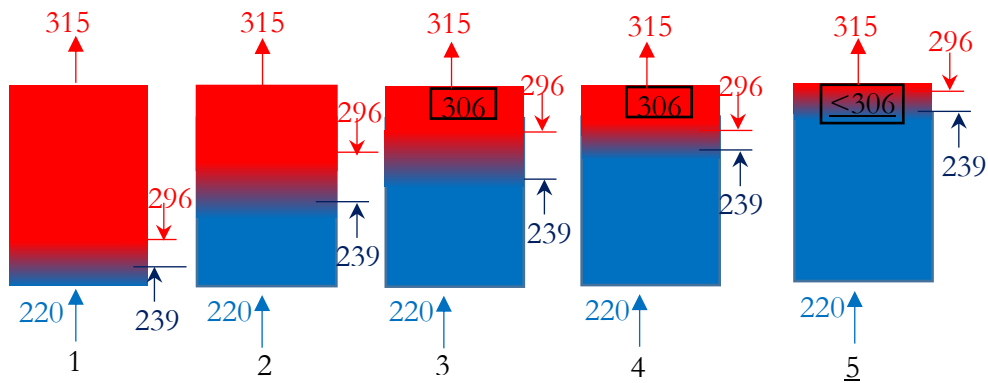


Figure 100. Depiction of thermocline thickness development during discharge in TPCM-S

Figure 101 plots the model-estimated liquid fraction against the tube radius for all rows at the end of discharge (outlet temperature reaches the discharge threshold). During discharge, the first row is in touch with alumina spheres, while the last row is at the thermocline outlet at the top of the tank (Figure 74).

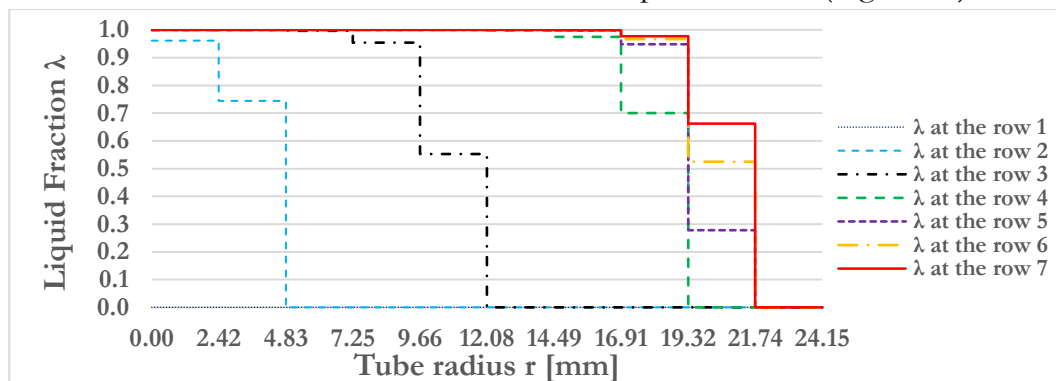
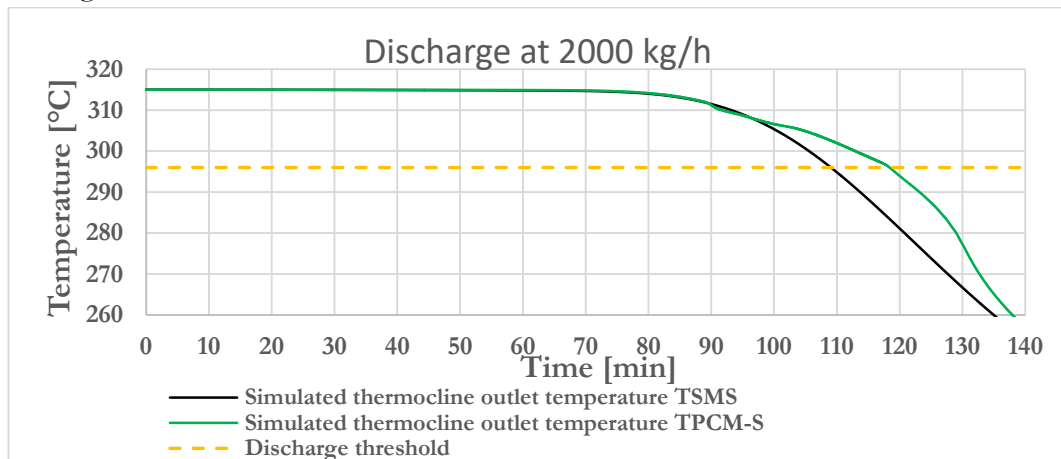


Figure 101. Estimated Liquid fraction all PCM rows during discharge when the threshold temperature is reached at 1600 kg/h

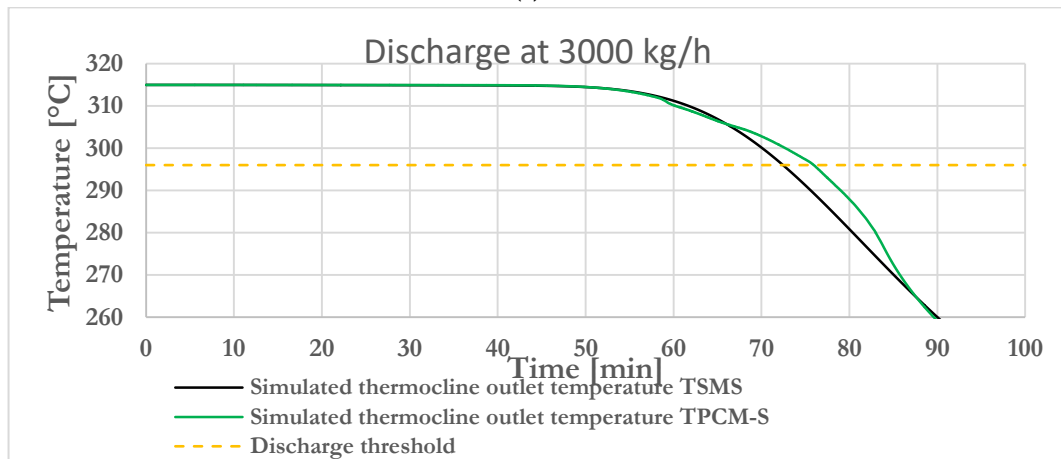
The figure suggests that more than 50% of the PCM in the last four rows of the layer are still in the liquid phase. It is insulated at the tube center from its surface, where the heat transfer occurs with the HTF, due to the low conductivity of the solidified PCM. This suggests that the TPCM-S performance could still be improved using a suitable solution such as adding metal fins or inoculating the PCM to improve its thermal conductivity.

5.4.2.1. The influence of increasing the mass flow rate

Two additional mass flow rates are simulated to compare the TPCM-S to TSMS, with the same previous operating temperatures Table 44, 2000 kg/h, and 3000 kg/h.



(a)



(b)

Figure 102. Simulated thermocline outlet temperature evolution in time during discharge (315–220) °C, TPCM-S versus TSMS at (a) 2000 kg/h and (b) 3000 kg/h

Figure 102 plots the thermocline outlet temperature during the simulated discharge of the TPCM-S and the TSMS at (a) 2000 kg/h, and (b) 3000 kg/h. It illustrates that at 2000 kg/h, the TPCM-S was discharged in 119 min, 9% longer

than the TSMS (109 min). While at the largest mass flow rate used in the experiment 3000 kg/h, the discharge duration in the TPCM-S lasts only for 7% longer than the TSMS, 76 min and 71 min, respectively.

Figure 99, Figure 102 (a), and (b) indicate that the PCM influence on the HTF temperature is less significant when the mass flow rate increases, suggesting that the heat release from PCM becomes negligible compared to heat transfer between the tubes and the HTF.

Table 48 summarizes the performance parameters obtained during the discharge simulations of TPCM-S and TSMS, at the two mass flow rates. It reflects that, the thermocline thickness in the TPCM-S is lower than the TSMS at both mass flow rates. Moreover, the thickness increases in the TPCM-S with the mass flow rate, which could also be attributed to the smaller influence of the PCM heat release compared to the heat transfer between the tubes and the HTF.

Similarly, the discharge efficiency in TPCM-S is reduced with the increase of the discharge rate. Table 48 shows that the discharge efficiency can be improved by about 4% using the TPCM-S with respect to the TSMS.

Table 48. Performance parameters comparison during discharge at various mass flow rates between TPCM-S and TSMS

Thermocline	TPCM-S	TSMS	TPCM-S	TSMS
mass flow [kg/h]	2000		3000	
Duration [min]	119	106	76	71
Thickness [%]	16.25%	25.76%	18.26%	26.52%
Efficiency [%]	83.52%	79.59%	81.30%	78.5%

Figure 103(a) and (b) plot the estimated liquid fraction of the PCM at all rows when the thermocline reaches its discharge threshold temperature at 2000 kg/h, 3000 kg/h, respectively. It indicates that less PCM is solidified inside the tubes at a lower discharge rate than at the higher discharge rate.

Figure 101, Figure 103 (a), and (b) indicate that the amount of solidified PCM is reduced with the discharge rate increase. Furthermore, the amount of liquid PCM indicates that there is additional potential energy that could be used to increase the discharge duration and efficiency. However, the heat transfer coefficient should be improved between the PCM tube and the HTF, using a suitable solution such as improving the thermal conductivity of the PCM, and metal fins within the tubes.

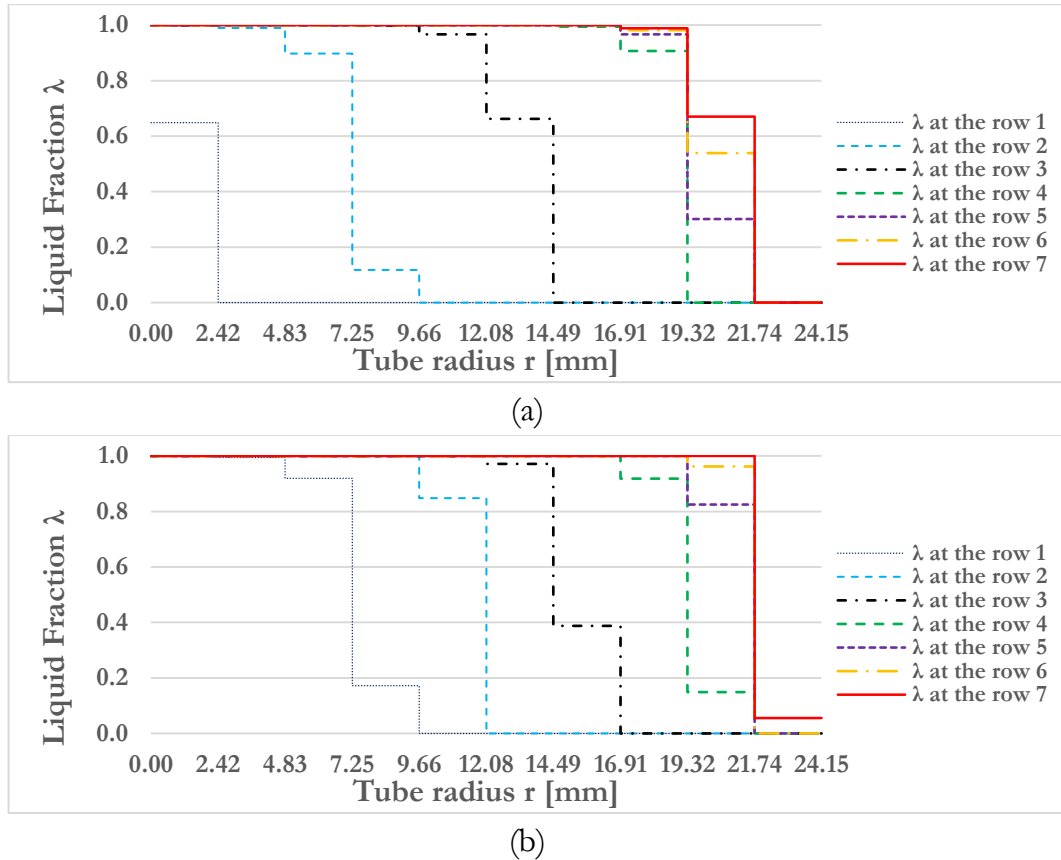


Figure 103. Estimated Liquid fraction all PCM rows during discharge when the threshold temperature is reached at (a) 2000 kg/h and (b) 3000 kg/h

5.4.3. Discussion

In the previous chapter, the suggested approach estimated about 8.5 vol.% of PCM to increase discharge efficiency and duration. However, due to the limited budget, the amount reduced to 5.5%.

Figure 104 compares the potential stored energy in the same 3.5 m³ TES between the reference sensible heat storage thermocline filled with alumina TSMS and the final achieved combined solution TPCM-S. The materials thermal properties are calculated at an average temperature with the actual measurement of the mass and volumes as obtained from the experiment.

The Figure indicates the thermocline storage energy increased by about 4% in the TPCM-S compared to the reference TSMS, with 226.2 KWh and 217.5 kWh, respectively. The ratio of the storage mediums energy to the thermocline is

10.8%, 55.6%, 32.2%, and 1.4% for the PCM, alumina spheres, HTF, and PCM envelope material respectively.

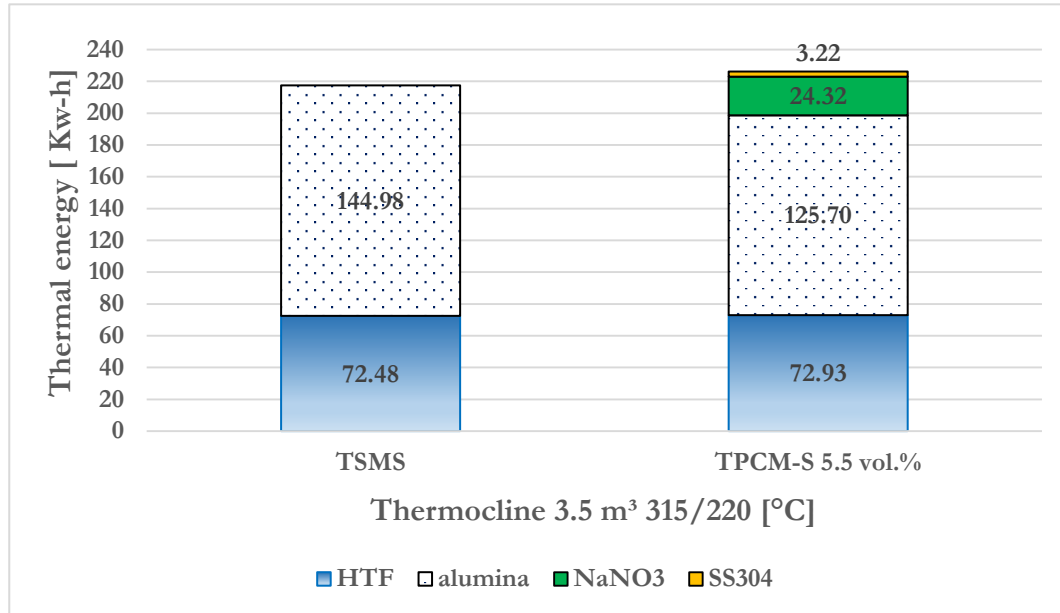


Figure 104. Comparison between thermal storages for the same 3.5 m³ thermocline of TSMS and TPCM-S at temperature 315-220°C

The final TPCM-S thermocline has 13.3% less energy stored in the alumina because the alumina spheres volume is reduced due to the PCM layer addition. This reduction is higher than the 5.5 vol.% added PCM layer, which is attributed to the difference in packing porosity (5.1.7).

Although the resulted in stored energy in the TPCM-S is smaller than the preliminary design, the presented results in this section demonstrate better performance in the TPCM-S than TSMS, with the potential of further improvements using a proper method to improve heat transfer between the HTF and the PCM. Moreover, the lower the mass flow rate, the better the performance of TPCM-S.

5.5. CONCLUSIONS

NaNO_3 provided a suitable solution as PCM for this experimental work because it has a melting point within the operating range of the experimental conditions, its latent heat of fusion is relatively good, it is compatible with a commercial envelop material such as SS304 steel, and safe to be deployed with the synthetic oil (HTF), as experimented in this work.

The stainless steel tubes provided a rigid and economical solution to replace the sphere design.

The developed model in this work that uses a combination of C-S on the sensible heat storage part and D-C EPM in the PCM layer provides a reasonable prediction of TPCM-S performance. They are validated against the experimental results for both charge and discharge.

Lower mass flow rate is favorable against higher mass flow rate during the charging process because of the lower the mass flow, the lower potential of sub-heating, the higher the charge efficiency, and the complete melting in the PCM.

Moreover, the lower inlet temperature is favorable during charge because the nearer the inlet temperature to the PCM's melting point, the lower the potential of sub-heating.

A low discharge rate increases the discharge duration, improves the discharge efficiency, and reduces the thermocline thickness.

Numerical comparison is performed to evaluate the performance parameters of the two solution, TPCM-S and TSMS, during charge and discharge.

The charge efficiency in TPCM-S is found 4% better than TSMS at 1600 kg/h mass flow rates, while at a higher charge rate, there are no significant changes in the thickness and efficiency. High charge rates should be avoided because it is associated with the potential of not melting the entire PCM at the charge threshold value and bigger potential of sub-cooling.

During the discharge simulations, the TPCM-S outperforms the TSMS in almost 4% better discharge efficiency, 4% smaller thermocline thickness, and longer discharge duration. The discharge duration improves by reducing the mass flow rate. The estimated liquid fractions at the discharge threshold temperature suggest that there is still a liquid PCM in the tubes. Hence, the thermocline performance can be improved by applying a suitable heat transfer improvement method in the PCM layer.

6. CONCLUSIONS SUMMARY AND PERSPECTIVES

In this work, the performance of asbestos-based waste material known as Cofalit® compared experimentally against alumina spheres as reference ceramic material, using the MICRO SOL-R CSP.

Cofalit® has a 22% lower volumetric heat capacity than alumina, which results in a 20% faster charge time and a 15% shorter discharge time. The thermocline thickness is lower, with 26% against 31% for the charge, and 20% against 26% for the discharge processes, respectively. Furthermore, the process efficiencies are better, with 82% against 80% for the charge and 90% against 83% for discharge.

Cofalit® outperforms alumina ceramic at the temperature level of this work, 300 °C, due to its smaller average diameter, lower volumetric heat capacity, and inhomogeneous shape.

A 1D C-S model is developed and validated from the experimental results for a sensible heat storage medium. The model is used to perform a parametric analysis of the thermocline thermal behavior. The analysis indicated that an optimum particle diameter could be achieved for a given solid filler material at specified operating conditions, to provide better discharge efficiency and smaller thermocline thickness. Moreover, an increase of volumetric heat capacity increases the process duration, while it decreases the discharge efficiency and increases the thermocline thickness.

The C-S model provides an excellent solution to simulate the thermocline thermal behavior when the solid filler has a $Bi < 0.1$. At the same time, the D-C model is better for the cases where $Bi > 0.1$. The enthalpy porosity method (EPM) affords a reliable way to model PCM melting/solidification compared to the effective heat capacity.

A 1D D-C EPM model is developed and validated from experimental findings from the literature. The two models C-S and D-C EPM, are coupled to simulate the thermal behavior of a combined 75% alumina spheres and 25% NaNO₃ spheres thermocline.

In this work, a general sizing approach is suggested to estimate a range of recommended PCM ratios for a combined thermocline. It indicated that for this study, a ratio of NaNO₃ between 8.5% and 19% is recommended for the alumina spheres based thermocline, and a range between 6.5% and 14.5% for the Cofalit® case.

A PCM layer with 5.5 vol.% is designed and implemented in the MICROSOL-R thermocline. The layer consists of stainless steel tubes and NaNO_3 as PCM. The experimental results suggested a lower mass flow rate is favorable against a higher mass flow rate during the charging and discharging process.

Moreover, the lower inlet temperature is favorable during charge because the nearer the inlet temperature to the PCM's melting point, the lower the potential of sub-cooling.

The combined model is modified to fit the tube's case and validated from the experimental results for charge and discharge. The simulations combined a C-S on the sensible heat storage part and D-C EPM in the PCM layer.

Numerical comparison is performed using the validated combined model to evaluate the two solution performance parameters, TPCM-S and TSMS, during charge and discharge.

The charge efficiency in TPCM-S is found 4% better than TSMS at 1600 kg/h mass flow rates, while at a higher charge rate, there are no essential changes in the thickness and efficiency. High charge rates should be avoided because it is associated with the potential of not melting the entire PCM at the charge threshold value and bigger potential of sub-cooling.

During the discharge simulations, the TPCM-S outperforms the TSMS in almost 4% better discharge efficiency, 4% smaller thermocline thickness, and longer discharge duration. The prolongation in discharge duration improves by reducing the mass flow rate. The estimated liquid fractions at the discharge threshold temperature suggest that there is still a liquid PCM in the tubes. Hence, the thermocline performance can be improved by applying a suitable heat transfer improvement method in the PCM layer.

6.1. PERSPECTIVES

- Although the TPCM-S outperforms the TSMS, there is still potential energy that can be utilized within the tubes, as suggested by the numerical findings. Hence, studying and evaluating the integration of metal fins to the inner side of the tubes to improve the TPCM-S thermocline's performance is needed, where the number, shape, and thickness of the fins should be optimized.
- Furthermore, the benefit of the TPCM-S could be more clearly seen by simulating cyclic charge and discharge. Because TPCM-S is characterized by a lower thermocline thickness compared to TSMS,

hence it is expected to have better overall cyclic performance. Therefore, a numerical cycling study is recommended to be performed to illustrate the add-value of the PCM layer.

- Moreover, the PCM thermophysical properties stability under thermal cycling is required to be addressed, mainly the latent heat of fusion and thermal conductivities, which may degrade under thermal cycling and corrosions from the envelope.
- Adding a PCM layer to the sensible heat thermocline TES is an interesting solution to extend the discharge duration and efficiency if the tank size is fixed due to design constraints. Otherwise, a techno-economical study should be performed to find which is more economically feasible, extending the tank size or adding a PCM layer.
- The main disadvantage of adding the PCM layer is removing part of the original sensible heat filler materials, which reduces the potential stored energy in the thermocline and increases the cost. Therefore, the PCM could be better integrated into the TES in the HTF distributor at the tank top and/or bottom. For example, in the current work integrating the PCM in the HTF distributor illustrated in (Figure 105) could be very interesting because this zone is not an energy storage volume. It is reserved to improve the HTF flow within the tank. Hence, the distributor's design could be optimized to integrate the PCM and extend its purpose to optimize the HTF temperature and HTF flow.



Figure 105 HTF distributor at the top of the thermocline

7. BIBLIOGRAPHY

- [1] IEA, “Energy and Climate Change,” *World Energy Outlook Spec. Rep.*, pp. 1–200, 2015.
- [2] International Energy Agency (IEA), “Renewable energy medium-term market report 2015. Market Analysis and Forecasts to 2020 - Executive Summary,” p. 14, 2015.
- [3] IEA, “Technology Roadmap,” *SpringerReference*, p. 52, 2014.
- [4] R. Sioshansi and P. Denholm, “The Value of Concentrating Solar Power and Thermal Energy Storage,” *IEEE Trans. Energy Convers.*, vol. 1, no. 3, pp. 173–183, 2010.
- [5] X. Py, N. Sadiki, R. Olives, V. Goetz, and Q. Falcoz, “Thermal energy storage for CSP (Concentrating Solar Power),” *EPJ Web Conf.*, vol. 148, pp. 1–24, 2017.
- [6] U. Herrmann and D. W. Kearney, “Survey of thermal energy storage for parabolic trough power plants,” *J. Sol. Energy Eng. Trans. ASME*, vol. 124, no. 2, pp. 145–152, 2002.
- [7] J. Forrester, “The value of CSP with thermal energy storage in providing grid stability,” *Energy Procedia*, vol. 49, pp. 1632–1641, 2014.
- [8] I. Dincer and R. M. A. *THERMAL ENERGY STORAGE SYSTEMS AND APPLICATIONS*, Second. WILEY, 2011.
- [9] IRENA and ETSAP, “Thermal Energy Storage. Technology Brief,” no. January, p. 24, 2013.
- [10] U. Pelay, L. Luo, Y. Fan, D. Stitou, and M. Rood, “Thermal energy storage systems for concentrated solar power plants,” *Renew. Sustain. Energy Rev.*, vol. 79, no. March 2016, pp. 82–100, 2017.
- [11] S. Kuravi, J. Trahan, D. Y. Goswami, M. M. Rahman, and E. K. Stefanakos, “Thermal energy storage technologies and systems for concentrating solar power plants,” *Prog. Energy Combust. Sci.*, vol. 39, no. 4, pp. 285–319, 2013.
- [12] J. E. Pacheco, S. K. Showalter, and W. J. Kolb, “Development of a Molten-Salt Thermocline Thermal Storage System for Parabolic Trough Plants,” *J. Sol. Energy Eng.*, vol. 124, no. 2, pp. 153–159, 2002.
- [13] C. Xu, Z. Wang, Y. He, X. Li, and F. Bai, “Sensitivity analysis of the numerical study on the thermal performance of a packed-bed molten salt thermocline thermal storage system,” *Appl. Energy*, vol. 92, pp. 65–75, 2012.
- [14] E. González-Roubaud, D. Pérez-Osorio, and C. Prieto, “Review of commercial thermal energy storage in concentrated solar power plants: Steam vs. molten salts,” *Renew. Sustain. Energy Rev.*, vol. 80, no. March 2016, pp. 133–148, 2017.
- [15] B. Kilic and S. Kakac, *Energy storage systems*. 1988.

- [16] J. Duffie and W. Beckman, *Solar Engineering of Thermal Processes*, 4th ed., vol. 116. 2013.
- [17] C. Mira-Hernández, S. M. Flueckiger, and S. V. Garimella, "Numerical Simulation of Single- and Dual-media Thermocline Tanks for Energy Storage in Concentrating Solar Power Plants," *Energy Procedia*, vol. 49, pp. 916–926, 2014.
- [18] A. M. Bonanos and E. V. Votyakov, "Sensitivity analysis for thermocline thermal storage tank design," *Renew. Energy*, vol. 99, pp. 764–771, 2016.
- [19] J.-F. Hoffmann, T. Fasquelle, V. Goetz, and X. Py, "Experimental and numerical investigation of a thermocline thermal energy storage tank," *Appl. Therm. Eng.*, vol. 114, pp. 896–904, 2017.
- [20] S. Khare, M. Dell'Amico, C. Knight, and S. McGarry, "Selection of materials for high temperature sensible energy storage," *Sol. Energy Mater. Sol. Cells*, vol. 115, pp. 114–122, 2013.
- [21] A. Gil *et al.*, "State of the art on high temperature thermal energy storage for power generation. Part 1-Concepts, materials and modellization," *Renew. Sustain. Energy Rev.*, vol. 14, no. 1, pp. 31–55, 2010.
- [22] G. Alva, Y. Lin, and G. Fang, "An overview of thermal energy storage systems," *Energy*, vol. 144, pp. 341–378, 2018.
- [23] T. Fasquelle, "Ph.D. Thesis: Modelisation Et Caracterisation Experimentale D'une Boucle Solaire Cylindro-Parabolique Integrant Un Stockage De Type Thermocline," Universite De Perpignan Via Domitia, 2017.
- [24] H. Grirate, H. Agalit, N. Zari, A. Elmchaouri, S. Molina, and R. Couturier, "Experimental and numerical investigation of potential filler materials for thermal oil thermocline storage," *Sol. Energy*, vol. 131, pp. 260–274, 2016.
- [25] R. Tiskatine *et al.*, "Suitability and characteristics of rocks for sensible heat storage in CSP plants," *Sol. Energy Mater. Sol. Cells*, vol. 169, no. May, pp. 245–257, 2017.
- [26] X. Py, N. Calvet, R. Olives, P. Echegut, C. Bessada, and F. Jay, "Thermal Storage for Solar Power Plants Based On Low Cost Recycled Material," in *EFFSTOCK, the 11th International Conference on Thermal Energy Storage*, 2009, vol. 3, no. 1.
- [27] X. Py *et al.*, "Recycled Material for Sensible Heat Based Thermal Energy Storage to be Used in Concentrated Solar Thermal Power Plants," *J. Sol. Energy Eng.*, vol. 133, no. 3, p. 031008, 2011.
- [28] J. Hoffmann, "Ph.D. Thesis: Stockage thermique pour centrale solaire thermodynamique à concentration mettant en oeuvre des matériaux naturels ou recyclés Préparée au sein de l'école doctorale : Présentée par Jean-François HOFFMANN Stockage thermique pour cent," 2015.
- [29] M. Liu *et al.*, "Review on concentrating solar power plants and new developments in high temperature thermal energy storage technologies," *Renew. Sustain. Energy*

- Rev.*, vol. 53, pp. 1411–1432, 2016.
- [30] T. Fasquelle, Q. Falcoz, P. Neveu, J. Walker, and G. Flamant, “Compatibility Study Between Synthetic Oil and Vitrified Wastes for Direct Thermal Energy Storage,” *Waste and Biomass Valorization*, vol. 8, no. 3, pp. 621–631, 2017.
 - [31] A. Elouali *et al.*, “Physical models for packed bed: Sensible heat storage systems,” *J. Energy Storage*, vol. 23, no. February, pp. 69–78, 2019.
 - [32] T. Nomura, N. Okinaka, and T. Akiyama, “Technology of Latent Heat Storage for High Temperature Application: A Review,” *ISIJ Int.*, vol. 50, no. 9, pp. 1229–1239, 2010.
 - [33] D. V Hale, M. J. Hoover, and M. J. O. Neill, “PHASE CHANGE MATERIALS HANDBOOK by NASA Contractor Report NASA CR-51363,” p. 232, 1971.
 - [34] H. Mehling and L. F. Cabeza, *Heat and cold storage with PCM*. Springer Berlin Heidelberg, 2008.
 - [35] A. Lazrak, J. F. Fourmigué, and J. F. Robin, “An innovative practical battery thermal management system based on phase change materials: Numerical and experimental investigations,” *Appl. Therm. Eng.*, vol. 128, pp. 20–32, 2018.
 - [36] H. Nazir *et al.*, “Recent developments in phase change materials for energy storage applications: A review,” *Int. J. Heat Mass Transf.*, vol. 129, pp. 491–523, 2019.
 - [37] V. Kapsalis and D. Karamanis, “Solar thermal energy storage and heat pumps with phase change materials,” *Appl. Therm. Eng.*, vol. 99, pp. 1212–1224, 2016.
 - [38] B. Xu, P. Li, and C. Chan, “Application of phase change materials for thermal energy storage in concentrated solar thermal power plants: A review to recent developments,” *Appl. Energy*, vol. 160, pp. 286–307, 2015.
 - [39] M. Kenisarin and K. Mahkamov, “Solar energy storage using phase change materials,” *Renew. Sustain. Energy Rev.*, vol. 11, no. 9, pp. 1913–1965, 2007.
 - [40] A. Safari, R. Saidur, F. A. Sulaiman, Y. Xu, and J. Dong, “A review on supercooling of Phase Change Materials in thermal energy storage systems,” *Renew. Sustain. Energy Rev.*, vol. 70, no. July 2016, pp. 905–919, 2017.
 - [41] A. Sharma, V. V. Tyagi, C. R. Chen, and D. Buddhi, “Review on thermal energy storage with phase change materials and applications,” *Renew. Sustain. Energy Rev.*, vol. 13, no. 2, pp. 318–345, 2009.
 - [42] G. Alva, L. Liu, X. Huang, and G. Fang, “Thermal energy storage materials and systems for solar energy applications,” *Renew. Sustain. Energy Rev.*, vol. 68, no. August 2016, pp. 693–706, 2017.
 - [43] E. Omaraa, “A Review on Thermophysical Properties Data of High Temperature Phase Change Materials for Thermal Energy Storage,” no. April, 2016.

- [44] E. Rojas, R. Bayón, and E. Zarza, "Liquid Crystals: A Different Approach for Storing Latent Energy in a DSG Plant," *Energy Procedia*, vol. 69, pp. 1014–1022, 2015.
- [45] S. Pincemin, R. Olives, X. Py, and M. Christ, "Highly conductive composites made of phase change materials and graphite for thermal storage," *Sol. Energy Mater. Sol. Cells*, vol. 92, no. 6, pp. 603–613, 2008.
- [46] G. Zanganeh, M. Commerford, A. Haselbacher, A. Pedretti, and A. Steinfeld, "Stabilization of the outflow temperature of a packed-bed thermal energy storage by combining rocks with phase change materials," *Appl. Therm. Eng.*, vol. 70, no. 1, pp. 316–320, 2014.
- [47] A. Ramos, J. Gonzalez-aguilar, M. M. Rahman, D. Y. Goswami, M. Romero, and E. K. Stefanakos, "The melting process of storage materials with relatively high phase change temperatures in partially filled spherical shells," *Appl. Energy*, vol. 116, pp. 243–252, 2014.
- [48] M. Liu, W. Saman, and F. Bruno, "Review on storage materials and thermal performance enhancement techniques for high temperature phase change thermal storage systems," *Renew. Sustain. Energy Rev.*, vol. 16, no. 4, pp. 2118–2132, 2012.
- [49] G. Wei *et al.*, "Selection principles and thermophysical properties of high temperature phase change materials for thermal energy storage: A review," *Renew. Sustain. Energy Rev.*, vol. 81, no. June 2017, pp. 1771–1786, 2018.
- [50] A. Shinde, S. Arpit, P. Km, P. V. C. Rao, and S. K. Saha, "Heat Transfer Characterization and Optimization of Latent Heat Thermal Storage System Using Fins for Medium Temperature Solar Applications," *J. Sol. Energy Eng. Trans. ASME*, vol. 139, no. 3, pp. 1–10, 2017.
- [51] K. D'Avignon and M. Kummert, "Experimental assessment of a phase change material storage tank," *Appl. Therm. Eng.*, vol. 99, pp. 880–891, 2016.
- [52] A. F. Regin, S. C. Solanki, and J. S. Saini, "Heat transfer characteristics of thermal energy storage system using PCM capsules: A review," *Renew. Sustain. Energy Rev.*, vol. 12, no. 9, pp. 2438–2451, 2008.
- [53] R. Jacob and F. Bruno, "Review on shell materials used in the encapsulation of phase change materials for high temperature thermal energy storage," *Renew. Sustain. Energy Rev.*, vol. 48, pp. 79–87, 2015.
- [54] P. B. Salunkhe and P. S. Shembekar, "A review on effect of phase change material encapsulation on the thermal performance of a system," *Renew. Sustain. Energy Rev.*, vol. 16, no. 8, pp. 5603–5616, 2012.
- [55] S. H. Goods and R. W. Bradshaw, "Corrosion of Stainless Steels and Carbon Steel by Molten Mixtures of Commercial Nitrate Salts," *ASM Int.*, vol. 13, no. February, pp. 78–87, 2003.
- [56] T. E. Alam, J. S. Dhau, D. Y. Goswami, and E. Stefanakos, "Macroencapsulation

- and characterization of phase change materials for latent heat thermal energy storage systems,” *Appl. Energy*, vol. 154, pp. 92–101, 2015.
- [57] B. Muñoz-Sánchez, I. Iparraguirre-Torres, V. Madina-Arrese, U. Izaguirre-Etxeberria, A. Unzueta-Iturbe, and A. García-Romero, “Encapsulated High Temperature PCM as Active Filler Material in a Thermocline-based Thermal Storage System,” *Energy Procedia*, vol. 69, pp. 937–946, 2015.
- [58] G. Peng, G. Dou, Y. Hu, Y. Sun, and Z. Chen, “Phase Change Material (PCM) Microcapsules for Thermal Energy Storage,” vol. 2020, 2020.
- [59] V. S. Dušan Medved, Milan Kvakovsky, “Latent Heat Storage Systems,” *Intensive Program. “Renewable Energy Sources,”* vol. i, no. May, 2010.
- [60] S. Jegadheeswaran and S. D. Pohekar, “Performance enhancement in latent heat thermal storage system : A review,” vol. 13, pp. 2225–2244, 2009.
- [61] Y. Lin, Y. Jia, G. Alva, and G. Fang, “Review on thermal conductivity enhancement, thermal properties and applications of phase change materials in thermal energy storage,” *Renew. Sustain. Energy Rev.*, vol. 82, no. May 2017, pp. 2730–2742, 2018.
- [62] A. Hoshi, D. R. Mills, A. Bittar, and T. S. Saitoh, “Screening of high melting point phase change materials (PCM) in solar thermal concentrating technology based on CLFR,” *Sol. Energy*, vol. 79, no. 3, pp. 332–339, 2005.
- [63] H. O. Paksoy, *Thermal Energy Storage for Sustainable Energy Consumption*. Springer, 2005.
- [64] L. Huang, E. Günther, C. Doetsch, and H. Mehling, “Subcooling in PCM emulsions-Part 1: Experimental,” *Thermochim. Acta*, vol. 509, no. 1–2, pp. 93–99, 2010.
- [65] M. Faucheux, G. Muller, M. Havet, and A. LeBail, “Influence of surface roughness on the supercooling degree: Case of selected water/ethanol solutions frozen on aluminium surfaces,” *Int. J. Refrig.*, vol. 29, no. 7, pp. 1218–1224, 2006.
- [66] S. F. Hosseinzadeh, F. L. Tan, and S. M. Moosania, “Experimental and numerical studies on performance of PCM-based heat sink with different configurations of internal fins,” *Appl. Therm. Eng.*, vol. 31, no. 17–18, pp. 3827–3838, 2011.
- [67] K. Kant, A. Shukla, and A. Sharma, “Solar Energy Materials and Solar Cells Advancement in phase change materials for thermal energy storage applications,” *Sol. Energy Mater. Sol. Cells*, vol. 172, no. April, pp. 82–92, 2017.
- [68] L. W. Fan, Z. Q. Zhu, and M. J. Liu, “A similarity solution to unidirectional solidification of nano-enhanced phase change materials (NePCM) considering the mushy region effect,” *Int. J. Heat Mass Transf.*, vol. 86, pp. 478–481, 2015.
- [69] G. Sukhorukov, A. Fery, and H. Möhwald, “Intelligent micro- and nanocapsules,” *Prog. Polym. Sci.*, vol. 30, no. 8–9, pp. 885–897, 2005.

- [70] F. Agyenim, N. Hewitt, P. Eames, and M. Smyth, "A review of materials, heat transfer and phase change problem formulation for latent heat thermal energy storage systems (LHTESS)," *Renew. Sustain. Energy Rev.*, vol. 14, no. 2, pp. 615–628, 2010.
- [71] R. Hendra, Hamdani, T. M. I. Mahlia, and H. H. Masjuki, "Thermal and melting heat transfer characteristics in a latent heat storage system using mikro," *Appl. Therm. Eng.*, vol. 25, no. 10, pp. 1503–1515, 2005.
- [72] V. Becattini, L. Geissbühler, G. Zanganeh, A. Haselbacher, and A. Steinfeld, "Pilot-scale demonstration of advanced adiabatic compressed air energy storage, Part 2: Tests with combined sensible/latent thermal-energy storage," *J. Energy Storage*, vol. 17, pp. 140–152, 2018.
- [73] N. I. Ibrahim, F. A. Al-Sulaiman, S. Rahman, B. S. Yilbas, and A. Z. Sahin, "Heat transfer enhancement of phase change materials for thermal energy storage applications: A critical review," *Renew. Sustain. Energy Rev.*, vol. 74, no. January, pp. 26–50, 2017.
- [74] X. Yang, P. Wei, X. Cui, L. Jin, and Y. L. He, "Thermal response of annuli filled with metal foam for thermal energy storage: An experimental study," *Appl. Energy*, vol. 250, no. May, pp. 1457–1467, 2019.
- [75] X. Yang, J. Yu, Z. Guo, L. Jin, and Y. L. He, "Role of porous metal foam on the heat transfer enhancement for a thermal energy storage tube," *Appl. Energy*, vol. 239, no. February, pp. 142–156, 2019.
- [76] X. Yang, Z. Guo, Y. Liu, L. Jin, and Y. L. He, "Effect of inclination on the thermal response of composite phase change materials for thermal energy storage," *Appl. Energy*, vol. 238, no. October 2018, pp. 22–33, 2019.
- [77] C. R. E. S. Nóbrega, K. A. R. Ismail, and F. A. M. Lino, "Correlations for predicting the performance of axial finned tubes submersed in PCM," *J. Energy Storage*, vol. 26, no. August, p. 100973, 2019.
- [78] G. Peiró, J. Gasia, L. Miró, and L. F. Cabeza, "Experimental evaluation at pilot plant scale of multiple PCMs (cascaded) vs. single PCM configuration for thermal energy storage," *Renew. Energy*, vol. 83, pp. 729–736, 2015.
- [79] H. Chirino, B. Xu, and X. Xu, "Parametric study of cascade latent heat thermal energy storage (CLHTES) system in Concentrated Solar Power (CSP) plants," *J. Energy Inst.*, vol. 92, no. 3, pp. 653–664, 2019.
- [80] A. M. Abdulateef, S. Mat, J. Abdulateef, K. Sopian, and A. A. Al-Abidi, "Geometric and design parameters of fins employed for enhancing thermal energy storage systems: a review," *Renew. Sustain. Energy Rev.*, vol. 82, no. June 2016, pp. 1620–1635, 2018.
- [81] J. M. Mahdi, S. Lohrasbi, and E. C. Nsofor, "Hybrid heat transfer enhancement for latent-heat thermal energy storage systems: A review," *Int. J. Heat Mass Transf.*,

- vol. 137, pp. 630–649, 2019.
- [82] W. Song, Y. Lu, Y. Wu, and C. Ma, “Effect of SiO₂ nanoparticles on specific heat capacity of low-melting-point eutectic quaternary nitrate salt,” *Sol. Energy Mater. Sol. Cells*, vol. 179, no. February, pp. 66–71, 2018.
- [83] A. R. Balakrishnan and D. C. T. Pei, “Heat Transfer in Gas-Solid Packed Bed Systems. 1. A Critical Review,” *Ind. Eng. Chem. Process Des. Dev.*, vol. 18, no. 1, pp. 30–40, 1979.
- [84] D. Kunii and J. M. Smith, “Heat transfer characteristics of porous rocks,” *AIChE J.*, vol. 6, no. 1, pp. 71–78, 1960.
- [85] T. Esence, A. Bruch, S. Molina, B. Stutz, and J. F. Fourmigué, “A review on experience feedback and numerical modeling of packed-bed thermal energy storage systems,” *Sol. Energy*, vol. 153, pp. 628–654, 2017.
- [86] K. Nithyanandam, R. Pitchumani, and A. Mathur, “Analysis of a latent thermocline storage system with encapsulated phase change materials for concentrating solar power,” *Appl. Energy*, vol. 113, pp. 1446–1460, 2014.
- [87] J. F. Hoffmann, T. Fasquelle, V. Goetz, and X. Py, “A thermocline thermal energy storage system with filler materials for concentrated solar power plants: Experimental data and numerical model sensitivity to different experimental tank scales,” *Appl. Therm. Eng.*, vol. 100, pp. 753–761, 2016.
- [88] D. E. Beasley and J. A. Clark, “Transient response of a packed bed for thermal energy storage,” *Int. J. Heat Mass Transf.*, vol. 27, no. 9, pp. 1659–1669, 1984.
- [89] K. A. R. Ismail and R. Stuginsky Jr, “A parametric study on possible fixed bed models for pcm and sensible heat storage,” *Appl. Therm. Eng.*, vol. 19, no. 7, pp. 757–788, 1999.
- [90] A. de Gracia and L. F. Cabeza, “Numerical simulation of a PCM packed bed system: A review,” *Renew. Sustain. Energy Rev.*, vol. 69, no. October 2014, pp. 1055–1063, 2017.
- [91] J. M. Smith, “Heat and mass transfer in packed beds, N. Wakao and S. Kaguei, Gordon and Breach Science Publishers, 1983, 364 pages,” *AIChE J.*, vol. 29, no. 6, pp. 1055–1055, Nov. 1983.
- [92] T. E. W. Schumann, “Heat transfer: A liquid flowing through a porous prism,” *J. Franklin Inst.*, vol. 208, no. 3, pp. 405–416, 1929.
- [93] J. T. Van Lew, P. Li, C. L. Chan, W. Karaki, and J. Stephens, “Transient Heat Delivery and Storage Process in a Thermocline Heat Storage System,” *Vol. 6 Emerg. Technol. Altern. Energy Syst. Energy Syst. Anal. Thermodyn. Sustain.*, pp. 139–148, 2009.
- [94] W. Karaki, J. T. Van Lew, and J. Stephens, “HEAT TRANSFER IN THERMOCLINE STORAGE SYSTEM WITH FILLER MATERIALS:

ANALYTICAL MODEL,” no. m, pp. 1–10, 2016.

- [95] P. Li, J. Van Lew, W. Karaki, C. Chan, J. Stephens, and Q. Wang, “Generalized charts of energy storage effectiveness for thermocline heat storage tank design and calibration,” *Sol. Energy*, vol. 85, no. 9, pp. 2130–2143, 2011.
- [96] M. M. Valmiki, W. Karaki, P. Li, J. Van Lew, C. Chan, and J. Stephens, “Experimental Investigation of Thermal Storage Processes in a Thermocline Tank,” *J. Sol. Energy Eng.*, vol. 134, no. 4, p. 041003, 2012.
- [97] B. Xu, P. W. Li, and C. L. Chan, “Extending the validity of lumped capacitance method for large Biot number in thermal storage application,” *Sol. Energy*, vol. 86, no. 6, pp. 1709–1724, 2012.
- [98] P. Li, B. Xu, J. Han, and Y. Yang, “Verification of a model of thermal storage incorporated with an extended lumped capacitance method for various solid-fluid structural combinations,” *Sol. Energy*, vol. 105, pp. 71–81, 2014.
- [99] D. Vortmeyer and R. J. Schaefer, “Equivalence of one- and two-phase models for heat transfer processes in packed beds: one dimensional theory,” *Chem. Eng. Sci.*, vol. 29, no. 2, pp. 485–491, 1974.
- [100] H. Littman and D. E. Silva, “GAS-PARTICLE HEAT TRANSFER COEFFICIENTS IN PACKED BEDS AT LOW REYNOLDS NUMBERS,” *Int. Heat Transf. Conf. Paris-Versailles*, vol. 7, 1970.
- [101] M. Hänchen, S. Brückner, and A. Steinfeld, “High-temperature thermal storage using a packed bed of rocks - Heat transfer analysis and experimental validation,” *Appl. Therm. Eng.*, vol. 31, no. 10, pp. 1798–1806, 2011.
- [102] N. Mertens, F. Alobaid, L. Frigge, and B. Eppele, “Dynamic simulation of integrated rock-bed thermocline storage for concentrated solar power,” *Sol. Energy*, vol. 110, pp. 830–842, 2014.
- [103] G. Zanganeh, A. Pedretti, S. Zavattoni, M. Barbato, and A. Steinfeld, “Packed-bed thermal storage for concentrated solar power – Pilot-scale demonstration and industrial-scale design,” *Sol. Energy*, vol. 86, no. 10, pp. 3084–3098, 2012.
- [104] G. Zanganeh, A. Pedretti, S. A. Zavattoni, M. C. Barbato, A. Haselbacher, and A. Steinfeld, “Design of a 100 MWhth packed-bed thermal energy storage,” *Energy Procedia*, vol. 49, pp. 1071–1077, 2013.
- [105] G. Zanganeh, A. Pedretti, A. Haselbacher, and A. Steinfeld, “Design of packed bed thermal energy storage systems for high-temperature industrial process heat,” *Appl. Energy*, vol. 137, pp. 812–822, 2015.
- [106] E. V. Votyakov and A. M. Bonanos, “A perturbation model for stratified thermal energy storage tanks,” *Int. J. Heat Mass Transf.*, vol. 75, pp. 218–223, 2014.
- [107] M. T. Mabrouk, A. Kheiri, and M. Feidt, “Using Generalized Integral Transforms to solve a perturbation model for a packed bed thermal energy storage tank,” *Int.*

- J. Heat Mass Transf.*, vol. 84, pp. 633–641, 2015.
- [108] M. Riaz, “Analytical Solutions for Single- and Two-Phase Models of Packed-Bed Thermal Storage Systems,” vol. 99, no. August 1977, pp. 489–492, 2014.
- [109] M. Cascetta, G. Cau, P. Puddu, and F. Serra, “Numerical investigation of a packed bed thermal energy storage system with different heat transfer fluids,” *Energy Procedia*, vol. 45, pp. 598–607, 2014.
- [110] Z. Yang and S. V. Garimella, “Thermal analysis of solar thermal energy storage in a molten-salt thermocline,” *Sol. Energy*, vol. 84, no. 6, pp. 974–985, 2010.
- [111] G. Angelini, A. Lucchini, and G. Manzolini, “Comparison of thermocline molten salt storage performances to commercial two-tank configuration,” *Energy Procedia*, vol. 49, pp. 694–704, 2013.
- [112] I. Hernández Arriaga, F. Zaversky, and D. Astrain, “Object-oriented Modeling of Molten-salt-based Thermocline Thermal Energy Storage for the Transient Performance Simulation of Solar Thermal Power Plants,” *Energy Procedia*, vol. 69, pp. 879–890, 2015.
- [113] R. Anderson, S. Shiri, H. Bindra, and J. F. Morris, “Experimental results and modeling of energy storage and recovery in a packed bed of alumina particles,” *Appl. Energy*, vol. 119, pp. 521–529, 2014.
- [114] A. Bruch, J. F. Fourmigué, and R. Couturier, “Experimental and numerical investigation of a pilot-scale thermal oil packed bed thermal storage system for CSP power plant,” *Sol. Energy*, vol. 105, pp. 116–125, 2014.
- [115] R. Bayón and E. Rojas, “Simulation of thermocline storage for solar thermal power plants: From dimensionless results to prototypes and real-size tanks,” *Int. J. Heat Mass Transf.*, vol. 60, no. 1, pp. 713–721, 2013.
- [116] R. Bayón and E. Rojas, “Analytical description of thermocline tank performance in dynamic processes and stand-by periods,” *Energy Procedia*, vol. 57, pp. 617–626, 2014.
- [117] R. Bayón, E. Rivas, and E. Rojas, “Study of Thermocline Tank Performance in Dynamic Processes and Stand-by Periods with an Analytical Function,” *Energy Procedia*, vol. 49, pp. 725–734, 2014.
- [118] I. A. S. Ehtiwesh and A. C. M. Sousa, “Numerical model for the thermal behavior of thermocline storage tanks,” 2017.
- [119] R. Anderson, L. Bates, E. Johnson, and J. F. Morris, “Packed bed thermal energy storage: A simplified experimentally validated model,” *J. Energy Storage*, vol. 4, pp. 14–23, 2015.
- [120] C. Xu, Z. Wang, Y. He, X. Li, and F. Bai, “Parametric study and standby behavior of a packed-bed molten salt thermocline thermal storage system,” *Renew. Energy*, vol. 48, pp. 1–9, 2012.

- [121] M. Sagara, P. Schneider, and J. M. Smiths, "The Determination of Heat-Transfer Parameters for Flow in Packed Beds using Pulse Testing and Chromatography Theory," 1969.
- [122] A. E. Saez, "Storage System--a Model for Solar Air Heating," vol. 29, no. 3, pp. 201–206, 1982.
- [123] B. Shiozawa and N. Wakao, "Dispersion-concentric packed bed heat," *Chem. Eng. Sci.*, vol. 32, no. 8, pp. 507–513, 1976.
- [124] C. Xu, X. Li, Z. Wang, Y. He, and F. Bai, "Effects of solid particle properties on the thermal performance of a packed-bed molten-salt thermocline thermal storage system," *Appl. Therm. Eng.*, vol. 57, no. 1–2, pp. 69–80, 2013.
- [125] Y. Dutil, D. R. Rousse, N. Ben Salah, S. Lassue, and L. Zalewski, "A review on phase-change materials: Mathematical modeling and simulations," *Renew. Sustain. Energy Rev.*, vol. 15, no. 1, pp. 112–130, 2011.
- [126] S. Liu, Y. Li, and Y. Zhang, "Mathematical solutions and numerical models employed for the investigations of PCMs' phase transformations," *Renew. Sustain. Energy Rev.*, vol. 33, pp. 659–674, 2014.
- [127] H. Hu and S. a Argyropoulos, "Mathematical modelling of solidification and melting: a review," *Model. Simul. Mater. Sci. Eng.*, vol. 4, no. 4, pp. 371–396, 1999.
- [128] J. P. Bedecarrats and J. P. Dumas, "Etude de la cristallisation de nodules contenant un materiau ?? changement de phase en vue du stockage par chaleur latente," *International Journal of Heat and Mass Transfer*, vol. 40, no. 1, pp. 149–157, 1996.
- [129] T. Kousksou, J. P. Bédécarrats, J. P. Dumas, and A. Mimet, "Dynamic modelling of the storage of an encapsulated ice tank," *Appl. Therm. Eng.*, vol. 25, no. 10, pp. 1534–1548, 2005.
- [130] Y. Cao and A. Faghri, "A Numerical Analysis of Phase-Change Problems Including Natural Convection," *ASME*, vol. 112, no. 20, 1990.
- [131] D. E. Beasley, C. Ramanarayanan, and H. Torab, "Thermal response of a packed bed of spheres containing a phase-change material," *Int. J. Energy Res.*, vol. 13, no. 3, pp. 253–265, 1989.
- [132] V. R. Voller, "FAST IMPLICIT FINITE-DIFFERENCE METHOD FOR THE ANALYSIS OF PHASE CHANGE PROBLEMS," *Numer. Heat Transf.*, vol. 17, no. September 2012, pp. 155–169, 1990.
- [133] E. Tumilowicz, C. L. Chan, P. Li, and B. Xu, "An enthalpy formulation for thermocline with encapsulated PCM thermal storage and benchmark solution using the method of characteristics," *Int. J. Heat Mass Transf.*, vol. 79, pp. 362–377, 2014.
- [134] B. Xu, P. Li, and C. Chan, "Volume Sizing for Thermal Storage With Phase Change Material for Concentrated Solar Power Plant," *ASME 2014 8th Int. Conf. Energy*

- Sustain. collocated with ASME 2014 12th Int. Conf. Fuel Cell Sci. Eng. Technol.*, pp. 1–11, 2014.
- [135] B. Xu, P. Li, C. Chan, and E. Tumilowicz, “General volume sizing strategy for thermal storage system using phase change material for concentrated solar thermal power plant,” *Appl. Energy*, vol. 140, pp. 256–268, 2015.
- [136] B. Xu and C. Chan, “Fluid Charge and Discharge Strategies of Dual-media Thermal Storage Systems in the Starting-up Process of Daily Cyclic Operations,” pp. 1–11, 2016.
- [137] A. Felix Regin, S. C. Solanki, and J. S. Saini, “An analysis of a packed bed latent heat thermal energy storage system using PCM capsules: Numerical investigation,” *Renew. Energy*, vol. 34, no. 7, pp. 1765–1773, 2009.
- [138] G. Manfrida, R. Secchi, and K. Stańczyk, “Modelling and simulation of phase change material latent heat storages applied to a solar-powered Organic Rankine Cycle,” *Appl. Energy*, vol. 179, pp. 378–388, 2016.
- [139] K. A. R. Ismail and J. R. Henriques, “Numerical and experimental study of spherical capsules packed bed latent heat storage system,” *Appl. Therm. Eng.*, vol. 22, no. 15, pp. 1705–1716, 2002.
- [140] K. Nithyanandam, R. Pitchumani, and A. Mathur, “Analysis of a latent thermocline energy storage system for concentrating solar power plants,” *ASME 2012 6th Int. Conf. Energy Sustain. ES 2012, Collocated with ASME 2012 10th Int. Conf. Fuel Cell Sci. Eng. Technol.*, no. PARTS A AND B, pp. 1–10, 2012.
- [141] J. H. L. IV and J. H. Lienhard, “A HEAT TRANSFER TEXTBOOK,” vol. Third Edit, p. 749, 2005.
- [142] S. Wu and G. Fang, “Dynamic performances of solar heat storage system with packed bed using myristic acid as phase change material,” *Energy Build.*, vol. 43, no. 5, pp. 1091–1096, 2011.
- [143] S. Wu, G. Fang, and X. Liu, “Dynamic discharging characteristics simulation on solar heat storage system with spherical capsules using paraffin as heat storage material,” *Renew. Energy*, vol. 36, no. 4, pp. 1190–1195, 2011.
- [144] Y. Li, G. Huang, T. Xu, X. Liu, and H. Wu, “Optimal design of PCM thermal storage tank and its application for winter available open-air swimming pool,” *Appl. Energy*, vol. 209, no. September 2017, pp. 224–235, 2018.
- [145] S. M. Flueckiger and S. V. Garimella, “Latent heat augmentation of thermocline energy storage for concentrating solar power - A system-level assessment,” *Appl. Energy*, vol. 116, pp. 278–287, 2014.
- [146] C. Arkar and S. Medved, “Influence of accuracy of thermal property data of a phase change material on the result of a numerical model of a packed bed latent heat storage with spheres,” *Thermochim. Acta*, vol. 438, no. 1–2, pp. 192–201, 2005.

- [147] M. A. Izquierdo-Barrientos, C. Sobrino, and J. A. Almendros-Ibáñez, "Modeling and experiments of energy storage in a packed bed with PCM," *Int. J. Multiph. Flow*, vol. 86, pp. 1–9, 2016.
- [148] S. Bellan *et al.*, "Numerical analysis of charging and discharging performance of a thermal energy storage system with encapsulated phase change material," *Appl. Therm. Eng.*, vol. 71, no. 1, pp. 481–500, 2014.
- [149] S. Bellan *et al.*, "Numerical and experimental studies on heat transfer characteristics of thermal energy storage system packed with molten salt PCM capsules," *Appl. Therm. Eng.*, vol. 90, pp. 970–979, 2015.
- [150] A. Raul, M. Jain, S. Gaikwad, and S. K. Saha, "Modelling and experimental study of latent heat thermal energy storage with encapsulated PCMs for solar thermal applications," *Appl. Therm. Eng.*, vol. 143, no. July, pp. 415–428, 2018.
- [151] L. Xia, P. Zhang, and R. Z. Wang, "Numerical heat transfer analysis of the packed bed latent heat storage system based on an effective packed bed model," *Energy*, vol. 35, no. 5, pp. 2022–2032, 2010.
- [152] K. Nithyanandam and R. Pitchumani, "Cost and performance analysis of concentrating solar power systems with integrated latent thermal energy storage," *Energy*, vol. 64, pp. 793–810, 2014.
- [153] K. Nithyanandam and R. Pitchumani, "Optimization of an encapsulated phase change material thermal energy storage system," *Sol. Energy*, vol. 107, pp. 770–788, 2014.
- [154] S. Karthikeyan, G. Ravikumar Solomon, V. Kumaresan, and R. Velraj, "Parametric studies on packed bed storage unit filled with PCM encapsulated spherical containers for low temperature solar air heating applications," *Energy Convers. Manag.*, vol. 78, pp. 74–80, 2014.
- [155] M. Wu, C. Xu, and Y. He, "Cyclic behaviors of the molten-salt packed-bed thermal storage system filled with cascaded phase change material capsules," *Appl. Therm. Eng.*, vol. 93, pp. 1061–1073, 2016.
- [156] M. Wu, C. Xu, and Y.-L. He, "Dynamic thermal performance analysis of a molten-salt packed-bed thermal energy storage system using PCM capsules," *Appl. Energy*, vol. 121, pp. 184–195, 2014.
- [157] P. A. Galione, O. Lehmkuhl, J. Rigola, and A. Oliva, "Numerical simulations of thermal energy storage systems with phase change materials," 2011.
- [158] E. Oró, J. Chiu, V. Martin, and L. F. Cabeza, "Comparative study of different numerical models of packed bed thermal energy storage systems," *Appl. Therm. Eng.*, vol. 50, no. 1, pp. 384–392, 2013.
- [159] H. Peng, H. Dong, and X. Ling, "Thermal investigation of PCM-based high temperature thermal energy storage in packed bed," *Energy Convers. Manag.*, vol. 81, pp. 420–427, 2014.

- [160] K. E. Elfeky, N. Ahmed, and Q. Wang, "Numerical comparison between single PCM and multi-stage PCM based high temperature thermal energy storage for CSP tower plants," *Appl. Therm. Eng.*, vol. 139, no. February, pp. 609–622, 2018.
- [161] S. Karthikeyan and R. Velraj, "Numerical investigation of packed bed storage unit filled with PCM encapsulated spherical containers - A comparison between various mathematical models," *Int. J. Therm. Sci.*, vol. 60, pp. 153–160, 2012.
- [162] N. Ahmed, K. E. Elfeky, L. Lu, and Q. W. Wang, "Thermal and economic evaluation of thermocline combined sensible-latent heat thermal energy storage system for medium temperature applications," *Energy Convers. Manag.*, vol. 189, no. March, pp. 14–23, 2019.
- [163] A. B. Hernández, I. Ortega-fernández, I. Uriz, A. Ortuondo, I. Loroño, and J. Rodríguez-aseguinolaza, "Parametric Analysis and Optimization of a Combined Latent-Sensible Packed Bed," *SolarPaces Conf.*, 2017.
- [164] P. A. Galione, C. D. Pérez-Segarra, I. Rodríguez, O. Lehmkuhl, and J. Rigola, "A New Thermocline-PCM Thermal Storage Concept for CSP Plants. Numerical Analysis and Perspectives," *Energy Procedia*, vol. 49, pp. 790–799, 2014.
- [165] P. A. Galione, C. D. Pérez-Segarra, I. Rodríguez, A. Oliva, and J. Rigola, "Multi-layered solid-PCM thermocline thermal storage concept for CSP plants. Numerical analysis and perspectives," *Appl. Energy*, vol. 142, pp. 337–351, 2015.
- [166] P. A. Galione, C. D. Pérez-Segarra, I. Rodríguez, S. Torras, and J. Rigola, "Multi-layered solid-PCM thermocline thermal storage for CSP. Numerical evaluation of its application in a 50MWe plant," *Sol. Energy*, vol. 119, pp. 134–150, 2015.
- [167] P. Galione, C. Pérez-Segarra, I. Rodríguez, S. Torras, and J. Rigola, "Numerical Evaluation of Multi-layered Solid-PCM Thermocline-like Tanks as Thermal Energy Storage Systems for CSP Applications," *Energy Procedia*, vol. 69, pp. 832–841, 2015.
- [168] B. chen Zhao, M. song Cheng, C. Liu, and Z. min Dai, "Thermal performance and cost analysis of a multi-layered solid-PCM thermocline thermal energy storage for CSP tower plants," *Appl. Energy*, vol. 178, pp. 784–799, 2016.
- [169] B. Zhao, M. Cheng, C. Liu, and Z. Dai, "An efficient tank size estimation strategy for packed-bed thermocline thermal energy storage systems for concentrated solar power," *Sol. Energy*, vol. 153, pp. 104–114, 2017.
- [170] B. chen Zhao, M. song Cheng, C. Liu, and Z. min Dai, "Cyclic thermal characterization of a molten-salt packed-bed thermal energy storage for concentrating solar power," *Appl. Energy*, vol. 195, pp. 761–773, 2017.
- [171] G. Zanganeh, R. Khanna, C. Walser, A. Pedretti, A. Haselbacher, and A. Steinfeld, "Experimental and numerical investigation of combined sensible-latent heat for thermal energy storage at 575 Deg C and above," *Sol. Energy*, vol. 114, pp. 77–90, 2015.

- [172] L. Geissbühler *et al.*, “Analysis of industrial-scale high-temperature combined sensible/latent thermal energy storage,” vol. 101, no. 2, pp. 657–668, 2015.
- [173] F. P. Incropera, D. P. DeWitt, T. L. Bergman, and A. S. Lavine, *Fundamentals of Heat and Mass Transfer*. 2007.
- [174] J. Wei, Y. Kawaguchi, S. Hirano, and H. Takeuchi, “Study on a PCM heat storage system for rapid heat supply,” *Appl. Therm. Eng.*, vol. 25, no. 17–18, pp. 2903–2920, 2005.
- [175] N. Wakao, S. Kaguei, and T. Funazkri, “Effect of Fluid Dispersion Coefficients Particle-To-Fluid Heat Transfer Coefficients In Packed Beds,” *Chem. Eng. Sci.*, vol. 34, no. 3, pp. 325–336, 1978.
- [176] H. Agalit, N. Zari, M. Maalmi, and M. Maaroufi, “Numerical investigations of high temperature packed bed TES systems used in hybrid solar tower power plants,” *Sol. Energy*, vol. 122, pp. 603–616, 2015.
- [177] S. Shiri, “A Model of Transient Heat Transfer in a Packed Bed of Alumina Particles,” 2013.
- [178] A. F. Regin, S. C. Solanki, and J. S. Saini, “Latent heat thermal energy storage using cylindrical capsule: Numerical and experimental investigations,” *Renew. Energy*, vol. 31, no. 13, pp. 2025–2041, 2006.
- [179] T. Hirata and K. Nishida, “An analysis of heat transfer using equivalent thermal conductivity of liquid phase during melting inside an isothermally heated horizontal cylinder,” *Int. J. Heat Mass Transf.*, vol. 32, no. 9, pp. 1663–1670, 1989.
- [180] A. Prasad and S. Sengupta, “Nusselt Number and Melt Time Correlations for Melting Inside a Horizontal Cylinder Subjected to an Isothermal Wall Temperature Condition,” *J. Sol. Energy Eng.*, vol. 110, no. 4, p. 340, 1988.
- [181] J. Felinks *et al.*, “Particle-particle heat transfer coefficient in a binary packed bed of alumina and zirconia-ceria particles,” *Appl. Therm. Eng.*, vol. 101, pp. 101–111, 2016.
- [182] T. Fasquelle, Q. Falcoz, P. Neveu, and J. F. Hoffmann, “A temperature threshold evaluation for thermocline energy storage in concentrated solar power plants,” *Appl. Energy*, vol. 212, no. January, pp. 1153–1164, 2018.
- [183] Y. Lalau, X. Py, A. Meffre, and R. Olives, “Comparative LCA Between Current and Alternative Waste-Based TES for CSP,” *Waste and Biomass Valorization*, vol. 7, no. 6, pp. 1509–1519, 2016.
- [184] N. Pflieger, T. Bauer, C. Martin, M. Eck, and A. Wörner, “Thermal energy storage – overview and specific insight into nitrate salts for sensible and latent heat storage,” pp. 1487–1497, 2015.
- [185] N. Calvet *et al.*, “Compatibility of a post-industrial ceramic with nitrate molten salts for use as filler material in a thermocline storage system,” *Appl. Energy*, vol. 109,

- pp. 387–393, 2013.
- [186] a. Meffre, R. Olives, X. Py, C. Bessada, P. Echegut, and U. Michon, “Design and Industrial Elaboration of Thermal Energy Storage Units Made of Recycled Vitrified Industrial Wastes,” *Vol. 4 Energy Syst. Anal. Thermodyn. Sustain. Combust. Sci. Eng. Nanoeng. Energy, Parts A B*, pp. 757–762, 2011.
 - [187] A. Jeanjean, R. Olives, and X. Py, “Selection criteria of thermal mass materials for low-energy building construction applied to conventional and alternative materials,” *Energy Build.*, vol. 63, pp. 36–48, 2013.
 - [188] A. Gutierrez *et al.*, “Advances in the valorization of waste and by-product materials as thermal energy storage (TES) materials,” *Renew. Sustain. Energy Rev.*, vol. 59, pp. 763–783, 2016.
 - [189] Z. S. Chang, X. Li, C. Xu, C. Chang, and Z. F. Wang, “The design and numerical study of a 2MWh molten salt thermocline tank,” vol. 69, pp. 779–789, 2015.
 - [190] M. MUNRO, “Evaluated Material Properties for a Sintered alpha-Alumina,” *J. Am. Ceram. Soc.*, vol. 80, no. 8, pp. 1919–1928, 2005.
 - [191] S. A. Mohamed *et al.*, “A review on current status and challenges of inorganic phase change materials for thermal energy storage systems,” *Renew. Sustain. Energy Rev.*, vol. 70, no. December 2016, pp. 1072–1089, 2017.
 - [192] B. I. Sandor, M. J. Moran, F. Kreith, and F. Kreith, “Mechanical Engineering HANDBOOK,” p. 2466, 1999.
 - [193] W. Yaïci, M. Ghorab, E. Entchev, and S. Hayden, “Three-dimensional unsteady CFD simulations of a thermal storage tank performance for optimum design,” *Appl. Therm. Eng.*, vol. 60, no. 1–2, pp. 152–163, 2013.
 - [194] G. Strang, *Computational science and engineering*. Wellesley, MA: Wellesley-Cambridge Press, 2007.
 - [195] A. N. Ford Versypt and R. D. Braatz, “Analysis of finite difference discretization schemes for diffusion in spheres with variable diffusivity,” *Comput. Chem. Eng.*, vol. 71, pp. 241–252, 2014.
 - [196] J. Thibault, S. Bergeron, and H. W. Bonin, “On finite-difference solutions of the heat equation in spherical coordinates,” *Numer. Heat Transf.*, vol. 12, no. 4, pp. 457–474, 1987.
 - [197] M. A. Keilany, M. Milhé, J. Bézian, Q. Falcoz, and G. Flamant, “Experimental evaluation of vitrified waste as solid fillers used in thermocline thermal energy storage with parametric analysis,” *J. Energy Storage*, vol. 29, no. February, p. 101285, 2020.
 - [198] T. Fasquelle, Q. Falcoz, P. Neveu, F. Lecat, N. Boullet, and G. Flamant, “Operating results of a thermocline thermal energy storage included in a parabolic trough mini power plant,” *AIP Conf. Proc.*, vol. 1850, 2017.

- [199] T. R. Davenne, S. D. Garvey, B. Cardenas, and M. C. Simpson, "The cold store for a pumped thermal energy storage system," *J. Energy Storage*, vol. 14, pp. 295–310, 2017.
- [200] Y. Zhang, K. Du, J. P. He, L. Yang, and Y. J. Li, "Impact factors analysis of the enthalpy method and the effective heat capacity method on the transient nonlinear heat transfer in phase change materials (pcms)," *Numer. Heat Transf. Part A Appl.*, vol. 65, no. 1, pp. 66–83, 2014.
- [201] M. Medrano, A. Gil, I. Martorell, X. Potau, and L. F. Cabeza, "State of the art on high-temperature thermal energy storage for power generation. Part 2-Case studies," *Renew. Sustain. Energy Rev.*, vol. 14, no. 1, pp. 56–72, 2010.
- [202] L. Lei *et al.*, "A review of solar collectors and thermal energy storage in solar thermal applications," *Appl. Energy*, vol. 104, no. 1, pp. 52–58, 2013.
- [203] A. R. Archibold, M. M. Rahman, D. Y. Goswami, and E. L. Stefanakos, "Parametric Investigation of the Melting and Solidification Process," *ASME 2012 6th Int. Conf. Energy Sustain. Parts A B*, pp. 1–12, 2012.
- [204] Martin Marietta Aerospace, "Sandia Report: Molten salt safety study," pp. 1–29, 1980.
- [205] J. Carvill, *Mechanical Engineer's Data HANDBOOK*. 1993.
- [206] G. J. Janz, C. B. Allen, N. P. Bansal, R. M. Murphy, and R. P. T. Tomkins, "Physical Properties data compilations relevant to energy storage." Secretary of Commerce U.S. government, p. 449, 1979.
- [207] T. Bauer, D. Laing, and R. Tamme, "Characterization of sodium nitrate as phase change material," *Int. J. Thermophys.*, vol. 33, no. 1, pp. 91–104, 2012.
- [208] J. P. Bédécarrats, J. Castaing-Lasvignottes, F. Strub, and J. P. Dumas, "Study of a phase change energy storage using spherical capsules. Part I: Experimental results," *Energy Convers. Manag.*, vol. 50, no. 10, pp. 2527–2536, 2009.
- [209] T. E. Alam, J. Dhau, D. Y. Goswami, M. M. Rahman, and E. Stefankos, "Imece2014-38307 Experimental Investigation of a Packed-Bed Latent Heat Thermal," pp. 1–6, 2014.
- [210] F. J. McQuillan, J. R. Culham, and M. M. Yovanovich, "Properties of dry air at one atmosphere," *Univ. Waterloo- ...*, no. June, 1984.

8. NOMENCLATURE

α_s	Shape factor	$[m^2/m^3]$
A_{int}	Internal Tank cross sectional area	$[m^2]$
$A_{w,cross}$	cross-sectional surface area of the tank's wall	$[m^2]$
$A_{f \leftrightarrow w}$	Exchange heat transfer area between fluid and tank's wall	$[m^2]$
$A_{s \leftrightarrow w}$	Exchange heat transfer area between particles and tank's wall	$[m^2]$
$A_{w \leftrightarrow ext}$	Exchange heat transfer area between tank's wall and surrounding environment	$[m^2]$
C_p	Heat capacity	$[Joul/kg.k]$
d_r	Average diameter of particle	$[m]$
d_{ch}	Hydraulic diameter (characterize diameter) of rocks	$[m]$
D	Tank diameter	$[m]$
E	Energy	$[Joul]$
g	gravitational acceleration constant	$[m^2/sec]$
H	Height	$[m]$
H_{Thick}	Thermocline thickness position	$[m]$
h_v	Volumetric convection heat transfer coefficient between HTF and Solid filler particles	$[w/m^3.K]$
h_w	convection heat transfer coefficient between HTF and tank's wall	$[w/m^2.K]$
h_{ext}	convection heat transfer coefficient between tank's wall and surrounding atmosphere	$[w/m^2.K]$
k	Thermal conductivity	$[w/m.K]$
k_c	Charge factor	$[-]$
k_d	Discharge factor	$[-]$
$k_{p,eff}$	Effective heat conductivity of Solid filler particles	$[w/m.K]$
$k_{f,eff}$	Effective heat conductivity of HTF	$[w/m.K]$
l_{ch}	Characterize length	$[m]$
L_{fus}	Laten heat of fusion	$[Kj/kg]$
T	Temperature	$[K]$
$T_{z,t}$	Temperature at axial position z at time t	$[K]$
t	Time	$[sec]$
V	Volume	$[m^3]$
v_f	Local velocity of HTF	$[m/sec]$
z	Axial coordinate	$[m]$

Greek symbols

ε	Tank porosity (void fraction)	[-]
α	Thermal diffusivity	[m ² /sec]
β	coefficient of thermal expansion	[1/°C]
δ	Thermocline thickness ratio	[-]
ρ	density	[kg/m ³]
θ	Non dimensional temperature	[-]
δ	Non dimensional thermocline thickness	[-]
η	Efficiency	
λ	Liquid fraction	

Subscripts

f	Heat transfer fluid
p	Solid filler particles
w	Tank's wall (wall)

Superscript

n	time reference
j	Positions reference in axial direction
*	Non dimensional quantity

Abbreviations

1D	One-dimensional
2D	Two-dimensional
GHG	greenhouse gas
CSP	Concentrated solar power
TES	thermal energy storage
PCM	Phase change material
HTF	Heat transfer fluid
DSC	Differential-Scanning-Calorimetry

ORC	organic Rankin cycle
C-S	continuous solid model
D-C	Dispersion concentric model
EPM	Enthalpy porosity method
Cp-eff	Effective heat capacity method
SHSM	sensible heat storage medium

**Non-
dimensional
Number**

St	Stefan number
Pe	Peclet number
Re	Reynolds number
Pr	Prandtl number
Nu	Nusselt number
Bi	Biot number
Ra	Rayleigh number
Gr	Grashof number

9. LIST OF FIGURES

Figure 1 TES for solar power plants (a) direct two-tanks, (b) indirect two-tank, and (c) indirect thermocline.	14
Figure 2 passive TES.....	15
Figure 3 categories of PCMs relating enthalpy of fusions to melting temperatures [34]	21
Figure 4 thermal conductivity for high-temperature PCMs [62]	26
Figure 5 DCS Heat flow for two PCMs paraffin and water emulsion	27
Figure 6 Means of heat transfer in thermocline	30
Figure 7 [17] Thermocline outlet temperature evolution in time two thermoclines: SMT at which HTF is the storage medium, DMT dual HTF and solid filler are used as storage mediums.....	39
Figure 8 experimental temperature against 1D-1P, 1D-2P, 1D-2P(+wall heat losses), and 1D-2P (+ solving wall energy equation) Hoffmann et al. [87].....	40
Figure 9 cycling effect on (a) TC thermocline thickness (b) efficiency for multiple non-dimensional velocity $v^* = (\rho C_p)_f H_{\text{rank}} V_f / k_f$ Bayón et al. [116]	41
Figure 10 2D temperature distribution of HTF in 14m thermocline (a) 50 min, (b) 100 min, (c) 150 min, (d) 200 min, and (e) 250 min Xu et al. [13]	42
Figure 11 Chao Xu et al. [124] thermocline discharge process (a) Outlet temperature as a function of time at various solid filler diameter. (b) efficiency as function to particle diameter for various materials.....	44
Figure 12 the influence of PCM thermal conductivity on (a) charge time and (b) cumulative stored heat Karthikeyan et al. [154].....	57
Figure 13 Thermocline outlet temperature during discharge for various capsule diameters Wu et al. [156].....	58
Figure 14. Schematic of MicroSol-R pilot plant.....	76
Figure 15. HTF distributor at the top of the thermocline.....	77
Figure 16. Thermocline tank size and thermocouple positions.....	77
Figure 17 . Filler materials shape.....	80
Figure 18 Typical operation in the thermocline TES (a) charge (b) discharge[23]	81
Figure 19 The influence of threshold temperature on the outlet temperature evolution in time during (a) charge (b) discharge of a thermocline[182]	82
Figure 20 tow-sections PCM and sensible heat thermocline depicted for this work	87
Figure 21. Algorithm of numerical solution for the C-S model	92
Figure 22 D-C model control volume	97
Figure 23 Solution algorithm for the D-C model.....	98

Figure 24 Comparison between thermal storages for the same 4 m ³ thermocline filled with three SHSMs synthetic oil, alumina, and Cofalit at temperature 290-220°C	103
Figure 25 non-dimensional outlet temperature evolution in time during charge (alumina and Cofalit®)	104
Figure 26 non-dimensional outlet temperature evolution in time during discharge (alumina and Cofalit®)	105
Figure 27 Thermocline thickness against the charge time (alumina and Cofalit®)	106
Figure 28 Thermocline thickness against the discharge time (alumina and Cofalit®) ..	106
Figure 29 Charge efficiency evolution in time (alumina and Cofalit®)	107
Figure 30 Discharge efficiency versus non-dimensional outlet temperature (alumina and Cofalit®)	108
Figure 31 Temperature profile for alumina, model against experiment during charge ..	110
Figure 32 Temperature profiles for Cofalit®, model against experiment during charge	110
Figure 33 Temperature of alumina during discharge model Vs. experiment.....	111
Figure 34 non-dimensional temperature of Cofalit® during discharge model Vs. experiment	112
Figure 35 Process duration against system parameters (a) charge (b) discharge	114
Figure 36 Thermocline thickness against system parameters (a) charge (b) discharge ..	115
Figure 37 faster thermal front in the cold region of the thermocline compared to the slower thermal front in the hot region	117
Figure 38 Process Efficiency against system parameters (a) charge (b) discharge	118
Figure 39 combining high thermal capacity SHSM to Cofalit ® in one thermocline Cofalit®.....	119
Figure 40 Thermocline outlet temperature during the discharge time for two SHSMs	120
Figure 41 C-S and D-C model's comparison of the HTF temperature at the thermocline outlet against time for charge and discharge	126
Figure 42 the outlet temperature during discharge of the thermocline filled with 2cm PCM spheres as per the four models.....	129
Figure 43 D-C model discretization during discharge.....	130
Figure 44 surface and center temperatures of the PCM sphere located at last control volume during discharge of D-C EPM model compared to the sphere temperature of a C-S EPM.....	130
Figure 45 estimated Liquid fraction of the PCM as per D-C EPM and C-S EPM at the sphere 132 during discharge when the threshold temperature is reached	131
Figure 46 surface and center temperatures of the PCM sphere located at last control volume during discharge of D-C Cp-eff model compared to the sphere temperature of a C-S Cp-eff.....	131

Figure 47 Inlet/outlet HTF temperature against time for Raul and outlet temperature as predicted by the D-C-EPM model	134
Figure 48 combining a layer of PCM to sensible heat thermocline TES	135
Figure 49 HTF temperature profile during the charging process of a thermocline containing 25% PCM and 75% alumina	136
Figure 50 HTF temperature profile during the discharge process of a thermocline contains 25% PCM and 75% alumina.....	137
Figure 51 Thermocline outlet temperature evolution in time comparison between 100% alumina sphere and 25% PCM-75% alumina sphere.....	138
Figure 52 Scenario 1 of PCM quantity estimation based on high-grade energy	142
Figure 53 Scenario 2 of PCM quantity estimation based on the whole remain energy.	143
Figure 54 The thermocline outlet temperature for various PCM percentages ratios [163]	144
Figure 55 discharge efficiency versus PCM ratios for combined NaNO ₃ -alumina sphere thermocline.....	147
Figure 56 thermocline thickness during discharge versus PCM ratios for combined NaNO ₃ -alumina sphere thermocline.....	148
Figure 57 discharge time versus PCM ratios for combined NaNO ₃ -alumina sphere thermocline.....	148
Figure 58 discharge efficiency versus PCM ratios for combined NaNO ₃ -Cofalit® thermocline.....	149
Figure 59 thermocline thickness during discharge versus PCM ratios for combined NaNO ₃ -Cofalit® thermocline.....	150
Figure 60 discharge time versus PCM ratios for combined NaNO ₃ -Cofalit® thermocline.....	150
Figure 61. DSC results for the commercial NaNO ₃	156
Figure 62. Tubes design of the PCM capsules for the topmost basket inside the thermocline.....	158
Figure 63. PCM concentric distribution inside the tubes	159
Figure 64. Envelope, PCM, and total thermal resistances for the evaluated tubes.....	163
Figure 65. Normalized parameters for each tube diameter.....	163
Figure 66. Internal pressure versus air ratios of NaNO ₃ fill SS304 48.3/45.1 tube.....	165
Figure 67. DSC measurements (a) 100% Oil (b) 91%wt.Oil-9%wt.NaNO ₃	166
Figure 68. DSC measurements (a) 100% NaNo ₃ (b) 86%wt. NaNO ₃ -16%wt.Oil	167
Figure 69. PCM layer design drawings	168
Figure 70. Stainless steel tubes as received from the supplier.....	169
Figure 71. Main steps of filling the PCM inside the tubes	170
Figure 72. The final PCM layer package	171

Figure 73. Temperature profile of TPCM-S during the charge process, model against experiment	173
Figure 74 Radial thermocouples positions at the PCM layer in the TPCM-S experiment	174
Figure 75. Radial temperature evolution during the charge at six axial reference positions TPCM-S experiment	175
Figure 76. Temperature profile of TPCM-S during the discharge process, model against experiment	176
Figure 77. Radial temperature evolution during the discharge at six axial reference positions TPCM-S experiment	177
Figure 78. Typical charge of the thermocline in the MICROSOL-R 220°C-320°C at a constant mass flow rate	178
Figure 79. Experimental results for charge process (285-315) °C at various mass flow rates of TPCM-S	179
Figure 80. Experimental thermocline thickness during charge (285-315) °C at various mass flow rates of TPCM-S	181
Figure 81. Experimental efficiency during charge (285-315) °C at various mass flow rates of TPCM-S	182
Figure 82. Experimental results for charge process (295-330) °C at various mass flow rates of TPCM-S	183
Figure 83. Experimental thermocline thickness during charge (295-330) °C at various mass flow rates of TPCM-S	184
Figure 84. Experimental efficiency during charge (295-330) °C at various mass flow rates of TPCM-S	185
Figure 85. Experimental results for the discharge process (315-220) °C at various mass flow rates of TPCM-S	187
Figure 86. Experimental thermocline thickness during discharge (315-220) °C at various mass flow rates of TPCM-S	188
Figure 87. Experimental efficiency during discharge (315-220) °C at various mass flow rates of TPCM-S	189
Figure 88. Outlet temperature versus efficiency during discharge (315-220) °C at various mass flow rates of TPCM-S	189
Figure 89. Experimental results for the discharge process (330-225) °C at various mass flow rates of TPCM-S	191
Figure 90. Experimental thermocline thickness during discharge (330-225) °C at various mass flow rates of TPCM-S	192
Figure 91. Experimental efficiency during discharge (330-225) °C at various mass flow rates of TPCM-S	193
Figure 92. Outlet temperature versus efficiency during discharge (330-225) °C at various mass flow rates of TPCM-S	193

Figure 93. Temperature profile of the of TPCM-S during a stand-by period of 5h.....	194
Figure 94. The simulated thermocline outlet temperature evolution with time during charge (220-315) °C, TPCM-S versus TSMS at 1600 kg/h	196
Figure 95. Estimated Liquid fraction at the tube 7 during charge when the threshold temperature is reached at 1600 kg/h.....	196
Figure 96. Simulated thermocline outlet temperature evolution in time during charge (220-315) °C, TPCM-S versus TSMS at (a) 3000 kg/h, and (b) 3900 kg/h	197
Figure 97. Estimated Liquid fraction at the tube 7 during charge when the threshold temperature is reached at 3000kg/h and 3900kg/h.....	198
Figure 98. Estimated Liquid fraction at all tubes as depicted by the D-C EPM at the end of the charge at 3900kg/h.....	198
Figure 99. Simulated thermocline outlet temperature evolution in time during discharge (315-220) °C, TPCM-S versus TSMS at 1600 kg/h.....	199
Figure 100. Depiction of thermocline thickness development during discharge in TPCM-S.....	200
Figure 101. Estimated Liquid fraction all PCM rows during discharge when the threshold temperature is reached at 1600 kg/h.....	200
Figure 102. Simulated thermocline outlet temperature evolution in time during discharge (315-220) °C, TPCM-S versus TSMS at (a) 2000 kg/h and (b) 3000 kg/h	201
Figure 103. Estimated Liquid fraction all PCM rows during discharge when the threshold temperature is reached at (a) 2000 kg/h and (b) 3000 kg/h	203
Figure 104. Comparison between thermal storages for the same 3.5 m ³ thermocline of TSMS and TPCM-S at temperature 315-220°C.....	204
Figure 105 HTF distributor at the top of the thermocline.....	211
Figure 106 [17] Evolution de la température de sortie de la thermocline dans le temps de deux systèmes de stockage	256
Figure 107 Schéma du projet pilote MicroSol-R.....	258
Figure 108 distributeur en haut de la thermocline.....	259
Figure 109 matériel de stockage solide	261
Figure 110 efficacité de décharge par rapport aux rapports MCP pour la thermocline combinée NaNO ₃ -sphère d'alumine.....	262
Figure 111 Le package de couche MCP final	263
Figure 112 Résultats expérimentaux pour le processus de décharge (315-220) °C à divers débits massiques stockage thermique combiné	264
Figure 113 Épaisseur de thermocline expérimentale pendant la décharge (315-220) °C à divers débits massiques.....	265
Figure 114 Modélisation des méthodes de thermocline basées sur des équations de bilan énergétique du caloporteur et des particules solides	266

Figure 115 Modélisation des stockages de chaleur sensible et concept combiné de stockage de chaleur sensible-latente.....	266
Figure 116 Profil de température pour (a) l'alumine, (b) Cofalit® modèle contre expérience pendant la charge	267
Figure 117 Température de (a) l'alumine (b) pendant le modèle de décharge Vs. expérience	267
Figure 118 Profil de température de la thermocline NaNO_3 -Alumine pendant le processus de charge, modèle contre expérience	268
Figure 119 Profil de température de la thermocline NaNO_3 -Alumine pendant le processus de décharge, modèle contre expérience	269
Figure 120 Simulation numérique de deux thermoclines combinées de sphères d'alumine NaNO_3 par rapport aux sphères d'alumine uniquement	270
Figure 121 temps de charge pour chaque taux de charge utilisé (220-315) °C.	270
Figure 122 Épaisseur de la thermocline pendant la charge pour chaque taux de charge utilisé.....	271
Figure 123 Efficacité de charge.....	271
Figure 124 Fraction liquide estimée au 7ème tube pendant la charge lorsque la température seuil est atteinte à 1600 kg/h.....	272
Figure 125 Fraction liquide estimée à tous les tubes telle que représentée par le D-C EPM à la fin de la charge à 3900kg/h	273
Figure 126 temps de décharge pour chaque taux de décharge utilisé (220-315) °C.....	273
Figure 127 Épaisseur de la thermocline pendant la décharge pour les taux de charge utilisé.....	274
Figure 128 Efficacité de décharge	274
Figure 129 Estimation de la fraction liquide toutes les rangées de MCP lors du rejet lorsque la température seuil est atteinte à 1600 kg/h.....	275
Figure 130 Estimation de la fraction liquide toutes les lignes PCM lors du rejet lorsque la température seuil est atteinte à 3000 kg/h.....	275

10. LIST OF TABLES

Table 1 commercial CSP plants with the integrated TES.....	8
Table 2 required characteristics in materials for sensible heat storage	16
Table 3 Average properties for liquid storage mediums	17
Table 4 Average properties for solid storage mediums	18
Table 5 PCM applications	19
Table 6 Advantages and disadvantages of organic and inorganic PCMs	20
Table 7 Prescribed features to use PCM in TES	22
Table 8 suitable salts, metals and eutectics as PCM for CSP TES 168-1083°C	23
Table 9 Required specifications for proper PCMs envelop design.....	24
Table 10 PCM thermal performance enhancement methods.....	29
Table 11 List of heat transfer methods inside thermocline.....	30
Table 12 Modelling methods of thermocline TES based on energy balance equations of HTF and solid particles	32
Table 13 calculating time for various models Ismail et al.....	45
Table 14 Different methodologies to study the phase change of materials.....	47
Table 15 Nu correlations for heat exchange between HTF and particle as they used in the literature	65
Table 16 modified heat convection coefficient as they appeared in the literature.....	66
Table 17 convection heat transfer between HTF and thermocline wall as appeared in the literature	67
Table 18 convection thermal losses at the outer thermocline wall	68
Table 19 effective axial thermal conductivity for the various modeling approach	69
Table 20 correlation from the literature to consider natural convection within the PCM envelope.....	70
Table 21 Thermocouples axial positions inside the thermocline	78
Table 22 Thermo-physical properties from literature at temperature range 200 – 300 °C	80
Table 23. List of correlations used in the modeling part of this work.....	99
Table 24 Experimental conditions for the experiments	104
Table 25 Biot number of Cofalit® and alumina for this experimental setup.....	109
Table 26 Numerical conditions for the parametric analysis	113
Table 27 Discharge performance parameters of Cofalit and alumina thermoclines against the combined two SHSMs solution.....	121

Table 28 numerical operating condition for the thermocline filled with alumina spheres (D-C vs. C-S)	125
Table 29 Performance indicators Comparison C-S to D-C for thermocline filled with 2 cm alumina spheres	126
Table 30 Biot for NaNO ₃ PCM at various spheres diameters	127
Table 31 Performance indicators Comparison C-S to D-C of thermocline filler with 2cm PCM spheres during the discharge process	132
Table 32 Thermophysical properties of HTF, PCM, and Stainless steel used in Raul experiment	133
Table 33 Experimental conditions of Raul et al. [150] setup.....	133
Table 34 Performance indicators during charge/discharge of a thermocline filled 25% PCM 75% alumina spheres compared to 100% alumina spheres	138
Table 35 Suggested PCM quantities for three PCMs according to Zanganeh [46], scenario1, and scenario2	144
Table 36 Suggested PCM quantities for the PCM according to Hernández [163], scenario1, and scenario2	145
Table 37 Estimated ratio of NaNO ₃ for alumina and Cofalit® thermoclines both scenarios	145
Table 38 Guide for corrosion weight loss used in the industry	156
Table 39 the estimated number of spheres to fulfill the 8.5% PCM volumetric ratio of the thermocline	157
Table 40. Number of rows correction factor [173].....	160
Table 41. Calculated PCM parameters based on the commercial data of pipe.....	161
Table 42. PCM mass, envelope mass, envelope volume, and filling ratio for each row.....	171
Table 43. Experimental and numerical conditions for the TPCM-S.....	173
Table 44. Numerical operating conditions for comparing TPCM-S to TSMS thermocline	195
Table 45 performance parameters TPCM-S and TSMS during the charge at 1600 kg/h	195
Table 46. Performance parameters comparison during the charge at various mass flow rates between TPCM-S and TSMS	197
Table 47. Performance parameters TPCM-S and TSMS during discharge at 1600 kg/h	199
Table 48. Performance parameters comparison during discharge at various mass flow rates between TPCM-S and TSMS	202
Table 49 Estimated ratio of PCM02 and PCM03 for alumina and Cofalit® thermoclines both scenarios	250
Table 50 commercial tube data for stainless steel 304L.....	251

11. APPENDIX

11.1. UNCERTAINTY OF MEASUREMENTS

In this work, we evaluated the combined standard uncertainty using the root-sum-square method of all associated uncertainties equation(133) [56].

$$U_c = \sqrt{(u_1^2 + u_2^2 + \dots + u_n^2)} \quad (133)$$

U_c : is the combined uncertainty

u_i : is the individual uncertainty source

The experimental setup uses PYRO-SYSTEM® thermocouples type PT100 1/3 B, which have ± 0.6 °C uncertainty, by neglecting the uncertainty of data acquisition switch, this results in 1.2% uncertainty in temperature reading relative to 100°C temperature difference. Moreover, each thermocouple has a position uncertainty of ± 2.5 cm that will give 1.9% uncertainty relative to 2.64m the tank height. The mass flow-metering device (Foxboro® Model 84F) has $\pm 0.5\%$ uncertainty of measurement. Applying equation(133) will give 2.3% of combined uncertainty.

Uncertainties in the temperature dependence of alumina thermophysical properties are estimated at 2% for heat capacity and 6% for thermal conductivity [190]. The accumulated uncertainty as per equation for the alumina spheres experiment is about 6.73%.

For Cofalit® experiment, the uncertainty in temperature dependence of thermophysical properties is about 0.6% for heat capacity, 6% for thermal conductivity, and 3.33% for density [27], which results in a combined uncertainty of 7.26% as per equation (133) .

NaNO₃ has an uncertainty of 6% in the measured thermophysical properties [209]. Therefore when deploying the PCM, the combined uncertainty equation of the NaNO₃ as PCM and alumina spheres as solid filler in one thermocline rises to 9%.

11.2. TEMPERATURE-DEPENDENT THERMOPHYSICAL PROPERTIES OF MATERIALS

AIR [210]

Property	Temperature dependence relation[K]
Density ρ [kg/m ³]	$(351.99/T) + (344.84/T^2)$
Heat Capacity C_p [J/kg.K]	$1030.5 - (0.19975T) + (3.9734 \cdot 10^{-4} T^2)$
Thermal conductivity k [W/m.K]	$2.334 \cdot 10^{-3} T^{(3/2)} / (164.54 + T)$
Dynamic viscosity μ [kg/m.sec]	$1.4592 \cdot 10^{-6} T^{(3/2)} / (109.1 + T)$

Jarysol® oil

Property	Temperature dependence relation[K]
Density ρ [kg/m ³]	$1261.569 - 0.7419173T$
Heat Capacity C_p [J/kg.K]	$649.84 + 3.1872180451T$
Thermal conductivity k [W/m.K]	$0.1521663 - 8.2406015038 \cdot 10^{-5} T$
Dynamic viscosity μ [kg/m.sec]	$\exp(19.75102 [\ln(T)]^4 - 492.2114 [\ln(T)]^3 + 4602.039 [\ln(T)]^2 - 19136.34 [\ln(T)] + 29858.54)$

Alumina spheres

Property	Temperature dependence relation[K]
Density ρ [kg/m ³]	$1000 (3.9853 - (7.158 \cdot 10^{-5} (T-273.15)) - (3.035 \cdot 10^{-8} (T-273.15)^2) + (7.232 \cdot 10^{-12} (T-273.15)^3))$ [190].
Heat Capacity C_p [J/kg.K]	$1117 + 0.14T - 411 \exp(-0.006T)$ [113]
Thermal conductivity k [W/m.K]	$(-2.469 \cdot 10^{-8} T^3) + (9.509 \cdot 10^{-5} T^2) - (0.124T) + 61.76$ [113]

COFALIT®

Property	Temperature dependence relation[K]
Density ρ [kg/m ³]	3120 [26]
Heat Capacity C_p [J/kg.K]	$-2.15^{-11} T^4 + 5.15^{-7} T^3 - 0.00125T^2 + 0.9841T + 768.1$; [176]
Thermal conductivity k [W/m.K]	1.52 [26]

NaNO₃ [148]

Property	Temperature dependence relation[K]
Solid density ρ [kg/m ³]	2160
Liquid density ρ [kg/m ³]	1908
Heat Capacity C_p [J/kg.K]	$444.53 + 2.18T$
Thermal conductivity k [W/m.K]	$0.3057 + 4.47^{-4} T$

11.3. COMPUTER SPECIFICATIONS

The computer which is used to perform all simulations is a 64-bit based processors, Intel® Core™, i7-6700HQ CPU @ 2.60 GHz 2.59 GHz, and 16 GB memory, under windows 10 operation system.

11.4. CASE STUDY: ODEILLO THERMOCLINE ADDITIONAL POTENTIAL PCMS

Additionally, two PCMs are investigated in order to evaluate the influence of latent heat of fusions on the results of the method presented in (4.3.1). These two PCM's have a melting temperature about 280°C that works with a range of 290°C/220°C T_H/T_L for a discharge cut-off of 276°C, which are modified accordingly in the scenarios.

The PCMs are :

- PCM2 :NaCl (5,7%mol)-Na₂CO₃(2,6%mol)-NaOH (91,7%mol) [44][43].
- PCM3 : ZnCl₂ [45].

Table 49 Estimated ratio of PCM02 and PCM03 for alumina and Cofalit® thermoclines both scenarios

Filler	T _m [°C]	L _{fus} [Kj/Kg]	PCM	Required PCM		T _H /T _L [°C]	T cut-off [°C]
				Scenario1	Scenario2		
Alumina	282	316	PCM2	2.60%	8.24%	290/220	276
Cofalit				1.38%	4.40%		
Alumina	280	75	PCM3	8.02%	23.41%	290/220	276
Cofalit				4.25%	12.50%		

Table 49 summarizes the results of the two scenarios of PCM2 and PCM3 for both case studies alumina spheres and Cofalit®. It reflects that using PCM2 reduces the required volume of PCM in scenario 1 by two third and about one half for scenario 2 compared to the NaNO₃. For the Cofalit case and PCM2 the two scenarios resulted in a values similar to the one found by Zanaghen et al. [46].

PCM3 that has a lower latent heat of fusion than the NaNO₃ indicated similar ratios for scenario1, while higher ratios of PCM3 than NaNO₃ are required with scenario2.¹

11.5. COMMERCIAL TUBE DATA

Table 50 commercial tube data for stainless steel 304L

Nominal Size [mm]	Outside diameter [mm]	Wall thickness [mm]	Inside dia [mm]	Weight [kg/m]
15	21.3	1.6	18.1	1
20	26.7	1.6	23.5	1.28
25	33.4	1.6	30.2	2.09
30	42.2	1.6	39	2.7
40	48.3	1.6	45.1	3.11
50	60.3	2.77	54.76	3.93
65	73	3.05	66.9	5.26
80	88.9	3.05	82.8	6.45
90	101.6	3.05	95.5	7.4
100	114.3	3.05	108.2	8.36
200	219.1	3.76	211.58	19.96

12. RESUME LONG DE THESE EN FRANÇAIS

12.1. INTRODUCTION

Les énergies renouvelables sont une solution clé pour répondre à la demande croissante d'énergie tout en respectant l'environnement et maintenir la croissance économique.

Or, les énergies renouvelables se caractérisent par leur caractère intermittent. Par exemple, les ressources solaires et éoliennes ne sont pas toujours disponibles lorsque nous en avons besoin. Par conséquent, le manque d'adéquation entre la demande et l'offre d'énergie bloque la pénétration généralisée du marché des énergies renouvelables.

La réponse à ce problème réside dans le déploiement du stockage d'énergie.

Ce qui permet de stocker de l'énergie supplémentaire pendant les périodes d'approvisionnements élevés, et de la réutiliser lorsque c'est très nécessaire.

L'énergie solaire à concentration (CSP) fait partie des énergies renouvelables prometteuses qui pourraient aider de nombreux pays à tenir leurs engagements envers la COP21. Où nous pouvons concentrer l'irradiance solaire au niveau du récepteur solaire pour obtenir de la chaleur, ensuite utilisez la chaleur pour produire de l'électricité. En effet, selon l' IEA [3] , le CSP pourrait fournir environ 10 % de la demande mondiale d'électricité en 2050 (environ 620 GWhe).

L'un des principaux avantages des centrales CSP est la capacité de stocker de l'énergie à grande échelle en utilisant le stockage d'énergie thermique (SET) pour fournir un fonctionnement 24/24 heures [5]. Étant donné que le SET permet aux centrales CSP de faire face à la nature intermittente du rayonnement solaire en fournissant un tampon énergétique pendant des conditions météorologiques transitoires, en décalant le temps, en augmentant le facteur de capacité et en ayant une distribution uniforme de la production d'électricité [6].

Il existe trois formes pour stocker l'énergie thermique : la chaleur sensible (milieu liquide et solide, ou souterrain), la chaleur latente (solide-liquide, liquide-gaz ou solide-solide) et thermochimique (réaction thermique, pompe à chaleur et pipeline chimique thermique) [9]. Kuravi et al. [11] a démontré que la technologie de stockage la plus adoptée commercialement pour les centrales CSP est la solution de chaleur sensible à deux réservoirs. Où le fluide chaud est stocké à l'intérieur du réservoir chaud, séparé du fluide froid dans l'autre réservoir.

D'autre part, la thermocline pourrait être une solution SET économiquement viable dans les CSP car elle remplace un système à deux

réservoirs par un seul réservoir. Parce qu'il remplace le fluide coûteux par la charge solide peu coûteuse et réduit le coût du réservoir supplémentaire avec ses accessoires tout en gardant la même capacité thermique [12].

Cependant, lors du fonctionnement de charge et de décharge, une couche de gradient thermique, généralement appelée épaisseur (ou région) de la thermocline, se développe entre les régions chaudes et froides du réservoir. La qualité de l'énergie stockée et libérée se dégrade à l'intérieur de cette région, tandis que cette couche se dilate au cours de l'opération. Il pourrait représenter jusqu'à 33 % de la hauteur totale du réservoir [13]. Ce qui réduit l'efficacité du système en raccourcissant le temps de fonctionnement utile et la chaleur disponible.

Lorsque l'on compare la température de sortie d'un réservoir de stockage (où le fluide est le caloporteur et le stockage en même temps) à un rempli de charge solide (quartzite dans ce cas), on peut voir sur Figure 106 une qualité énergétique inférieure lors de la décharge [17]. La zone entre les deux courbes représente une diffusion thermique supplémentaire qui est attribuée à l'échange de chaleur entre le fluide et le remplissage solide, ce qui affecte négativement les performances thermiques de l'unité de stockage.

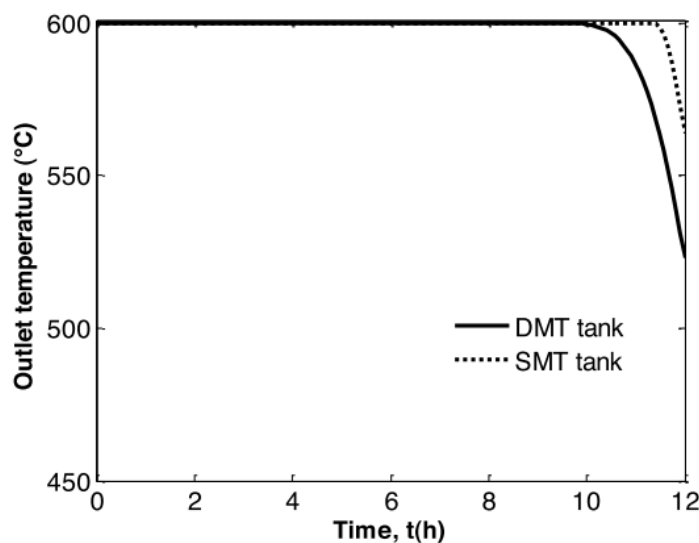


Figure 106 [17] Evolution de la température de sortie de la thermocline dans le temps de deux systèmes de stockage

Une analyse de sensibilité a été réalisée pour trouver le principal paramètre d'influence sur l'épaisseur de la thermocline [18]. L'étude a indiqué que cette épaisseur est principalement gérée par la taille du réservoir et les propriétés thermophysiques de la charge solide.

Dans ce contexte, les objectifs de cette recherche sont :

- Observer l'opportunité de re-valeuriser le bi produit industriel (déchets contenant de l'amiante – COFLAIT®) qui permet de réduire les impacts environnementaux des déchets indésirables et il a un faible coût. Notre objectif est de mettre du COFLAIT® dans un réservoir de stockage à l'échelle pilote et de comparer ses performances réelles aux matériaux de remplissage solides de référence.
- Améliorer la qualité énergétique lors du déchargement en utilisant une couche de matériau à changement de phase (MCP) adapté en haut de la cuve.
- Concevoir la couche MCP qui comprend la conception de l'enveloppe, la sélection des matériaux et développe l'approche de dimensionnement.
- Effectuer une analyse expérimentale de la solution SET suggérée qui combine une couche MCP à un milieu de chaleur sensible.
- Développer et valider un outil numérique adapté au stockage visé.

12.2. LA CONFIGURATION DE L'EXPERIENCE

Le montage expérimental utilisé dans ce travail est l'installation MicroSol-R à Odeillo à PROMES Figure 107, qui dispose de 3 récepteurs solaires d'une puissance nominale de 50KW thermique chacun.

(TC) est le stockage thermique, c'est une cuve thermocline de 4 m³ de 3,24 m de hauteur et 1,276 m de diamètre intérieur. Le réservoir contient quatre paniers positionnés verticalement pour permettre un accès facile au matériau de stockage solide lors du remplissage et du vidage. De plus, ces paniers réduisent la possibilité de cliquet thermique.

Pendant le processus de charge, la vanne V1 est ouverte tandis que la pompe de charge (P1) est activée pour permettre à l'huile synthétique (fluide caloporteur CP) d'être chauffée par un réchauffeur électrique de 70 kW (EH). Si une puissance de chauffage supplémentaire est requise, la vanne à trois voies (V2) est ouverte pour déployer les capteurs solaires.

La vanne trois voies (V3) est réglée pour envoyer toute l'huile à la thermocline (fermée) alors que la vanne (V4) est fermée. Le CP chaud est injecté à partir du point le plus haut du réservoir, extrayant le CP froid par le bas. Cette conception de processus limite la stratification thermique due à la différence de densité entre le fluide chaud et froid pendant la charge et la décharge.

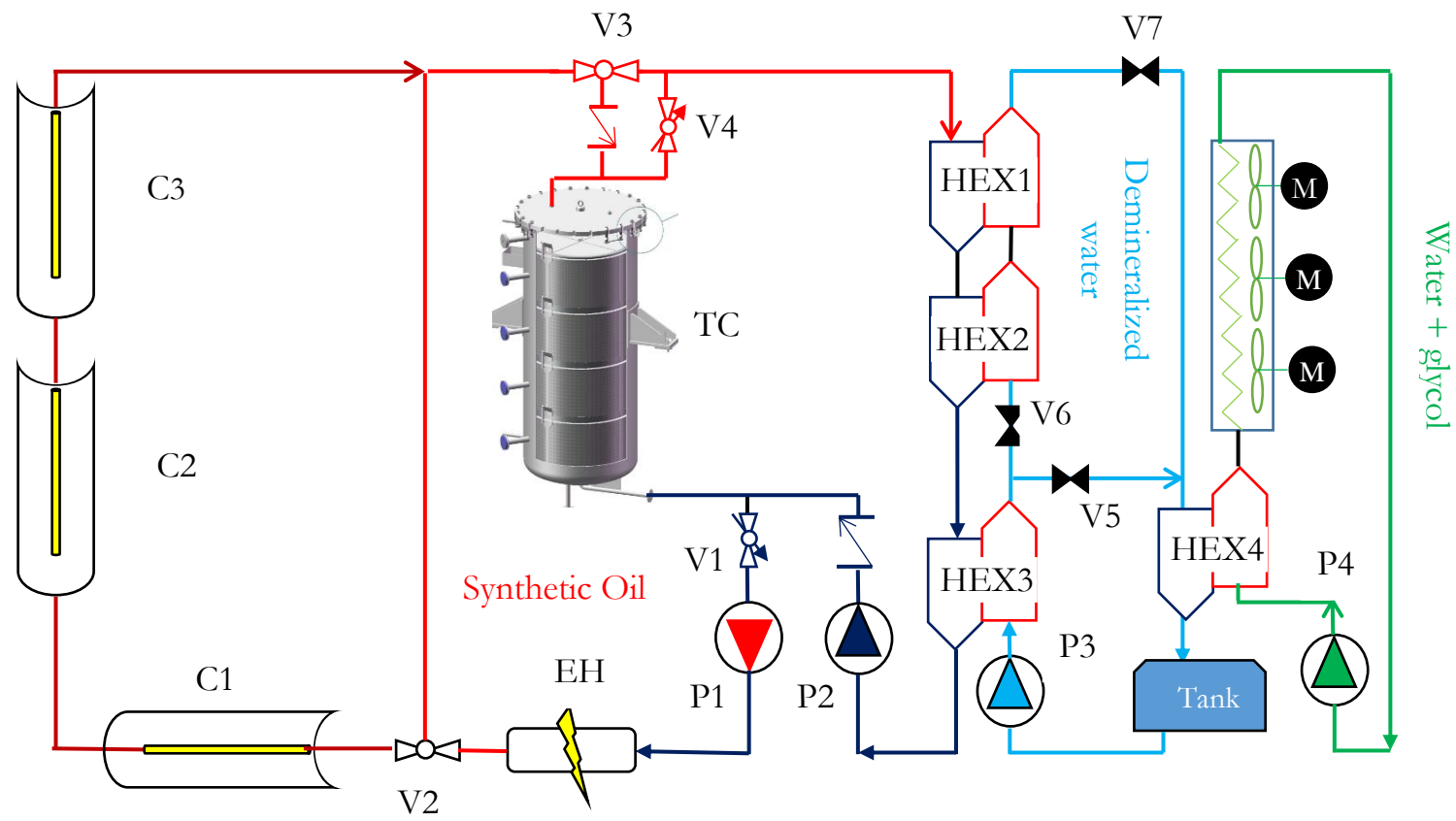


Figure 107 Schéma du projet pilote MicroSol-R

Pour le processus de décharge, la vanne (V1) est fermée et la pompe de décharge (P2) commence à injecter du CP froid dans la thermocline par le bas. L'huile chaude sort du réservoir par le haut, (V4) est ouvert et la vanne (V3) est fermée.

Le CP est refroidi à l'aide de trois échangeurs de chaleur refroidis à l'eau (HEX1, HEX2 et HEX3). La température de sortie de (HEX3), qui représente la température d'entrée de la thermocline, peut être contrôlée à l'aide de quatre paramètres : la puissance de la pompe à eau (P3), et le pourcentage d'ouverture des vannes (V6, V7 et V8).

L'eau est refroidie à l'aide d'un échangeur de chaleur refroidi eau-glycol (HEX4) actionné par la pompe (P4), où la chaleur est rejetée dans l'atmosphère environnante à l'aide de trois ventilateurs d'air à commande électrique.

La thermocline contient deux zones tampons qui incluent des distributeurs tubulaires CP qui permettent une distribution homogène Figure 108.



Figure 108 distributeur en haut de la thermocline

La hauteur intérieure du réservoir est de 2,64 m, et des thermocouples sont utilisés pour enregistrer la température de l'huile toutes les 2 secondes avec une précision de $\pm 0,6^{\circ}\text{C}$. Ils sont répartis dans les positions axiale et radiale.

L'expérience est préconçue, il y a donc certaines contraintes qui devaient être respectées :

- Les sphères d'alumine sont utilisées comme matériau de référence, non seulement parce qu'elles ont une forme sphérique standard et une très bonne capacité thermique, mais surtout parce qu'elles ont été largement évaluées dans la même configuration lors de précédents travaux de thèse.
- La différence de température de fonctionnement préférée selon la conception d'origine est comprise entre 220°C et 300°C .

- La fluide caloporteur est une huile synthétique qui a une plage de température de fonctionnement de 0 °C -350 °C
- où le système s'arrêtera complètement si la température dépasse 345 °C à n'importe quel point du circuit pour des raisons de sécurité.

12.3. PARAMETRES DE PERFORMANCE

La performance thermique dans ce travail est identifiée par trois paramètres principaux : l'épaisseur de la thermocline, la durée du processus et l'efficacité.

La température seuil ou (cut-off) d'un processus de charge est définie comme : La température maximale qui peut être renvoyée au champ solaire afin d'éviter d'endommager le récepteur solaire. Il est calculé à partir de l'équation (134).

$$T_{thr,c,k_c} = T_{low} + k_c(T_{high} - T_{low}) \quad (134)$$

En revanche lors du processus de déchargement, il existe une température minimale du fluide qui peut être envoyé au processus thermique en aval. En dessous de cette température, le processus ne peut pas s'exécuter. C'est ce qu'on appelle la décharge (cut-off) ou la température de seuil équation (135).

$$T_{thr,d,k_d} = T_{high} - k_d(T_{high} - T_{low}) \quad (135)$$

- L'épaisseur de la thermocline est définie comme la hauteur à laquelle se situe la température de refoulement (cut-off), moins la hauteur à laquelle la température de charge (cut-off) est positionnée à l'intérieur du réservoir, puis elle est divisée par la hauteur du réservoir pour obtenir son pourcentage value équation (136).

$$\delta = \frac{H(T_{thr,d,20\%}) - H(T_{thr,c,20\%})}{H_{Tank}} \quad (136)$$

Cette épaisseur doit être aussi minimale que possible pour améliorer la qualité de l'énergie au cours d'un processus.

- L'efficacité du processus de charge est le rapport entre l'énergie accumulée et l'énergie potentielle stockée dans le réservoir équation(137) [23].

$$\eta_{charge}(t) = \frac{E_{acc}(t)}{E_{max}} \quad (137)$$

- Pendant le processus de décharge, l'équation (138) calcule l'efficacité de décharge comme le rapport de l'énergie déchargée à l'énergie maximale stockée dans le système à l'étape initiale.

-

$$\eta_{discharge}(t) = \frac{\int_0^t m_f \cdot Cp_f \cdot (T_{outlet} - T_{low}) \cdot dt}{E_{max}} \quad (138)$$

12.4. RESULTATS EXPERIMENTAUX

Pour les expériences de stockage de chaleur sensible, 6,4 tonnes de sphères d'alumine et 4 tonnes de COFLAIT® avaient été utilisées Figure 109.



Figure 109 matériel de stockage solide

Le COFLAIT® a le potentiel d'augmenter de 18 % la capacité thermique du stockage par thermocline et de réduire de 40 % le coût de son matériau de remplissage solide par rapport à l'huile.

Les performances des déchets à base d'amiante connus sous le nom de COFLAIT® ont été comparées expérimentalement à des sphères d'alumine comme matériau céramique de référence, à l'aide du MICROSOL-R CSP. Les principaux résultats sont les suivants :

- Le COFLAIT® a une capacité calorifique volumétrique de 22 % inférieure à celle de l'alumine, ce qui se traduit par un temps de charge 20 % plus rapide et un temps de décharge 15 % plus court.
- L'épaisseur de la thermocline se retrouve dans le COFLAIT® plus faible que l'alumine, respectivement 26 % contre 31 % pour la charge et 20 % contre 26 % pour les procédés de décharge.
- Les rendements du procédé pour le COFLAIT® sont meilleurs que pour l'alumine avec respectivement 82 % contre 80 % pour la charge et 90 % contre 83 % pour la décharge.
- COFLAIT® surpasse la céramique d'alumine au niveau de température de ce travail, 300 °C, en raison de son diamètre moyen plus petit ainsi que de sa capacité calorifique volumétrique inférieure et de sa forme inhomogène.

Pour le travail expérimental consistant à combiner la couche MCP à des expériences de stockage de chaleur sensible, des sphères d'alumine ont été utilisées comme matériaux de base du stockage thermique. En raison de sa forme régulière et du fait qu'il y a beaucoup de résultats expérimentaux dessus.

Le nitrate de sodium (NaNO_3) est choisi comme MCP car il a une température de fusion de 306°C [191][45] qui correspond à la température de fonctionnement. De plus, il a prouvé sa compatibilité avec d'excellents matériaux candidats pour l'enveloppe.

L'acier inoxydable 304L est choisi comme matériau d'encapsulation car il a été testé avec du NaNO_3 et a montré une stabilité appropriée pour les sels à haute température [11].

Bien qu'aucun contact direct entre le MCP et l'huile ne soit assuré dans cette expérience, la réactivité du mélange de NaNO_3 avec l'huile Jarytherm® est étudiée. Les mesures DSC ont prouvé qu'il n'y a pas de réaction exothermique lors du mélange de l'huile avec du NaNO_3 à une température allant jusqu'à 350°C , il est donc tout à fait sûr d'utiliser le NaNO_3 dans l'expérience.

Nous développons une méthodologie générale pour dimensionner la couche MCP, dans laquelle l'objectif est d'optimiser l'efficacité de décharge. Les résultats ont indiqué une plage de ratio entre 8,5% jusqu'à 19% pour le MicroSol-R avec les sphères d'alumine et NaNO_3 comme MCP Figure 110.

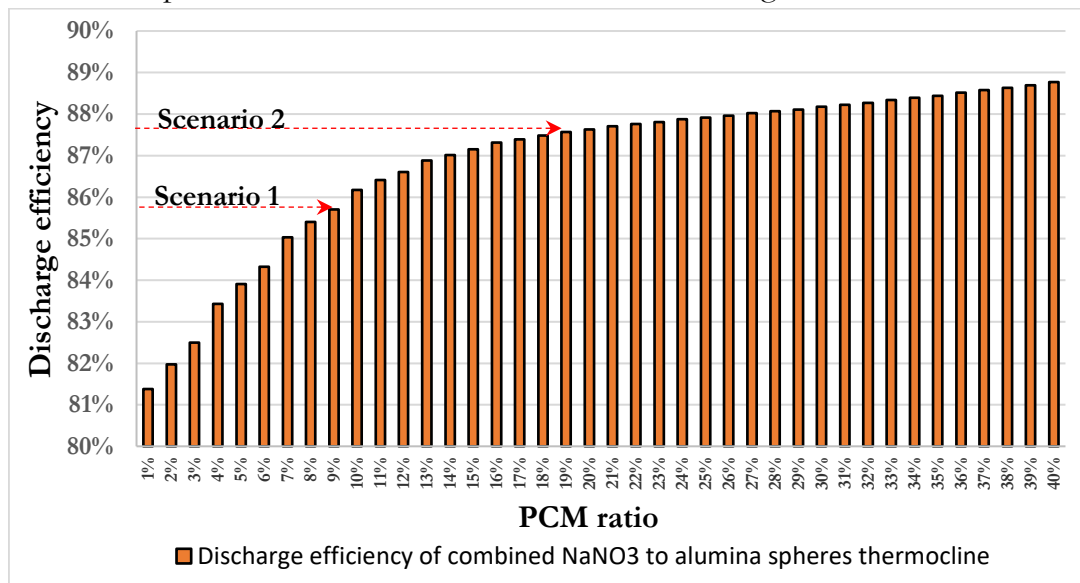


Figure 110 efficacité de décharge par rapport aux rapports MCP pour la thermocline combinée NaNO_3 -sphère d'alumine

Pour la partie fabrication, aucun fabricant ne pouvait fournir le NaNO_3 requis avec des sphères en acier inoxydable pour de grandes quantités. Ainsi, la conception doit être révisée des sphères aux tubes.

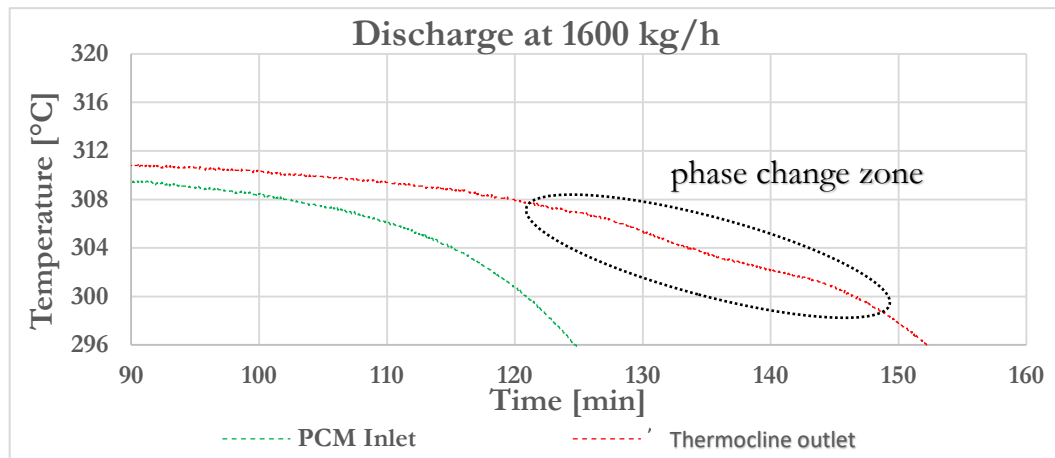
Nous devons également réduire plus le ratio PCM à 5,5% en raison de la limitation budgétaire. Le produit final est illustré dans Figure 111.



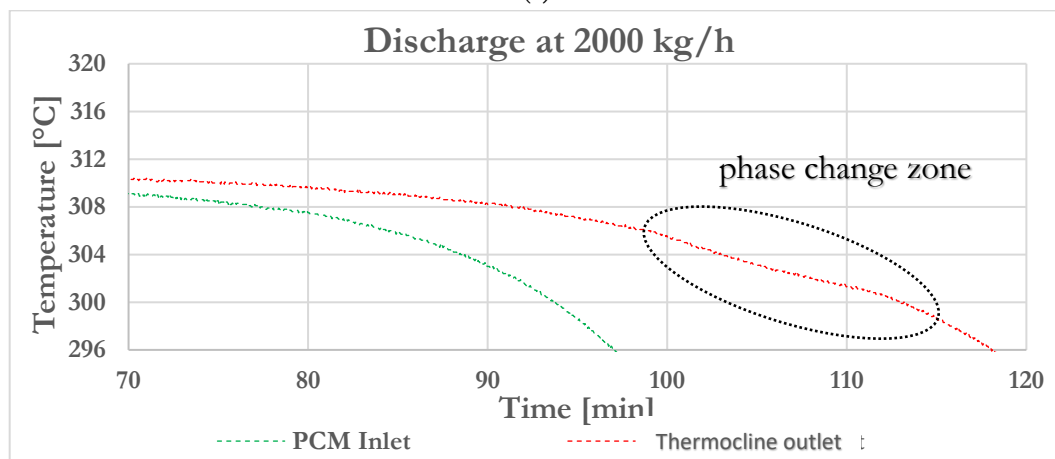
Figure 111 Le package de couche MCP final

Tracé de l'évolution de la température à l'entrée de la couche MCP et à la sortie de la thermocline pendant le processus de décharge :

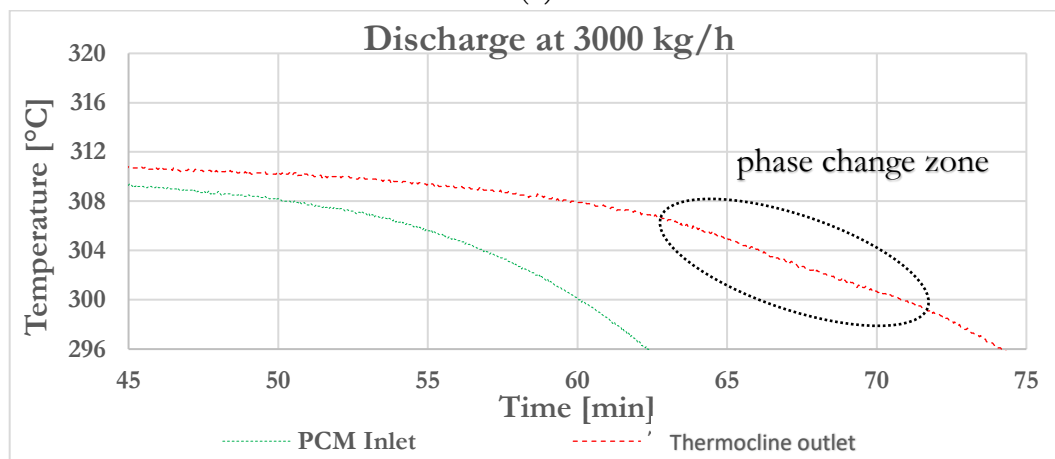
L'influence de la solidification du NaNO_3 est apparue à la température proche de la température de changement de phase de notre PCM. La courbe à la sortie a changé par rapport à la tendance de l'alumine Figure 112. Et c'est exactement ce pour quoi le design a été conçu.



(a)



(b)



(c)

Figure 112 Résultats expérimentaux pour le processus de décharge (315-220) °C à divers débits massiques stockage thermique combiné

Lors du tracé de l'épaisseur de la thermocline résultante à la coupure de décharge pour les débits massiques appliqués Figure 113, il peut être déduit qu'une épaisseur relativement faible est apparue max. 15%. De plus, l'augmentation du

débit de décharge s'accompagne d'une épaisseur de thermocline plus importante, ce qui n'est pas vraiment favorable lors de l'opération.

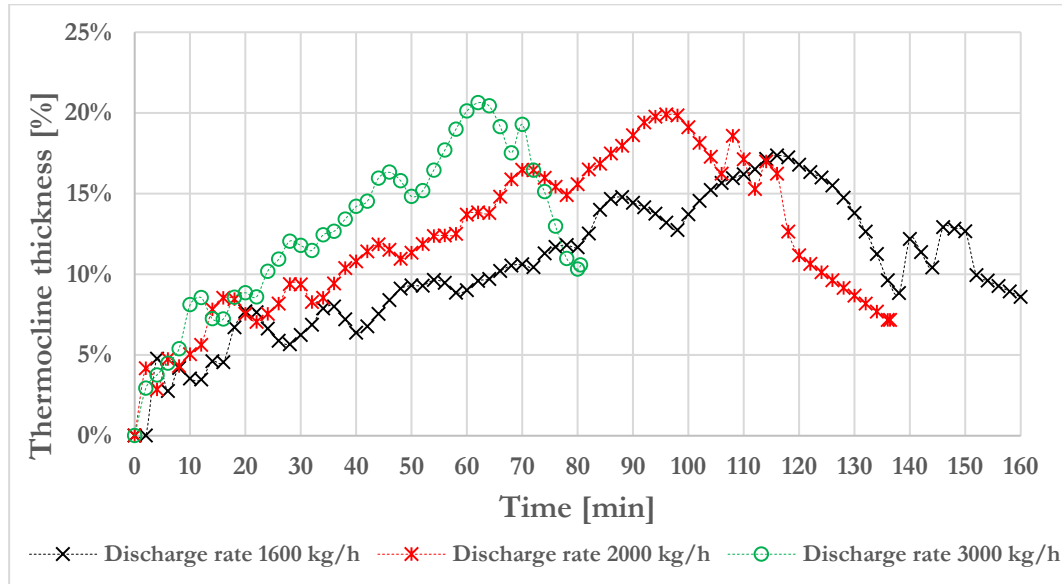


Figure 113 Épaisseur de thermocline expérimentale pendant la décharge (315-220) °C à divers débits massiques

L'efficacité lors de la décharge est réduite en augmentant le débit massique.

Compte tenu des trois indicateurs appliqués dans ce travail, cela pourrait suggérer que, l'augmentation du taux de décharge, réduit les performances du réservoir combiné, et diminue l'influence du MCP.

12.5. LES SIMULATIONS NUMERIQUES

Un transfert de chaleur complexe est attendu à l'intérieur du réservoir de stockage en raison des interactions entre différentes méthodes de transfert de chaleur en même temps. Pour simplifier l'étude, quelques hypothèses peuvent être faites.

Basé sur les équations du bilan énergétique pour le fluide et les particules les modèles qui sont utilisés pour simuler le stockage à un réservoir peuvent être classés en 6 catégories principales, soit pour sensible ou latent ou même combiné sensible/latente Figure 114.

Ce travail utilise (modèle 5) contentieux-solide a (C-S) pour notre stockage de chaleur sensible car la condition du nombre de Biot (Bi) est satisfaite pour le matériau de stockage sensible. Et dans la partie sensible du cas combiné. Et un modèle concentrique de dispersion (D-C) dans la couche MCP car Bi de l'encapsulation MCP est supérieur à 0,1 Figure 115.

La méthode de porosité enthalpie est utilisée pour simuler le changement de phase dans les matériaux

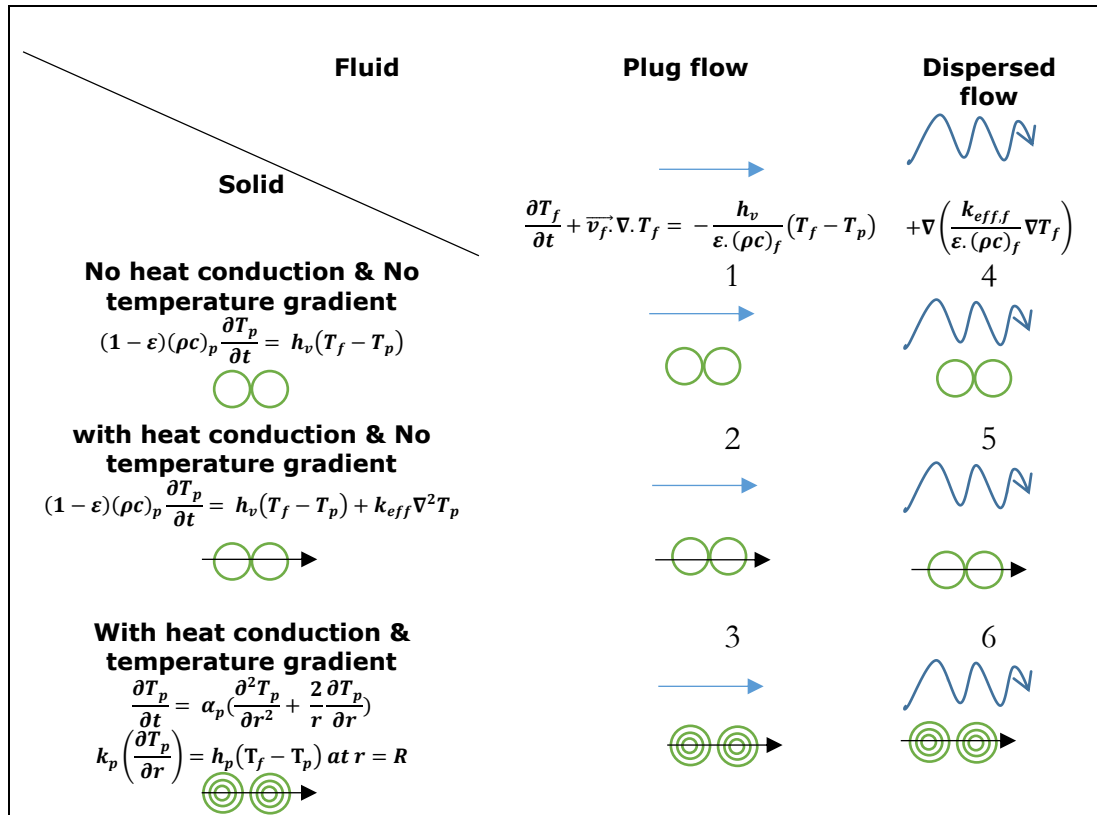


Figure 114 Modélisation des méthodes de thermocline basées sur des équations de bilan énergétique du caloporteur et des particules solides

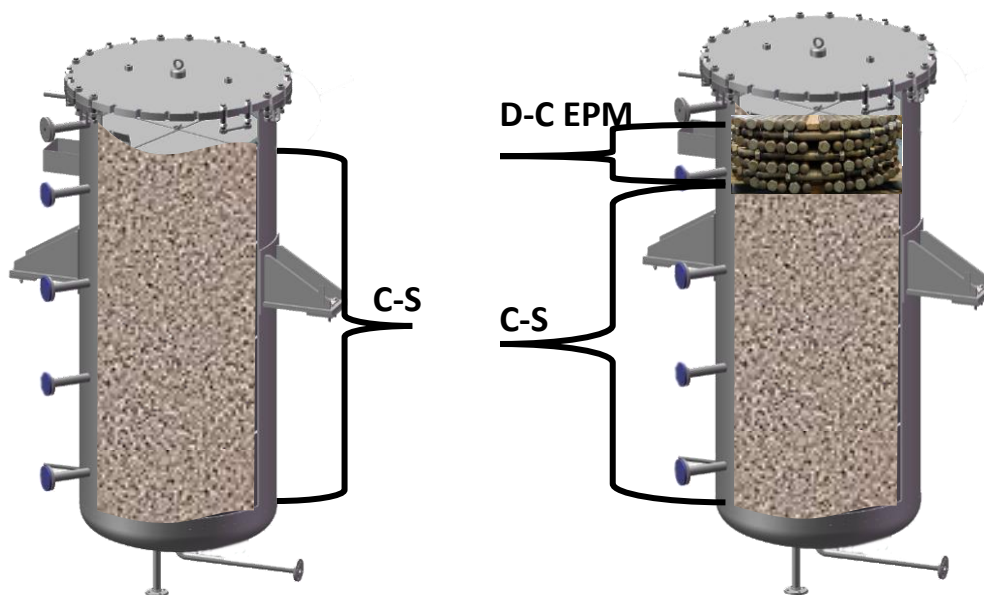


Figure 115 Modélisation des stockages de chaleur sensible et concept combiné de stockage de chaleur sensible-latente

La Figure 116 (a) et (b) comparent le profil de température simulé du modèle à celui expérimental pour l'alumine et le Cofalit®, respectivement. Un bon accord est démontré entre les résultats simulés et les données expérimentales dans les deux matériaux pendant le processus de charge.

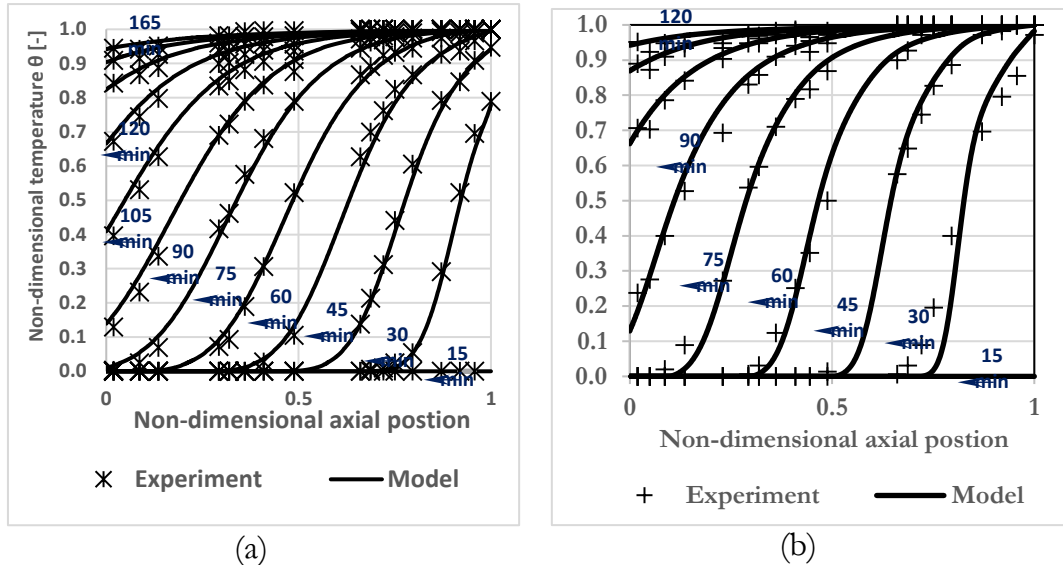


Figure 116 Profil de température pour (a) l'alumine, (b) Cofalit® modèle contre expérience pendant la charge

Pour le processus de décharge, les températures du modèle ont légèrement dévié des températures expérimentales dans les deux cas, à des températures inférieures à 20% de la température maximale près de l'entrée de la thermocline (en bas), Figure 117 (a) et (b), respectivement.

Cet écart peut être attribué aux écarts entre la température d'entrée constante de la thermocline supposée par le modèle et la température d'entrée instable réelle.

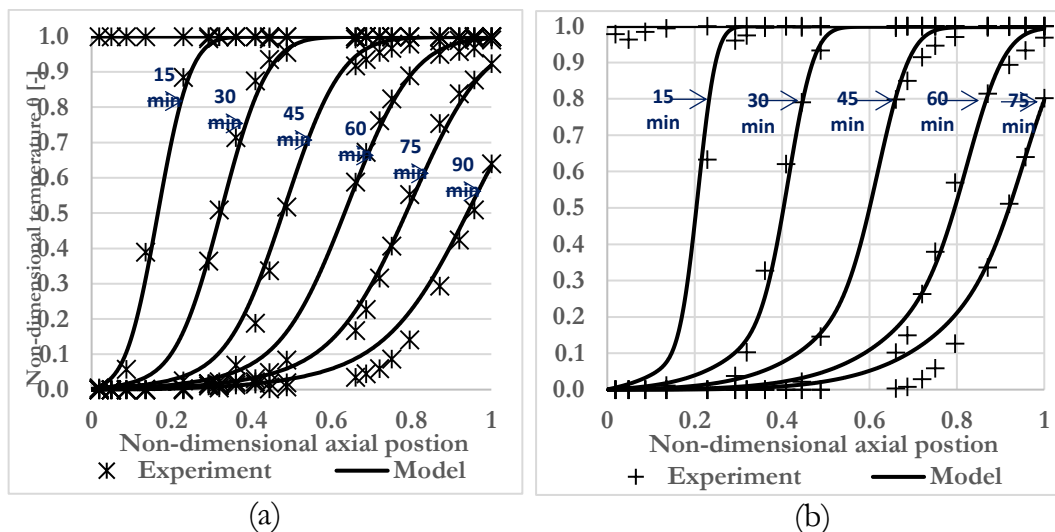


Figure 117 Température de (a) l'alumine (b) pendant le modèle de décharge Vs. expérience

Par conséquent, le modèle a fourni une précision appropriée du profil de température prédit par rapport aux expériences pendant le processus de décharge pour l'alumine ainsi que pour le Cofalit®.

Pendant la charge de l'expiration des sphères combinées NaNO_3 -alumine, le fluide chaud pénètre dans le stockage par le haut du réservoir (où se trouvent les tubes MCP), et l'huile froide est extraite du fond des réservoirs Figure 118.

Les points représentent la température expérimentale tandis que les lignes sont les résultats du modèle et le profil est tracé tous les 30 minutes.

Le modèle a un bon accord avec les températures mesurées. L'influence de la fusion du MCP se reflète sur la température du fluide près de la fusion thermique du MCP à plusieurs pas de temps 30, 60 et 90 minutes

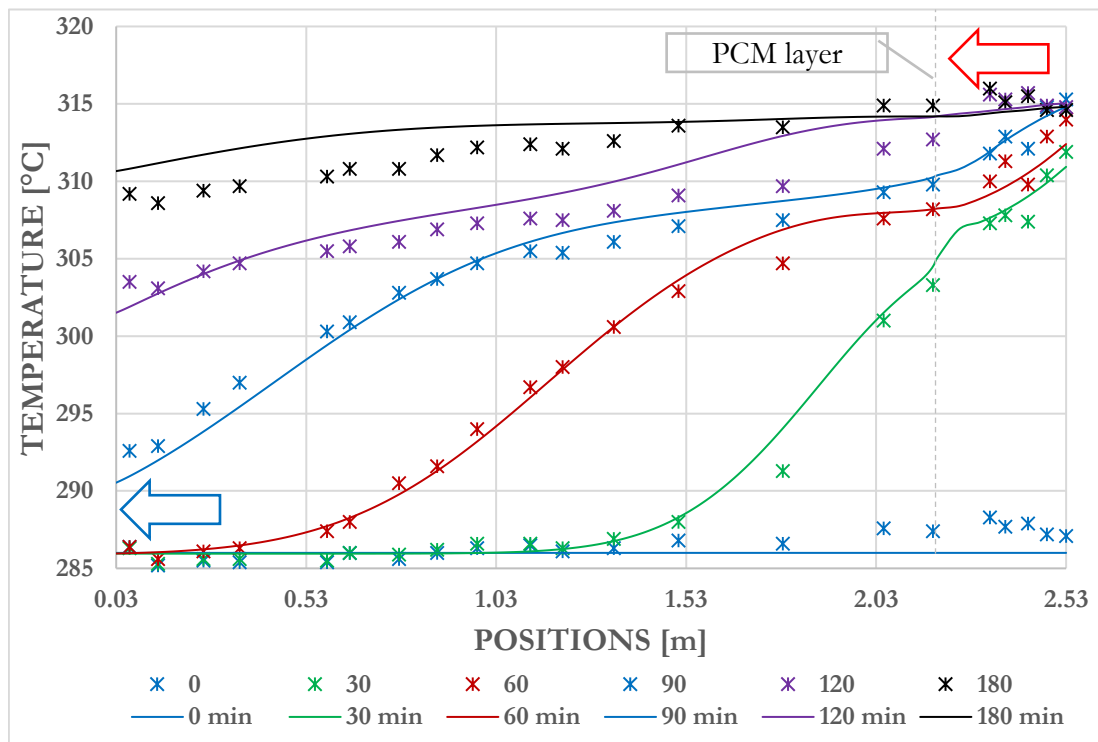


Figure 118 Profil de température de la thermocline NaNO_3 -Alumine pendant le processus de charge, modèle contre expérience

Lors du décharge, l'huile froide est injectée depuis le point le plus bas des réservoirs, et l'huile chaude est extraite à la sortie des réservoirs en haut, (où les tubes MCP). Les températures expérimentales sont illustrées en points tandis que les résultats simulés sont les lignes, et le profil de température est tracé tous les 15 minutes Figure 119.

Le modèle avait également un accord acceptable avec les températures expérimentales. Le comportement isotherme du MCP se reflète sur la température

du fluide après 75 minutes jusqu'à 105 à une température proche de la température théorique de solidification du MCP.

Le modèle s'est écarté de l'expérimental au cours des 30 dernières minutes entre 120 et 135 minutes, ce qui pourrait être attribué au débit massique instable dans le cadre expérimental.

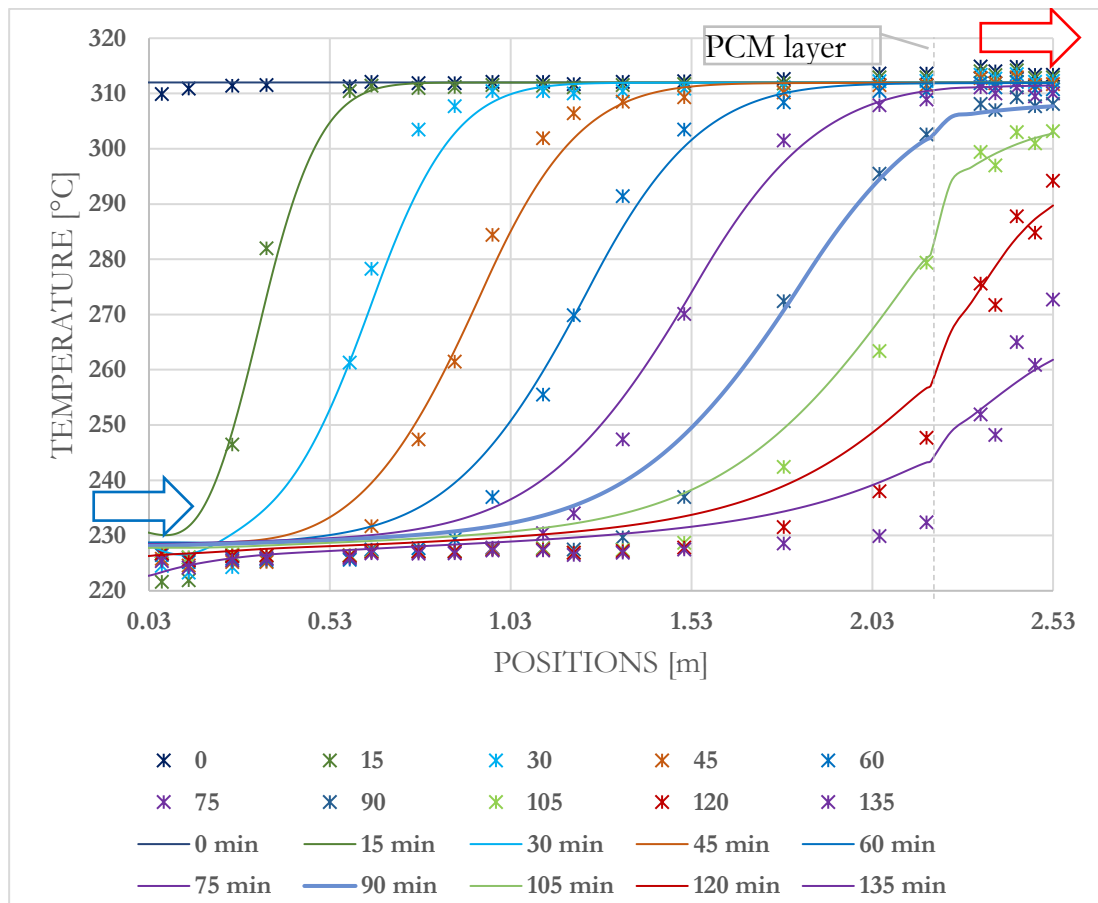


Figure 119 Profil de température de la thermocline NaNO_3 -Alumine pendant le processus de décharge, modèle contre expérience

Afin de constater la valeur ajoutée de la couche de tubes MCP, nous devons comparer les performances des réservoirs entre le cas où NaNO_3 -alumine-sphères, au stockage de base rempli uniquement de sphères d'alumine Figure 120.

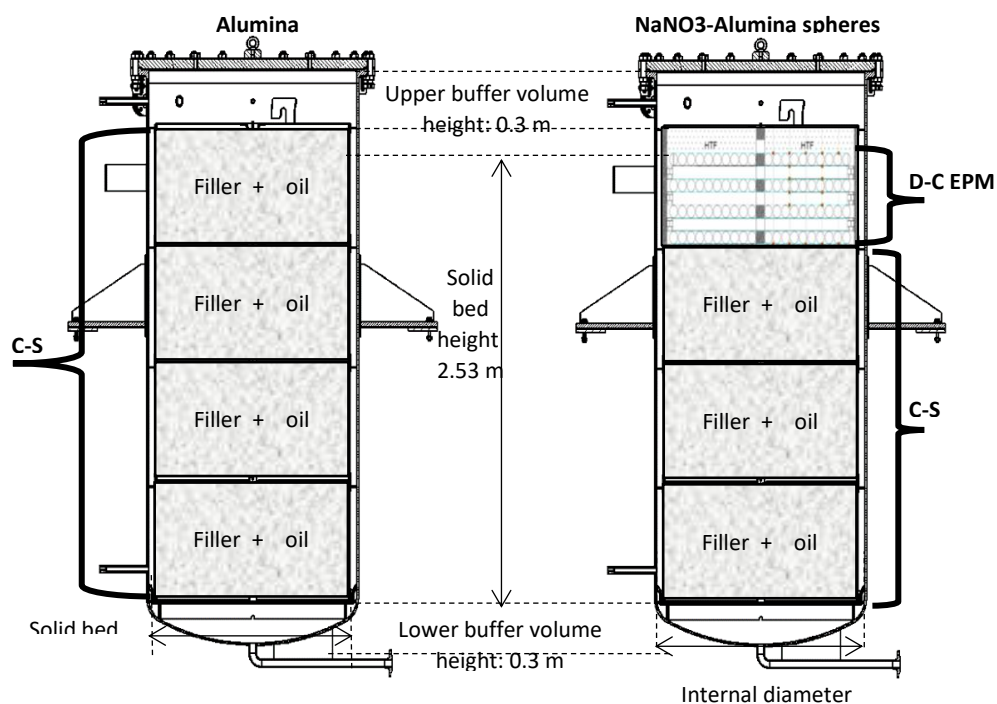


Figure 120 Simulation numérique de deux thermoclines combinées de sphères d'alumine NaNO_3 par rapport aux sphères d'alumine uniquement

En traçant le temps de charge par rapport aux trois taux de charge utilisés Figure 121, on peut voir que le réservoir combiné a besoin de plus de temps pour se charger à tous les débits massiques, ce qui est attribué à sa plus grande capacité thermique par rapport à la chaleur sensible uniquement.

De plus, l'augmentation du taux de charge réduit le temps de charge, dans les deux cas.

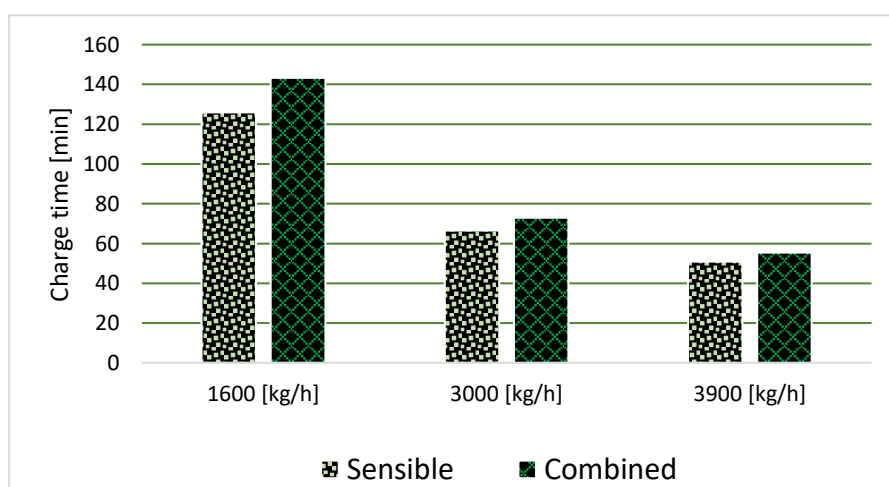


Figure 121 temps de charge pour chaque taux de charge utilisé (220-315) °C.

Pour l'épaisseur de la thermocline pendant la charge, Figure 122 montre qu'elle n'est pas influencée par le taux de charge. Mais l'épaisseur était un peu plus grande dans le réservoir combiné par rapport au réservoir sensible.

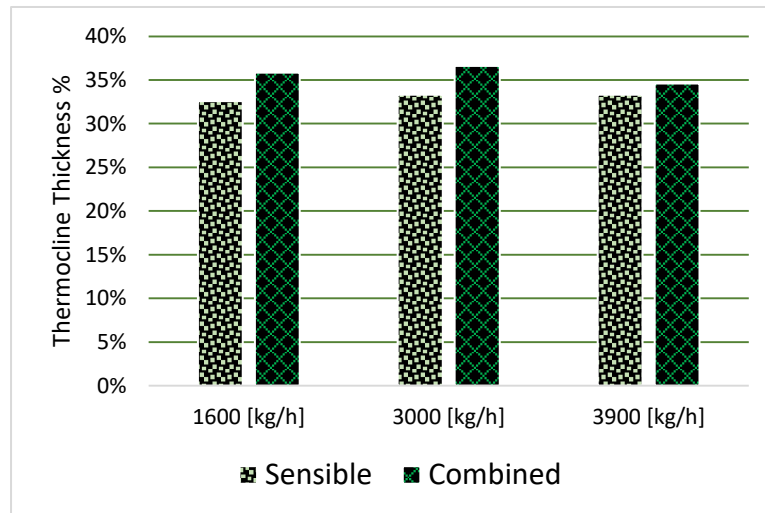


Figure 122 Épaisseur de la thermocline pendant la charge pour chaque taux de charge utilisé

L'efficacité de charge est meilleure à plus faible débit massique dans le cas combiné par rapport au sensible Figure 123.

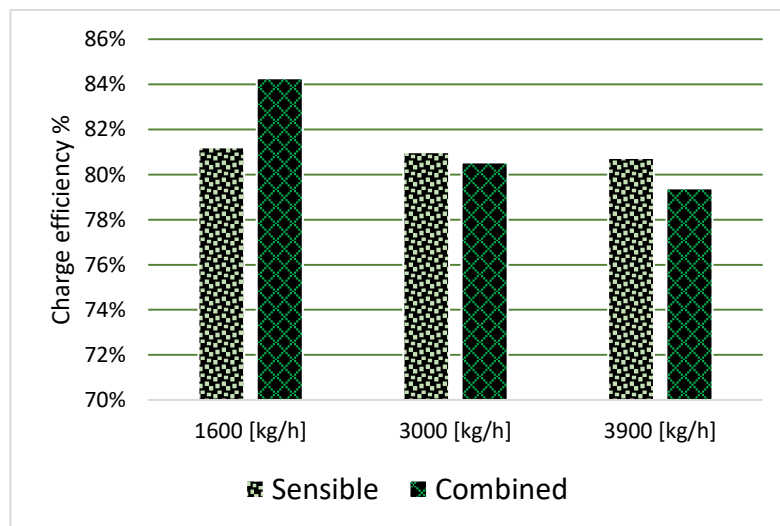


Figure 123 Efficacité de charge

Cependant, en augmentant le débit massique, l'efficacité a chuté dans le réservoir combiné à une valeur encore plus faible que le sensible. Pour enquêter sur ce qui se passe, la qualité du MCP peut être vérifiée en observant la fraction liquide.

L'avantage de la méthode de porosité enthalpique est la possibilité d'estimer la fraction liquide dans le MCP.

Par conséquent, le graphique montre un instantané de la distribution de la fraction liquide le long du volume de contrôle du rayon du tube. Si le matériau est solide, la fraction liquide est de 0, Si le matériau est liquide, elle doit être de 1. Toute valeur intermédiaire indique une proportion entre les deux.

Il est important de noter ici, que la fraction liquide n'est pas une valeur définitive, le modèle est 1D et la géométrie des tubes est complexe à part il y a quelques hypothèses, donc ce n'est qu'une indication sur la qualité du MCP.

Figure 124 montre la fraction liquide au 7ème tube en fin de charge au débit le plus bas. on peut noter la, la fraction liquide est de 1 ce qui signifie que tout le MCP est fondu et c'est normalement le résultat souhaité, tout le MCP doit être fondu pendant la charge.

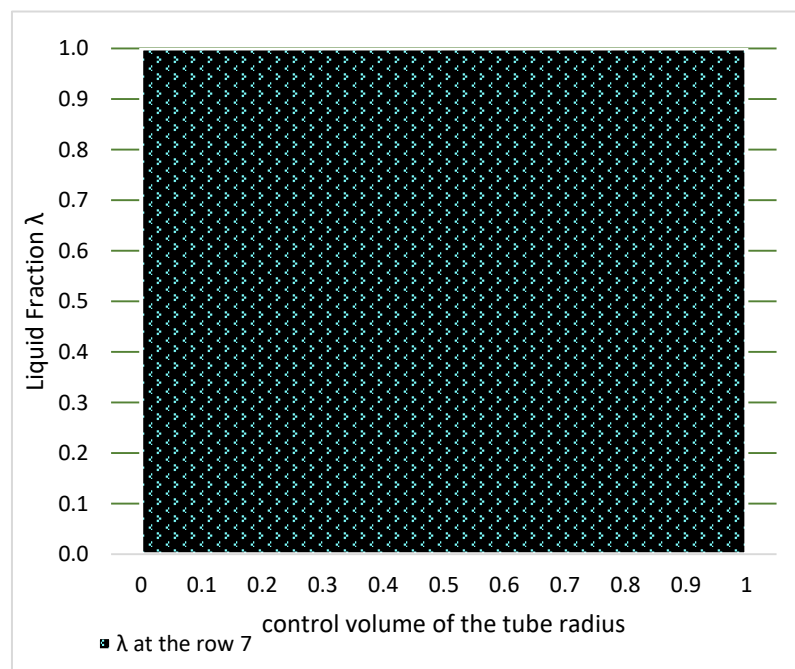


Figure 124 Fraction liquide estimée au 7ème tube pendant la charge lorsque la température seuil est atteinte à 1600 kg/h

D'autre part, au taux de charge maximum Figure 125, les deux premières rangées ont un MCP complètement fondu, les deux deuxièmes rangées ont une fraction liquide restante, tandis que les trois dernières rangées le MCP est encore complètement solide.

Cela suggère que des précautions doivent être prises lors de l'utilisation d'un taux de charge élevé car cela réduit l'efficacité. Plus important encore, tout le MCP n'est pas fondu, ce qui affectera certainement le processus de décharge après

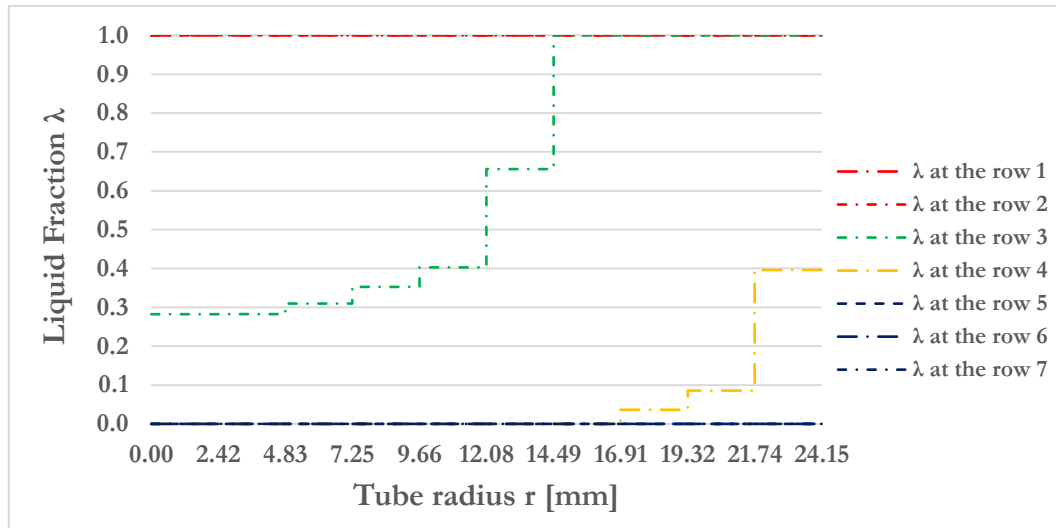


Figure 125 Fraction liquide estimée à tous les tubes telle que représentée par le D-C EPM à la fin de la charge à 3900kg/h

Ensuite, les performances thermiques de décharge qui sont notre objectif principal dans cette recherche.

Figure 126 montre le temps de décharge en fonction du taux de décharge pour les deux cas comparés. Le cas combiné décharge plus longtemps que le raisonnable pour les trois taux, ce qui répond à l'objectif principal du travail.

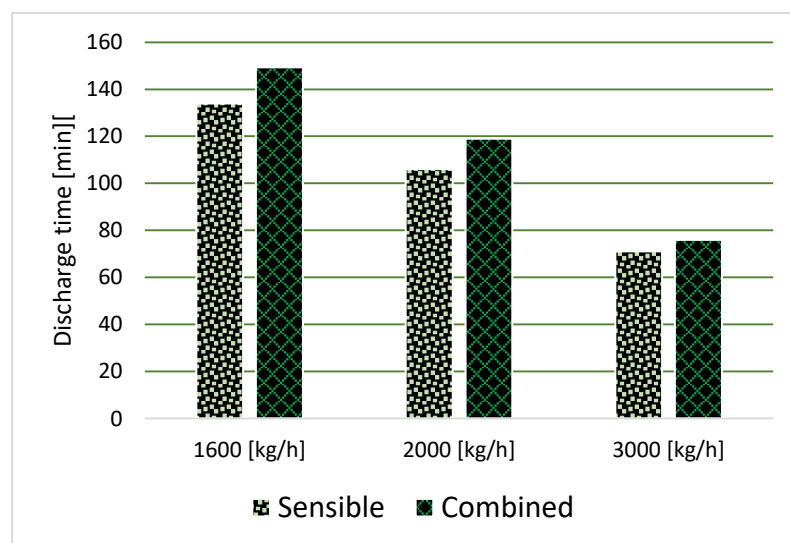


Figure 126 temps de décharge pour chaque taux de décharge utilisé (220-315) °C

Figure 127 trace l'épaisseur de la thermocline pendant le processus de décharge par rapport aux trois taux évalués. L'épaisseur est également meilleure (plus petite) dans le cas combiné par rapport au sensible dans tous les cas. Mais il augmente avec l'augmentation du débit massique.

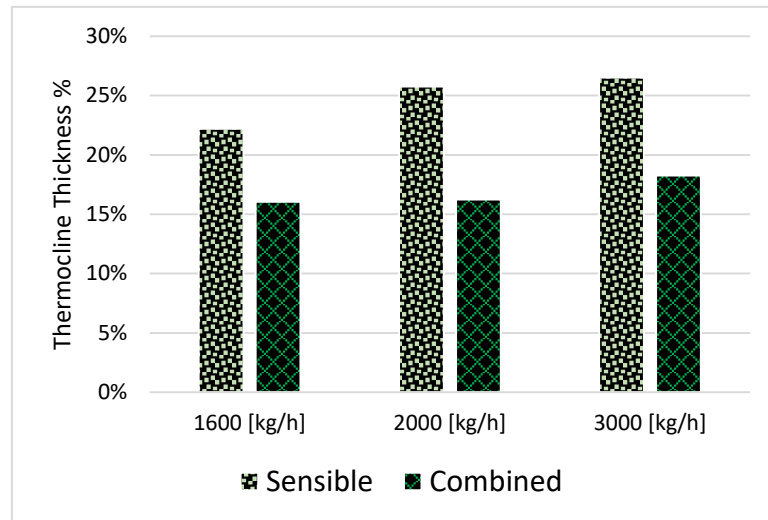


Figure 127 Épaisseur de la thermocline pendant la décharge pour les taux de charge utilisé

L'efficacité de décharge, que la conception essaie de l'optimiser. D'après la Figure 128, on peut voir que l'efficacité est meilleure dans le stockage combiné par rapport au stockage sensible aux trois taux. On peut aussi remarquer que l'efficacité de décharge pour le cas combiné diminue avec l'augmentation du taux. Par conséquent, nous avons voulu étudier la qualité du MCP.

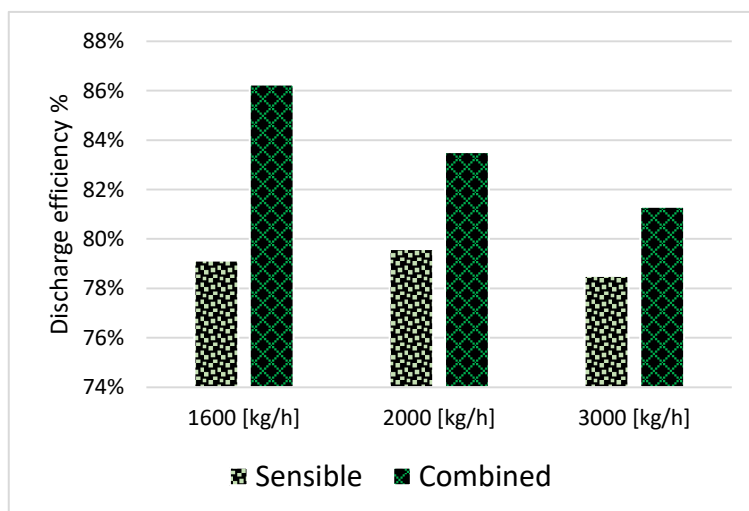


Figure 128 Efficacité de décharge

Dans ce cas, Figure 129 illustre un instantané de la fraction liquide le long du volume de contrôle du diamètre du tube à la coupure de décharge, au débit de décharge le plus bas.

L'objectif lors de la décharge est de solidifier tout le MCP c'est-à-dire que toute la fraction liquide doit être à 0. Figure 129 illustre que la première rangée est solidifiée mais la rangée 4 à 7 a une quantité importante de MCP est encore en phase liquide.

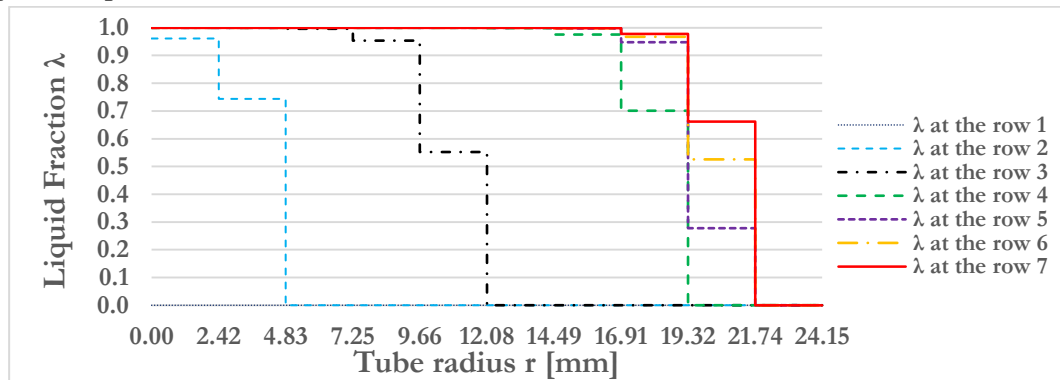


Figure 129 Estimation de la fraction liquide toutes les rangées de MCP lors du rejet lorsque la température seuil est atteinte à 1600 kg/h

Et à un débit massique plus élevé, la qualité MCP est bien inférieure à celle requise à la fin de la décharge Figure 130.

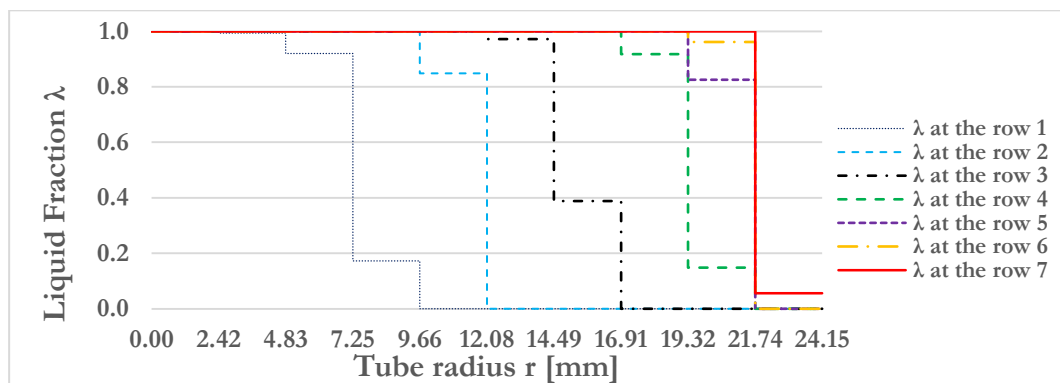


Figure 130 Estimation de la fraction liquide toutes les lignes PCM lors du rejet lorsque la température seuil est atteinte à 3000 kg/h

Ces résultats suggèrent qu'un taux de décharge élevé n'est pas favorable à la solidification du MCP car il réduit l'efficacité du système, ainsi que la quantité de MCP solidifié. De plus, même à faible débit massique, il est possible d'améliorer les performances du système en essayant d'améliorer le transfert de chaleur dans les tubes MCP à la fin du processus.

12.6. RESUME DES CONCLUSIONS

Dans ce travail, les performances de déchets à base d'amiante appelés Cofalit® ont été comparées expérimentalement à des sphères d'alumine comme matériau céramique de référence, en utilisant l'installation MICRO SOL-R de PROMES Odiello.

Le Cofalit® a une capacité calorifique volumétrique de 22 % inférieure à celle de l'alumine, ce qui se traduit par un temps de charge 20 % plus rapide et un temps de décharge 15 % plus court. L'épaisseur de la thermocline est plus faible, avec respectivement 26 % contre 31 % pour la charge et 20 % contre 26 % pour les procédés de décharge. De plus, les rendements des procédés sont meilleurs, avec 82 % contre 80 % pour la charge et 90 % contre 83 % pour la décharge.

Cofalit® surpasse la céramique d'alumine au niveau de température de ce travail, 300 °C, en raison de son diamètre moyen plus petit, de sa capacité calorifique volumétrique inférieure et de sa forme inhomogène.

Un modèle 1D C-S est développé et validé à partir des résultats expérimentaux pour un milieu de stockage de chaleur sensible. Le modèle est utilisé pour effectuer une analyse paramétrique du comportement thermique de la thermocline. L'analyse a indiqué qu'un diamètre de particule optimal pouvait être obtenu pour un matériau de remplissage solide donné dans des conditions de fonctionnement spécifiées, afin de fournir une meilleure efficacité de décharge et une épaisseur de thermocline plus petite. De plus, une augmentation de la capacité calorifique volumétrique augmente la durée du processus, tandis qu'elle diminue l'efficacité de décharge et augmente l'épaisseur de la thermocline.

Le modèle C-S fournit une excellente solution pour simuler le comportement thermique de la thermocline lorsque la charge solide a un $Bi < 0,1$. En même temps, le modèle D-C est meilleur pour les cas où $Bi > 0,1$. La méthode de porosité enthalpique (EPM) offre un moyen fiable de modéliser la fusion/solidification du PCM par rapport à la capacité thermique effective.

Un modèle 1D D-C EPM est développé et validé à partir des résultats expérimentaux de la littérature. Les deux modèles C-S et D-C EPM, sont couplés pour simuler le comportement thermique d'une thermocline combinée à 75 % de sphères d'alumine et 25 % de sphères de $NaNO_3$.

En outre, une approche de dimensionnement générale est suggérée pour estimer une plage de rapports MCP recommandés pour une thermocline

combinée. Il a indiqué que pour cette étude, un ratio de NaNO_3 compris entre 8,5% et 19% est recommandé pour la thermocline à base de sphères d'alumine, et une fourchette comprise entre 6,5% et 14,5% pour le cas Cofalit®.

Une couche MCP à 5,5 % en volume est conçue et mise en œuvre dans la thermocline MICROSOL-R. La couche est constituée de tubes en acier inoxydable et de NaNO_3 en tant que MCP. Les résultats expérimentaux suggèrent qu'un débit massique inférieur est favorable par rapport à un débit massique plus élevé pendant le processus de charge et de décharge.

De plus, la température d'entrée inférieure est favorable pendant la charge car plus la température d'entrée est proche du point de fusion du MCP, plus le potentiel de (SUPER-COOLING) est faible.

Le modèle combiné est modifié pour s'adapter au cas du tube et validé à partir des résultats expérimentaux pour la charge et la décharge. Les simulations ont combiné un C-S sur la partie de stockage de chaleur sensible et un D-C EPM dans la couche MCP.

Une comparaison numérique est effectuée à l'aide du modèle combiné validé pour évaluer les deux paramètres de performance de la solution, NaNO_3 -Alumine-sphères et sphères d'alumine uniquement thermocline, pendant la charge et la décharge.

Le rendement de charge dans le stockage thermique combiné s'avère supérieur de 4 % à l'achat sensible seulement à des débits massiques de 1600 kg/h, tandis qu'à un taux de charge plus élevé, il n'y a pas de changements essentiels dans l'épaisseur et le rendement. Des taux de charge élevés doivent être évités car ils sont associés au potentiel de ne pas faire fondre l'ensemble du MCP à la valeur seuil de charge et à un potentiel plus élevé de (SUPER-COOLING).

Au cours des simulations de décharge, le stockage thermique combiné surpasse les sphères d'alumine uniquement avec une efficacité de décharge supérieure de près de 4 %, une épaisseur de thermocline inférieure de 4 % et une durée de décharge plus longue. L'allongement de la durée de décharge s'améliore en diminuant le débit massique. Les fractions liquides estimées à la température de seuil de décharge suggèrent qu'il y a encore un MCP liquide dans les tubes. Par conséquent, les performances de la thermocline peuvent être améliorées en appliquant un procédé d'amélioration du transfert de chaleur approprié dans la couche MCP.

12.7. LES PERSPECTIVES

- Bien que le stockage thermique combiné surpasse celui de la chaleur sensible uniquement, il existe encore de l'énergie potentielle qui peut être utilisée dans les tubes, comme le suggèrent les résultats numériques. Par conséquent, il est nécessaire d'étudier et d'évaluer l'intégration d'ailettes métalliques sur la face interne des tubes pour améliorer les performances de la couche MCP, où le nombre, la forme et l'épaisseur des ailettes doivent être optimisés.
- De plus, l'avantage du stockage thermique combiné pourrait être vu plus clairement en simulant une charge et une décharge cycliques. Parce qu'il se caractérise par une épaisseur de thermocline inférieure à celle de la thermocline à sphères d'alumine, on s'attend donc à ce qu'il ait de meilleures performances cycliques globales. Par conséquent, une étude de cyclage numérique est recommandée pour illustrer la valeur ajoutée de la couche MCP.
- La stabilité des propriétés thermophysiques du MCP sous cyclage thermique doit être abordée, principalement la chaleur latente de fusion et les conductivités thermiques, qui peuvent se dégrader sous le cyclage thermique et les corrosions de l'enveloppe.
- L'ajout d'une couche de MCP à la thermocline de chaleur sensible SET est une solution intéressante pour prolonger la durée et l'efficacité de décharge si la taille du réservoir est fixe en raison de contraintes de conception. Sinon, une étude technico-économique doit être réalisée pour trouver ce qui est le plus économiquement faisable, en étendant la taille du réservoir ou en ajoutant une couche de MCP.
 - Le principal inconvénient de l'ajout de la couche MCP est de retirer une partie des matériaux de remplissage de chaleur sensible d'origine, ce qui réduit l'énergie potentielle stockée dans la thermocline et augmente le coût. Par conséquent, le MCP pourrait être mieux intégré dans le SET dans le distributeur de fluide en haut et/ou en bas du réservoir. Par exemple, dans les travaux en cours intégrer le MCP dans le distributeur de fluide caloporteur pourrait être très intéressant car cette zone n'est pas un volume de stockage d'énergie. Il est réservé à l'amélioration de l'écoulement du fluide à l'intérieur du réservoir. Ainsi, la conception du distributeur pourrait être optimisée pour intégrer le MCP et étendre sa fonction pour optimiser la température du fluide ainsi que son débit.

Etude théorique et expérimentale d'un composant de stockage thermocline avec matériau à changement de phase : intégration à une centrale électro-solaire à concentration

Mots clés: Centrale solaire à concentration (CSC), Stockage d'énergie thermique (SET), Thermocline, Chaleur latente, Chaleur sensible, matériau à changement de phase (MCP), Déchets recyclés, Projet pilote, Modélisation numérique, Modèle solide continu (C-S), Modèle concentrique de dispersion (D-C), Paramètres de performance thermique, Méthode de porosité enthalpique.

Le résumé :

La chaleur produite dans les centrales solaires à concentration (CSC) peut être stockée à faible coût dans le but d'étendre la durée de production d'électricité quotidienne, ce qui représente un avantage sur les systèmes photovoltaïques. La technique la plus souvent employée repose sur deux réservoirs de fluide caloporteur, un chaud et un froid. Des travaux sur le stockage «thermocline» sont actuellement menés en vue de réduire les coûts d'installation du stockage : la chaleur sensible est stockée dans un lit poreux de matériaux inertes, la charge et la décharge se faisant par deux entrées opposées dans le réservoir. Cette technique est limitée par le fait que le gradient de températures (la thermocline) est de plus en plus large au sein du lit poreux au fur et à mesure de son utilisation, donc la température du fluide réchauffé n'est pas constante et le groupe de production perd en puissance. Les travaux porteront sur l'intégration de matériaux à changement de phase (MCP) dans une CSC de 150 kWth. L'objectif est de concevoir un système de stockage à chaleur latente permettant de garantir une meilleure stabilité des températures du fluide caloporteur que le système de thermocline à chaleur sensible. En particulier, les sujets suivants seront abordés: identification des MCP d'intérêt pour l'installation étudiée et caractérisation de leurs propriétés thermo-physiques, mise au point d'une solution d'encapsulation des MCP, implémentation dans l'installation existante et essais, modélisation de l'ensemble de l'installation, incluant les phénomènes de transfert externes et internes des MCP encapsulés, établissement d'un système de contrôle commande adapté au stockage mixte MCP/chaleur sensible.

Experimental and modeling study of a thermocline latent/sensible heat storage system integrated with a cylindrical-parabolic concentrated solar power plant

Keywords : Concentration solar power (CSP), Thermal energy storage (TES), Thermocline, Pilot-scale, Numerical modeling, Continuous solid model (C-S), Concentric dispersion model (D-C), Recycled waste as a solid filler, Phase change materials (PCM), Enthalpy porosity method (EPM), Thermal performance parameters.

Abstract:

Heat from concentrated solar plants (CSP) can be efficiently stored at low cost in order to increase the daily operating time of energy production, which represents an advantage on photo voltaic systems. The most common solution for this consists in adding two storage tanks, one for the hot fluid after the concentrators and the other for the cold fluid before them. In order to reduce the operational and capital cost of the installations, research on the thermocline solutions is ongoing: sensible heat is stored in a single tank containing a porous mineral bed, this tank being alternatively charged during day-time and discharged at night with the heat transfer fluid. An issue with this technique is that a temperature gradient exists in such storage systems, which limits the efficiency of the thermocline as a hot source for the thermodynamic cycle combined to the CSP. We are working on the integration of phase-change materials (PCM) in a CSP coupled to a micro solar power plant with 150 kWth capacity and 15 kW ORC turbine. The objective is to design a system offering a more stable outlet temperature than the actual thermocline based on sensible heat storage. The following issues will be addressed during this PhD work: Identify interesting PCM in regard of the potential operating conditions (about 300°C), Measure the thermo-physical properties of the selected materials, Design and develop an encapsulation solution, Install the necessary monitoring probes, Integrate encapsulated PCM into the existing thermocline (working with sensible heat storage) and perform tests with complete system (about 250 kWth storage capacity), Model the whole plant, focusing on heat transfer phenomena around and inside the encapsulated PCM, and in the storage tank, Develop a control system adapted to the management of the thermocline with PCM, Assess the potential of micro-CSP plants with mixed sensible material-PCM as storage solution; in particular the size effect will be studied.